NEW APPROACHES
IN SCIENCE AND ENGINEERING - 2025

Editors:
Assoc. Prof. Dr. Serap ÇEKLİ & Assoc. Prof. Dr. Uğur ODABAŞI

ARTİKEL AKADEMİ: 407

New Approaches in Science and Engineering 2025

Editor: Assoc. Prof. Dr. Serap ÇEKLİ & Assoc. Prof. Dr. Uğur ODABAŞI
Istanbul University-Cerrahpaşa
Department of Engineering Sciences

ISBN 978-625-5674-44-9

1st Edition: December 2025

Publisher Certificate No: 19708

Cover and Book Design: Artikel Akademi

PRINTING: Uzunist Dijital Matbaa Anonim Şirketi
Akçaburgaz Mah.1584.Sk.No:21 / Esenyurt - İSTANBUL

Certification No.: 68922

KARADENİZ KİTAP LTD. ŞTİ.
Koşuyolu Mah. Mehmet Akfan Sok. No:67/3 Kadıköy-İstanbul
0530 076 94 90

mail: destek@artikelakademi.com
www.artikelakademi.com

NEW APPROACHES
IN SCIENCE AND ENGINEERING - 2025

Editors:
Assoc. Prof. Dr. Serap ÇEKLİ & Assoc. Prof. Dr. Uğur ODABAŞI

WRITERS
Alev ER

Aysen E. OZEL

Cengiz Polat UZUNOGLU

Elif IŞIKÇI KOCA

Emin ÖZDEMİR

Ferhat GÜNGÖR
Gökhan ÇAYLI

Hasan TÜRKMEN

Meral ÖZOMAY
Mert DİNÇ

Ozan ERCAN

Ömer ALGORABİ

Rüçhan YILDIZ

Seçil Bahar KORKMAZ

Seda ŞANSAL POLAT
Sefa CELIK

Serhat ERYAMAN

artikel akademi

CONTENTS

FOREWORD..... 7

CHAPTER 1

SYNTHESIS, POLYMERIZATION AND APPLICATION OF ITACONIC ACID 9

Prof. Dr. Gökhan ÇAYLI & Mert DİNÇ

CHAPTER 2

BACTERIAL CELLULOSE-BASED APPROACHES FOR WOUND HEALING AND REGENERATION..... 45

Asst.Prof. Dr. Elif IŞIKÇI KOCA

CHAPTER 3

MECHANICAL PROPERTIES OF HEMP FIBER REINFORCED COMPOSITES..... 65

Öğr. Gör. Dr. Emin ÖZDEMİR & Seçil Bahar KORKMAZ

CHAPTER 4

COMPUTATIONAL STUDY OF FORMONONETIN AND PICROPODOPHYLLIN INTERACTIONS WITH CANCER RECEPTORS, ESPECIALLY DNA AND EGFR.....93

Prof. Dr. Sefa CELIK & Prof. Dr. Aysen E. OZEL

CHAPTER 5

MOLECULAR DOCKING STUDIES OF GRISEOFULVIN AND NEOMYCIN MOLECULES USED IN STAPHYLOCOCCUS AUREUS AND E.COLI TREATMENTS..... 101

Assoc. Prof. Dr. Alev ER & Prof. Dr. Sefa CELIK & Prof. Dr. Aysen E. OZEL

CHAPTER 6

ANTIBACTERIAL POTENTIAL OF CEFACLOR AND EMBELIN: MOLECULAR DOCKING ANALYSIS 109

Assoc. Prof. Dr. Alev ER &Prof. Dr. Sefa CELIK

CHAPTER 7

SYNERGISTIC EFFECTS OF BORAX, ALUMINUM HYDROXIDE, AND MAGNESIUM HYDROXIDE ON THE FLAME RETARDANCY, THERMAL STABILITY, AND VERTICAL BURNING BEHAVIOR OF EPOXY COMPOSITES 117

Arş. Gör. Hasan TÜRKMEN & Rüçhan YILDIZ

CHAPTER 8

THE AERODYNAMIC AND HYDRODYNAMIC DESIGN OF SAILING YACHTS 135

Öğr. Gör. Dr. Emin ÖZDEMİR & Ozan ERCAN

CHAPTER 9

ELECTRIC VEHICLE CHARGING STATIONS 161

Serhat ERYAMAN & Prof. Dr. Cengiz Polat UZUNOGLU

CHAPTER 10

BIBLIOMETRIC MAPPING OF FEDERATED LEARNING AND ENERGY EFFICIENCY: AN ANALYSIS OF APPLICATIONS AND OPTIMIZATION TRENDS DURING 2020–2024 185

Dr. Ömer ALGORABİ

CHAPTER 11

FISHBONE TECHNIQUE FOR CAUSE-AND-EFFECT ANALYSIS OF BIOLOGICAL RISKS IN MUSEUM TEXTILES.....207

Seda ŞANSAL POLAT & Asst. Prof. Dr. Ferhat GÜNGÖR & Assoc. Prof. Dr. Meral ÖZOMAY

FOREWORD

As a species, we have the greatest potential for understanding and influencing the natural world through the scientific and technical disciplines. In addition to expanding our current understanding, these disciplines have long been a key engine of social advancement through the introduction of novel ideas, practices, and technology. Given the current rate of scientific and technological development, it is essential to think outside of the box and embrace new ideas.

For modern scientific and engineering challenges, the editors of "New Approaches in Science and Engineering—2025" set out to compile fresh perspectives, cross-disciplinary approaches, and cutting-edge practical applications. Presenting theoretical underpinnings with cutting-edge experimental, computational, and practical methods, this book illuminates the state of the art in the field.

This initiative seeks to foster the establishment of a unified scientific lexicon among academics across diverse disciplines, in light of the growing interplay between science and engineering. The novel methodologies introduced in materials science, chemistry, physics, biology, environmental sciences, and other engineering disciplines are centered on core principles like sustainability, efficiency, and technological innovation.

We anticipate that students, instructors, researchers, and practitioners will regard New Approaches in Science and Engineering-2025 as a contemporary and inspiring resource. We earnestly hope this book will motivate readers to engage in creative thinking, collaborate across disciplines, and make a lasting impact on the field of science.

Editors:

Assoc. Prof. Dr. Serap ÇEKLİ & Assoc. Prof. Dr. Uğur ODABAŞI

CHAPTER 1

SYNTHESIS, POLYMERIZATION AND APPLICATION OF ITACONIC ACID

Prof. Dr. Gökhan ÇAYLI
Istanbul University-Cerrahpaşa
Department of Engineering Sciences
https://orcid.org/0000-0002-3395-5642

Mert DİNÇ
Istanbul University-Cerrahpaşa
Department of Engineering Sciences
https://orcid.org/0000-0003-2411-5534

1. INTORDUCTION

As a bio-based organic acid that can replace a variety of petroleum-based chemicals, including acrylic and methacrylic acids, itaconic acid (IA) can be extremely significant for sustainable development. Unlike petroleum, IA is rapidly renewable (Bafana, 2017). Hence, it can reduce the dependency on petroleum and associated harmful effects on the environment (El-Imam AA, 2014)

The presence of the vinyl group in IA makes it useful for the synthesis of polymers such as poly-itaconic acid (Fleischhaker F, 2013), which can have wide industrial applications. The industrial potential of IA has been well reported by Okabe et al. (Okabe, 2009).

However, the production cost of IA is very high and needs to be reduced to at least $0.5/kg to be commercially competitive with petroleum-based products (Huang X, 2014). This can be achieved by reducing the number of synthesis steps, improving the microbial biocatalyst, reducing the byproduct formation,

increasing the volumetric productivity to at least 2.5 g $L^{-1}h^{-1}$, or lowering the cost of the recovery process and up-scaling (Geiser, 2015).

IA is presented in the form of white crystals, and it is chemically defined as an unsaturated dicarboxylic acid with one of the carboxylic groups conjugated to a methyl group. Some of IA characteristics are listed on Table 1

IA was found in 1837 and given the name "citric acid" after Baup described it as a byproduct of citric acid's pyrolysis. (Turner, 1841) (Kane, 1945) (Tate 1967). It was dubbed itaconic acid by Crassus in 1840, who described it as the result of citric acid's third stage of thermal breakdown. (Turner, 1841). Only one chemical route was known at the time.

Table 1: Properties of itaconic acid

IUPAC Name	2-Methylidenebutanedioc acid
Synoyms	Itaconic acid, 2-Methylenesuccinic acid, Propylenedicarboxylic acid, Methylenebutanedioic acid, 2-Propene-1,2-dicarboxylic acid
Abbreviation	IA
CAS Number	97-65-4
Molecular formula	$C_5H_6O_4$
Molecular weight(g/mol)	130.09874
Melting point	165-168 °C
Density (g/cm3)	1.573

The IA chemical synthesis is as follows:

- distillation of citric acid;
- oxidation of isopropene or from mesityl oxide to citraconic acid and subsequent isomerization;

- carboxylation of acetylene derivatives, for example, propargyl chloride or butynoates;
- condensation of succinate or succinic anhydride with formaldehyde to generate citraconic acid with subsequent isomerization.

However, this series of chemical reactions is not economically viable. The requirement for several stages resulted in an unsatisfactory yield and used components that were not readily available (Merger, 1991).

IA was first polymerized by Swarts as a form of ethyl ester in 1873 (Tate 1967). Dialkyl ester polymers were developed with properties close to glass in a process that lasted about 3 days (Hope, 1927). Despite the interesting properties, it was only possible to obtain IA at a low scale due to the already mentioned low efficiency of the chemical route, which was a potential limitation for obtaining the end product on a large scale.

In 1931, Kinoshita first reported the production of IA by the microbial route. In his study, a filamentous fungus isolated from salted prune juice was cultivated under surface fermentation conditions in the presence of concentrated solutions of sugars and high concentrations of chlorides, reaching a yield of up to 0.24 (g IA/g substrate). Because the used microorganism was an IA producer, the filamentous fungus was named Aspergillus itaconicus (Kinoshita, 1931). The production condition of that study, however, was never developed commercially (Kane, 1945). Calam et al. (1939) presented that some A. terreus strains produced IA in Czapek-Dox medium containing 50 g/L of glucose. That was the first study that demonstrated that A. terreus was able to produce IA (0.12 g IA/g substrate after 25 days). The authors also showed that not all strains—5 out of the 6 strains tested—produced this organic acid in the extracellular medium at the conditions used (Calam, 1939).

The production of IA by the microbial route was first patented in 1945 (Kane et al. 1945). Pfizer Company accomplished 28% of the theoretical yield for producing IA with sucrose after 14 days of fermentation (Kane, 1945). IA was included in the company's product portfolio in 1945 (Okabe, 2009). More recently, IA was identified to be secreted by mammalian immune cells, such as macrophages, responsible for the antimicrobial activity by those cells in situations of inflammatory conditions (Sugimoto, 2011). IA was previously detected in the lungs of mice infected with tuberculosis, but it had been assumed that the metabolite was produced by the contaminating bacteria (Shin ve ark., 2011; Cordes, 2015). Michelucci et al. (Michelucci, 2013) identified that, in mammalian cells, IA is produced by the immunoresponsive gene 1 (Irgl), a highly expressed gene

by macrophages in inflammation. That IA characteristic was explored by Bajpai et al. (Bajpai, 2016) as a component of antimicrobial biofilm with potential application in the biomedical field.

IA was first commercially produced by Pfizer Company in 1945. Since then, other companies such as Iwata Chemical (started in 1970, in Japan), Rhodia (started in 1995, in France), and Cargill (started in 1996, in the USA) have been great producers (Okabe, 2009). The production interruption by Cargill, Pfizer, and Rhodia made China the current largest IA producer (El-Imam, 2014). China has been receiving robust investments from companies and from the Chinese government, including in bioprocess industries. The increasing research background, human resources, and financial support have provided the biotechnology industry growth over recent years in that country (Huang, 2010).

The IA market is characterized as a niche among other chemicals, mainly due to limited assimilation of IA products in the market and the large availability of substitutes for those. The decrease of production costs would increase IA economic feasibility and expand the commercial interest for IA (Transparency Market Research, 2015). Because of its market potential in a world scenario with increasing demand for bio-based chemicals, the IA market is expected to exceed 216 million dollars by 2020 (Global Industry Analysis, 2016). Currently, the most promising applications of IA are as synthetic latex, methyl methacrylate (MMA), unsaturated polyester resins (UPR), and superabsorbent polymer (SAP) (Global Market Insights 2016). Synthetic latex represents over 50% of the global market share of IA products, mostly used for polymer stabilization—SBR latex (styrene–butadiene rubber). As this niche market is already the most demanding of IA, it is expected to have less prominent growth over the next years (Global Market Insights 2016). The expansion of the MMA market, currently produced from acetone cyanohydrin (Weastra SRO, 2012), is expected to further fuel IA demand. MMA requirements in liquid-crystal display (LCD) screens, smartphone screens, and video equipment are some of the most likely applications of IA (Global Market Insights 2016).

Synthesis of IA involves shuttling of intermediate metabolites between the cytosol and mitochondria and utilizes enzymes of both the compartments (Figure x). Decarboxylation of cis-aconitate into IA, mediated by cis-aconitate decarboxylase (CadA), takes place in cytosol, whereas the preceding steps, that is, citrate and cis-aconitate synthesis, mediated by citrate synthase and aconitase, respectively, take place in mitochondria. In A. terreus, the key gene cadA is localized in a gene cluster that also contains genes encoding mitochondrial and plasma membrane transporter proteins, which are transcriptionally upregulated

during IA production (Li, 2011). Steiger et al. (Steiger, 2016) characterized MttA (a part of the IA synthesis gene cluster) as a mitochondrial cis-aconitic acid transporter protein and found that it specifically transports cis-aconitic acid from mitochondria to cytosol and does not transport IA during IA-producing conditions.

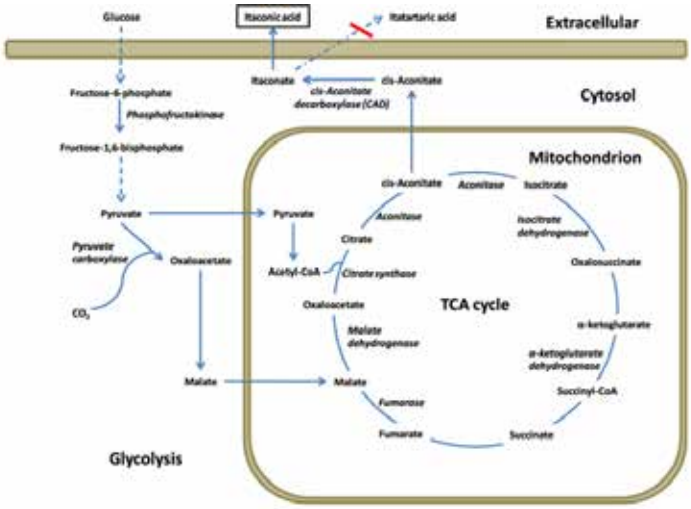

Figure 1: Biosynthesis of IA, taken from Itaconic acid—A biotechnological process in change—Scientific www.researchgate.net/figure/Biosynthesis-pathway-of-itaconic-acid-in-Aspergillus-terreus-Metabolites-are-given-in_fig1_234088434 [accessed 14 Oct 2025]

Several natural producers of IA have been identified, such as *Aspergillus terreus* (Calam, 1939), *Ustilago zeae* (Haskins, 1955), *Ustilago maydis* (Guevarra, 1990), and *Candida sp*. (Tabuchi, 1981), *Pseudozyma antarctica* (Levinson, 2006), *Rhodotorula* species (Kawamura, 1981), and even mammalian cells (Strelko, 2011). However, due to a relatively low yield compared to *A. terreu*s, none of them is used commercially (Steiger, 2013)

1.2. Synthesis of Itaconic Acid

1.2.1. Process parameters for itaconic acid production

Laboratory and pilot plant production of IA was first reported by the Rese-

arch Laboratories of the US Department of Agriculture. They used *A. terreus* NRRL 1960 strain to optimize the surface and submerged culture fermentation. Currently, IA is produced by the improved Pfizer process (Nubel, 1962), which involves pre-culture of A. terreus followed by submerged culture fermentation on pretreated molasses for 4 days under phosphate-limited conditions (Willke, 2001). pH and dissolved oxygen (DO) supply play a very important role in achieving good IA yields. The effect of initial pH on IA production with *A. terreus* was investigated several times, but the results were inconsistent. The effect of DO, on the other hand, is clearer. Fermentative production of IA by A. terreus is a strictly aerobic process requiring a sufficient oxygen supply of around 1.5 mol O_2 mol^{-1} IA produced from glucose (Klement, 2013). Low oxygen levels can result in increased NADH levels and depletion of ATP, which can damage the biomass and affect fungal metabolism. NADH can further inhibit both citrate synthase and phosphofructokinase. Hence, the regeneration of NAD as a cofactor is of extreme importance. Pfeifer et al. (Pfeifer, 1952) reported that the IA fermentation rate increased as the aeration rate increased to about 1=4 vvm (volume of air per volume of medium per minute) on the pilot plant scale. Addition of micronutrients also plays a very important role in successful IA production. For example, a sufficient iron supply is necessary to maintain the aconitase enzyme's functionality. Calcium, copper and zinc are also important cofactors for IA production (Klement, 2013).

1.2.2. Continuous processes for itaconic acid production

Nowadays, research is directed toward improving productivity by a continuous process. Continuous fermentation has several advantages compared to batch processing since it can be maintained at the optimal production conditions for a very long period. It also benefits downstream processing by providing a constant product stream, allowing the use of smaller equipment with less storage capacity, which in turn decreases costs and plant size. The most important problem faced during IA production is end-product inhibition. Continuous processes can overcome this problem by continuous replacement of the growth medium. Several studies are available with continuous fermentation of A. terreus, the most common IA producer (Klement, 2013). Conventional continuous processes use suspended cells, which are continuously produced in the bioreactor and removed in the product stream. Kobayashi and Nakamura and Rychtera and Wase (Rychtera, 1981) employed free submerged A. terreus cells and achieved productivity of 0.48 and 0.32 g L^1h^1 from glucose, respectively. In comparison, the available literature data revealed that batch productivity of

IA using A. terreus ranged between 0.4 and 0.6 g $L^{1}h^{1}$ (Kuenz, 2012). Thus, conventional continuous processes allow very low yield and productivity, which is in the same range as batch productivity. To overcome this, researchers are focusing on immobilization of the biocatalyst with biocompatible polymers, which can also facilitate process handling and downstream processing. With immobilized A. terreus cells, very high IA productivity, up to 1.2 g $L^{1}h^{1}$, has been reported (Kautola, 1985). The first matrix used in IA production was the polyacrylamide gel reported by Horitsu et al. (Horitsu, 1983). Various other matrices, such as porous disks, silica-based materials, alginate, polyurethane cubes, polyacrylamide, and fibrous networks of pawpaw trunk wood, were proposed for immobilization (Iqbal 2005). Kautola (Kautola, 1990) optimized continuous IA production from sucrose with *A. terreus* TKK 200-5-3 cells were immobilized on polyurethane foam cubes in column bioreactors and reported production of 15.8 g L^{1} with a sucrose concentration of 13.5%, an aeration rate of 150 mL min^{1}, and a residence time of 178 h. They also reported that IA production was stable for at least 4.5 months in a continuous column bioreactor.

1.2.3. Downstream processing

Production of biochemicals by fermentation is still limited in the modern market because their recovery from the dilute stream of a bioreactor is a cost-intensive process. The first step in the downstream process is biomass removal, after which the product is separated, concentrated, and purified to the desired extent. Various separation methods have been developed for recovery and purification of IA, including crystallization, precipitation, extraction, electrodialysis, and membrane separation. The choice of purification method depends on the desired product quality as well as its concentration in the medium.

Crystallization is a classical method for IA recovery. IA is easy to recover because it is crystallized at low pH via cooling or via evaporation–crystallization. Dwiarti et al. (Dwiarti, 2007) separated IA from the fermented broths of hydrolyzed sago starch and glucose using crystallization and achieved purity of about 97.2 and 99.2%, respectively, at the end of purification. Okabe et al. (Okabe, 2009) reported total IA recovery of 80% for industrial production using crystallization. IA can also be precipitated using calcium or lead salt. Lead is preferred over calcium salt precipitation because the lead salt of IA is almost insoluble in water and thus does not require pre-concentrating of the broth. Carbonates or bicarbonates of alkali metals or ammonium are used to generate lead itaconate and lead carbonate. Then, IA is separated from salt

using a cation exchange step (Kobayashi, 1971). Solvent extraction has been applied to separate a variety of carboxylic acids at the industrial scale. Kaur et al. (Kaur 2015) purified IA by solvent extraction using n-butanol. In a modified approach, Schute et al. (Schute, 2016) investigated selective recovery of IA from aqueous solution by liquid phase adsorption on hydrophobic adsorbents such as the hyper-cross-linked polymers. They reported that temperature had an insignificant effect on adsorption and the operation could be carried out over a broad temperature range, whereas selectivity decreased with increasing pH.

1.2.4. Process Intensification

Huang et al. (Huang, 2014) carried out direct IA production from liquefied cornstarch by integrating saccharification and fermentation into a single step. They used *A. terreus* overexpressing the glucoamylase gene for this purpose and achieved production of 77.6 g/L IA after 3 days of cultivation, which is very close to the industrial titer (80 g/L) from saccharified starch hydrolysates. Bressler and Braun (Bressler, 2000) designed a novel liquid membrane bioreactor to convert citric acid to IA by A. terreus. The bioreactor was divided into three chambers by two supported liquid membranes: a feed chamber, reaction chamber, and product chamber. These membranes allowed only unidirectional flow of the substrate from the feed chamber to the reaction chamber and of the product from the reaction chamber to the product chamber, thus maintaining a low concentration of substrate and product. This helped to overcome their inhibitory effect on a conversion process, which led to an increase in the IA yield by two orders of magnitude compared to the conventional batch process.

Carstensen et al. (Carstensen, 2013) introduced a new ISPR process called "reverse-flow diafiltration" (RFD) using a membrane reactor. In this method, the product containing the stream is passed through a membrane by outside-in filtration, and a replenishing stream is supplied over the same membrane inside-out. Thus, the two streams are exchanged over the membrane, and the overall volume of the medium in the bioreactor remains constant. Cake 10-layer buildup can be prevented by changing the filtration direction periodically. Application of RFD to IA, a production from *U. maydis,* resulted in a tenfold increase in yield.

A first general process scheme for the production of itaconic acid from wooden biomass was already proposed by Kobayashi in 1978. (Kobayashi, 1978) (Regestein, 2018) The process chain from biomass to itaconic acid is shown as a block flow diagram in Fig. x. The process starts with the mechanical pretreat-

ment of beech wood (Yan, 2014), which subsequently is subjected to chemo-catalytic biomass fractionation (OrganoCat) into three phases, which comprise cellulose pulp, aqueous hemicellulose, and organic lignin solutions (Grande, 2015). Lignin is transferred to further chemical valorization (Stiefel, 2016). The aqueous phase containing oxalic acid as well as hemi-cellulosic sugars (mainly pentoses) is treated by nanofiltration to recycle the catalyst back to the chemo-catalytic fractionation process and to concentrate the sugar hydrolysate. In a parallel step, the cellulose pulp is enzymatically hydrolyzed to yield glucose (Jäger, 2011), which—together with the pentose-rich stream—can be used as a carbon source in the fermentation (Jäger, 2012). The fermentation for the conversion of the sugar fraction into itaconic acid can either be performed with the established A. terreus or with Ustilago maydis, a fungus growing with a yeast-like morphology (Geiser, 2016). Both fermentation concepts were realized and evaluated. Depending on the fermentation, different downstream strategies can be applied to concentrate and purify itaconic acid. In this study, (in situ) filtration, (in situ) extraction, and crystallization were investigated, and the influence of the preceding on the subsequent purification process was evaluated.

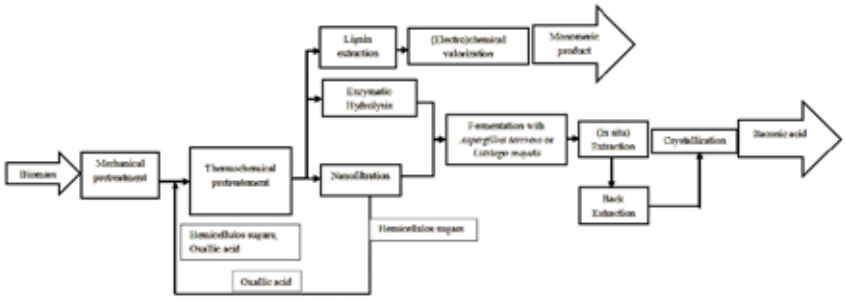

Figure 2: Block flow diagram of itaconic acid

In 2014, Tippkötter et al. investigated the enzymatic hydrolysis of beech wood to produce IA. Crude beech wood cellulose fractions prepared by an Organosolv process are used up to solid concentrations of 9%, 17%, and 23% (w/w) at very low enzyme dosages; thus, crude monosaccharide hydrolysates are obtained. The hydrolysate is used for different platform chemical fermentations.

At enzymatic hydrolysis, 152 g/L of glucose concentration was achieved at 23% solid content, but the yield of glucose has decreased with increasing solid content due to product inhibition. Also, it has been noted that using a solid-state reactor (Terrafors) showed lower yields (0.29 g/g), but applying a washing/sepa-

ration step increases the yield up to 0.49 g/g. In the fermentation step, *Clostridium acetobutylicum*, *Actinobacillus succinogenes,* and *Aspergillus terreus* bacteria have been used for fermentation of butanol, succinic acid, and itaconic acid, respectively. Butanol has been achieved with a yield of 0.33 g/g from beech wood hydrolysate; succinic acid has been obtained in a yield of 0.7 g/g. For obtaining IA, detoxification of hydrolysate was necessary. After that, IA has been gained in a yield of 0.3 g/g with a concentration of 7.2 g/L. (Tippkötter, 2014)

Guevarra et al. has explored the capacity of various strains of the genus *Ustilago* to produce various extracellular organic acids such as 2-hydroxypropanoic acid (HP), itatartaric acid (ITT), L-malic acid, and succinic acid in addition to IA during glucose fermentation in shake culture. Several of the 54 strains from 4 strains of *Tolyposporium bullatum* strains and 16 *Ustilago* species—most notably *U. cynodontis*, *U. maydis*, and *U. rabenhorstiana*—were found to be effective itaconate producers. The regular co-production of HP and ITT with IA in numerous strains was a significant discovery, indicating a biosynthetic connection between them. Furthermore, tests using toluene-permeabilized *U. cynodontis* cells demonstrated that enzymes could convert HP to ITT, confirming the presence of a metabolic pathway from the tricarboxylic acid (TCA) cycle to HP. Although it occurred at a much slower rate, nonenzymatic interconversion between HP and ITT under neutral pH was also seen. (Guevarra, 1990)

Noh, Myung Hyun, et al. focuses on developing an engineered *Escherichia coli* strain to efficiently produce itaconic acid from acetate, an inexpensive and abundant carbon source, aiming to reduce production costs and enhance economic viability in biochemical manufacturing. Aspergillus terreus fermentation is the main process used to produce itaconic acid; however, this approach has drawbacks, including high expenses, unpredictable byproduct formation, and a lack of genetic engineering tools. To eliminate these limitations, *E. coli* W. was chosen as the host due to its high acetate tolerance and assimilation rate. The engineering strategy involved several key steps: First, the heterologous expression of *cis*-aconitate decarboxylase (cad) from *A. terreus* was introduced into *E. coli* W, utilizing an optimized synthetic promoter and 5' UTR to ensure high catalytic activity. However, the initial WC strain produced only 0.13 g/L of itaconic acid, largely due to low acetate uptake. To overcome this, they amplified the acetate assimilation pathway by overexpressing the *acs* gene (encoding acetyl-CoA synthetase), demonstrating its effectiveness in increasing acetate consumption and biomass, although itaconic acid production only marginally improved. A more significant breakthrough came from activating the glyoxylate shunt pathway. This was achieved by deleting the *iclR* gene, which regulates the expression of key glyoxylate shunt genes (*aceBAK*). The resulting

WCI strain showed a substantial 3.92-fold increase in itaconic acid production to 0.51 g/L and improved acetate assimilation. Further amplification of the glyoxylate shunt pathway was performed by additionally overexpressing *gltA* (encoding citrate synthase) and *aceA* (encoding isocitrate lyase) under synthetic promoters. This iterative engineering led to the WCIAG4 strain, which demonstrated the highest itaconic acid production. In fed-batch fermentation, the WCIAG4 strain achieved a remarkable 3.57 g/L of itaconic acid after 88 hours, with a theoretical maximum yield of 16.1%, confirming the success of the metabolic engineering strategies. This study highlights the potential of acetate as an alternative carbon source for platform chemical production and provides a robust framework for engineering microorganisms for efficient bioconversion. (Noh, 2018)

2. APPLICATIONS OF ITACONIC ACID

Itaconic acid (IA) is a very exceptional organic acid. It is a white crystalline unsaturated dicarbonic acid in which one carboxyl group is conjugated to the methylene group. IA is utilized all over the world in the production of bioactive compounds for use in pharmaceutical, medical, and agricultural components as well as in the industrial synthesis of resins like polyester, plastic, and artificial glass. The development of biological processes to create double-bonded compounds that are useful for the production of different polymers is still of interest. (Brannon-Peppas, 1990)

2.1. Resins, Lattices, and Fibers

The polymerized methyl, ethyl, or vinyl esters of IA are extensively used as plastics, adhesives, elastomers, and coatings, forming robust and flexible materials. Copolymers incorporating IA create rubber-like resins with excellent strength and flexibility and provide waterproofing coatings with superior electrical insulation properties. In particular, styrene-butadiene lattices containing 1-5% IA demonstrate enhanced adhesion, making them ideal for critical applications like carpet backings and paper coatings. IA also improves the adhesion of polymers in emulsion paints. Acrylic lattices supplemented with IA are widely employed as binders for nonwoven fabrics. Even small amounts (less than 2%) of IA added to vinylidene chloride coatings drastically improve adhesion to various films, including paper, cellophane, and poly(ethylene terephthalate), which is crucial for the packaging and photography industries. For instance, a

cellophane film coated with an IA-containing polymer can exhibit approximately 3.5 times greater heat-seal strength compared to films coated with a non-IA copolymer. In the textile industry, polyacrylonitrile copolymers with low levels of IA show improved dye receptivity, leading to more efficient dyeing processes and deeper, richer shades. Furthermore, pigmented dispersion resins containing 0.1-1.5% IA demonstrate enhanced wet abrasion resistance. IA also finds application as a hardening agent in organosiloxanes, particularly for the production of contact lenses. Emerging research areas include its use in artificial gems and synthetic glasses with specialized nonlinear optical characteristics. (Willke, 2001)

2.2. Detergents, Cleaners, and Other Products:

Alkali salts of poly (itaconic acid) homopolymers have been recommended for use in detergents and as sequestrants for metal ions. Copolymers of acrylic acid and IA (ranging from 5 to 95%) can be effectively used at concentrations up to 100 ppm as scale inhibitors in industrial boilers, preventing mineral buildup. A significant chemical reaction of IA with amines yields N-substituted pyrrolidones, which serve as effective thickeners in lubricating greases and are also found in detergents, shampoos, pharmaceuticals, and herbicides. An imidazoline derivative of IA has been specifically claimed as an active component in shampoos. In the detergent industry, IA serves as a competitive alternative to fumaric or malic acid. Sulfonated poly(itaconic) acid is also utilized as a powerful industrial cleaner (marketed as "Citrex"), capable of removing various stubborn substances such as unsaturated polyester resins, cleaning gel coat lines, paint guns, uncured polyurethane foam, most paints, graffiti, and inks. Terpolymers containing up to 10% IA can be incorporated into drilling fluids. Beyond these, IA monoester compounds, known for their excellent hardness, compression strength, and durability, are valuable components in dental adhesives and dental fillers. (Willke, 2001)

2.3. Bioactive Components:

Several mono- and diesters of partially substituted IA have demonstrated significant anti-inflammatory or analgesic activities, indicating their potential in pharmaceutical applications. IA also serves as a precursor in the synthesis of certain potential nootropic agents, which are compounds believed to enhance cognitive function. In the field of plant growth regulation, some monoesters of IA possess properties that influence plant development. Extensive research,

particularly in Eastern Europe and Japan during the 1980s, focused on studying the effects of IA-methylester and IA-hexylester on various aspects of plant physiology, highlighting their role as plant growth regulators. (Willke, 2001)

Sakthivel et al. used a green approach, stressing an environmentally friendly and solventless synthesis process, and concentrated on the synthesis of pH-sensitive polymeric hydrogels derived from IA (Figure 3). The group used a two-step polymerization process to create the hydrogels: to create a pre-polymer, itaconic acid and ethylene glycol (EG) are condensed and polymerized in an acidic medium. Subsequently, this pre-polymer is copolymerized with acrylic acid (AA) through free radical polymerization using potassium persulphate (KPS) as an initiator. By precisely controlling the monomeric composition, this technique makes it possible to examine how it affects the dynamic and equilibrium swelling properties of the hydrogels.

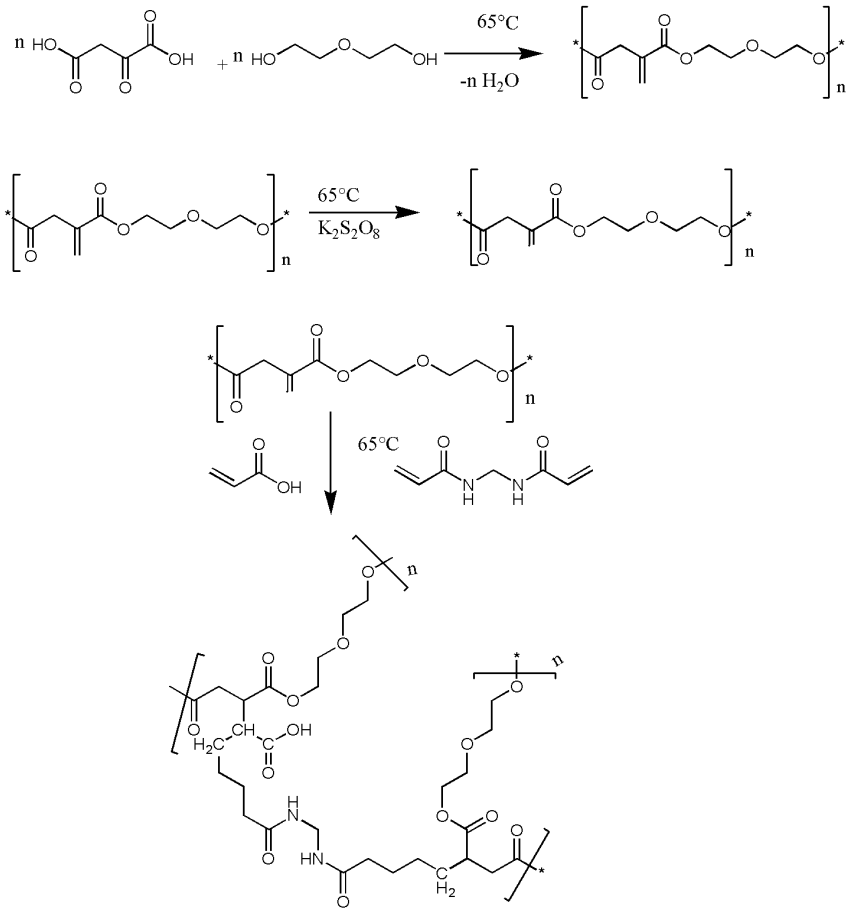

Figure 3: General mechanism of Sakthivel's method

The intrinsic pH sensitivity of these synthesized hydrogels is a crucial feature that is mainly explained by the presence of carboxylic acid groups from both acrylic and itaconic acid within their polymeric network. Sakthivel's group emphasized that this sensitivity enables the hydrogels to exhibit varying degrees of swelling based on the external pH, which is crucial for their performance in environmental applications. The synthesized hydrogels undergo rigorous characterization using a variety of analytical techniques to confirm their structure, morphology, and thermal stability. Fourier-transform infrared (FT-IR) spectroscopy is utilized to elucidate the chemical structure and identify key functional groups, confirming the presence of O-H, C=O, C-H, and COO- groups. Scanning Electron Microscopy (SEM) provides insights into the hydrogels' surface morphology, revealing small, uneven cavities that facilitate their swelling behavior. Thermal characterization is performed using Thermogravimetric Analysis (TGA), Differential Thermal Analysis (DTA), and Differential Scanning Calorimetry (DSC), which indicate that the hydrogels undergo three distinct decomposition stages and that their thermal stability generally increases with a higher itaconic acid content. The swelling behavior of the hydrogels is extensively investigated across a pH range of 4.0 to 10.0. The results demonstrate that the swelling equilibrium is directly influenced by the composition of IA, EG, and AA. Significantly, higher pH values lead to increased swelling capacity due to the complete dissociation of the carboxylic groups. The study also finds that an elevated concentration of itaconic acid within the hydrogel composition results in higher swelling, even at lower pH values, underscoring IA's critical role in enhancing swelling properties. A major application explored in this research is the removal of cationic dyes from aqueous solutions, with Methylene Blue (MB) selected as a model dye due to its widespread use and environmental relevance. The synthesized anionic hydrogels exhibit excellent capacity for removing methylene blue across the tested pH range of 4.0 to 10.0. The dye removal efficiency is observed to increase with increasing pH, further reinforcing the correlation between the hydrogels' pH-sensitive swelling and their adsorption capabilities. The composition of itaconic acid is confirmed to have a strong influence on the dye removal capacity. (Sakthivel, 2016.)

Also in 2018, Sakthivel et al. investigated biocompatibility, antimicrobial, and biodegradation properties of pH/salt-responsive multifunctional polymers. The investigation of swelling behavior reveals remarkable pH-responsiveness, with the hydrogels exhibiting significantly higher swelling (up to 2200%) in alkaline media (pH 7.4 and 10.0). This is attributed to the deprotonation of numerous carboxylic acid groups from IA and AA at higher pH, leading to inc-

reased electrostatic repulsion within the network and enhanced water uptake. The study also confirms a direct correlation between increased IA concentration and augmented swelling capacity. Furthermore, the salt-responsive behavior demonstrates that swelling equilibrium decreases with increasing charge of the cation in the surrounding medium, consistent with polyionic gel theory, where counter-ion screening reduces electrostatic repulsion.

Despite the absence of loaded metal ions or antibiotics, the anionic nature of the hydrogels, stemming from the carboxylic groups of IA and AA, confers notable inhibitory zones against Gram-positive bacteria (e.g., *Staphylococcus aureus*, *Bacillus cereus*) and fungi (*Candida albicans*). This suggests a potential mechanism involving charge-mediated interaction with microbial cell membranes. (Sakthivel, 2018.)

2.4. Hydrogels:

Crucially, the hydrogels exhibit excellent biocompatibility, as confirmed by MTT cytotoxicity assays using 3T3 fibroblast cells, demonstrating low IC-50% values and non-toxic behavior. This finding is paramount for their envisioned biomedical applications. Additionally, the presence of hydrolyzable ester bonds from DEG facilitates significant biodegradability (up to 88% degradation in 90 days) under soil-buried conditions, addressing environmental sustainability concerns for end-of-life disposal. (Sakthivel, 2018)

Panic et al. propose the use of dialkyl itaconates (specifically dimethyl itaconate (DMI), diethyl itaconate (DEI), diisopropyl itaconate (DiPI), and dibutyl itaconate (DBI)) as viable replacements for styrene. These bio-based monomers are characterized by significantly lower toxicity and volatility compared to styrene, thus offering substantial environmental and health benefits. To ensure the entirety of the UPR system is bio-based and to enhance miscibility between the prepolymer and the new reactive diluents, the prepolymer was synthesized from itaconic acid (IA) and 1,2-propanediol via melt polycondensation. (Figure 4)

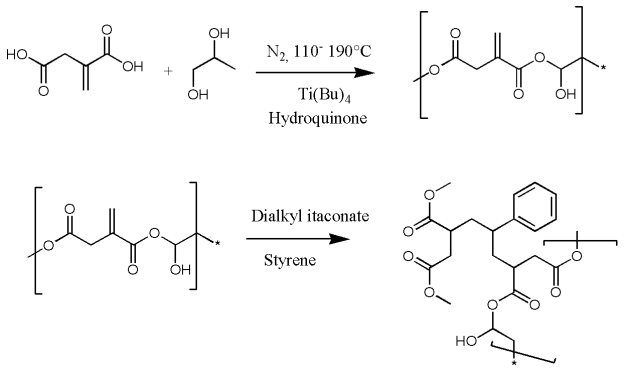

Figure 4: Synthesis of UPR resin

The study systematically investigates the synthesis and subsequent curing of these novel UPRs. The prepolymer was formed through a controlled polycondensation reaction and then blended with the various dialkyl itaconates or styrene (for comparative analysis). Curing was initiated by methyl ethyl ketone peroxide (MEKPO) at elevated temperatures (80-120°C). A crucial discovery of this research is the dramatic reduction in reactive diluent evaporation rates. The evaporation of dialkyl itaconates in the prepared resins was several orders of magnitude lower than that of styrene, which under the same conditions showed over 82% evaporation (ranging from 5% to 9.5% after 15 hours). This achievement is paramount for improving workplace safety and reducing environmental emissions. Furthermore, the research rigidly characterized the thermal and mechanical properties of the cured UPRs. When compared to their styrene-cured counterparts, the resins cured with dimethyl itaconate (UPR-DMI) showed similar, and in some cases, even better, mechanical and thermal performance. UPR-DMI, in particular, exhibited the highest glass transition temperature (Tg) and storage modulus (G'), indicative of excellent stiffness and mechanical integrity. The study also clarified the tangled relationship between the alkyl chain length of the itaconate side groups and the resulting crosslinking density. Generally, an increase in alkyl chain length led to a decrease in crosslinking density, which correlated well with observed reductions in gel content and mechanical properties. One notable exception was DPI, which showed surprisingly better qualities in spite of its larger alkyl group and anticipated lower reactivity. This phenomenon was attributed to potential intramolecular chain-transfer reactions during polymerization, highlighting the complex polymerization kinetics involved. (Panic, 2017)

Moshaverinia et al. investigated the synthesis and application of a novel poly (acrylic acid-co-itaconic acid-co-N-vinylpyrrolidone) (PAA-IA-NVP) terpolymer, specifically focusing on its preparation in supercritical CO_2 (sc-CO_2) with methanol as a co-solvent and its subsequent incorporation into dental glass-ionomer cements (GICs). The overarching aim is to leverage the unique properties of supercritical fluids to enhance polymer synthesis kinetics and ultimately improve the mechanical and handling characteristics of GICs.The authors determined a strategy of a free-radical polymerization approach for the terpolymer synthesis. A key aspect of their methodology is the use of sc-CO_2/methanol, which is posited as a superior alternative to conventional aqueous polymerization media. They rigorously characterize the synthesized polymer using ^{1}H-NMR, Raman, FT-IR spectroscopy, viscometry, and static light scattering to confirm its chemical structure and determine its molecular weight.

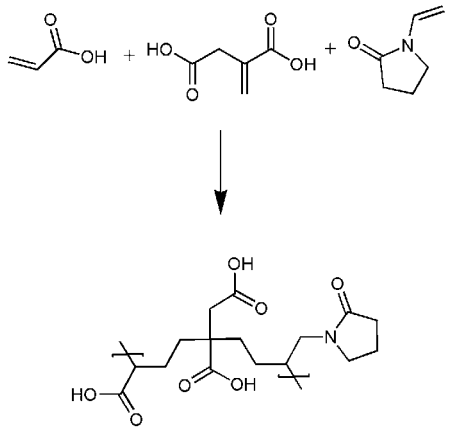

Figure 5 Synthesis of PAA-IA-NVP

Several benefits of the sc-CO_2-mediated synthesis are highlighted by the main findings. Firstly, the polymerization reaction in the sc-CO_2/methanol mixture was demonstrably faster (4 hours vs. 10 hours) and yielded a higher conversion rate (78% vs. 67%) compared to the analogous reaction in water. Furthermore, the purification processes for the polymer produced in the supercritical medium were much easier, faster, and used less energy.

Crucially, the study evaluates the performance of these sc-CO_2-synthesized terpolymers in GIC formulations. In addition to handling characteristics like working and setting times, mechanical attributes such as compressive strength (CS), diametral tensile strength (DTS), and biaxial flexural strength (BFS) were evaluated. The results indicate that GIC samples formulated with the terpoly-

mer synthesized in sc-CO_2/methanol exhibited higher CS and DTS compared to those prepared from the same polymer synthesized in water and significantly higher mechanical strengths across all tested parameters when compared to the commercial Fuji II GIC control group. Although the BFS values for the water-prepared and sc-CO_2-prepared polymers were similar, the general pattern suggests better mechanical integrity. Regarding handling properties, the working and setting times of GICs incorporating the sc-CO_2-synthesized polymer were generally comparable to, and in some select cases, better than those made with water-synthesized polymers. The inclusion of NVP in the polyacid structure was found to increase the working time, a desirable feature in clinical dentistry. The enhanced working time observed with the sc-CO_2-synthesized polymer is attributed to a more complete polymerization reaction in the supercritical medium, potentially leading to a greater availability of hydrophilic NVP molecules in the terpolymer structure, improving its mixing properties with the glass powder. Conversely, the slightly decreased setting time of the sc-CO_2-modified cements is linked to a higher availability of carboxylic groups and higher viscosities of the synthesized polymers, facilitating a faster acid/base reaction within the cement (Moshaverinia, 2008)

Early work in 1991 by Singh et al. demonstrated the use of IA-PEG polyesters as precursors for bio-erodible vaccine-loaded hydrogel microspheres, where crosslinking controlled vaccine release. (Singh, 1991) Barrett et al. achieved remarkable thermal polycondensation of IA, other dicarboxylic acids, and trimethylolpropane without catalysts or inhibitors, yielding branched polyesters with tunable mechanical properties upon UV crosslinking. (Barrett, 2010) These materials exhibited favorable cytotoxicity and moldability, indicating high potential for drug delivery, tissue engineering, and medical implants.

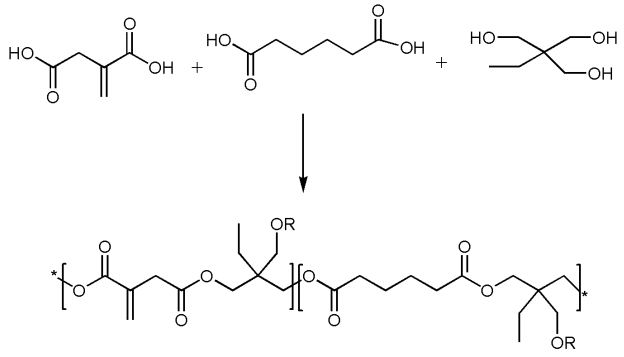

Figure 6 Thermal Synthesis of Poly(trimethylolpropane itaconate-co-trimethylolpropane adipate)

Tang et al. utilized a low-temperature polycondensation approach to crosslinking unsaturated polyesters containing maleic and itaconic anhydride, producing high molecular weight delivery. (s that could be photo-crosslinked into hydrogels for drug delivery. (Tang, 2013) Subsequent work demonstrated selective aza-Michael additions of subsequent moieties, allowing for materials with dual crosslinking mechanisms (figure 7) (Tang, 2015).

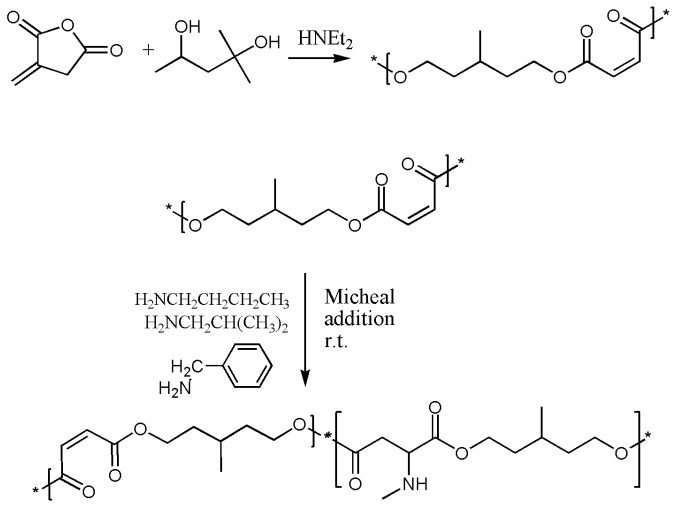

Figure 7 Michael addition of primary amines with poly(MAn-alt-MPD).

Liu et al. also reported biodegradable copolyesters by partially replacing succinic acid with IA in poly (butylene succinate), which, despite some reduction in molecular weight and degradation rate with increasing IA, showed potential for biomedical applications.(Figure 8) (Liu, 2015) IA-derived polyesters have proven effective as precursors for shape memory polymers (SMPs). Guo et al. Synthesized SMPs almost entirely from bio-based monomers (IA, sebacic acid, 1,3-propanediol), achieving high molecular weights through controlled polycondensation. SMPs with shape memory effects were created by drastically crosslinking these polyesters. (Guo, 2011) Ritter et al. (2013, 2014) also explored IA-based polyesters for SMPs, demonstrating the feasibility of using isosorbide as a diol and various crosslinking methods, including 1,3-dipolar cycloaddition with bio-derived dinitrones, to improve the properties of these materials. (Goerz, 2014)

In the field of elastomers and composites, IA-derived polyesters have been utilized as crosslinkable components. Wei et al. reported fully bio-derived pol-

yesters containing IA, which, when thermally crosslinked, yielded elastomers with competitive mechanical properties. (Wei, 2012) Reinforcement with nano-silica further produced transparent, rubber-like materials with low Tgs and superior mechanical performance. Sakuma et al. demonstrated the use of IA-based polyesters as the organic component in organic-inorganic hybrid composites with methacryl-substituted polysilsesquioxanes, leading to enhanced thermal stability and improved storage modulus in the rubbery state. (Sakuma, 2008)

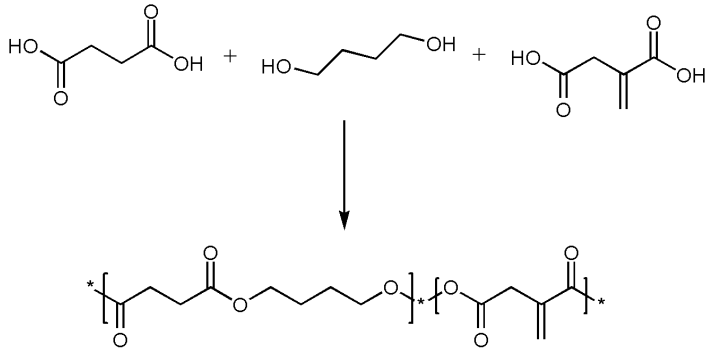

Figure 8 Synthesis of Poly(butylene succinate-co-butylene itaconate)

Itaconic acid's structural similarity to acrylic and methacrylic acid positions it as a valuable renewable alternative for reactive groups in radiation-curing binders for coatings. Dai et al. reported the synthesis of COOH-terminated IA-based polyesters for UV-curable, water-based emulsions (Figure 9). (Dai, 2015) These coatings exhibited high hardness and good water/solvent resistance, though initial formulations faced challenges with adhesion and flexibility. Subsequent research incorporated glycerol and acrylated epoxidized soybean oil (AESO) to improve adhesion and flexibility, respectively (Dai, 2015). Furthermore, thermally cured compositions based on IA polyesters and AESO were developed, showing improved Tgs and tensile strength. The research group of Robert and Friebel has also successfully developed IA-based dispersions for wood coating applications, utilizing a robust polycondensation method to synthesize polyester resins with controlled molecular weights and viscosities from various bio-based building blocks (Friebel, 2016). These findings underscore the versatility of IA-based polyesters in developing sustainable and high-performance coating formulations.

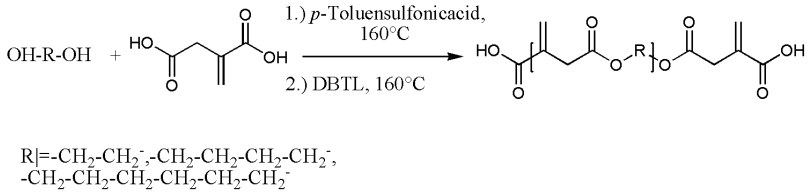

Figure 9 Synthesis of COOH-terminated IA-based polyesters

The growing environmental impact of materials derived from petrochemicals has made a paradigm shift toward sustainable alternatives necessary. Because they are biodegradable, have a smaller carbon footprint, and require fewer fossil fuels, bio-based polymers—which come from renewable resources—present an attractive alternative. Because of their advantageous combination of mechanical qualities, affordability, and processability, unsaturated polyester resins (UPRs) are one of the most widely used thermoset polymer materials in a variety of industries. Significant obstacles are presented by the petrochemical origin of the majority of commercial UPRs as well as the health hazards connected to styrene, a common reactive diluent that is categorized as a neurotoxin and suspected carcinogen. (US Department of Health and Human Services, 2011)

In response, extensive research has focused on synthesizing "green" UPRs from biomass-derived monomers. Fatty acid-based monomers have been explored as styrene alternatives, demonstrating low volatility but often presenting challenges related to high viscosity and elastomeric properties due to lower crosslinking density and a lack of rigid aromatic groups (Campanella, 2009) (Luo, 2013). Aromatic bio-based monomers, frequently derived from lignin, have shown promise in enhancing UPR stiffness (Stanzione, 2012), yet their high viscosity limits processability. While various bio-based methacrylates have been investigated as styrene replacements, their industrial production is currently limited, impacting the overall bio-based content of the resin (Jiang, 2014) (Cousinet, 2015). The inherent reactivity differences between prepolymer fumarate groups and other double bonds in bio-based reactive diluents have also contributed to issues such as increased resin viscosities, low glass transition temperatures, and reduced elastic and storage moduli in these materials (Cousinet, 2015). To address these limitations, recent studies have explored UPRs where both the prepolymer and reactive diluent are based on itaconic acid, demonstrating improved applicative properties (Fidanovski, 2018). However, further enhancement of mechanical properties remains crucial for

broader application.

The development of novel composites, particularly those incorporating waste materials, has emerged as an efficient and cost-effective strategy to improve the properties of bio-based UPRs. The abundance, low cost, and reduced carbon footprint of waste materials make them attractive fillers. Poly(ethylene terephthalate) (PET), a widely used ductile material in bottles, containers, and packaging, presents an enormous waste management challenge globally, with discarding rates exceeding recycling rates and leading to severe environmental issues (Sharma 2016). Given its excellent mechanical strength, chemical inertness, and thermal resistance, along with a chemical structure similar to UPR, waste PET offers a promising opportunity as a reinforcing filler in composite materials (Dębska, 2015)

Fidanovski et al. successfully developed novel composite materials by integrating Teflon molds into fully bio-based unsaturated polyester resins (UPRs). They achieved enhanced mechanical properties in these composites through the incorporation of functionalized Teflon particles, using dimethyl itaconate as a reactive diluent. Specifically, their results indicated that adding PET particles generally increased the mechanical properties of the composites. However, they also found that exceeding a certain concentration of Teflon (9 wt%) led to particle agglomeration, which subsequently caused a decrease in the composite's mechanical performance. This work demonstrated the viability of utilizing waste Teflon as a sustainable reinforcing agent for bio-based UPRs, offering a promising pathway toward creating environmentally friendly materials with improved characteristics (Fidanovski, 2018).

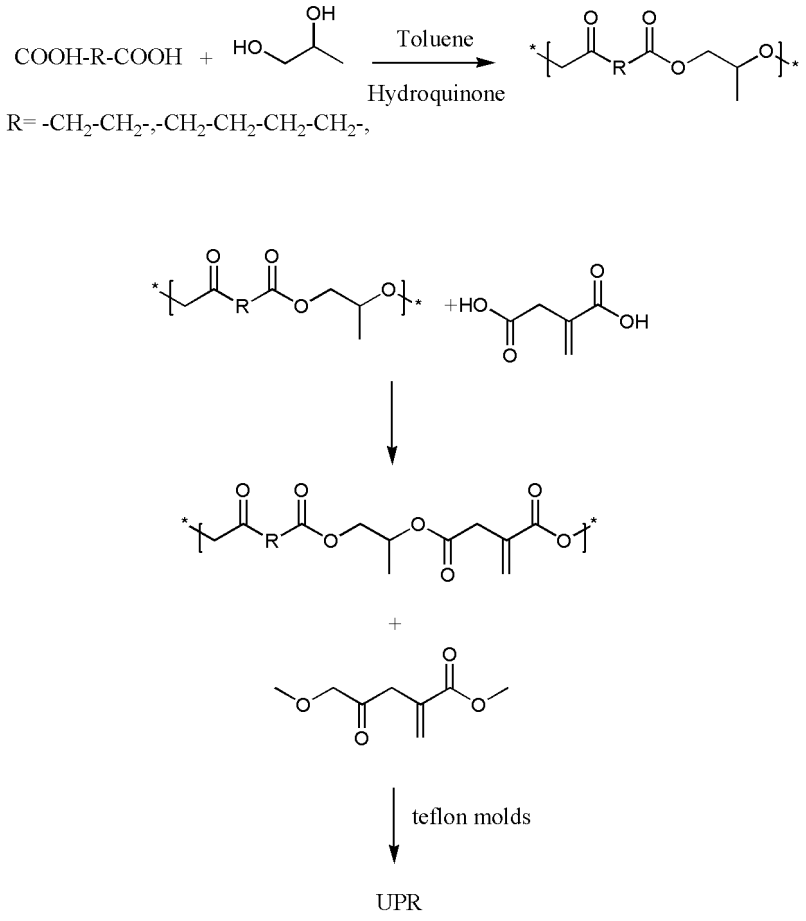

Figure 10 Syhnthesis of teflon integrated unsaturated polyester resins

Yang et al. has investigated the effectiveness of poly(itaconic acid) (PIA) and *in situ* polymerized itaconic acid (IA) as formaldehyde-free crosslinking agents for cotton cellulose, focusing on their impact on fabric mechanical strength retention. While both PIA and *in situ* polymerized IA yielded comparable wrinkle recovery angles (WRAs), indicating similar levels of durable press performance, a critical distinction emerged regarding tensile strength loss. In order to better understand the overall integrity of the material, the researchers distinguished between strength loss resulting from cellulose degradation and that caused by crosslinking. It was discovered that, in comparison to fabrics treated with PIA, fabrics treated with in situ polymerized IA lost more tensile strength as a result of cellulose degradation. This was probably caused by the oxidative effects of the $K_2S_2O_8$ initiator system on the cellulose during in situ polymerization. On the other hand—and this may seem

counterintuitive—the percentage of tensile strength loss directly related to crosslinking was higher in fabric treated with PIA. This was explained by the difference in molecular size: the larger PIA molecules showed less penetration into the interior amorphous regions of the cotton fiber, resulting in a more concentrated distribution of crosslinks on the near-surface of the fiber. Although this concentrated surface crosslinking was successful in preventing wrinkles, it also decreased abrasion resistance and increased the concentration of localized stress, which ultimately led to a greater loss of strength from the crosslinking itself. On the other hand, the smaller IA molecules that underwent in situ polymerization most likely produced a more uniform distribution of crosslinks across the cellulose matrix, reducing localized stress and improving the retention of mechanical strength overall. This research highlights the crucial role of crosslinking agent molecular size and penetration characteristics in optimizing the mechanical performance and durability of formaldehyde-free durable press cotton fabrics (Yang, 2003).

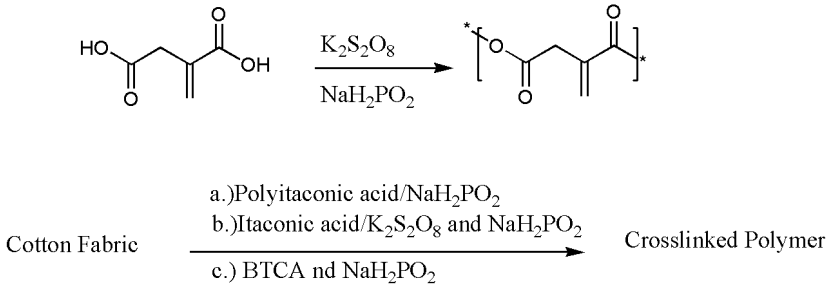

Figure 11 Synthesis of cotton fabric crosslinked polymers

2.5. Drug Delivery

Cancer remains a formidable global health challenge, with projections indicating a substantial increase in new cases over the coming decades (Teo, 2017). Although chemotherapy is a mainstay of cancer treatment, serious systemic toxicities and the emergence of multi-drug resistance (MDR) often reduce its effectiveness, making the search for novel therapeutic approaches necessary. (Kumar, 2017) (Rai, 2016). Doxorubicin (DOX), a highly potent anthracycline, exemplifies this dilemma; despite its broad-spectrum anticancer activity, its clinical utility is significantly constrained by dose-limiting toxicities, including cardiotoxicity, nephrotoxicity, and hepatotoxicity (Kumar, 2017). These inherent drawbacks have driven extensive research into alternative solutions, prominently featuring multidrug therapy and the advent of nanocarrier-based

drug delivery systems (Kumar, 2017) (Rai, 2016).

Multidrug therapy, involving the co-administration of conventional chemotherapeutics with natural bioactive compounds, offers a compelling approach to enhance therapeutic efficacy while potentially reducing the required dose of highly toxic drugs. Betanin (BET), a natural pigment derived from red beet, is a promising candidate for such synergistic combinations due to its documented antioxidant, anti-inflammatory, and anticarcinogenic properties (Farabegoli, 2017) (Han, 2015**)**. Furthermore, BET has been shown to induce apoptosis in cancer cells and can potentially overcome MDR, thereby augmenting the growth-arresting capabilities of conventional anticancer agents (Das, 2016) (Guo, 2017). However, the therapeutic application of BET is severely limited by its poor oral absorption (below 1% bioavailability) and rapid degradation under various external conditions, including temperature, pH, oxygen, and light (Amjadi, 2018)

Nanoscale carriers offer a transformative solution to these challenges by facilitating the accumulation of drugs at tumor sites via the enhanced permeation and retention (EPR) effect, improving drug bioavailability, prolonging circulation time, and enabling controlled drug release (Suh, 2017) (Zeng, 2017). Among the diverse array of natural biopolymers, gelatin nanoparticles (GNPs) have garnered significant attention for their biocompatibility, biodegradability, low cost, and abundant functional groups that facilitate the attachment of cross-linkers and targeting ligands (Bini, 2017). Nevertheless, unmodified GNPs can be rapidly cleared from circulation by the mononuclear phagocyte system due to their charged surface (Ghorbani, 2017). To circumvent this rapid clearance and induce 'stealth' features, surface modification with hydrophilic polymers like poly (ethylene glycol) (PEG), known as PEGylation, is a widely adopted strategy to reduce immunogenicity, minimize protein adsorption, and extend blood circulation time (Grossen, 2017).

Beyond stealth properties, the development of stimuli-responsive nanoparticles is crucial for achieving targeted and on-demand drug release at disease sites. The acidic microenvironment (lower pH) characteristic of tumor tissues and intracellular compartments, compared to normal physiological conditions, makes pH-responsive nanoparticles particularly attractive for cancer therapy (Verma, 2018) (Xu, 2016).

The design of pH-sensitive drug delivery systems has gained significant attention due to the varying pH environments within the human body. Hydrogels, as three-dimensional polymeric networks capable of absorbing large amounts of water or biological fluids, are prime candidates for such applications. Their sensitivity to external stimuli like pH makes them particularly attractive for

controlled drug release, allowing for targeted delivery and improved therapeutic outcomes (Okano, 1994). For instance, the swelling behavior of cross-linked chitosan with glutaraldehyde interpenetrating polyether polymer networks (semi-IPN) has been shown to be pH-dependent, influencing drug release (Yau, 1994). Similarly, cationic polymer networks containing amine and ammonium pendant groups demonstrate pH-dependent swelling and transport mechanisms, impacting the release rate of drugs like insulin (Hariharan 1996)

Amjadi et al. achieved the successful development and characterization of a novel pH-responsive PEGylated gelatin nanoparticle (PGNP) system for the co-delivery of doxorubicin (DOX) and betanin (BET), aiming to enhance cancer chemotherapy. They engineered PGNPs by decorating gelatin nanoparticles (GNPs) with a synthesized methoxy poly (ethylene glycol)-poly((2-dimethylamino) ethyl methacrylate-co-itaconic acid) (PEG-P(DMAEA-co-IAc)) copolymer, demonstrating high loading capacities for both DOX (20.5%) and BET (16.25%) within an optimal particle size of 162 nm. A key success was the confirmation of pH-triggered drug release, with significantly higher release rates observed in simulated tumor acidic microenvironments (pH = 5) compared to physiological conditions (pH = 7.4), allowing for targeted delivery. Furthermore, *in vitro* cytotoxicity assays on MCF-7 breast cancer cells revealed a synergistic therapeutic effect from the co-delivered DOX and BET, resulting in decreased cell viability superior to individual or free drug combinations, alongside enhanced cellular uptake and apoptosis induction. This research thus established a promising smart nanocarrier strategy for advanced and more effective cancer therapy (Amjadi, 2019,)

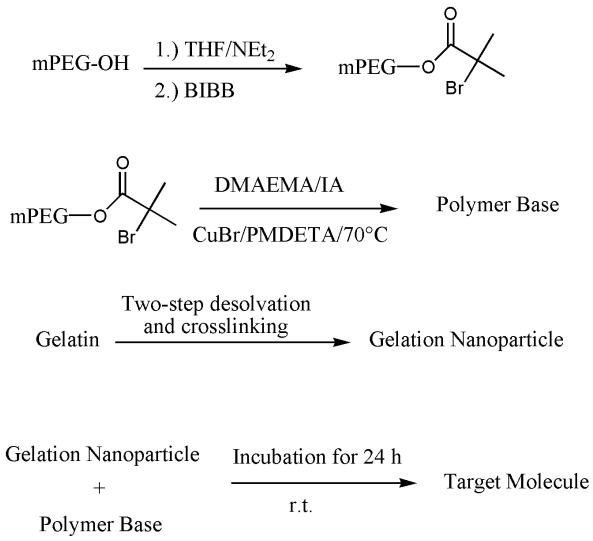

Figure 12 Preparation of gelatin nanoparticles coated with pH-sensitive polymer.

Polyelectrolytes, characterized by a high concentration of ionizable groups along their polymer backbone, exhibit unique properties that make them particularly suitable for biomedical applications (H. Brøndsted, 1992) (Karadağ, 1994). Their propensity to interact with oppositely charged surfaces and form complexes with oppositely charged polymers has led to their extensive use, for instance, as enteric coatings and controlled-release devices. Such systems also frequently demonstrate antithrombogenic characteristics.

Terbinafine hydrochloride (TER-HCl) is a potent allylamine antifungal agent, effective both topically and orally, that inhibits fungal ergosterol biosynthesis by selectively targeting fungal squalene oxidase (Balfour, 1992). Its broad spectrum of activity against dermatophyte filamentous, dimorphic, dematiaceous fungi, and yeasts makes it a valuable therapeutic agent for various skin infections. The superior efficacy of topical terbinafine compared to other antifungal drugs and its lower dosage requirements present significant advantages for its incorporation into transdermal drug delivery systems (TDDS). The development of TER-HCl-loaded hydrogels is anticipated to offer a more efficient and comfortable alternative to frequent applications of topical creams, thereby enhancing patient compliance. Previous research on polydiprotic acid-containing hydrogel systems, such as poly (acrylamide/maleic acid) P(AAm/MA) hydrogels, has demonstrated their potential as carriers for cationic antifungal drugs like TER-HCl (Şen, 1999)(Şen, 2000).

Şen et al. focused on the development and characterization of pH-sensitive hydrogels, specifically poly (N-vinyl 2-pyrrolidone/itaconic acid) (P(VP/IA)) (Figure 14, for the precise and controlled release of terbinafine hydrochloride (TER-HCl), a vital antifungal medication. The research involved the synthesis of these hydrogels through a carefully controlled gamma-irradiation process applied to ternary monomer mixtures. A significant achievement was demonstrating that the drug adsorption capacity of the hydrogels was directly proportional to both the increasing content of itaconic acid within the gel structure and the higher initial concentration of the drug in the surrounding solution.

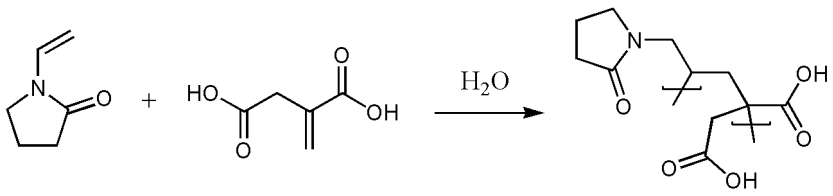

Figure 13 Synthesis of poly(N-vinyl 2-pyrrolidone/itaconic acid) hydrogels

Beyond mere adsorption, a pivotal aspect of their findings was the elucidation of a highly pH-dependent drug release mechanism. The hydrogels exhibited a characteristic pH-sensitive swelling behavior, reaching maximum swelling at pH 7, which in turn profoundly influenced the rate and extent of drug release. This pH responsiveness is crucial for targeted drug delivery within varying physiological environments. Furthermore, the researchers were able to distinguish between non-specifically and specifically adsorbed TER-HCl. While some non-specific release occurred at pH 8, indicating a general desorption, a far more controlled and sustained release of the specifically adsorbed drug was observed at lower pH values (7.0, 6.1, and 5.2). Notably, they found that an increased itaconic acid content in the hydrogel led to a decreased release rate and percentage at pH 6.1, signifying stronger specific binding interactions and enhanced control over drug efflux. The overall implication of this research is substantial: these P(VP/IA) hydrogels present a highly promising platform for advanced drug delivery systems, particularly for the localized and sustained transdermal application of cationic therapeutic agents such as TER-HCl, thereby potentially improving patient compliance and therapeutic efficacy by offering a more efficient and comfortable treatment alternative to traditional topical creams. (Şen, 2001)

3. FUTURE PROSPECTS

Itaconic acid is quickly emerging as a bio-based chemical with financial significance that is primed to compete against petroleum-based industry leaders across a number of fields. The market for sustainable products across the world results in an apparent rise in its market value.

Given a market value of over $100 million, itaconic acid is anticipated to continue to grow at a Compound Annual Growth Rate (CAGR) of 4% to 8%. By 2030, the market is anticipated to expand to a market worth between $140 million and $178 million. (Maximize Market Research, 2024; Verified Market Research, 2024).

The economic appeal of itaconic acid lies in its role as a “green” alternative to chemicals like acrylic acid. Its growth is fueled by:

3.1. Regulatory and Consumer Pressure: Stricter environmental regulations and consumer demand for eco-friendly goods are pushing manufacturers to adopt bio-based materials. The U.S. Department of Energy has long recognized it as a top value-added chemical from biomass (Werpy & Petersen, 2004).

3.2. High-Value Applications: It is a key ingredient in profitable sectors, including synthetic latex (for coatings and carpet backing), detergents, unsaturated polyester resins, and the high-potential market for bio-based superabsorbent polymers (SAPs) used in hygiene products.

Itaconic acid's major economic challenge is the production cost, which has always been higher than that of its petrochemical counterparts. Another further issue is the fluctuation of the costs of agricultural feedstocks like corn. Nevertheless, due to significant advances in bioprocessing and fermentation technologies, this price difference is gradually narrowing and becoming more competitive. (Gopaliya ve ark., 2021).

In summary, while cost remains a critical factor, the powerful market shift towards sustainability ensures a promising economic future for itaconic acid.

REFERENCES

Amjadi, S., Hamishehkar, H., & Ghorbani, M. (2019). A novel smart PEGylated gelatin nanoparticle for co-delivery of doxorubicin and betanin: A strategy for enhancing the therapeutic efficacy of chemotherapy. *Materials Science and Engineering: C*, *97*, 833-841.

Bafana, R., & Pandey, R. A. (2017). New approaches for itaconic acid production: bottlenecks and possible remedies. *Critical Reviews in Biotechnology*. https://doi.org/10.1080/07388551.2017.1312268

Bajpai, S. K., Jyotishi, P., & Bajpai, M. (2016). Synthesis of nanosilver-loaded chitosan/poly(acrylamide-co-itaconic acid)-based interpolyelectrolyte complex films for antimicrobial applications. *Carbohydrate Polymers*, *154*, 223–230. https://doi.org/10.1016/j.carbpol.2016.08.044

Balfour, J. A., & Faulds, D. (1992). *Drugs*, *43*(2), 259–284.

Barrett, D. G., Merkel, T. J., Luft, J. C., & Yousaf, M. N. (2010). *Macromolecules*, *43*(23), 9660–9667.

Bini, R. A., Silva, M. F., Varanda, L. C., da Silva, M. A., & Dreiss, C. A. (2017). *Colloids and Surfaces B: Biointerfaces*, *157*, 191–198.

Brannon-Peppas, L. (1990). Preparation and characterization of crosslinked hydrophilic networks. In *Studies in Polymer Science* (Vol. 8, pp. 45–66). Elsevier.

Bressler, E., & Braun, S. (2000). Conversion of citric acid to itaconic acid in a novel liquid membrane bioreactor. *Journal of Chemical Technology & Biotechnology*, *75*(1), 66–72.

Brøndsted, H., & Kopeček, J. (1992). In R. S. Harland & R. D. Prud'homme (Eds.), *ACS Symposium Series 480* (p. 285). American Chemical Society.

Calam, C. T., Oxford, A. E., & Rainstrick, H. (1939). Studies in the biochemistry of micro-organisms: itaconic acid, a metabolic product of a strain of Aspergillus terreus Thom. *Biochemical Journal*, *33*(9), 1488–1495.

Campanella, A., La Scala, J. J., & Wool, R. P. (2009). *Polymer Engineering & Science*, *49*(12), 2384–2392.

Carstensen, F., Klement, T., Büchs, J., & Leitner, W. (2013). Continuous production and recovery of itaconic acid in a membrane bioreactor. *Bioresour Technol*, *137*, 179–187.

Cordes, T., Michelucci, A., & Hiller, K. (2015). Itaconic acid: the surprising role of an industrial compound as a mammalian antimicrobial metabolite. *Annual Review of Nutrition*, *35*, 451–473. https://doi.org/10.1146/annurev-nutr-071714-034243

Cousinet, S., Ghadban, A., Fleury, E., Lortie, F., Pascault, J. P., & Portinha, D. (2015). *European Polymer Journal*, *67*, 539–550.

Dai, J., Ma, S., Liu, X., Han, L., Wu, Y., Dai, X., & Zhu, J. (2015). *Progress in Organic Coatings*, *78*, 49–54.

Dai, J., Ma, S., Wu, Y., Han, L., Zhang, L., Zhu, J., & Liu, X. (2015). *Green Chemistry*, *17*(4), 2383–2392.

Das, S., Filippone, S. M., Williams, D. S., Das, A., & Kukreja, R. C. (2016). *Molecular and Cellular Biochemistry*, *421*(1-2), 89–101.

Dębska, B. (2015). In P. M. Visakh & M. Liang (Eds.), *Poly(Ethylene Terephthalate) Based Blends, Composites and Nanocomposites* (ch. 10, pp. 195–212). William Andrew Publishing.

Dwiarti, L., Otsuka, M., Miura, S., & Okabe, M. (2007). Itaconic acid production using sago starch hydrolysate by Aspergillus terreus TN484-M1. *Bioresour Technol*, *98*(17), 3329–3337.

El-Imam, A. A., & Chenyu, D. (2014). Fermentative itaconic acid production. *J Biodivers Biopros Dev*, *1*(119).

Farabegoli, F., Scarpa, E. S., Frati, A., Serafini, G., Papi, A., & Spisni, E. (2017). *Food Chemistry*, *218*, 356–364.

Fidanovski, B. Z., Spasojevic, P. M., Panic, V. V., Seslija, S. I., Spasojevic, J. P., & Popovic, I. G. (2018). *Journal of Materials Science*, *53*(6), 4635–4644.

Fleischhaker, F., Schade, C., & Muller-Cristadoro, A. (2013). *Preparation of itaconic acid homo- or copolymers and amine- or amide-containing alcohols for me-*

tal surface treatment. US Patent 0037175 A1.

Friebel, R., Friebel, T., & Friebel, S. (2016). *Green Chemistry*, *18*(10), 2922–2934.

Geiser, E. (2015). *Itaconic acid production by Ustilago maydis* [PhD thesis]. RWTH Aachen University, Germany.

Geiser, E., Przybilla, S. K., Friedrich, A., Buckel, W., Wierckx, N., Blank, L. M., & Bölker, M. (2016). Ustilago maydis produces itaconic acid via the unusual intermediate trans-aconitate. *Microbial Biotechnology*, *9*(1), 116–126.

Global Industry Analysis. (2016). *The global itaconic acid market*. http://www.strategyr.com/MarketResearch/Itaconic_Acid_IA_Market_Trends.asp. Accessed 4 May 2017.

Goerz, O., & Ritter, H. (2013). *Polymer International*, *62*(5), 709–712.

Goerz, O., & Ritter, H. (2014). *Beilstein Journal of Organic Chemistry*, *10*, 902–909.

Gopaliya, D., Kumar, V., & Khare, S. K. (2021). *Recent advances in itaconic acid production from microbial cell factories*. Cranfield University DSpace Repository.

Grande, P. M., Viell, J., Theyssen, N., Marquardt, W., de Dominguez Maria, P., & Leitner, W. (2015). Fractionation of lignocellulosic biomass using the OrganoCat process. *Green Chemistry*, *17*(6), 3533–3539.

Grossen, P., Witzigmann, D., Sieber, S., & Huwyler, J. (2017). *Journal of Controlled Release*, *260*, 46–60.

Guevarra, E. D., & Tabuchi, T. (1990). Accumulation of itaconic, 2-hydroxyparaconic, itatartaric, and malic acids by strains of the genus Ustilago. *Agricultural and Biological Chemistry*, *54*(9), 2353–2358.

Guo, B., Chen, Y., Lei, Y., Zhang, L., Zhou, W. Y., Rabie, A. B. M., & Zhao, J. (2011). *Biomacromolecules*, *12*(4), 1312–1321.

Guo, Y., He, W., Yang, S., Zhao, D., Li, Z., & Luan, Y. (2017). *Colloids and Surfaces B: Biointerfaces*, *151*, 119–127.

Han, J., Tan, C., Wang, Y., Yang, S., & Tan, D. (2015). *Chemical and Biological Interactions*, *227*, 37–44.

Hariharan, D., & Peppas, N. A. (1996). *Polymer*, *37*(1), 149–161.

Haskins, R. H., Thorn, J. A., & Boothroyd, B. (1955). Biochemistry of the Ustilaginales. XI. Metabolic products of Ustilago zeae in submerged culture. *Canadian Journal of Microbiology*, *1*(7), 749–756.

Hope, E. (1927). *Manufacture of glass or glass-like objects*. US Patent 1 644 131.

Horitsu, H., Takahashi, Y., Tsuda, J., & Kawano, Y. (1983). Production of itaconic acid

by Aspergillus terreus immobilized in polyacrylamide gels. *European Journal of Applied Microbiology and Biotechnology*, *18*(6), 358–360.

Huang, J., Huang, L., Lin, J., Xu, Z., & Cen, P. (2010). Organic chemicals from bioprocesses in China. In G. T. Tsao, P. Ouyand, & J. Chen (Eds.), *Advances in Biochemical Engineering/Biotechnology* (pp. 43–71). Springer.

Huang, X., Chen, M., Lu, X., & et al. (2014). Direct production of itaconic acid from liquefied cornstarch by genetically engineered Aspergillus terreus. *Microbial Cell Factories*, *13*(1), 108.

Iqbal, M., & Saeed, A. (2005). Novel method for cell immobilization and its application for production of organic acid. *Letters in Applied Microbiology*, *40*(2), 178–182.

Jäger, G., & Büchs, J. (2012). Biocatalytic conversion of lignocellulose to platform chemicals. *Biotechnology Journal*, *7*(9), 1122–1136.

Jäger, G., Girfoglio, M., Dollo, F., Rinaldi, R., Bongard, H., Commandeur, U., Fischer, R., Spiess, A. C., & Büchs, J. (2011). How recombinant swollenin from Kluyveromyces lactis affects cellulosic substrates and accelerates their hydrolysis. *Biotechnology for Biofuels*, *4*(1), 33.

Jiang, Y., van Ekenstein, G. O. R. A., Woortman, A. J. J., & Loos, K. (2014). *Macromolecular Chemistry and Physics*, *215*(22), 2185–2197.

Kane, J. H., Finlay, A. C., & Amann, P. F. (1945). *Production of itaconic acid*. US Patent 2 385 283.

Karadağ, E., Saraydın, D., Öztop, H. N., & Güven, O. (1994). *Polymer Advanced Technology*, *5*(10), 664–668.

Kaur, R., Goswami, G. K., & Pathak, A. N. (2015). Comparative study on production and purification of itaconic acid by Aspergillus terreus utilizing maize flour, corn starch and waste potatoes. *International Journal of Pure & Applied Bioscience*, *3*(3), 242–250.

Kautola, H. (1990). Itaconic acid production from xylose in repeated-batch and continuous bioreactors. *Applied Microbiology and Biotechnology*, *33*(1), 7–11.

Kinoshita, K. (1931). Über eine neue Aspergillus-Art, Asp. itaconicus nov. spec. *Botanical Magazine, Tokyo*, *45*(530), 45–60.

Klement, T., & Buchs, J. (2013). Itaconic acid – a biotechnological process in change. *Bioresour Technol*, *135*, 422–431.

Kobayashi, T. (1978). Production of itaconic acid from wood waste. *Process Biochemistry*, *13*(5), 15–17.

Kobayashi, T., & Nakamura, I. (1971). *Process for recovering itaconic acid and salts*

thereof from fermented broth. US Patent 693706.

Kuenz, A., Gallenmuller, Y., Willke, T., & Vorlop, K. D. (2012). Microbial production of itaconic acid: developing a stable platform for high product concentrations. *Applied Microbiology and Biotechnology*, *96*(5), 1209–1216.

Kumar, S., Meena, V. K., Hazari, P. P., & Sharma, R. K. (2017). *International Journal of Pharmaceutics*, *527*(1-2), 142–150.

Li, A., van Luijk, N., ter Beek, M., & et al. (2011). A clone-based transcriptomics approach for the identification of genes relevant for itaconic acid production in Aspergillus. *Fungal Genetics and Biology*, *48*(6), 602–611.

Liu, Q., & Zhou, X.-M. (2015). *Journal of Macromolecular Science, Part A: Pure and Applied Chemistry*, *52*(10), 745–751.

Luo, C., Grigsby, W. J., Edmonds, N. R., & Al-Hakkak, J. (2013). *Acta Biomaterialia*, *9*(2), 5226–5233.

Maximize Market Research. (2024). *Itaconic acid market – Global industry analysis and forecast (2024-2030)*.

Merger, F., & Liebe, J. (1991). *Preparation of 1,1-disubstituted ethylene compounds*. US Patent 4(997):955.

Michelucci, A., Cordes, T., Ghelf, J., Pailot, A., Reiling, N., Goldmann, O., Binz, T., Wegner, A., Tallam, A., Rausell, A., Buttini, M., Linster, C. L., Medina, E., Balling, R., & Hiller, K. (2013). Immune-responsive gene 1 protein links metabolism to immunity by catalyzing itaconic acid production. *Proceedings of the National Academy of Sciences*, *110*(19), 7820–7825. https://doi.org/10.1073/pnas.1218599110

Moshaverinia, A., Moshaverinia, M., Moshaverinia, M., & Moshaverinia, M. (2008). Synthesis of N-vinylpyrrolidone modified acrylic acid copolymer in supercritical fluids and its application in dental glass-ionomer cements. *Journal of Materials Science: Materials in Medicine*, *19*(7), 2705–2711.

Noh, M. H., Kim, M. J., Kim, S. Y., Lee, S. Y., & Lee, J. W. (2018). Production of itaconic acid from acetate by engineering acid-tolerant Escherichia coli W. *Biotechnology and Bioengineering*, *115*(3), 729–738.

Nubel, R. C., & Ratajak, E. D. (1962). *Process for producing itaconic acid*. US Patent 3044941.

Okabe, M., Lies, D., Kanamasa, S., & et al. (2009). Biotechnological production of itaconic acid and its biosynthesis in Aspergillus terreus. *Applied Microbiology and Biotechnology*, *84*(4), 597–606.

Okabe, M., Lies, D., Kanamasa, S., & et al. (2009). Biotechnological production of ita-

conic acid and its biosynthesis in Aspergillus terreus. *Applied Microbiology and Biotechnology*, *84*(4), 597–606.

Okano, T., Yui, N., Yokoyama, M., & Yoshida, R. (1994). *Advances in Polymeric Systems for Drug Delivery* (p. 5). Gordon and Breach Science Publishers.

Panic, V. V., Spasojevic, P. M., Fidanovski, B. Z., Seslija, S. I., Spasojevic, J. P., & Popovic, I. G. (2017). Simple one-pot synthesis of fully biobased unsaturated polyester resins based on itaconic acid. *Biomacromolecules*, *18*(12), 3881–3891.

Pfeifer, V. F., Vojnovich, C., & Heger, E. N. (1952). Itaconic acid by fermentation with Aspergillus terreus. *Industrial & Engineering Chemistry*, *44*(12), 2975–2980.

Rai, G., Mishra, S., Suman, S., & Shukla, Y. (2016). *Phytomedicine*, *23*(3), 233–242.

Regestein, L., Klement, T., Grande, P. M., Büchs, J., Leitner, W., & Modigell, M. (2018). From beech wood to itaconic acid: case study on biorefinery process integration. *Biotechnology for Biofuels*, *11*(1), 1–11.

Report on carcinogens. US department of health and human services. Public health services; 2011.

Rychtera, M., & Wase, D. A. J. (1981). The growth of Aspergillus terreus and the production of itaconic acid in batch and continuous cultures. The influence of pH. *Journal of Chemical Technology and Biotechnology*, *31*(9), 509–521.

Sakthivel, M., Franklin, D. S., & Guhanathan, S. (2016). pH-sensitive Itaconic acid based polymeric hydrogels for dye removal applications. *Ecotoxicology and Environmental Safety*, *134*, 427–432.

Sakthivel, M., Franklin, D. S., Guhanathan, S., & Guhanathan, S. (2018). Investigation on pH/salt-responsive multifunctional itaconic acid based polymeric biocompatible, antimicrobial and biodegradable hydrogels. *Reactive and Functional Polymers*, *122*, 9–21.

Sakuma, T., Kumagai, A., Teramoto, N., & Shibata, M. (2008). *Journal of Applied Polymer Science*, *107*(4), 2159–2164.

Schute, K., Detoni, C., Kann, A., & et al. (2016). Separation in biorefineries by liquid phase adsorption: itaconic acid as case study. *ACS Sustainable Chemistry & Engineering*, *4*(11), 5921–5928.

Şen, M., & Güven, O. (1999). *Radiation Physics and Chemistry*, *55*(1), 113–120.

Şen, M., & Yakar, A. (2001). *International Journal of Pharmaceutics*, *228*(1-2), 33–41.

Şen, M., Uzun, C., & Güven, O. (2000). *International Journal of Pharmaceutics*, *203*(1-2), 149–157.

Sharma, R., & Bansal, P. P. (2016). *Journal of Cleaner Production*, *112*, 473–478.

Shin, J. H., Yang, J. Y., Jeon, B. Y., Yoon, Y. J., Cho, S. N., Kang, Y. H., Ryu, D. H., & Hwang, G. S. (2011). 1H NMR-based metabolomic profiling in mice infected with Mycobacterium tuberculosis. *Journal of Proteome Research*, *10*(5), 2238–2247. https://doi.org/10.1021/pr101054m

Singh, M., Rathi, R., Singh, A., Heller, J., Talwar, G. P., & Kopecek, J. (1991). *International Journal of Pharmaceutics*, *76*(1-2), R5–R8.

Stanzione, J. F., Sadler, J. M., La Scala, J. J., & Wool, R. P. (2012). *ChemSusChem*, *5*(7), 1291–1297.

Steiger, M. G., Punt, P. J., Ram, A. F., & et al. (2016). Characterizing MttA as a mitochondrial cis-aconitic acid transporter by metabolic engineering. *Metabolic Engineering*, *35*, 95–104.

Stiefel, S., Schmitz, A., Peters, J., Di Marino, D., & Wessling, M. (2016). An integrated electrochemical process to convert lignin to value-added products under mild conditions. *Green Chemistry*, *18*(18), 4999–5007.

Sugimoto, M., Sakagami, H., Yokote, Y., Onuma, H., Kaneko, M., Mori, M., Sakaguchi, Y., Soga, T. (2011). Non-targeted metabolite profiling in activated macrophage secretion. *Metabolomics*, *8*(4), 624–633. https://doi.org/10.1007/s11306-011-0353-9

Suh, M. S., Shen, J., Kuhn, L. T., & Burgess, D. J. (2017). *International Journal of Pharmaceutics*, *517*(1-2), 58–66.

Tabuchi, T., Sugisawa, T., Ishidori, T., & et al. (n.d.). Itaconic acid fermentation by a yeast belonging to the genus Candida. *Agricultural and Biological Chemistry*.

Tang, T., & Takasu, A. (2013). *Macromolecules*, *46*(14), 5464–5472.

Tang, T., & Takasu, A. (2015). *RSC Advances*, *5*(1), 819–829.

Tate, B. E. (1967). Polymerization of itaconic acid derivatives. *Advances in Polymer Science*, *5*(4), 214–232. https://doi.org/10.1002/pol.1967.15005040

Teo, J. Y., Chin, W., Ke, X., Gao, S., Liu, S., Cheng, W., & Chen, Z. W. (2017). *Nanomedicine: Nanotechnology, Biology and Medicine*, *13*(1), 431–442.

Tippkötter, N., Kampmann, M., & Büchs, J. (2014). Enzymatic hydrolysis of beech wood lignocellulose at high solid contents and its utilization as substrate for the production of biobutanol and dicarboxylic acids. *Bioresource Technology*, *167*, 447–455.

Transparency Market Research. (2015). *Itaconic acid market for synthetic latex, unsaturated polyester resins, detergents, superabsorbent polymers (SAP), and other applications—global industry analysis, size, share, growth, trends and*

forecast 2015—2023. http://www.transparencymarketresearch.com/itaconic-acid-market.html. Accessed 4 May 2017.

Turner, E., & Liebig, J. (1841). *Elements of chemistry* (6th ed.). Taylor and Walton.

Verified Market Research. (2024). *In-depth industry outlook: Itaconic acid market size & forecast*.

Verma, G., Shetake, N. G., Barick, K. C., Pandey, B. N., Hassan, P. A., & Priyadarsini, K. I. (2018). *New Journal of Chemistry*, *42*(8), 6283–6292.

Weastra SRO. (2012). *Determination of market potential for selected platform chemicals itaconic acid, succinic adis, 2,5-furandicarboxylic acid*. http://www.bioconsept.eu/wp-content/uploads/BioConSepT_Market-potential-for-selected-platform-chemicals_report1.pdf.

Wei, T., Lei, L., Kang, H., Qiao, B., Wang, Z., Zhang, L., Coates, P., Hua, K.-C., & Kulig, J. (2012). *Advanced Engineering Materials*, *14*(3), 112–118.

Werpy, T., & Petersen, G. (2004). *Top value-added chemicals from biomass*. U.S. Department of Energy Office of Scientific and Technical Information. https://doi.org/10.2172/15008859

Willke, T., & Vorlop, K.-D. (2001). Biotechnological production of itaconic acid. *Applied Microbiology and Biotechnology*, *56*(3-4), 289–295.

Xu, X., Li, L., Zhou, Z., Sun, W., & Huang, Y. (2016). *International Journal of Pharmaceutics*, *507*(1-2), 50–60.

Yan, Q., Miazek, K., Grande, P. M., de Domínguez María, P., Leitner, W., & Modigell, M. (2014). Mechanical pretreatment in a screw press affecting chemical pulping of lignocellulosic biomass. *Energy & Fuels*, *28*(11), 6981–6987.

Yang, C. Q., Hu, C., & Lickfield, G. C. (2003). *Journal of Applied Polymer Science*, *87*(13), 2023–2030.

Yau, K. D., Peng, T., Feng, H. B., & He, Y. Y. (1994). *Journal of Polymer Science Part A: Polymer Chemistry*, *32*(7), 1213–1223.

Zeng, S.-Q., Chen, Y.-Z., Chen, Y., & Liu, H. (2017). *New Journal of Chemistry*, *41*(4), 1518–1525.

CHAPTER 2

BACTERIAL CELLULOSE-BASED APPROACHES FOR WOUND HEALING AND REGENERATION

Asst.Prof. Dr. Elif IŞIKÇI KOCA
Işık University
Faculty of Engineering and Natural Sciences,
Electrical and Electronics Engineering Department,
Biomedical Engineering Program
https://orcid.org/0000-0002-2636-1467

1. INTRODUCTION

Cellulose is a biologically derived polymer that occurs naturally in abundance in the environment, with origins from both plant and microbial sources. The substance under scrutiny is comprised of β-1,4-linked D-glucose units that are organised in a linear arrangement, forming a polysaccharide structure. When produced by specific bacterial strains, this polymer is known as bacterial cellulose (BC), a biomaterial that has attracted major concern in biomedical research because of its outstanding mechanical resilience, structural stabilities, and marked biocompatibility. The present research highlights the pivotal function of BC in the advancement of wound healing materials, thereby signifying a significant development in the domain of biomedical technologies.

The increase in the use of cellulose in many areas has accelerated the consumption of natural plant resources. However, it is a fact that these resources are not sustainable enough to meet the demand. For this reason, research on the use of alternative materials that can be sustainable, not disrupting the ecological cycle and which can be obtained naturally, instead of vegetable cellulose, have gained momentum. BC becomes prominent as a new material on which studies are focused (Choi ve ark., 2022).

The results of studies focusing on BC have shown that this material has some advantages over plant-based cellulose. In the utilization of cellulose of plant origin, the separation of structures such as lignin and hemicellulose, which coexist with the cellulose, is a prerequisite. Conversely, in the application of bacterial cellulose, this additional step is not necessary (Choi ve ark., 2022). Furthermore, the hydrophilic property of BC enables it to exhibit a hydrogel-like characteristic, attributable to its high water-retention capacity. BC is characterised by elevated levels of purity and demonstrated compatibility with biological systems (Sulaeva ve ark., 2020). BC, which has approved to be biocompatible, is a prevalent component in tissue engineering studies involving the repair of artificial veins, skin, and cartilage tissues. BC is considered as a material within the scope of green biotechnology with a high potential for use in different areas (Figure 1), with both its structure and functional properties (Choi ve ark., 2022).

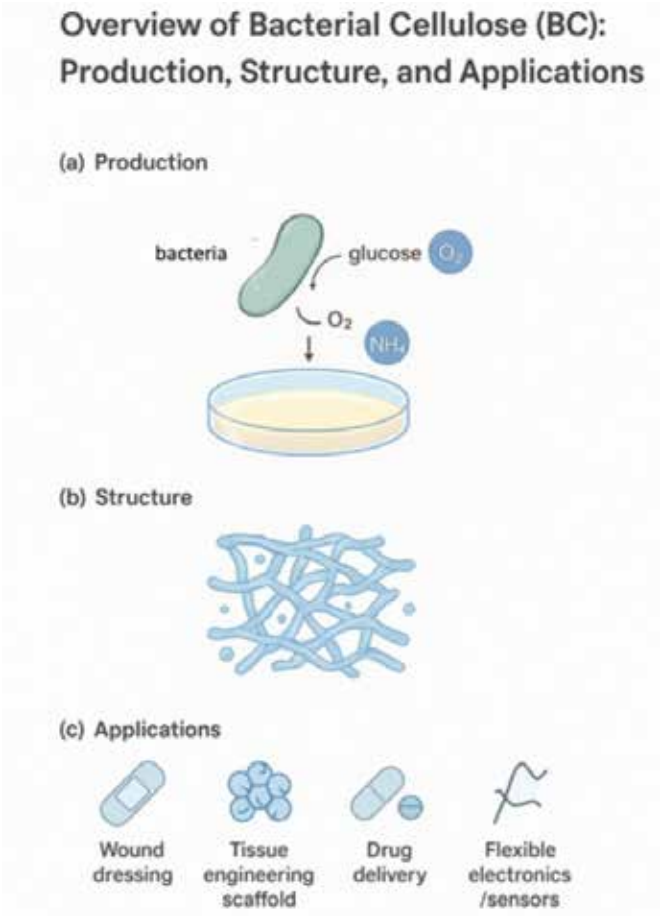

Figure 1. Overview of bacterial cellulose

Recent research trends emphasize the replacement of petroleum-derived materials with sustainable, eco-friendly alternatives developed through green biotechnology. Of these substances, cellulose must be noted as a particularly salient example of an abundant and naturally biodegradable polymer that can be found on Earth. Cellulose, a polysaccharide, is constituted of D-glucose molecules that are bonded to each other by β-1,4-glycoside linkages, resulting in a linear structure. In contrast to cellulose originating from plant resources, BC has the ability to be biosynthesised by a diversity of bacterial genera, namely Acetobacter, Gluconobacter, Sarcina, Rhizobium, Agrobacterium and Komagataeibacter. This provides an environmentally sustainable and biologically compatible material platform with significant potential for advanced applications. The determination of BC's physical and mechanical properties is facilitated by its nanostructure. The production of BC can be accomplished under controlled conditions by ensuring the growth of bacteria in a bioreactor (Choi ve ark., 2022). It is evident that the presence of nanoscale porous structures within the BC material leads to an augmented surface area-to-volume ratio in comparison to that of vegetable cellulose. Moreover, the remarkable mechanical stability, elevated polymerization level, and high crystallinity (around 90%), combined with its excellent water retention capability, make bacterial cellulose distinctly superior to plant-derived cellulose in terms of structural performance and functional versatility. BC is preferred in many studies due to its high purity, non-toxicity and biodegradable form. The physicochemical behaviour of BC, encompassing attributes such as tensile stress, degree of crystallinity, polymerisation level, and water-holding ability, is significantly influenced by the bacterial strain employed during its production process. In addition, variations in nutrient composition and growth-promoting factors within the cultivation medium have been shown to significantly affect the overall quality and performance of BC. According to Stanisławska et al. (2020), the material's tensile strength is influenced by its dehydration and rehydration behavior. Furthermore, additional studies have demonstrated that the processing conditions applied during the fabrication of polymers have a considerable influence on the resulting mechanical behaviours of BC (Indriyati ve ark., 2019). In their study, Mani Pujitha's team of researchers sought to ascertain the impact of various microorganism species on the characteristics of the resulting BC. The researchers' findings indicated that the drying technique employed in the manufacturing of BC had a considerable effect on the characteristics of the product (Mani Pujitha ve ark., 2019). In addition, research conducted by Kiziltaş and colleagues investigated the impact of the components of the cultivation medium and the pH shift on the

crystallinity of BC (Kiziltas, ve ark., 2015). Additionally, to these observations, changes in the properties of BC have been detected through the examination of the use of different materials in conjunction with BC. For instance, it has been documented that the material formed by the impregnation of alginate with BC (Figure 4), exhibits an augmented water-holding capacity (Sulaeva ve ark., 2020). Moreover, research findings indicate that incorporating wax into the BC layer results in enhanced hydrophobic characteristics (Chaiyasat ve ark., 2018). Dai et al. documented that the thermal stability of fabricated BC-based materials was improved and cyto-compatibility with collagen fibrillogenesis increased with the study that included the inclusion of collagen between BC fibers (Dai ve ark., 2019).

2. WOUND HEALING PROCESS

Wound healing is a sophisticated phenomenon that the body is capable of performing through a series of distinct stages. These stages encompass a multitude of cellular and chemical processes that facilitate the reconstruction and regeneration of damaged tissue (Farzaei ve ark., 2014). The phenomenon of wound repairing is comprised of four distinct phases (Figure 2), which are commonly delineated as follows: hemostasis, inflammation, proliferation, and maturation. Although the progression of these phases is predominantly contingent on the nature of the wound, the pathological condition thereof, and the materials employed for the steps of dressing, the wound repairing is also subject to the influence of these factors (Kushwaha ve ark., 2022).

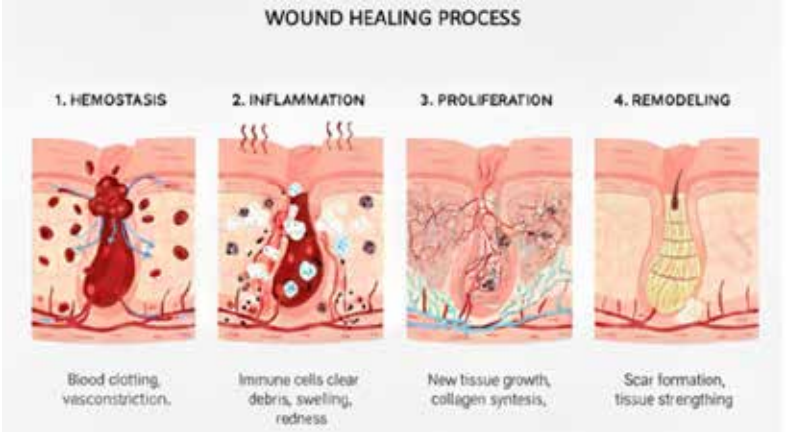

Figure 2. Wound healing process

The ideal dressing to be used in wound healing is expected to provide suitable conditions for the wound. The wound dressing should support the moist environment required for wound healing and allow ideal gas exchange (oxygen, CO2 and water vapor). It should also be able to absorb the exudate from the wound and not interfere with angiogenesis. This material should act as a thermal insulation in the wound area and should not allow bacterial growth and should eliminate the risk of microbial infection. It is expected that the wound dressing to be developed will not only support wound healing but also provide physical support to the wound. For example, it is expected that the dressings will not cleave into to the wound and be non-toxic and non-allergenic so as not to cause infection (Niculescu ve ark., 2022). It should also be inexpensive, flexible and easy to use, sterile, and should not release non-biodegradable particles (Firmanda ve ark., 2022). Wound dressings are typically composed of cotton gauze, a material that lacks active healing properties. Synthetic polymers are often engineered and utilized across various biomedical applications, including tissue regeneration and wound management. Despite their versatility, these materials exhibit inherent drawbacks, particularly concerning their biocompatibility and overall functional performance (George ve ark., 2019; Pei ve ark., 2015).

3. THE IMPORTANCE OF BACTERIAL CELLULOSE IN WOUND HEALING PROCESS

The existence of a number of distinctive characteristics, BC is a versatile resource that lends itself to application in a variety of domains. One of the most widely utilized domains of BC is biomedical engineering applications, particularly in the domain of wound healing (Figure 3). This is attributable to its biocompatibility and its capacity to mimic the extracellular matrix (ECM) (Firmanda ve ark., 2022), studies on its usability both as pure BC and as composite structures with the support of different materials are quite abundant (Choi ve ark., 2022). BC has emerged as a prominent matter in wound care studies, largely owing to its advantageous mechanical properties and cost-effective availability. The occurrence of -OH functional groups and networks of nanofibrils within the BC structure provides a favourable environment for wound healing, representing a significant advancement in research conducted within this field of study. It is stated that pure BC material supports tissue regeneration in scaffolds (Firmanda ve ark., 2022).

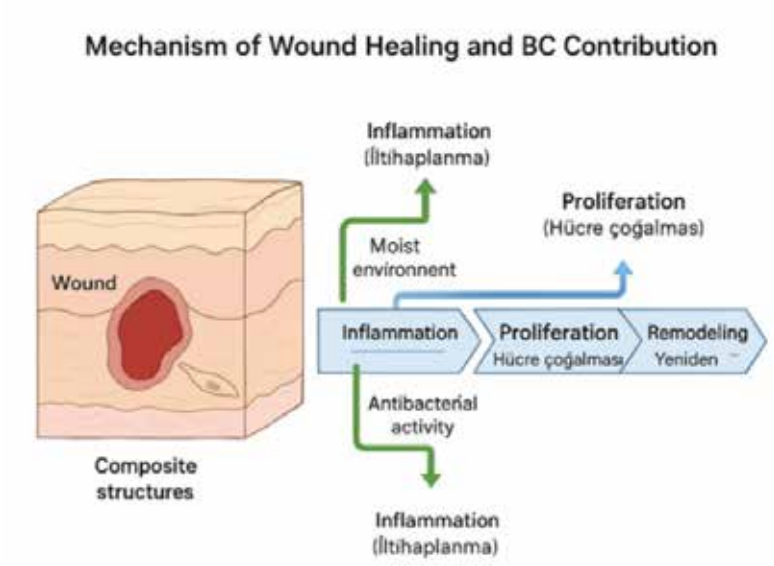

Figure 3. The function of BC in the process of wound healing

In addition, BC's permeability, water holding capacity and flexible structure make it a priority in wound healing studies (Lemnaru ve ark., 2022). Due to its 3-dimensional structure, BC ensures the retention of drugs and active substances in wound repairing (Faisul Aris ve ark., 2019; Pang ve ark., 2020) and is beneficial in wound healing by supporting the release of these substances. In addition, BC can help protect the wound surface by contributing to the rapid drying of the wound and preventing infection. With its large surface area provided by porosity, BC shows high mechanical strength. It is evident that BC possesses a Young's modulus of 118 GPa, which is commensurate with that of steel (Lemnaru ve ark., 2022). BC is among the most studied materials in biotechnology studies as a material that has proven usability in wound care applications thanks to its special properties.

4. COMMERCIAL BC PRODUCTS

Many commercial products are also available today, proving that BC can be used in the healthcare industry. Examples of these products are; Bioprocess® (Curitiba, Brazil), DermafillTM (Londrina, Brazil), Gengiflex® (Curitiba, Brazil), xCell® (New York, NY, USA), Membracel® (Curitiba, Brazil) & BioFillTM® (Curitiba, Brazil) may be given. Corporations including BioFillTM &

DermafillTM have employed BC in the manufacture of wound treatments, with the aim of treating burns and ulcers in patients, thereby providing instant relief of pain and reducing discomfort. BioFill® dressings have been employed in excess of 300 test cases, in which they have demonstrated efficacy in accelerating wound healing (Czaja ve ark., 2007). Another commercial product that can be used as a wound dressing is DermafillTM, which is used without drying and thus absorbs the leaks of the wound quickly, which supports wound healing and repair much faster (in 81 days) than BC-free materials (315 days) (Portal ve ark., 2009). Membracel® is another valuable commercial product that can be employed in the treatment process of venous leg ulcers and wounds. The xCell®, produced for a similar purpose and developed by Xylos Corporation, is also used for venous leg ulcers. Innovatec, on the other hand, has enhanced a new product by adding silver ions (Nanoskin® (São Carlos, Brazil)) to the antimicrobial BC material in order to improve its antibacterial properties. EpiProtect® (Royal Wootton Bassett, UK) is another commercial product that is effective in the healing of first and second degree burn wounds and can provide healing in 28 days compared to silver sulfadiazine and gauze used in such burn wounds, which heal in 32 days (Cielecka et at., 2019).

Notwithstanding the documented effectiveness of BC in the treatment of wounds, attributable to its physicochemical properties, it is unable to satisfy the full spectrum of requirements of the contemporary wound dressing market. The extant evidence would thus far appear to indicate that the presence of active ingredients is of consequence in preventing the potential for wound infection via microbial contaminants and reactive oxygen species, and consequently ensuring more efficient wound healing (Firmanda ve ark., 2022). In the interest of mitigating the potentially deleterious consequences of this condition, the utilization of antibacterial pharmaceuticals and antimicrobial agents within the BC is a potential solution. This approach involves the functionalization of the BC, thereby facilitating the suppression of bacterial proliferation within the wound and its immediate vicinity. This functionalization step has been demonstrated to trigger tissue regeneration, thereby facilitating the rapid healing of significant injuries.

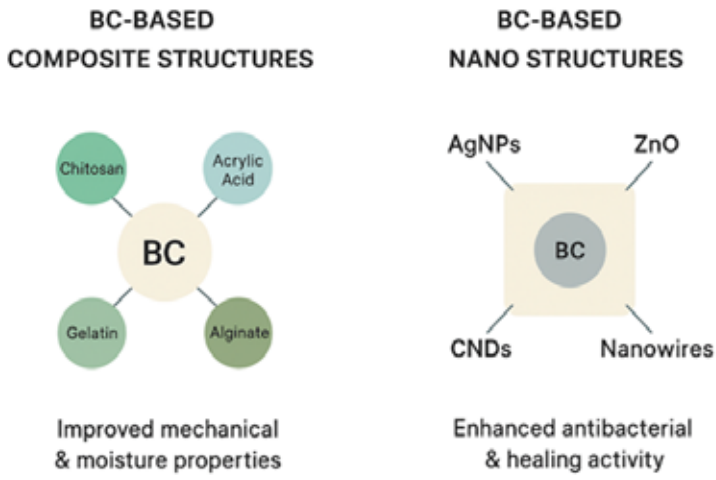

Figure 4. The employment of BC in diverse disciplines involving a range of materials

5. BC BASED COMPOSITE STRUCTURES

The use of different bio-structured materials together with BC is also being investigated in wound healing studies (Figure 4). Chitosan (CS) is one of the most frequently employed materials for these applications. The investigation revealed that the combination of CS and BC recorded in a greater degree of water absorption in comparison with the implementation of BC in isolation (Cacicedo ve ark., 2020; Cazón ve ark., 2019; Piasecka-Zelga ve ark., 2018). Besides, research has demonstrated that CS can be metabolized into N-acetyl-beta-D-glucosamine, a substance that has been shown to promote fibroblast growth and collagen deposition, which is a pivotal aspect of wound healing. As an example of studies conducted for this purpose, CS-BC material loaded with ciprofloxacin, which is reported to be compatible with human fibroblast cells, can be shown (Cacicedo ve ark., 2020). Researchers have stated that this material has the capacity to release ciprofloxacin by 30% and exhibit antibacterial behaviour during the wound-healing process against P. aeruginosa and S. aureus. Sun's study stated that the inclusion of glycerin in the BC structure showed a moisturizing effect on burn wounds (Sun ve ark., 2018).

Having sufficient moisture in the wound environment is of great importance for epithelialization and other tissue regeneration steps in wound healing. In this context, some studies are carried out on providing and maintaining the

optimum moisture level required for wound healing by using hydrogels. As a case in point, we can consider the studies carried out for this purpose, which involved the development of a BC-acrylic acid (AA) (BC-AA) hydrogel through electron beam irradiation. It has been reported that the material exhibits a substantial water uptake capacity (4000–6000% in 24 hours) and high water vapour transmission rate (WVTR) (2175–2280 g/m²/day) (Mohamad ve ark., 2014). As demonstrated by the team's testing in in vivo trials of the hydrogel, the results indicate that the treatment has been indicated to support rapid wound repairing, re-epithelialization and fibroblast proliferation in comparison with BC only. Furthermore, an additional study demonstrated that the integration of epidermal keratinocytes & dermal fibroblasts into the BC-AA hydrogel (see Figure 4) enhanced the recovery process of burn wounds, thereby emphasising its potential as a therapeutic agent. The present study demonstrated that wound contraction was considerably enhanced by cell-loaded hydrogel (77.34 ± 6.21%) in comparison to cell-free BC–AA hydrogel (64–79 ± 6.84%), thus indicating that cell-loaded hydrogels also increase collagen accumulation (Mohamad ve ark., 2019).

A further study that contributes to the advancement of BC-based composite structures involves a material synthesized by He's team, which incorporates BC, tannic acid (TA) & magnesium chloride (BC-TA-Mg) (He at al., 2021). It has been demonstrated that this BC-based material, the surface properties of which have been shown to be effective in combating biofilms in chronic wounds, has been subjected to rigorous testing. This comprehensive evaluation encompasses a multitude of parameters, including mechanical strength, thermal stability, water uptake and retention capabilities, release behaviour, and anti-biofilm activity. The material has also been assessed for potential toxicity. The findings of this exhaustive testing programme have indicated that the subject material has the capacity to be utilized in the repair of wounds, thus offering a promising solution in the management of chronic injuries. As stated in the aforementioned study, the surface topography of the BC membranes was successfully achieved by firmly adhering TA and MgCl2 particles to the BC nanofibres, thereby enhancing the hydrophobicity of the membrane. Moreover, an investigation was conducted to ascertain the impact of the incorporation of pure BC and TA and $MgCl_2$ to BC composites on their mechanical properties. The results of this investigation revealed a considerable enhancement in the tensile strength of the BC-TA-Mg & BC-TA structures, and an increase in elongation in the tensile tests. It has been documented that BC-TA-Mg material possesses a superior water-retention capacity in comparative analysis of pure

BC and BC-TA composite, a salient attribute when assessing its efficacy in the management of wound exudates. Moreover, research has demonstrated that BC-TA-Mg composite, a material that has been shown to meet standard toxicity classifications, has the potential to inhibit TA release in both single-culture P. aeruginosa and S. aureus biofilm models, as well as co-cultivated S. aureus and P. aeruginosa biofilm. In physical tests, researchers have asserted that the transparency of the membrane remains unaffected by the incorporation of TA and MgCl2 into the composite. This finding suggests that the membrane may be utilized to facilitate examinations during the healing process of wounds.

In the course of research undertaken for the purpose of developing wound dressings, the focus has been on the creation of new materials through the combination of natural products. In this particular context, the development of a wound dressing has been rendered a prominent research focus, with a study at the forefront of this field combining red and green propolis extract with biochanin A and p-coumaric acid, along with BC. The investigation undertaken by Hodel et al. involved the blending of BC (containing 2–4% green and red propolis extract) with a quantity of biochanin A and p-coumaric acid materials ranging from 8–16 mg, resulting in the production of a new composite material (Hodel ve ark., 2022). Mechanical and physical tests were applied on different composite materials, different composites synthesized with different ratios and control group. Characterization of the composites was realized, and morphological examinations were carried out. When the results are examined, it has been proven that the classification of the active ingredient added in the composite structure affects the composite properties depending on the applied concentration. According to the test results, the transparency (28.59–110.62T600 mm–1) and thickness (0.023–0.046 mm) values of the composites were reported. An observation was made concerning the swelling capacity of the composites. It was determined through observation that the said capacity fell within the range of 48.93-405.55%. Furthermore, an additional observation was made concerning the water vapour permeability rate. It was established that the rate fell within the range of 7.86-38.11 g m^2 day^{-1}. The determination of the mechanical characteristics of the composites was made possible by the assessment of their varying elongation capacities, ranging between 99.13% to 62.39 %. The antioxidant capacities of the synthesized structures also vary between 21.23–86.76 µg mL-1. When the results of the study were examined, the researchers informed that the only material showing antimicrobial activity was BC and red propolis-based composite.

Another example of BC-based studies with natural products is Lemnura's

study (Lemnura ve ark., 2022). In their study, the team carried out experiments to synthesize new wound dressing materials by adding cinnamon oil to BC membranes. A research study utilised essential oils, comprising bioactive ingredients such as monoterpenes, sesquiterpenes and phenolic substances, distinguished by their unique biological activity. The scientific principle underlying the therapeutic benefits of essential oils involves the irreversible rupture of bacterial cell walls and cytoplasmic membranes. In the study, experiments were designed based on the use of these specific effects to treat infections in the body and their use in various antimicrobial applications. In order to load CEO (cinnamon essential oil) into the BC membrane structure, emulsions of this oil were made at 1, 3 and 5% concentrations. The results reported by the team indicate that the synthesized membranes exhibit considerable water retention capability and facilitate the establishment of a moisture environment that is conducive to wound healing. Moreover, the results demonstrated that the prepared samples exhibited antimicrobial activity.

In a separate study, the focus was on the production of self-healing hydrogels, with bacterial cellulose nanofibers (BCN) being utilized because of their high mechanical resistance. The central theme of this study was the synthesis of multifunctional hydrogels containing naturally derived biomass, incorporating silver hybrid BC nanofibres (Ag-BCN), carbon nanodots (CNDs) and resveratrol (Res). The findings of in vitro investigations illustrate that the introduction of Ag-BCN resulted in a six-fold enhancement of the mechanical resistance of the hybrid hydrogel, whilst concurrently exhibiting noteworthy antibacterial efficacy (E. coli 99.68% and S. aureus 99.99%). A thorough review of the study's findings indicates that hydrogels comprising CNDs possess the capability to monitor the repair progress of the fracture in actual time. Moreover, evidence suggests that these hydrogels can achieve the controlled release of Res via photothermal processes. Furthermore, the experimental findings on animal models have demonstrated that the fabricated hydrogel has the capacity to decrease the incidence of wound infection and efficiently reduce the healing process (from 21 days to 14 days) (Li ve ark., 2024).

In an alternative investigation, a multifunctional wound dressing was synthesised by employing BC-Cot, which was formulated with hydrolysate derived of cotton materials and combined using an antimicrobial peptide (AMP) that draws inspiration from sea cucumber lectin. The procedures of cotton fabrication, hydrolysis, and BC generation were systematically optimised. A subsequent examination of the results yielded the finding that BC-Cot exhibited comparative yield of production and finer fibre diameter in contrast to BC pro-

duced via glucose. The grafting of the peptides to DBC was achieved through a Schiff bases interaction, resulting in the formation of a multifunctional wound dressing (DBCP). The present study demonstrated that the structure exhibited effective antimicrobial activity and a positive effect on wound healing. Moreover, it is hypothesized that this structure will be efficacious in rapidly arresting hemorrhaging in wounds due to its robust adhesive properties. A decrease in the quantity of inflammation-associated cells in wound tissues, recently developed hair follicles, and substantial collagen accumulation were observed (Hou ve ark., 2025).

In a subsequent study, an antibiotic and oxidation-resistant polymeric material with accelerated self-regenerative capabilities was synthesised through covalent borate ester cross-links amongst catechol-grafted chitosan (CS-CA) and polyvinyl alcohol in the present of borax, accompanied by the introduction of ellagic acid (EA). The synthesised hydrogel was found to exhibit concentrated antibacterial dual functions in addition to its adhesion property, which renders it suitable for use in wound healing, and its antioxidant property. This hydrogel displays noteworthy biocompatibility and pH-sensitive characteristics, attributable to the reversible character of borate ester linkages, which facilitate the controlled release of EA. The structure is multifunctional in nature. As demonstrated by in vivo evaluations in a complete-thickness skin defect modelling system, significant regenerative effects have been observed in the wounded tissue healing process (Zhong ve ark., 2025).

6. BC BASED NANO STRUCTURES

Various studies were designed considering the ability of BC to assemble in nanostructures (Natale ve ark., 2022). In the course of studies on the processes of wound healing in the existence of silver, the effect of silver nanoparticles was also investigated (Figure 4), given the established antibacterial activity of silver ions. This antibacterial activity has been demonstrated to be effective in opposition to a variety of pathogens by means of cell membrane breakage, and by interfering with processes such as DNA replication and transcription. Furthermore, an increase in the speed of wound healing has been observed (Le ve ark., 2015). In addition, research has indicated that AgNPs have the capacity to induce the release of reactive oxygen species (ROS), with the consequent destruction of bacteria. Composite structures gained by absorbing AgNPs into the structures provide a transparent appearance, making it easier to visually follow

the healings in the scar tissue. Pal et al. studied a silver-functionalized BC-based material for use in wound repairing studies and showed that this structure exhibits antimicrobial activity on E. coli (Pal ve ark., 2017).

In the course of in vitro experimentation focused on the treatment of third-degree burns, Jiji's team obtained a new material by impregnating polydopamine (PDA)-coated BC matrices with AgNPs. Through the application of redox chemistry, it was demonstrated that the material can rapidly reduce Ag ions to AgNPs, as well as convert catechol to quinone. They think that the catechol parts in PDA coated on BC are involved in this reaction. In vitro cytotoxicity tests of BC – PDA – AgNP compounds confirmed their biocompatible behavior. The team observed that by adding AgNP to their studies, notable antibacterial efficacy occurred against both Gram-negative (E. coli, K. pneumoniae and P. aeruginosa) & Gram-positive (S. aureus) bacteria. When the results were examined, it was concluded that the antibacterial effects of AgNps materials on gram-negative bacteria were higher. In histopathological experiments conducted with BC–PDA–AgNP, it was observed that fibroblast proliferation and granulation tissue formation were significantly supported. In biocompatibility evaluations employing NIH-3T3, the BC-PDAg composite demonstrated enhanced cellular proliferation relative to the control, BC, and BC-PD samples (Jiji ve ark., 2020). It has also been reported that angiogenesis and re-epithelialization processes are positively affected using BC–PDA–AgNP. For in vivo wound healing investigations, the Wistar rat model was utilized to examine the influence of BC-PDAg on the tissue regeneration process. Although no major variations were detected in the 5th day assessments of the injury recovery process, healing advanced in the BC;BC-PDAg groups on the 10th day. By the time the treatment reached its 15th day, a marked improvement in the wound closure process was evident in subjects administered with BC-PDAg. On day 20, the healing outcomes of the BC-PDAg samples showed a statistically significant improvement, reaching 94.35%, compared to 74.58% for the BC group and 65.35% for the control. By the 25th day, full wound closure was achieved in the BC-PDAg-treated animals, indicating the material's strong therapeutic efficacy in promoting tissue regeneration.

Some of the pioneering studies on the utilisation of BC with nanostructures are also carried out with silver nanowires (AgNWs). In this context, studies show that the materials in which AgNWs are used don't block skin pores, which is important for maintaining air circulation. Additionally, researchers state that, according to the results of the experiments, AgNWs do not release silver ions quickly and thus improve the biocompatibility of composite structures

containing AgNWs (Choi ve ark., 2022). Wan et al. also drew attention to the properties of AgNWs and succeeded in developing a strong and stretchable wound dressing material by developing BC composite structures containing AgNWs (Wan ve ark., 2020). The researchers' method of producing the new material includes purification and freeze-drying steps by repeated spraying of BC culture medium containing AgNW. It is evident that the BC–AgNW composite, as evidenced by experimental findings derived from animal testing, has been demonstrated to absorb wound secretions and facilitate the creation of a humid microenvironment conducive to the healing process, it has been reported that BC-AgNWs containing 38.4% AgNWs provide higher cytokeratin-10 and integrin-β4 expression levels. Additionally, more keratinocyte proliferation was observed with this composite. In addition, researchers reported that BC–AgNWs support the formation of epithelial tissues more than pure BC, which significantly improves skin regeneration (Wan ve ark., 2020). In the study, 3 groups of 16 mice each were created; One group is known as the BC group and the wounds of each animal in the group are covered with BC dressing, the second group is designated BC/AgNW-3, which corresponds to AgNW dispersion ratios to culture of 10:4.5 and the wounds are coated with BC/AgNW-3, the last group is the control group in which no treatment was applied to mouse wounds. Each experimental group of mice was maintained in a single cage. They had full access to food and water. The healing processes of the groups were monitored with the help of an optical microscope on days 3, 6, 9 and 12. A thorough examination of the experimental data revealed that on the third day, the BC/AgNW-3 group exhibited a wound recovery rate of 28%, which was significantly higher than the 10% recovery rate recorded in both the control and BC groups. Consistent with this trend, the BC/AgNW-3 samples exhibited substantially faster healing on days 6 and 9 compared to the other groups. By day 12, nearly 90% closure was achieved in the control and BC-treated wounds, whereas complete recovery was recorded in the BC/AgNW-3. The cytocompatibility of the AgNW-enriched BC dressing was assessed using NIH-3T3. After six hours of incubation, all samples displayed over 80% inhibition of S. aureus, reaching nearly 100% for BC/AgNW-3. Furthermore, antibacterial testing revealed that BC/AgNW-based dressings exhibited stronger inhibitory effects against S. aureus than E. coli.

Considering that metal oxides such as TiO2 and ZnO show antimicrobial properties by releasing ROS, researchers designed BC-based TiO2 and ZnO-enriched composite structures (Figure 4). With subsequent experiments, they showed that this structure allows cellular adhesion and proliferation of

fibroblast cells and has antibacterial properties (Khan ve ark., 2015). Researchers state that all these results they obtained will contribute to the wound repairing process (Ul-Islam ve ark., 2014). A new BC-based nanocomposite structure containing ZnO was synthesized by Khalid ve ark., and it was observed that this composite provided antibacterial activity in burn wounds. In the study, approximately 90%, 87.4%, 94.3% and 90.9% antibacterial activity was detected in the tests performed with E. coli, P. aeruginosa, S. aureus & C. freundii, respectively. In addition, in animal studies, it was reported that a 66% improvement was observed when the nanocomposite was applied. Wound surfaces covered with regenerated epithelium have been reported to be observed in tissues treated with BC-ZnO nanocomposites (Khalid ve ark., 2017).

The present study of BC-based research has revealed that the material exhibits the capacity to acquire a multitude of functions through interaction with diverse materials. The findings of studies involving BC are summarized according to two criteria: their areas of use and the target groups affected. Figure 5 presents a visual representation of the interaction between other materials and areas with BC, offering a comprehensive overview of the subject matter.

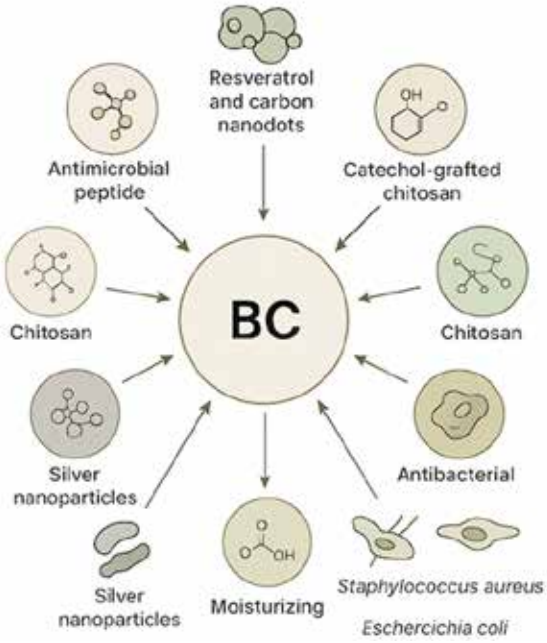

Figure 5. Schematic illustration of BC-based healing materials and their biological effect

7. CONCLUSION

The central objective of the current study is to offer a comprehensive evaluation of the significance of BC in the domain of biomedical engineering. Emphasizing studies that explore its role in healing processes of wounds, the study examines the synthesis, structural characteristics, and prospective biomedical applications of innovative BC-derived materials. The present study discusses the evaluation of ecologically renewable and sustainable resources within the scope of green biotechnology, and their subsequent applications in the domain of medicine. In this review, recent investigations into the role of functionalized materials integrated with the superior structural and mechanical features of bacterial cellulose (BC) in promoting wound repair are comprehensively analyzed. In the present review article, the potential uses of BC-based products are highlighted, and it is demonstrated that bio-based materials can readily be incorporated into current applications. We hope that this study will guide the synthesis of new materials to be evaluated in medical applications using bio-based and renewable source materials.

Author Contributions

The authors utilized AI-assisted platforms, such as ChatGPT and Gemini, for language refinement, grammatical review, and visual illustration during the preparation of this work.

REFERENCES

Cacicedo, M.L., Pacheco, G., Islan, G.A., Alvarez, V.A., Barud, H.S., & Castro, G.R. (2020) Chitosan-bacterial cellulose patch of ciprofloxacin for wound dressing: Preparation and characterization studies, Int. J. Biol. Macromol., 147, 1136–1145.

Cazón, P., Velazquez, G., & Vázquez, M. (2019). Characterization of bacterial cellulose films combined with chitosan and polyvinyl alcohol: Evaluation of mechanical and barrier properties, Carbohydr. Polym., 216, 72–85.

Chaiyasat, A., Jearanai, S., Moonmangmee, S., Moonmangmee, D., Christopher, L.P., Alam, M.N., & Chaiyasat, P. (2018). Novel green hydrogel material using bacterial cellulose, Orient. J. Chem., 34, 1735–1740.

Choi, S. M., Rao, K. M., Zo, S. M., Shin, E. J., & Han, S. S. (2022). Bacterial Cellulose and Its Applications, Polymers, 14, 1080.

Cielecka, I., Szustak, M., Kalinowska, H., Gendaszewska-Darmach, E., Ryngajłło, M.,

Maniukiewicz, W., & Bielecki, S. (2019). Glycerolplasticized bacterial nanocellulose-based composites with enhanced flexibility and liquid sorption capacity, Cellulose, 26, 5409–5426.

Czaja, W.K., Young, D.J., Kawecki, M., & Brown, R.M. (2007). The future prospects of microbial cellulose in biomedical applications.,Biomacromolecules, 8, 1–12.

Dai, L., Nan, J., Tu, X., He, L., Wei, B., Xu, C., Xu, Y., Li, S., Wang, H., & Zhang, J. (2019). Improved thermostability and cytocompatibility of bacterial cellulose/collagen composite by collagen fibrillogenesis, Cellulose, 26, 6713–6724.

Faisul Aris, F.A., et al. (2019). Interaction of silver sulfadiazine with bacterial cellulose via ex-situ modification method as an alternative diabetic wound healing, Biocatalysis and Agricultural Biotechnology, 21: p. 101332.

Farzaei, M. H., Abbasabadi, Z., Shams-Ardekani, M. R., Abdollahi, M., & Rahimi, R. (2014). A comprehensive review of plants and their active constituents with wound healing activity in traditional Iranian medicine, Wounds, 26(7), 197–206.

George, B., & Suchithra, T. V. (2019). Plant-derived bioadhesives for wound dressing and drug delivery system, Fitoterapia, 137, 104241.

Hodel, K. V. S., Machado, B. A. S., Sacramento, G. C., Maciel, C. A. O., Oliveira-Junior, G. S., Matos, B. N., Gelfuso, G. M., Nunes, S. B., Barbosa, J. D. V., & Godoy, A. L. P. C. (2022). Active Potential of Bacterial Cellulose-Based Wound Dressing: Analysis of Its Potential for Dermal Lesion Treatment, Pharmaceutics, 14, 1222.

Hou, S., Gou, L., Li, F., Li, C., Yin, X., Zhao, P., Meng, Y., Yin, X., Xia, Z., Ren, J., Zhang, L., & Xia, X. (2025). A multifunctional bacterial cellulose wound dressing based on cotton fabric for infected wound healing, International Journal of Biological Macromolecules, 322(3), 146850, ISSN 0141-8130.

Indriyati, I., Irmavati, Y., & Puspitasari, T. (2019). Comparative study of bacterial cellulose film dried using microwave and air convection heating, J. Eng. Technol. Sci., 51, 121–132.

Jiji, S., Udhayakumar, S., Maharajan, K., Rose, C., Muralidharan, C., & Kadirvelu, K. (2020). Bacterial cellulose matrix with in situ impregnation of silver nanoparticles via catecholic redox chemistry for third degree burn wound healing, Carbohydr. Polym., 245, 116573.

Khalid, A., Khan, R., Ul-Islam, M., Khan, T., & Wahid, F. (2017). Bacterial cellulose-zinc oxide nanocomposites as a novel dressing system for burn wounds,

Carbohydr. Polym., 164, 214–221.

Khan, S., Ul-Islam, M., Khattak, A., Ullah, M.W., & Park, J.K. (2015). Bacterial cellulose-titanium dioxide nanocomposites: Nanostructural characteristics, antibacterial mechanism, and biocompatibility, Cellulose, 22, 565–579.

Kiziltas, E.E, Kiziltas, A., & Gardner, D.J. (2015). Synthesis of bacterial cellulose using hot water extracted wood sugars, Carbohydr. Polym., 124, 131–138.

Kushwaha, A., Goswami, L., & Kim, B.S. (2022). Nanomaterial-based therapy for wound healing, Nanomaterials, 12, 618.

Le Ouay, B., & Stellacci, F. (2015). Antibacterial activity of silver nanoparticles: A surface science insight, Nano Today, 10, 339–354.

Li, W., Yu, J., Li, Q., Wang, H., Liu, X., Li, P., Jiang, X., & Yang, J. (2024). Bacterial cellulose nanofiber reinforced self-healing hydrogel to construct a theranostic platform of antibacterial and enhanced wound healing, International Journal of Biological Macromolecules, 281(2), 136336.

Lemnaru, G. M., Motelica, L., Trusca, R. D., Ilie, C. I., Ficai, D., Oprea, O., Stoica-Guzun, A., Ficai, A., Constantinescu, G., & Ditu, L. M. (2022) Bacterial Cellulose Membranes Loaded With Cinnamon Essential Oil., U.P.B. Sci. Bull., 84, 4.

Mani Pujitha, I., Chandra, S.S., & Mudrika, K. (2019). Tuning the physiochemical properties of bacterial cellulose: Effect of drying conditions, J. Mater. Sci., 54, 12024–12035.

Mohamad, N., Mohd Amin, M.C., Pandey, M., Ahmad, N., & Rajab, N.F. (2014). Bacterial cellulose/acrylic acid hydrogel synthesized via electron beam irradiation: Accelerated burn wound healing in an animal model, Carbohydr. Polym., 114, 312–320.

Mohamad, N., Loh, E.Y.X., Fauzi, M.B., Ng, M.H., & Amin, M.C.I.M. (2019). In vivo evaluation of bacterial cellulose/acrylic acid wound dressing hydrogel containing keratinocytes and fibroblasts for burn wounds, Drug Deliv. Transl. Res., 9, 444–452.

Natale, C. D., Gregorio, V. D., Lagreca, E., Mauro, F., Corrado, B., Vecchione, R., & Netti, P. A. (2022). Engineered bacterial cellulose nanostructured matrix for ıncubation and release of drug-loaded oil in water nanoemulsion, Frontiers in Bioengineering and Biotechnology, 10:851893.

Niculescu, A.G., & Grumezescu, A.M. An up-to-date review of biomaterials application in wound management, Polymers, 14, 421.

Pal, S., Nisi, R., Stoppa, M., & Licciulli, A. (2017). Silver-functionalized bacterial

cellulose as antibacterial membrane for wound-healing applications, ACS Omega, 2, 3632–3639.

Pang, M., ve ark., (2020). Application of bacterial cellulose in skin and bone tissue engineering, European Polymer Journal, 122: p. 109365.

Pei, Y., Ye, D., Zhao, Q., Wang, X., Zhang, C., Huang, W., Zhang, N., Liu, S., & Zhang, L. (2015). Effectively promoting wound healing with cellulose/gelatin sponges constructed directly from a cellulose solution, J. Mater. Chem. B, 3(38), 7518–7528.

Piasecka-Zelga, J., Zelga, P., Szulc, J., Wietecha, J., & Ciecha'nska, D. (2018). An in vivo biocompatibility study of surgical meshes made from bacterial cellulose modified with chitosan, Int. J. Biol. Macromol., 116, 1119–1127.

Portal, O., Clark, W.A., & Levinson, D.J. (2009). Microbial cellulose wound dressing in the treatment of nonhealing lower extremity ulcers, Wounds, 21, 1–3.

Stanisławska, A., Staroszczyk, H., & Szkodo, M. (2020). The effect of dehydration/rehydration of bacterial nanocellulose on its tensile strength and physicochemical properties, Carbohydr. Polym., 236, 116023.

Sulaeva, I., Hettegger, H., Bergen, A., Rohrer, C., Kostic, M., Konnerth, J., Rosenau, T., & Rotthast, A. (2020). Fabrication of bacterial cellulose-based wound dressings with improved performance by impregnation with alginate, Mater. Sci. Eng. C, 110, 110619.

Sun, Y., Meng, C., Xie, Y., He, W., Wang, Y., Qiao, K., & Yue, L. (2018). The effects of two biocompatible plasticizers on the performance of dry bacterial cellulose membrane: A comparative study, Cellulose, 25, 5893–5908.

Ul-Islam, M., Khattak, W.A., Ullah, M.W., Khan, S., & Park, J.K. (2014). Synthesis of regenerated bacterial cellulose-zinc oxide nanocomposite films for biomedical applications, Cellulose, 21, 433–447.

Wan, Y., Yang, S., Wang, J., Gan, D., Gama, M., Yang, Z., Zhu, Y., Yao, F., & Luo, H. (2020). Scalable synthesis of robust and stretchable composite wound dressings by dispersing silver nanowires in continuous bacterial cellulose, Compos. B Eng., 199, 108259.

CHAPTER 3

MECHANICAL PROPERTIES OF HEMP FIBER REINFORCED COMPOSITES

Öğr. Gör. Dr. Emin ÖZDEMİR
İstanbul Üniversitesi-Cerrahpaşa,
Mühendislik Fakültesi, İstanbul / Türkiye
https://orcid.org/0000-0002-6517-9270

Seçil Bahar KORKMAZ
İstanbul Üniversitesi-Cerrahpaşa,
Mühendislik Fakültesi, İstanbul / Türkiye

1. INTRODUCTION

The growing environmental concerns and the global shift toward sustainable production have led to increasing interest in the utilization of natural fibers in composite materials. Among these, hemp fiber stands out as a promising alternative to conventional synthetic fibers due to its minimal environmental footprint, rapid renewability, and biodegradable nature. With its high specific strength, low density, and abundance as a natural resource, hemp fiber offers significant potential for use in various industrial sectors including automotive, construction, sports equipment, and packaging (Srivastava ve ark., 2025; Kiruthika & Khan 2021; Pickering ve ark., 2016).

Composite materials are engineered systems that combine two or more distinct components to achieve superior mechanical, thermal, physical, and chemical properties unattainable by individual constituents (Kiruthika & Khan 2021; Sathishkumar ve ark., 2013; Beckermann & Pickering, 2008). Typically, they consist of a matrix phase that transfers loads and preserves structural integrity,

and a reinforcement phase that enhances strength and stiffness (Kiruthika & Khan 2021; Pickering ve ark., 2016; Beckermann & Pickering, 2008). Due to their lightweight nature, excellent strength-to-weight ratio, corrosion resistance, and design versatility, composites have become integral to modern engineering applications (Srivastava ve ark., 2025; Kiruthika & Khan 2021; Pickering ve ark., 2016; Sathishkumar ve ark., 2013).

The incorporation of natural fibers into composite fabrication aligns with global sustainability goals, offering advantages such as low cost, biodegradability, and renewability. Among natural fibers—such as flax, jute, and sisal—hemp fiber has gained particular attention for its favorable mechanical properties and environmentally friendly cultivation. The hemp plant grows rapidly without requiring pesticides or herbicides, consumes minimal water, and contributes to soil health, making it an eco-efficient raw material (Srivastava ve ark., 2025; Kiruthika & Khan 2021; Pickering ve ark., 2016).

However, several technical challenges accompany the use of hemp fiber in composite manufacturing. The hydrophilic nature of hemp fibers often leads to poor interfacial bonding with hydrophobic polymer matrices, thereby limiting mechanical performance (Pickering ve ark., 2016; Beckermann & Pickering, 2008; Beckermann, 2004). Additional issues such as moisture absorption, biological degradation, and limited thermal stability also affect the overall durability and functionality of the composites (Dahal et al. 2022; Pickering ve ark., 2016; Ahmad et al. 2020). To overcome these limitations, researchers have explored fiber surface modifications, the use of suitable coupling agents, and the optimization of processing techniques. Chemical treatments, such as alkali modification, have been shown to enhance interfacial adhesion and improve both mechanical and thermal properties (Pickering ve ark., 2016; Beckermann & Pickering, 2008; Beckermann, 2004).

Previous studies have demonstrated that parameters including fiber content, orientation, length, and matrix type significantly influence the mechanical performance of hemp fiber-reinforced composites (Kiruthika & Khan 2021; Pickering ve ark., 2016; Beckermann & Pickering, 2008; Shahzad, 2013; Shahzad, 2012a). Increasing the fiber content can enhance tensile strength and stiffness, whereas the quality of the fiber–matrix interface critically determines the composite's overall behavior. (Kolak & Oltulu 2025; Güney ve ark., 2023; Pickering ve ark., 2016).

In light of these considerations, this research aims to comprehensively examine the chemical and physical characteristics of hemp fibers, the various mat-

rices and processing methods used in their composites, and the resultant mechanical behaviors. Moreover, the study highlights the sustainability advantages of hemp fiber composites and discusses the technical challenges that must be addressed to expand their industrial applicability.

2. HEMP FIBERS AND PROPERTIES

Hemp fiber (Cannabis sativa L.) is a natural bast fiber sourced from the stem's bark of the plant and is recognized for its strong mechanical properties. Figure 1 shows the hemp plant cultivated in open fields and the fibers obtained from the stem of the plant. The bast fibers extracted from the outer layer of the stem form the basis for the excellent mechanical and ecological performance as detailed below.

Figure 1. Field-grown hemp plants (Cannabis sativa L.) and fibers

The cultivation of hemp supports sustainable agriculture due to its rapid growth cycle, minimal requirement for pesticides and herbicides, and low water needs (Beckermann, 2004). The hemp plant, from which the fiber is harvested, can reach heights of 3-5 meters, is rich in fiber content, and demonstrates resilience to environmental factors. The chemical makeup of hemp fiber is defined by a high cellulose percentage (55-85%), a low lignin percentage (4%), and hemicellulose content (16%) (Dahal ve ark., 2022; Shahzad, 2013; Shahzad 2012a).

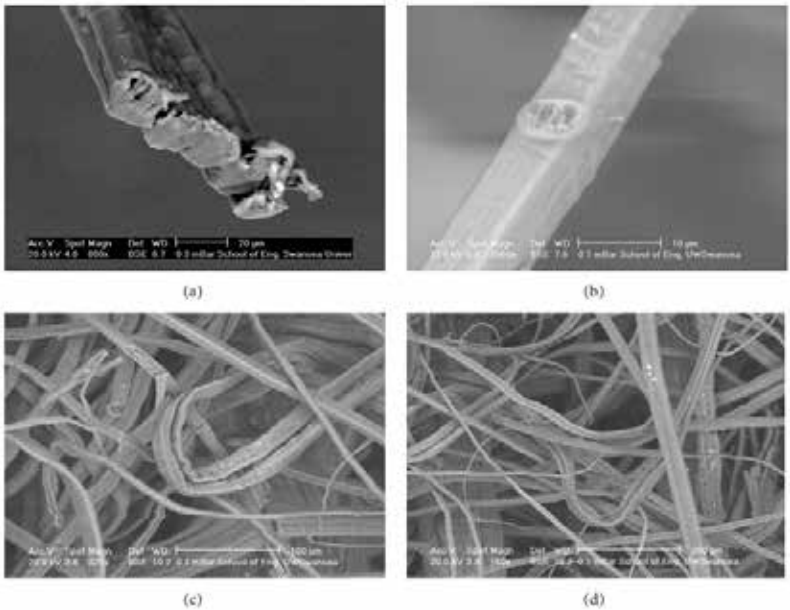

FIGURE 9: SEM micrographs of a hemp fibre bundle, (a) and (b), and loose fibres, (c) and (d).

Figure 2. SEM micrographs of a hemp fiber bundle and loose fibers.(a, b) Cross-sectional and longitudinal views of a fiber bundle showing surface and lumen,(c, d) Detailed morphology of loose fibers with rough texture and microfibrils.(Ahmad ve ark., 2020)

The primary reason for the increased tensile strength and elastic modulus of the fiber is its high cellulose content. Furthermore, a lower lignin content facilitates the separation and processing of fibers (Dahal ve ark., 2022; Shahzad, 2013; Shahzad 2012a). On a microscopic level, the fibers' cell walls are made up of crystalline microfibrils, which help resist tensile forces (Ahmad ve ark., 2020; Shahzad 2012a). This microstructural detail is illustrated in Figure 2,

which presents SEM images of hemp fiber bundles and individual loose fibers. Images (a) and (b) reveal the surface morphology and internal lumen of the fiber bundle, while (c) and (d) show the rough and fibrillated surfaces of loose fibers. Such structures enhance the fiber's surface area, improve interfacial bonding with matrices, and contribute to mechanical interlocking.

In terms of mechanical properties, hemp fiber exhibits a tensile strength between 550-900 MPa and an elastic modulus ranging from 50-70 GPa (Shahzad, 2013; Shahzad 2012a). These characteristics allow hemp fiber to compete with various synthetic fibers. When compared to E-glass fiber, hemp fiber shows a comparable specific strength while having a lower density (1.48 g/cm³) (Kiruthika & Khan 2021; Shahzad, 2013; Shahzad 2012a). Such attributes make hemp fiber a compelling choice for creating lightweight yet strong composites.

From an ecological standpoint, hemp fiber is considered a carbon-neutral resource, as it captures CO_2 from the air during its growth and can be combusted for energy recovery at the end of its lifecycle (Srivastava ve ark., 2025; Dahal ve ark., 2022; Shahzad 2012a). Moreover, its ability to biodegrade ensures it causes minimal environmental impact once discarded. Nonetheless, the hygroscopic characteristic of hemp fibers, along with their moisture absorption and vulnerability to microbial breakdown, may restrict their application in composites (Dahal ve ark., 2022; Shahzad 2012a). To address these issues, treatments such as alkali and acetylation are employed to modify the fiber surfaces (Shahzad 2012a; Beckermann & Pickering, 2008).

The ecological and mechanical benefits of hemp fiber have made it an appealing material for a range of uses, including in automotive, construction, sports equipment, and biocomposite markets (Shahzad, 2013; Shahzad 2012a). However, in order to optimize performance, factors such as fiber morphology, length, orientation, and compatibility with the matrix must be managed carefully (Kiruthika & Khan 2021; Shahzad 2012a).

3. PRODUCTION METHODS OF HEMP FIBER REINFORCED COMPOSITES

Hemp fiber reinforced composites are materials in which hemp fibers are embedded within a polymer matrix to improve strength, stiffness, and environmental sustainability. The choice of production method significantly affects the mechanical and thermal properties of the resulting composite. The most com-

monly used production methods (Figure 3) include hand lay-up, compression molding, injection molding, extrusion, and vacuum-assisted techniques.

The fabrication methods used in the production of hemp fiber-reinforced polymer composites play a decisive role in defining the microstructural integrity, mechanical strength, and thermal stability of the final material. The choice of manufacturing technique influences the fiber dispersion, fiber–matrix adhesion, and degree of void formation within the composite (Pickering ve ark., 2016; Shahzad, 2012a; Kiruthika & Khan, 2021).

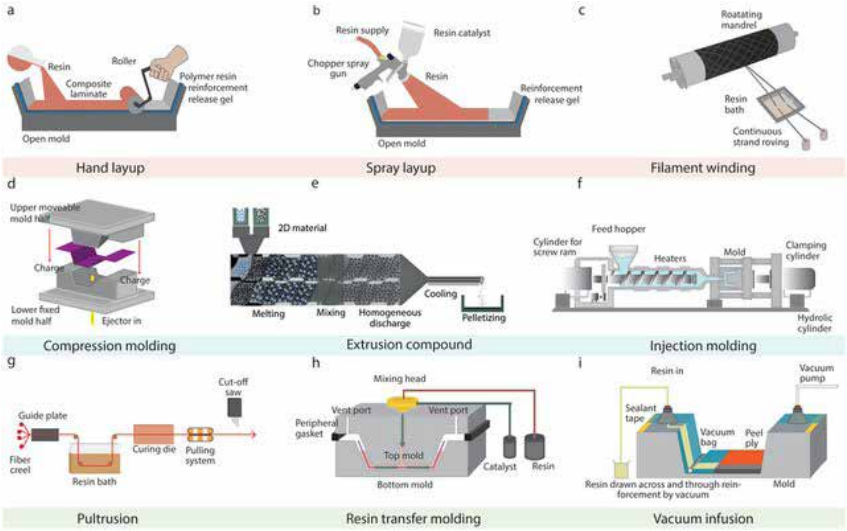

Figure 3. Manufacturing techniques for fiber reinforced composites (Maiti ve ark., 2022)

In general, composite processing employs either thermoplastic or thermoset polymer matrices. Thermoplastic matrices such as polypropylene (PP) and polyethylene (PE) are widely used due to their recyclability and reprocessability, while thermoset matrices such as epoxy, unsaturated polyester, and vinyl ester provide superior dimensional stability, chemical resistance, and heat tolerance (Beckermann & Pickering, 2008; Kiruthika & Khan, 2021). Table 1 compares the fundamental characteristics of thermoplastics and thermosets commonly used in natural fiber composite manufacturing.

Table 1. Comprasion of Thermoplastics and Thermosets (Kiruthika & Khan 2021; Shahzad 2012a; Beckermann & Pickering, 2008).

Property	**Thermoplastics**	**Thermosets**
Recyclability	High	Low
Processing Temperature	Low to Moderate	High
Chemical Resistance	Moderate	High
Curing Time	None (Thermoplastic)	Requires Curing
Toughness	High	Moderate to Low
Repairability	Yes	No
Cost	Generally Lower	Generally Higher

3.1. Hand Lay-Up Process

The **hand lay-up method** is one of the earliest and most economical fabrication techniques for natural fiber composites. It is particularly suitable for small-scale or experimental production. In this method, layers of hemp fiber mats or woven fabrics are manually placed within an open mold. Liquid resin—typically epoxy, polyester, or a bio-based matrix—is then applied by brushing or spraying over the fiber layers. Once the desired laminate thickness is achieved, the composite is cured at ambient or elevated temperature to solidify the matrix (Kiruthika & Khan, 2021; Dahal ve ark., 2022).

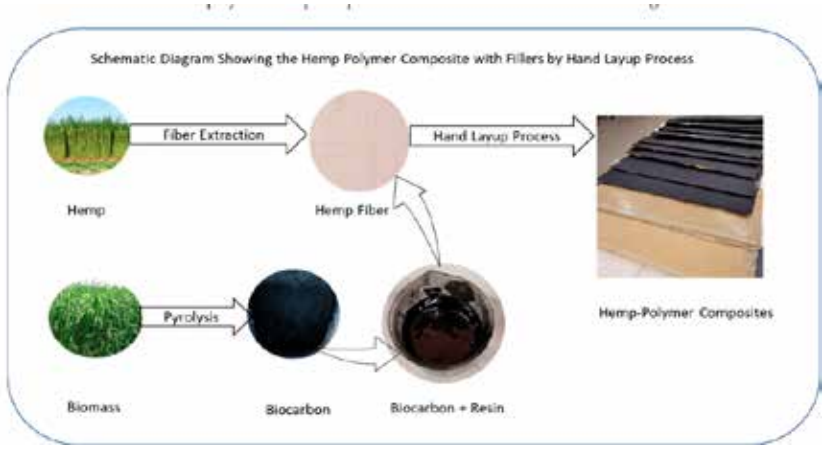

Figure 4. Schematic diagram of the hand lay-up process for hemp fiber-reinforced polymer composites with biocarbon fillers (Dahal ve ark., 2022)

This process allows flexibility in fiber orientation and layer thickness, but it is labor-intensive and susceptible to voids or uneven fiber dispersion. The simplicity of the technique, however, makes it ideal for prototyping and laboratory-scale research (Beckermann, 2004). Figure 4 illustrates a schematic flow diagram of the hand lay-up process for hemp fiber–biopolymer composites, showing steps from fiber extraction and filler preparation to composite curing.

3.2. Compression Molding

Compression molding is widely applied for medium to large-scale production of hemp fiber composites. In this method, a pre-measured mixture of hemp fibers and a thermoset or thermoplastic resin is placed inside a heated mold cavity. The mold is then closed under high pressure and temperature, facilitating resin flow and fiber impregnation (Pickering ve ark., 2016). The curing process produces dense composites with superior surface finish and uniform fiber distribution.

This technique is suitable for producing **automotive interior panels, construction boards, and semi-structural components**, combining moderate cost with high repeatability. However, control of moisture content and fiber alignment remains crucial to avoid porosity and thermal degradation (Güney ve ark., 2023).

3.3. Injection Molding

The injection molding process is primarily used for the mass production of composites reinforced with short hemp fibers. In this method, thermoplastic pellets containing dispersed hemp fibers are melted and injected under high pressure into a closed mold. After cooling, the part solidifies into the desired shape (Beckermann & Pickering, 2008; Panaitescu ve ark., 2020).

Injection molding offers high-speed production, excellent dimensional accuracy, and automation potential, making it ideal for consumer goods and lightweight automotive parts. However, because the process employs **short fibers (typically <5 mm)**, the reinforcement efficiency and load transfer capacity are lower compared to long-fiber composites (Pickering ve ark., 2016; Shahzad, 2013).

3.4. Extrusion Process

In the extrusion process, hemp fibers are blended with molten thermoplas-

tic polymers and forced through a die to produce continuous profiles, such as sheets, pipes, or decking materials. The extruded strands can subsequently be pelletized or thermoformed (Dahal ve ark., 2022).

This method provides continuous manufacturing capability, good process control, and compatibility with recycling, making it suitable for producing sustainable construction and packaging materials (Kolak & Oltulu, 2025). However, fiber degradation during high-temperature processing and uneven dispersion remain important challenges.

3.5. Vacuum-Assisted and Resin Transfer Molding (RTM)

To overcome limitations of hand lay-up, **vacuum-assisted resin transfer molding (VARTM)** has gained attention in recent years. Here, dry hemp fibers are arranged inside a sealed mold, and resin is drawn through the fiber preform under vacuum pressure (Srivastava ve ark., 2025). The method ensures superior fiber wetting, reduced void content, and enhanced mechanical integrity compared to manual lay-up (Shahzad, 2012a). Despite its higher equipment cost, RTM provides reproducibility and consistent fiber volume fractions, essential for structural applications.

Each manufacturing technique offers a distinct balance among cost, performance, and scalability. The hand lay-up process remains the most preferred approach for small-scale research and prototype development due to its simplicity, low equipment requirements, and flexibility. In contrast, compression molding and injection molding dominate large-scale industrial production, providing high reproducibility, uniform quality, and fast processing cycles suitable for automotive and construction components.

The extrusion process enables continuous manufacturing of profiles and sheets, making it ideal for structural and consumer products that require consistent geometry. Meanwhile, resin transfer molding (RTM) and other vacuum-assisted processes deliver composites with superior mechanical strength, low void content, and excellent surface finish, making them suitable for advanced structural applications.

Ultimately, the selection of a production method depends on multiple factors, including the targeted mechanical and thermal performance, production scale, cost efficiency, and application requirements. When combined with appropriate fiber surface treatments (e.g., alkali treatment, coupling agents) and optimized processing parameters, hemp fiber-reinforced composites can achie-

ve enhanced interfacial bonding and improved overall performance.

With their renewable origin and favorable strength-to-weight ratio, hemp fiber composites represent a sustainable alternative to conventional synthetic fiber composites in sectors such as automotive, construction, packaging, and consumer goods (Srivastava ve ark., 2025; Pickering ve ark., 2016; Shahzad, 2012a).

4. MECHANICAL PROPERTIES

Hemp fiber reinforced composites (HFRCs) are materials in which natural hemp fibers are embedded within a polymer matrix to improve mechanical performance. The key mechanical properties include:

- **Tensile Strength**: It is the maximum stress that a material can withstand while being stretched or pulled before breaking. Composites with aligned and long hemp fibers show higher tensile strength compared to randomly oriented or short fibers. Fiber length, orientation, fiber-matrix adhesion and fiber ratio are the factors affecting tensile strength.
- **Flexural Strength**: It is the ability of a material to resist deformation under bending. Alkali-treated hemp fibers and coupling agents like MAPP increase flexural strength by enhancing interfacial bonding.
- **Impact Strength:** It is the capacity of a material to absorb energy during sudden impact. Moderate fiber content (e.g., 30%) often shows maximum impact strength. Excessive fiber content or over-treatment may reduce toughness and cause brittleness.
- **Elastic Modulus / Stiffness:** It is a measure of a material's resistance to deformation under load. HFRCs with well-dispersed fibers (achieved through compression or injection molding) exhibit higher stiffness due to reduced porosity and better load transfer.
- **Fiber-Matrix Interface:** Proper bonding between hydrophilic hemp fibers and hydrophobic polymer matrices is crucial. Chemical treatments like NaOH remove lignin and hemicellulose, increasing surface roughness and adhesion. Coupling agents further enhance mechanical properties by forming chemical bonds at the interface.

The mechanical characteristics of composites reinforced with hemp fibers are influenced by several factors, including the physical and chemical composition of the fiber, as well as the fiber content, length, orientation, bonding at the fiber-matrix interface, type of matrix utilized, and method of production. Research indica-

tes that these elements have a direct impact on tensile strength, flexural strength, impact resistance, elastic modulus, and fatigue behavior (Sathishkumar ve ark., 2013; Pickering ve ark., 2016; Beckermann & Pickering, 2008).

4.1. Fiber Content and Mechanical Performance

Fiber content plays a crucial role in determining the load-bearing capacity of the composite. Beckermann & Pickering (2008) found that in polypropylene matrix composites consisting of 20%, 30%, and 40% fiber, a higher fiber content notably improved both the elastic modulus and tensile strength; however, performance declined beyond 40% due to fiber clumping and a negative effect on matrix continuity. Likewise, Srivastava et al. (2025) identified that 30% fiber content represented the optimal level, with tensile strength diminishing at higher contents because of incompatibility at the fiber-matrix interface. Etaati et al. (2016) and Benhadou et al. (2016) reported that polypropylene composites containing 35% hemp fiber experienced a 15% rise in tensile strength but displayed a reduction in impact resistance. This trend is visually supported in Figure 5, where tensile strength increases with fiber content up to approximately 50%, after which a slight decline is observed (Alavudeen ve ark., 2011). Beckermann & Pickering (2008) observed that tensile strength continued to ascend until reaching 40% fiber content, but beyond 45%, there was an increased likelihood of fracture due to uneven fiber distribution within the matrix.

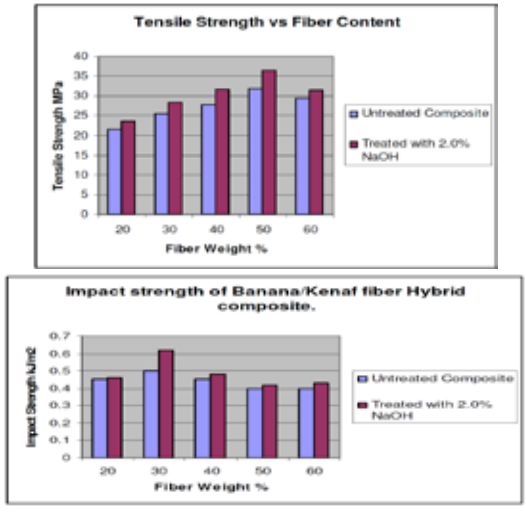

Figure 5. Tensile strength and impact strength of untreated and NaOH-treated fiber-reinforced composites as a function of fiber weight percentage (Alavudeen ve ark., 2011).

On the other hand, impact strength indicates how well composites withstand sudden forces. According to Beckermann & Pickering (2008), polypropylene composites containing 30% fiber exhibited an impact strength of 14 kJ/m². However, increasing the fiber content to 40% resulted in a decrease in impact strength to 11 kJ/m². According to Pickering et al. (2016), increasing impact energy leads to a progressive degradation in both tensile strength and elastic modulus of hemp/epoxy laminates. This reduction indicates that higher impact loads induce interfacial debonding and microcrack propagation, highlighting the importance of balancing toughness with impact resistance during composite design. Similar trends were also noted by Kiruthika & Khan (2021) for natural fiber-reinforced epoxy systems, where higher impact energy resulted in decreased stiffness and tensile performance. Further insights into impact-related degradation are provided in Figure 6, which illustrates how increasing impact energy reduces both tensile strength and elastic modulus in hemp/epoxy laminates. This behavior highlights the importance of balancing toughness with impact resistance during composite design (De Vasconcellos ve ark., 2014). These results suggest that the ideal fiber content might differ based on the specific application and type of matrix used.

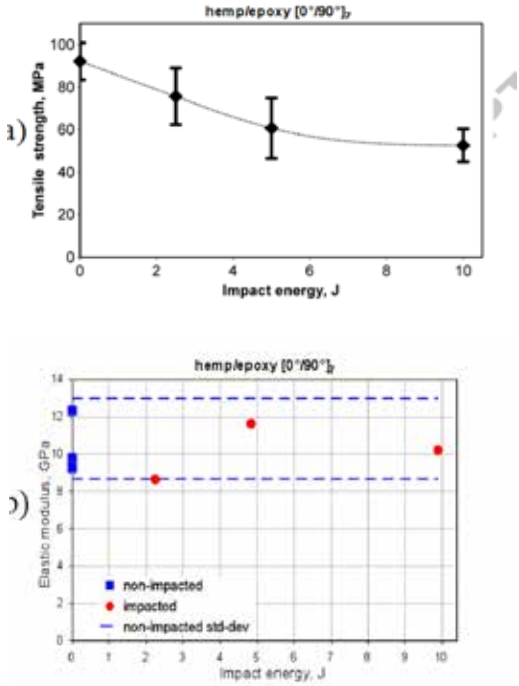

Figure 6. Effect of impact energy on tensile strength and elastic modulus of hemp/epoxy laminates ($[0°/90°]_7$ configuration) (De Vasconcellos ve ark., 2014).

4.2. Effect of Fiber Properties, Surface Treatment, and Interfacial Bonding on Mechanical Properties

The mechanical performance of hemp fiber composites is strongly governed by the characteristics of the fibers and the quality of the fiber–matrix interfacial bonding. Since natural fibers are inherently hydrophilic and most polymer matrices are hydrophobic, poor interfacial adhesion typically occurs, resulting in reduced mechanical performance (Vijayakumar & Palanikumar, 2020; Pickering ve ark., 2016; Shahzad, 2012b; Beckermann & Pickering, 2008).

To enhance compatibility between the fiber and matrix, **chemical surface treatments** such as alkaline (NaOH) and silane coupling methods are commonly applied. These treatments remove surface impurities like lignin and hemicellulose, increase surface roughness, and promote stronger matrix adhesion (Shah ve ark., 2022; Sepe ve ark., 2018; Shahzad, 2012b; Beckermann & Pickering, 2008;).

Experimental investigations have demonstrated that **alkali treatment (typically 2–10% NaOH)** significantly improves the tensile and flexural properties of hemp fiber composites by enhancing interfacial bonding (Sun ve ark., 2024; Alavudeen ve ark., 2011; Islam ve ark., 2011). For example, Sun et al. (2024) reported that composites made with NaOH-treated fibers exhibited a 20–25% increase in tensile strength compared to untreated fibers. Similarly, alkaline treatment removes lignin and hemicellulose from the fiber surface, increases fiber surface energy, and enables stronger chemical bonding with the matrix. On the other hand, Shahzad (2012b) discovered that alkali-treated fibers could increase impact strength by 10–15%. Nonetheless, if the chemical treatment is excessively strong, it can lead to brittleness in the fibers and a decline in mechanical performance.

The effects of NaOH treatment and MAPP coupling agent on flexural strength are presented in Figure 7, which shows that both NaOH treatment and the addition of MAPP substantially increase the flexural strength of hemp fiber composites compared to untreated fibers. The highest flexural strength was observed for fibers treated with **10% NaOH and 6 wt.% MAPP**, while flexural strength increased linearly with fiber loading, reaching approximately **2–2.3 times** the neat matrix strength at **50 wt.% fiber content** (Vilaseca ve ark., 2020).

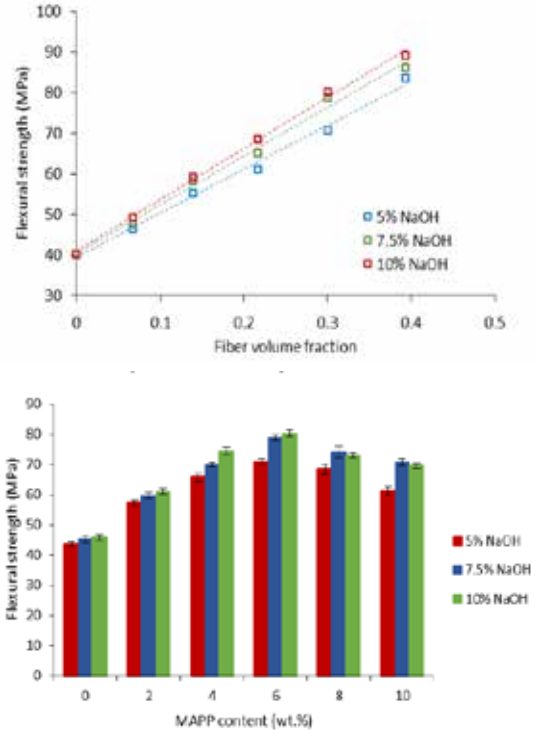

Figure 7. Effect of NaOH treatment and MAPP content on the flexural strength of hemp fiber composites (Vilaseca ve ark., 2020).

Additionally, the incorporation of coupling agents, particularly maleic anhydride-grafted polypropylene (MAPP), further strengthens the interface by forming chemical linkages between the fiber and polymer matrix. These coupling agents improve both tensile and flexural strength (Vilaseca ve ark., 2020; Pickering ve ark., 2016; Sepe ve ark., 2018). Experimental results indicate that composites containing 2 wt.% MAPP exhibited a 15–20% increase in tensile strength and a 10–13% increase in flexural strength, confirming the synergistic effect between alkali treatment and coupling agents.

Further verification of these results is provided in Figure 8, which illustrates how surface treatments (NaOH and ETAD) affect the tensile strength and modulus of hemp fiber-reinforced LDPE composites. The figure shows that both treatments improve mechanical performance, particularly at higher fiber loadings (20–30 wt.%), confirming the role of chemical surface modification in enhancing interfacial bonding (Sun ve ark., 2024).

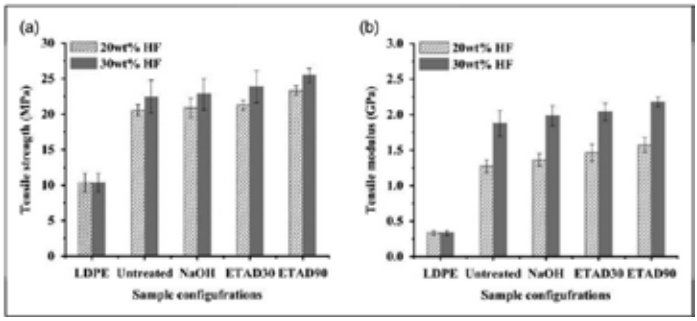

Figure 8. Effect of surface treatments (NaOH and ETAD) on the tensile strength and modulus of 20 wt% and 30 wt% hemp fiber-reinforced LDPE composites (Sun ve ark., 2024).

Overall, these findings demonstrate that surface modification—through alkali treatment and coupling agents such as MAPP—plays a crucial role in improving the mechanical behavior of hemp fiber composites by strengthening the interfacial bonding between the fiber and matrix.

4.3. Effects of Fiber Length and Orientation on Mechanical Properties

The length of fibers plays a critical role in determining the mechanical performance of hemp fiber-reinforced composites. According to Udaya Kiran et al. (2007), composites fabricated with 25 mm long fibers exhibited a 30% increase in tensile strength compared to those made with 5 mm fibers. As can be clearly seen from Figure 9, the tensile strength of the sun hemp fiber reinforced composite increases with increasing fiber length up to 30 mm and then decreases.

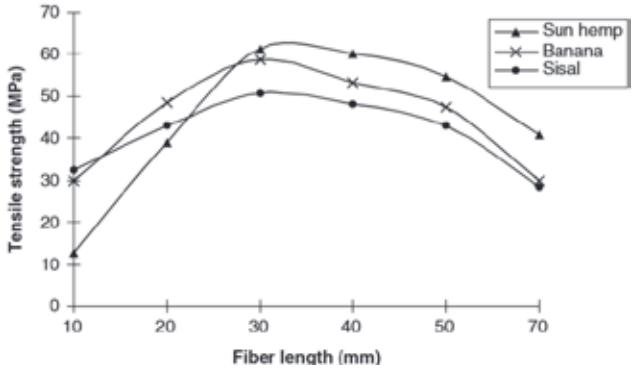

Figure 9. Effect of fiber length on the tensile strength of various natural fiber based composites (Udaya Kiran ve ark., 2007).

However, longer fibers pose challenges in maintaining uniform distribution and controlling fiber orientation during processing (Beckermann & Pickering, 2008; Pickering ve ark., 2016; Kiruthika & Khan, 2021). The results of the researches reported that unidirectional hemp fiber composites achieved a 25–35% improvement in tensile strength compared to randomly oriented fibers, while randomly oriented fibers provided better energy distribution for impact resistance (Lu ve ark., 2022; Yuanjan & Isaac, 2007; Kobayashi & Takada, 2013). As noted by Shahzad (2013), randomly oriented fibers can enhance impact strength by distributing energy more evenly and helping to halt crack propagation.

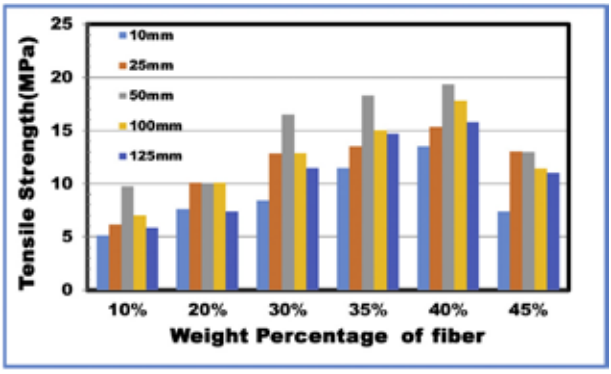

Figure 10. Effect of fiber length and fiber loading on the tensile strength of composites (Vijayakumar & Palanikumar, 2020).

Srivastava et al. (2025) emphasized that oriented fibers also enhanced flexural strength, though they increased manufacturing complexity and cost. Fiber length and orientation also influence the thermal properties and load transfer capabilities of composites. Short fibers are easier to process but offer limited stress transfer, whereas long fibers improve tensile strength and modulus but are more difficult to align uniformly (Lotfi ve ark., 2021; Panaitescu ve ark., 2020; Beckermann & Pickering, 2008). As shown in Figure 10, tensile strength increases with fiber length up to an optimum point, beyond which agglomeration and poor dispersion lead to a reduction in performance (Vijayakumar & Palanikumar, 2020).

4.4. Effect of Production Methods on Mechanical Performance

The method of production significantly influences mechanical properties.

Etaati et al. (2016) and Benhadou et al. (2016) stated that hemp fiber composites produced through compression molding exhibit superior tensile strength and elastic modulus compared to those fabricated using hand lay-up techniques. They demonstrated that injection molding facilitates better fiber distribution and minimizes porosity, thereby enhancing mechanical strength. Researchers found that hybrid composites incorporating both hemp and jute fibers were 20% stronger in tension and exhibited a 15% improvement in bending performance compared to composites made exclusively from hemp fibers. This improvement is attributed to the synergistic effect between the two fibers, which enhances stress transfer and interfacial adhesion within the matrix (Islam ve ark., 2024; Mahmud ve ark., 2025). This suggests that combining different types of fibers can enhance mechanical characteristics. A comparative schematic is presented in Figure 11, outlining the production methods most commonly used in hemp fiber composites. As seen, more advanced techniques like compression and injection molding offer notable gains in tensile and flexural properties due to better fiber distribution and reduced porosity (Etaati ve ark., 2016; Benhadou ve ark., 2016; Beckermann & Pickering, 2008).

Processing influence in summary:

- Hand lay-up is simple but may produce uneven fiber distribution.
- Compression and injection molding improve fiber alignment and reduce voids, resulting in better tensile, flexural, and impact properties.
- Hybrid composites (e.g., hemp + jute) can further enhance strength and bending performance.

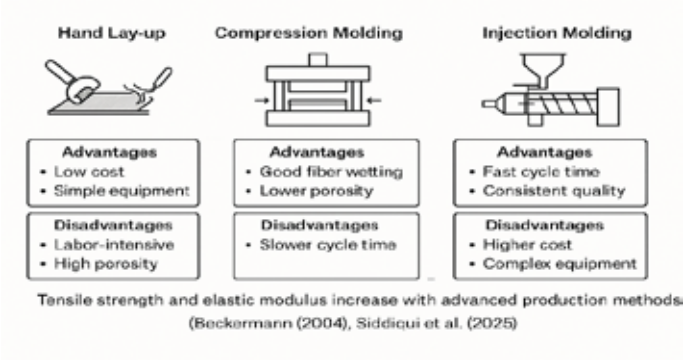

Figure 11. Comparison of hand lay-up, compression molding, and injection molding methods used in fiber-reinforced composite production, showing relative effects on mechanical performance.

5. INDUSTRIAL APPLICATIONS

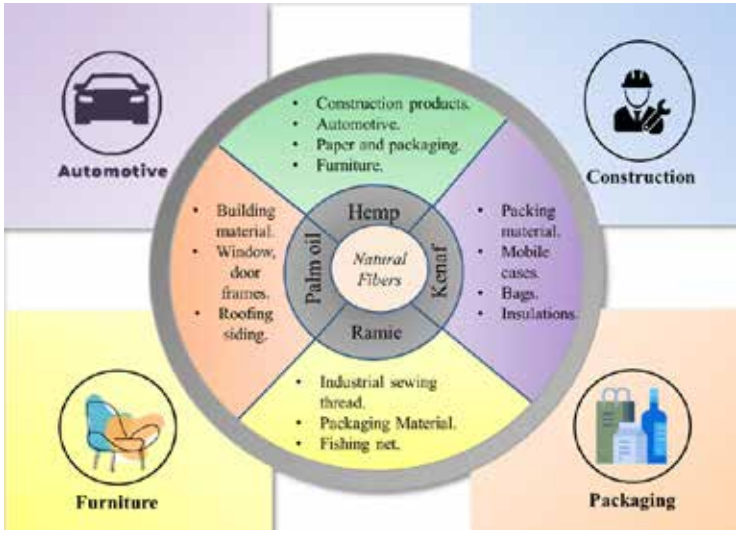

Figure 12. Applications of natural fibers (Mundhe & Kandasubramanian; 2024)

Hemp fiber-reinforced composites are becoming increasingly popular as eco-friendly alternatives to traditional composites across various industries due to their sustainability, lightweight nature, and adequate mechanical and thermal characteristics. Numerous studies in the literature have explored the potential uses of these composites, especially within the automotive, construction, sports equipment, furniture, packaging, energy, biomedical, and textile industries (Mundhe & Kandasubramanian; 2024; Kiruthika & Khan; 2021; Shahzad; 2012a). The following sections provide a breakdown of hemp fiber composite applications by industry. These applications are visually summarized in Figure 12, which illustrates the sector-specific uses of hemp and other natural fibers across industries such as automotive, construction, furniture, and packaging (Mundhe & Kandasubramanian; 2024).

5.1. Automotive

The automotive sector was among the pioneers in utilizing natural fiber-reinforced composites, recognizing their lightweight structure, cost efficiency, and environmentally friendly attributes. Hemp fibers are commonly incorporated into interior trim elements, including door panels, trunk linings, roof panels, and seat backs. Manufacturers such as BMW, Mercedes-Benz, and Audi have implemented hemp fiber composite interior components to achieve weight

reductions of 20-30% and lessen their environmental impact (Sapuan ve ark., 2025; Mundhe & Kandasubramanian 2024).

Beckermann (2004) and Beckermann & Pickering (2008) reported that polypropylene composites reinforced with 30% hemp fiber achieved around 25% weight reduction and 10% cost saving in automotive door panel applications, while their use in exterior components remained limited due to moisture sensitivity and durability issues.

5.2. Construction

In the construction industry, composites reinforced with hemp fiber are utilized in lightweight panels, insulation materials, concrete reinforcements, and roofing elements (Islam & Hasan, 2025; Pickering ve ark., 2016). Hemp fiber-reinforced concrete enhances resistance to cracking while also minimizing the carbon footprint (Islam & Hasan, 2025) Moreover, "hempcrete," a lightweight building material derived from hemp, offers thermal insulation and moisture management and is gaining popularity in various countries (Stevulova ve ark., 2015, Stevulova ve ark., 2018).

Researchs by Stevulova ve ark., (2015, 2018) demonstrated that gypsum panels reinforced with hemp fiber exhibited 15% greater bending strength and 25% improved thermal insulation compared to standard gypsum panels. Additionally, hemp fiber insulation boards provide breathable characteristics and low thermal conductivity, which contributes to better indoor air quality.

5.3. Sports Equipment and Recreation

Composites reinforced with hemp fiber are favored in sports equipment because of their lightweight nature, flexibility, and adequate strength. They find applications in skis, snowboards, bicycle frames, racket frames, and surfboards (Kiruthika & Khan, 2021; Pickering ve ark., 2016). According to Mundhe, & Kandasubramanian, (2024), surfboards made from hemp fiber have a 30% lower environmental footprint compared to those made from carbon fiber, despite being 15% less strong.

Mundhe, & Kandasubramanian, (2024) reported that hemp fiber-reinforced racket frames provided vibration damping similar to glass fiber-reinforced frames, enhancing user comfort. The growing interest in eco-friendly and bio-

degradable materials in this field is driving the increased adoption of hemp fiber-based products in the future.

5.4. Furniture and Interior Design

Hemp fiber-reinforced composites are utilized in furniture and interior design applications. They are commonly used for chair seats, table tops, cabinet panels, and decorative elements. Researchers noted that hemp fiber composite panels for furniture had a 20% lower density and released no formaldehyde compared to conventional materials such as MDF and chipboard (Mundhe, & Kandasubramanian, 2024; Kiruthika & Khan, 2021).

The ability to regulate moisture and the appealing look of the natural fiber enhance their attractiveness for interior design. Nevertheless, it is advisable to use protective coatings to boost surface hardness and resistance to scratches (Mundhe, & Kandasubramanian, 2024).

5.5. Packaging and Disposable Products

Biocomposites reinforced with hemp fiber are used in the packaging of food and consumer goods, as well as in disposable containers, plates, and cutlery. When mixed with biopolymer matrices, it becomes feasible to produce packaging materials that are 100% biodegradable and compostable (Sapuan ve ark., 2025; Mundhe, & Kandasubramanian, 2024). Kiruthika & Khan (2021) reported that hemp fiber-reinforced PLA (polylactic acid) composites exhibited 18% higher tensile strength and 12% reduced moisture permeability compared to pure PLA.

In this domain, hemp fiber presents a sustainable substitute for plastic-based packaging due to its renewable and natural characteristics. However, challenges related to production costs and scalability persist (Sapuan ve ark., 2025; Mundhe, & Kandasubramanian, 2024).

5.6. Energy and Insulation Applications

Hemp fiber is also employed as an insulation material due to its low thermal conductivity and soundproofing capabilities. Researchers have highlighted that insulation panels made from hemp fiber exhibit a lower environmental impact and contribute to improved indoor air quality compared to conventional glass

wool and stone wool options (Mundhe & Kandasubramanian, 2024; Stevulova ve ark., 2018; Stevulova ve ark., 2015). The porous structure of hemp fibers enables effective thermal and acoustic insulation, while their moisture-regulating properties help prevent mold growth, further enhancing the healthiness of indoor environments. Additionally, hemp fiber insulation supports energy efficiency objectives in construction, offering sustainable alternatives for wall panels, roofing elements, subfloor insulation, acoustic boards, and prefabricated building components. Production methods for hemp-based insulation are generally energy-efficient, and performance can be further optimized through mechanical or chemical modifications of the fibers, making these materials a promising option for green building solutions (Mundhe & Kandasubramanian, 2024).

5.7. Textile Applications

Hemp fibers have long been recognized for their potential in textile applications due to their excellent mechanical properties, durability, and eco-friendly nature. They are naturally strong, lightweight, and resistant to wear, making them suitable for a variety of textile products such as clothing, ropes, canvas, and technical textiles. Additionally, hemp fibers exhibit good moisture absorption and breathability, enhancing wearer comfort. Researchers have also highlighted the role of chemical treatments and surface modifications in improving the spinnability, softness, and compatibility of hemp fibers with other textile fibers, enabling blended fabrics and advanced textile composites (Shahzad, 2012a; Ahmad ve ark., 2020; Kiruthika & Khan, 2021; Maiti ve ark., 2022; Lotfi ve ark., 2021).

Hemp-based textiles are increasingly valued for their sustainability. They are biodegradable, require relatively low water and pesticide inputs, and can replace conventional cotton and synthetic fibers in both apparel and technical textile applications, thereby reducing environmental impacts (Srivastava ve ark., 2025; Mundhe & Kandasubramanian, 2024). Moreover, hemp fibers can be used in high-performance technical fabrics for protective clothing, geotextiles, and industrial applications due to their strength, durability, and thermal properties (Dahal ve ark., 2022; Ahmad ve ark., 2020).

5.8. Biomedical Applications

Hemp fibers have recently attracted growing interest in the biomedical field due to their biocompatibility, non-toxicity, antimicrobial properties, and bi-

odegradability, which align well with the increasing demand for sustainable biomaterials. Researchers emphasize that the chemical composition of hemp fibers—mainly cellulose, hemicellulose, lignin, and minor bioactive compounds—contributes to their antimicrobial and hydrophilic behavior, making them suitable for wound dressings, tissue scaffolds, and technical medical fabrics (Kiruthika & Khan, 2021; Ahmad ve ark., 2020; Dahal ve ark., 2022).

Studies have demonstrated that alkali treatment and other surface modification techniques improve the cleanliness, surface roughness, and interfacial adhesion of hemp fibers, enhancing their compatibility with polymeric matrices such as polylactic acid (PLA), polyethylene (PE), and epoxy resins (Beckermann, 2004; Beckermann & Pickering, 2008; Sepe ve ark., 2018; Narayana & Rao, 2021). These treatments not only enhance mechanical integrity but also promote cellular adhesion and proliferation, key factors for biomedical applications such as wound healing and tissue engineering scaffolds. For instance, PLA/hemp composites have been developed as biodegradable materials for disposable medical products and wound care devices, offering a balance of strength, flexibility, and environmental safety (Sapuan ve ark., 2025; Srivastava ve ark., 2025).

In addition to wound dressings, hemp fiber-reinforced composites have shown promise in antimicrobial filtration media, prosthetic devices, and medical textiles, where their breathability and moisture management properties improve patient comfort and hygiene (Maiti ve ark., 2022; Lotfi ve ark., 2021). The presence of natural phenolic compounds in hemp fibers provides intrinsic antibacterial effects, reducing the need for synthetic antimicrobial additives (Dahal ve ark., 2022; Mundhe & Kandasubramanian, 2024).

Moreover, the porous microstructure and tunable surface chemistry of hemp fibers make them potential candidates for drug delivery systems and bioresorbable implants (Shahzad, 2013; Beckermann & Pickering, 2008). However, challenges remain—particularly regarding standardization of fiber processing, sterilization methods, and long-term biocompatibility testing—which must be addressed to ensure clinical adoption (Srivastava ve ark., 2025; Güney ve ark., 2023).

Overall, the literature highlights hemp fiber's potential as a sustainable, multifunctional biomaterial that merges mechanical durability with environmental and physiological safety. As biotechnology and materials science progress, hemp-based composites are expected to expand into next-generation biomedical textiles, tissue scaffolds, and eco-friendly medical packaging (Kiruthika & Khan, 2021; Sapuan ve ark., 2025; Dahal ve ark., 2022).

In conclusion, the broad range of hemp fiber-reinforced composite appli-

cations is summarized in Table 2, which categorizes the sectors, specific uses, performance advantages, and limitations. This overview highlights the versatility of hemp fiber while emphasizing the key challenges that future research and development efforts should aim to overcome.

Table 2. Applications of hemp fiber-reinforced composites across various industries, including use cases, benefits, and associated challenges.

Sector	Applications	Benefits	Challenges
Automotive	Door panels, trims, seat backs	Lightweight, recyclable, weight reduction	Moisture sensitivity (exterior use)
Construction	Hempcrete, insulation boards, gypsum panels	Thermal insulation, CO_2 reduction	Fire resistance, long-term durability
Sports Equipment	Skis, rackets, surfboards	Low vibration, eco-friendly, flexible	Lower strength than carbon fiber
Furniture & Interior	Chair seats, table tops, cabinet panels	No formaldehyde, natural aesthetics	Surface hardness, scratch resistance
Packaging	PLA-based trays, food containers, cutlery	Biodegradable, stronger than pure PLA	Cost and production scalability
Energy & Insulation	Thermal and acoustic insulation panels	Low thermal conductivity, better air quality	Fire safety compliance
Biomedical & Textiles	Wound dressings, technical fabrics	Antimicrobial, breathable, strong	Regulatory approval and testing

6. CONCLUSION

Hemp fiber-reinforced composites (HFRCs) have emerged as one of the most promising classes of sustainable materials for modern engineering applications, offering an attractive balance between mechanical strength, low density, and environmental responsibility (Beckermann & Pickering, 2008; Pickering ve ark., 2016; Srivastava ve ark., 2025). Their superior strength-to-weight

ratio, high cellulose content, and biodegradability position hemp fibers as a viable alternative to conventional synthetic reinforcements across automotive, construction, packaging, and consumer product sectors (Kiruthika & Khan, 2021; Shahzad, 2012; Dahal ve ark., 2022).

Despite these advantages, several challenges continue to constrain the full industrial exploitation of HFRCs. The hydrophilic nature of hemp fibers leads to poor interfacial adhesion with hydrophobic polymer matrices, reducing load transfer efficiency and, consequently, mechanical performance (Islam ve ark., 2011; Narayana & Rao, 2021; Sepe ve ark., 2018). Surface modification techniques such as alkali treatment, silane coupling, acetylation, and maleic anhydride grafting have proven effective in enhancing fiber–matrix compatibility; however, excessive chemical processing can compromise fiber morphology and mechanical integrity (Oza ve ark., 2013; Shah ve ark., 2022). Moisture absorption remains another critical issue, as swelling and debonding in humid environments adversely affect dimensional stability and tensile strength (Islam & Hasan, 2025; Stevulova ve ark., 2015). Similarly, the limited thermal stability of cellulose-based fibers restricts their use in high-temperature manufacturing processes such as injection molding, though progress in fiber pre-treatments and matrix design shows promise in mitigating these effects (Benhadou ve ark., 2016; Zhan ve ark., 2021).

Beyond technical constraints, variations in fiber quality and inconsistent processing standards introduce mechanical property variability across different production batches (Panaitescu ve ark., 2020; Kolak & Oltulu, 2025). To address this, standardization of retting, extraction, and conditioning procedures is necessary to achieve reproducible composite behavior. Future advancements in fiber alignment, dispersion, and hybridization technologies—such as ultrasonic mixing and 3D-printed preforms—are expected to enhance the structural efficiency and predictability of HFRCs (Lu ve ark., 2022; He ve ark., 2023).

Research trends also indicate a paradigm shift toward multifunctional and hybrid composites, incorporating flame-retardant, antimicrobial, and UV-stabilizing additives to expand the functional scope of hemp-based materials (Maiti ve ark., 2022; Mundhe & Kandasubramanian, 2024). Furthermore, hybridization with jute, flax, or glass fibers enables synergistic improvements in tensile and impact resistance, facilitating broader applications in transport and structural components (Islam ve ark., 2024; Seid & Adimass, 2024). The integration of biodegradable matrices such as PLA, PHA, or geopolymers further enhances environmental sustainability and end-of-life management through recyclability and compostability (Sapuan ve ark., 2025; Filazi ve ark., 2025).

In conclusion, while the mechanical performance of hemp fiber composites is strongly influenced by fiber orientation, volume fraction, and surface chemistry, significant progress is being made toward overcoming inherent material and processing limitations. Continued multidisciplinary efforts focusing on interface engineering, eco-efficient processing, and performance optimization will be essential to unlock their full potential. As the literature consistently highlights, future developments in hybrid design, nanomodification, and bio-based matrices are likely to transform hemp fiber composites from a niche sustainable material into a mainstream engineering solution for lightweight, high-performance, and environmentally responsible applications (Beckermann, 2004; Pickering ve ark., 2016; Srivastava ve ark., 2025).

REFERENCES

Ahmad, S., Ullah, T., & Ziauddin. (2020). Fibers for technical textiles. In Fibers for Technical Textiles (pp. 21-47). Cham: Springer International Publishing.

Alavudeen, A., Thiruchitrambalam, M., Venkateshwaran, N., Elayaperumal, A., & Athijayamani, A. (2011). Improving mechanical properties of eco-friendly polymer hybrid composites. International Journal of Performability Engineering, 7(2), 172.

Beckermann, G. W., & Pickering, K. L. (2008). Engineering and evaluation of hemp fibre reinforced polypropylene composites: fibre treatment and matrix modification. Composites Part A: Applied Science and Manufacturing, 39(6), 979-988.

Beckermann, G. (2004). The processing, production and improvement of hemp-fibre reinforced polypropylene composite materials. Doctoral dissertation, The University of Waikato.

Benhadou, B., Haddout, A., Benhadou, M., & Bakhtari, H. (2016). Study and optimization of the injection molding of composites based on short hemp fibers. International Journal of Mechanical Engineering and Technology (IJMET), 7(4), 38-47.

Dahal, R. K., Acharya, B., & Dutta, A. (2022). Mechanical, thermal, and acoustic properties of hemp and biocomposite materials: a review. Journal of Composites Science, 6(12), 373.

De Vasconcellos, D. S., Sarasini, F., Touchard, F., Chocinski-Arnault, L., Pucci, M., Santulli, C., ... & Sorrentino, L. (2014). Influence of low velocity impact on fatigue behaviour of woven hemp fibre reinforced epoxy composites. Com-

posites Part B: Engineering, 66, 46-57.

Etaati, A., Pather, S., Cardona, F., & Wang, H. (2016). Injection molded noil hemp fiber composites: Interfacial shear strength, fiber strength, and aspect ratio. Polymer Composites, 37(1), 213-220.

Filazi, A., Akat, R., Pul, M., Tortuk, S., & Özdin, A. (2025). Physical Structural Mechanical and Thermal Insulation Properties of Hemp Fiber-Substituted Geopolymer Composites. Materials, 18(11), 2536.

Güney, O., Bilici, İ., Doğan, D., & Metin, A. Ü. (2023). Mechanical and thermal properties of recycled polyethylene/surface treated hemp fiber bio-composites. Polymer Composites, 44(8), 4976-4992.

He, L., Xia, F., Chen, D., Peng, S., Hou, S., & Zheng, J. (2023). Optimization of molding process parameters for enhancing mechanical properties of jute fiber reinforced composites. Journal of Reinforced Plastics and Composites, 42(9-10), 446-454.

Islam, S., & Hasan, B. (2025). An overview of the effects of water and moisture absorption on the performance of hemp fiber and its composites. SPE Polymers, 6(1), e10167.

Islam, M. S., Pickering, K. L., & Foreman, N. J. (2011). Influence of alkali fiber treatment and fiber processing on the mechanical properties of hemp/epoxy composites. Journal of applied polymer science, 119(6), 3696-3707.

Islam, M. Z., Sabir, E. C., & Syduzzaman, M. (2024). Experimental investigation of mechanical properties of jute/hemp fibers reinforced hybrid polyester composites. SPE Polymers, 5(2), 192-205.

Kiruthika, A. V., & Khan, A. (2021). Properties of hemp fibre reinforced polymer composites. In Vegetable Fiber Composites and their Technological Applications (pp. 255-274). Singapore: Springer Singapore.

Kobayashi, S., & Takada, K. (2013). Processing of unidirectional hemp fiber reinforced composites with micro-braiding technique. Composites Part A: Applied Science and Manufacturing, 46, 173-179.

Kolak, M. N., & Oltulu, M. (2025). Investigation of physical, mechanical and thermal properties of hemp and camelina reinforced polymer composites. Construction and Building Materials, 487, 142066.

Lotfi, A., Li, H., Dao, D. V., & Prusty, G. (2021). Natural fiber–reinforced composites: A review on material, manufacturing, and machinability. Journal of Thermoplastic Composite Materials, 34(2), 238-284.

Lu, C., Wang, C., Liu, S., Zhang, H., Tong, J., Yi, X., & Zhang, Y. (2022). Towards high-performance textile-structure composite: Unidirectional hemp fiber tape

and their composite. Industrial Crops and Products, 189, 115821.

Mahmud, M. Z. A., Rabbi, S. F., Islam, M. D., & Hossain, N. (2025). Synthesis and applications of natural fiber-reinforced epoxy composites: A comprehensive review. SPE Polymers, 6(1), e10161.

Maiti, S., Islam, M. R., Uddin, M. A., Afroj, S., Eichhorn, S. J., & Karim, N. (2022). Sustainable fiber-reinforced composites: a review. Advanced Sustainable Systems, 6(11), 2200258.

Mundhe, A., & Kandasubramanian, B. (2024). Advancements in natural fiber composites: innovative chemical surface treatments, characterizaton techniques, environmental sustainability, and wide-ranging applications. Hybrid Advances, 7, 100282.

Narayana, V. L., & Rao, L. B. (2021). A brief review on the effect of alkali treatment on mechanical properties of various natural fiber reinforced polymer composites. Materials Today: Proceedings, 44, 1988-1994.

Oza, S., Lu, N., & Korman, T. (2013). Effect of alkali treatment on the mechanical properties of hemp-HDPE composites: virgin versus recycled polymer matrix. In ICSDEC 2012: Developing the Frontier of Sustainable Design, Engineering, and Construction (pp. 818-825).

Panaitescu, D. M., Fierascu, R. C., Gabor, A. R., & Nicolae, C. A. (2020). Effect of hemp fiber length on the mechanical and thermal properties of polypropylene/SEBS/hemp fiber composites. Journal of Materials Research and Technology, 9(5), 10768-10781.

Pickering, K. L., Efendy, M. A., & Le, T. M. (2016). A review of recent developments in natural fibre composites and their mechanical performance. Composites Part A: Applied Science and Manufacturing, 83, 98-112.

Sapuan, S. M., Siddiqui, V. U., & Ilyas, R. A. (2025). Natural Fibre Polylactic Acid Composites: Properties and Applications. CRC Press.

Sathishkumar, T. P., Navaneethakrishnan, P., Shankar, S., Rajasekar, R., & Rajini, N. (2013). Characterization of natural fiber and composites–A review. Journal of Reinforced Plastics and Composites, 32(19), 1457-1476.

Seid, A. M., & Adimass, S. A. (2024). Review on the impact behavior of natural fiber epoxy based composites. Heliyon, 10(20).

Sepe, R., Bollino, F., Boccarusso, L., & Caputo, F. (2018). Influence of chemical treatments on mechanical properties of hemp fiber reinforced composites. Composites Part B: Engineering, 133, 210-217.

Shah, I., Jing, L., Fei, Z. M., Yuan, Y. S., Farooq, M. U., & Kanjana, N. (2022). A review on chemical modification by using sodium hydroxide (NaOH) to in-

vestigate the mechanical properties of sisal, coir and hemp fiber reinforced concrete composites. Journal of Natural Fibers, 19(13), 5133-5151.

Shahzad, A. (2012a). Hemp fiber and its composites–a review. Journal of composite materials, 46(8), 973-986.

Shahzad, A. (2012b). Effects of alkalization on tensile, impact, and fatigue properties of hemp fiber composites. Polymer Composites, 33(7), 1129-1140.

Shahzad, A. (2013). A study in physical and mechanical properties of hemp fibres. Advances in Materials Science and Engineering, 2013(1), 325085.

Srivastava, P., Arumugam, A. B., Kumar, R., Yadav, T., Savilov, S. V., Dhapola, P. S., & Agrawal, A. P. (2025, February). Exploring the potential of hemp fiber composites for sustainable materials in engineering applications. In Macromolecular Symposia (Vol. 414, No. 1, p. 2300255).

Stevulova, N., Cigasova, J., Purcz, P., Schwarzova, I., Kacik, F., & Geffert, A. (2015). Water absorption behavior of hemp hurds composites. Materials, 8(5), 2243-2257.

Stevulova, N., Cigasova, J., Schwarzova, I., Sicakova, A., & Junak, J. (2018). Sustainable bio-aggregate-based composites containing hemp hurds and alternative binder. Buildings, 8(2), 25.

Sun, S., Pillay, S., & Ning, H. (2024). Mechanical behaviors of composites made of natural fibers through environmentally friendly treatment. Journal of Thermoplastic Composite Materials, 37(12), 3715-3734.

Udaya Kiran, C., Ramachandra Reddy, G., Dabade, B. M., & Rajesham, S. (2007). Tensile properties of sun hemp, banana and sisal fiber reinforced polyester composites. Journal of reinforced plastics and composites, 26(10), 1043-1050.

Vijayakumar, S., & Palanikumar, K. (2020). Evaluation on mechanical properties of randomly oriented Caryota fiber reinforced polymer composites. Journal of Materials Research and Technology, 9(4), 7915-7925.

Vilaseca, F., Serra-Parareda, F., Espinosa, E., Rodríguez, A., Mutjé, P., & Delgado-Aguilar, M. (2020). Valorization of hemp core residues: Impact of NaOH treatment on the flexural strength of PP composites and intrinsic flexural strength of hemp core fibers. Biomolecules, 10(6), 823.

Yuanjian, T., & Isaac, D. H. (2007). Impact and fatigue behaviour of hemp fibre composites. Composites Science and Technology, 67(15-16), 3300-3307.

Zhan, J., Li, J., Wang, G., Guan, Y., Zhao, G., Lin, J., ... & Coutellier, D. (2021). Review on the performances, foaming and injection molding simulation of natural fiber composites. Polymer Composites, 42(3), 1305-1324.

CHAPTER 4

COMPUTATIONAL STUDY OF FORMONONETIN AND PICROPODOPHYLLIN INTERACTIONS WITH CANCER RECEPTORS, ESPECIALLY DNA AND EGFR

Prof. Dr. Sefa CELIK
Istanbul University
Science Faculty, Physics Department
https://orcid.org/0000-0001-6216-1297

Prof. Dr. Aysen E. OZEL
Istanbul University
Science Faculty, Physics Department
https://orcid.org/0000-0002-8680-8830

1. INTRODUCTION

Cancer is defined as abnormal cell growth resulting from multiple changes in gene expression. This condition is associated with an imbalance between cell proliferation and cell death. Over time, this process can lead to the development of a cell population that has the potential to invade tissues and metastasize to distant sites. If left untreated, this cell population can cause significant morbidity and ultimately threaten the host's life (Ruddon, 2007). Cancer has been around for 200 million years. Research has shown that cancer also affected the ancestors of Homo sapiens, but that the disease was not as prevalent historically (Hausman, 2019). However, a significant increase in cancer cases has been observed in the past few decades. Data from 2020 indicate that more than 10 million deaths were caused by cancer worldwide (Tewari, 2022). Formononetin

has been shown to have anticancer activity on cells from various cancer types. Furthermore, in vivo experiments support that formononetin can effectively suppress tumor growth. Formononetin can suppress multiple myeloma, breast, colon, prostate, bone, and nasopharynx tumors (Tay ve ark., 2019). Picropodophyllin, a stereoisomer of podophyllotoxin, is an antitumor agent that inhibits cell proliferation and has been shown to significantly prolong survival in vivo in human adrenocortical carcinoma, hepatocellular carcinoma, and uveal melanoma (Lu ve ark., 2013). Piropodophilin, a naturally occurring podophyllotoxin epimer and a member of the ciclolignan family, has been shown to specifically inhibit IGF-IR activity by blocking IGF-IR phosphorylation and downstream signaling pathways. Due to its high specificity, low toxicity and anti-tumor activity in various types of cancer, picropodophyllin has recently attracted increasing attention (Dong ve ark., 2019). Deoxyribonucleic acid is essential to life because it carries genetic information and tells cells how to make proteins and enzymes by copying and transcribing that information. It is also really beneficial to know how DNA is structured, how genes change, where some diseases come from, how some antiviral and antitumor drugs work, and how to make new and better DNA-targeted drugs to treat genetic diseases. Anticancer drugs interact with DNA in many different ways, including intercalation, non-covalent groove binding, covalent binding/cross-linking, DNA scission, and nucleoside analogy (Rauf ve ark., 2005). Epidermal growth factor receptor (EGFR) is an important part of epithelial cancers, and its activity makes tumors grow, invade, and spread to other parts of the body. EGFR is a type of tyrosine kinase receptor in the ErbB family that sends a signal to cells that have been activated by an EGFR ligand that makes them grow. However, in cancer, EGFR is always stimulated due to either a mutation in EGFR that keeps the receptor in a state of constant activation or the persistent synthesis of EGFR ligands in the tumor microenvironment (Sasaki ve ark., 2013). Molecular modeling can accelerate the discovery of new chemical entities to treat or manage diseases. Several in silico-based studies in the computational modeling community have demonstrated that small molecule hits inhibit the activity of target receptors (Adelusi et al. 2022). The binding modes and binding energies of the formononetin-1bna, picropodophyllin-1bna, formononetin-4hjo, and picropodophyllin-4hjo complexes were ascertained through molecular docking studies that assessed the binding mechanisms and interactions of these two compounds with DNA (PDB ID: 1BNA)/epidermal growth factor receptor (PDB ID: 4HJO).

2. METHODS AND CALCULATIONS

The National Library of Medicine used the YASARA program (Krieger ve ark., 2014) and the NOVA force field (Krieger ve ark., 2002) to energy minimize the molecular structures of formononetin (PubChem CID 5280378) and picropodophyllin (PubChem CID 72435). The energy- minimized formononetin and picropodophyllin molecules were used as input for the docking simulation, as shown in **Figures 1** and **2**. Additionally, the energy minimization procedure using the NOVA force field of the YASARA structure program was applied to receptors (PDB IDs: 1BNA; 4HJO) from the protein database (Drew ve ark., 1981; Park ve ark., 2012) before docking simulations. The YASARA program (v22.9.24) and the VINA docking technique (Trott ve ark., 2010) were used to examine the molecular docking. In order to prepare the target protein for docking, polar hydrogen atoms were added and ligands and water molecules were eliminated from the PDB.

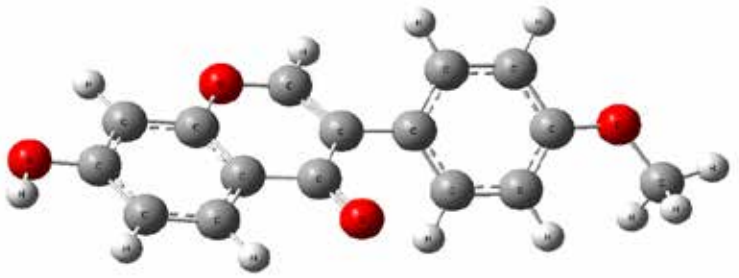

Figure 1. The optimized geometry of formononetin

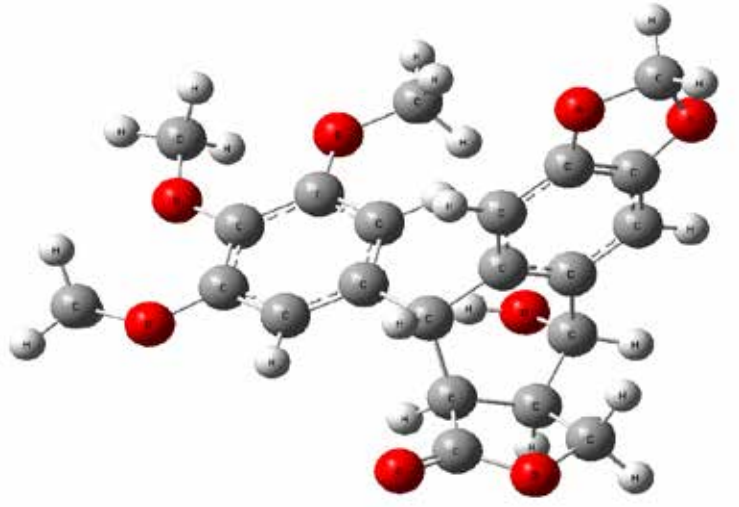

Figure 2. The optimized geometry of the picropodophyllin

3. RESULTS

The docking results of the formononetin-1bna and formononetin-4hjo complexes are shown in **Figures 3 and 4**, respectively. The formononetin molecule docked into the active site of the 1BNA receptor, exhibiting 2.55 Å length hydrogen bond with DG10; 2.62 Å length carbon hydrogen bond with DC11; 2.07 Å length hydrogen bond with DG16 (**Figure 3**). The binding energy of the formononetin-1bna complex was calculated to be -7.557 kcal/mol. The formononetin molecule docked into the active site of the 4hjo receptor, exhibiting 3.76 Å length and 4.16 Å length pi-alkyl interactions with LEU694; 4.45 Å length and 5.28 Å length pi-alkyl interactions with VAL702; 4.77 Å length pi-alkyl interaction with ALA719; 4.74 Å length and 5.2 Å length pi-alkyl interactions with LEU820 (**Figure 4**). The binding energy of the formononetin-4hjo complex was calculated to be -7.88 kcal/mol.

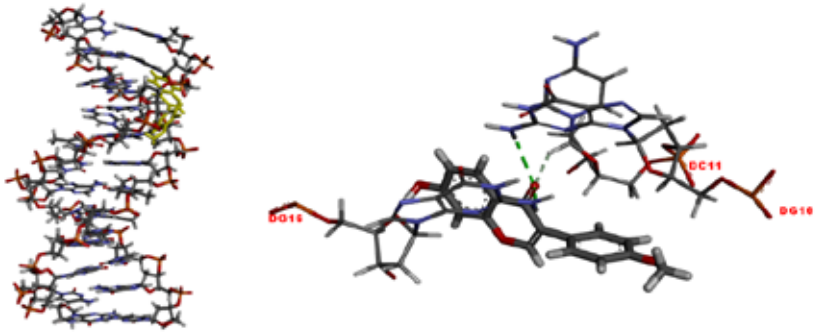

Figure 3. The docking outcomes of formononetin in the active site of 1BNA (binding energy -7.557 kcal/mol).

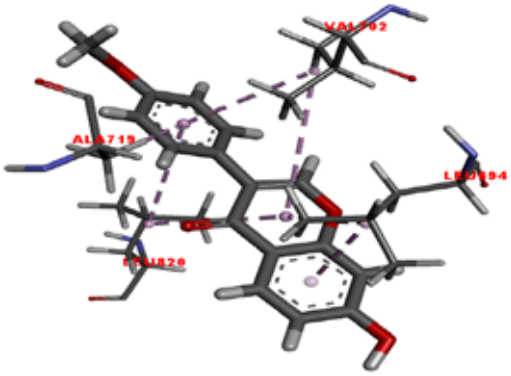

Figure 4. The docking outcomes of formononetin in the active site of 4HJO (binding energy -7.88 kcal/mol).

The docking results of the picropodophyllin-1bna and picropodophyllin-4hjo complexes are shown in **Figures 5 and 6**, respectively. The picropodophyllin molecule docked into the active site of the 1BNA receptor, exhibiting 2.43 Å length hydrogen bond with DG10; 2.12 Å length hydrogen bond with DG12; 2.66 Å length carbon hydrogen bond with DC15 (**Figure 5**). The binding energy of the picropodophyllin-1bna complex was calculated to be -7.126 kcal/mol. The picropodophyllin molecule docked into the active site of the 4HJO receptor, exhibiting 2.84 Å length carbon hydrogen bond with ALA840; 2.15 Å length hydrogen bond with GLY850; 2.53 Å length carbon hydrogen bond with LYS851; 2.62 Å length hydrogen bond and 3.86 Å length pi-alkyl interaction with VAL852; 2.81 Å length carbon hydrogen bond with

ILE862; 3.07 Å length hydrogen bond and 4.21 Å length pi-cation interaction with ARG865 (**Figure 6**). The binding energy of the picropodophyllin-4hjo complex was calculated to be -6.898kcal/mol.

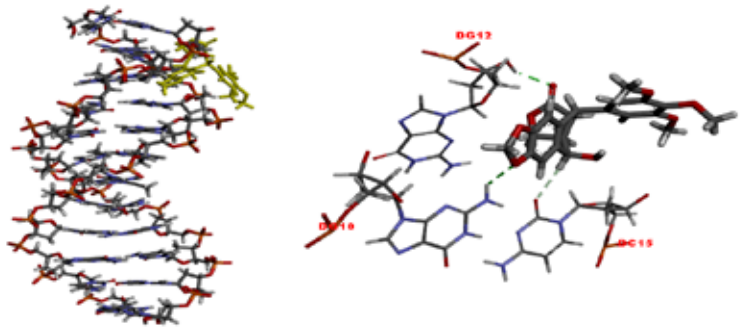

Figure 5. The docking outcomes of picropodophyllin in the active site of 1BNA (binding energy -7.126 kcal/mol).

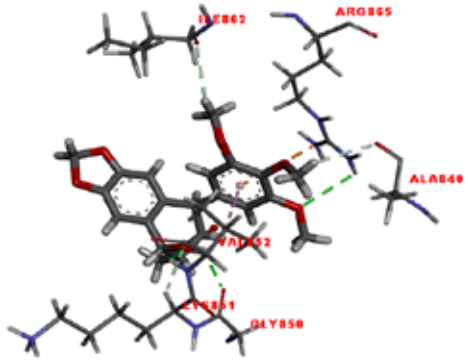

Figure 6. The docking outcomes of picropodophyllin in the active site of 4HJO (binding energy -6.898 kcal/mol).

4. CONCLUSIONS

Molecular docking simulations were performed with DNA (PDB ID: 1BNA) and epidermal growth factor receptor (PDB ID: 4HJO) to study the effects of picropodophyllin and formononetin on various cancer cells. Molecular docking simulations showed that formononetin-1bna, picropodophyllin-1bna, formononetin-4hjo, and picropodophyllin-4hjo complexes had high binding energies of -7.557, -7.126, -7.88, and -6.898 kcal/mol.

REFERENCES

Adelusi, T. I., Oyedele, A. Q. K., Boyenle, I. D., Ogunlana, A. T., Adeyemi, R. O., Ukachi, C. D., ... & Abdul-Hammed, M. (2022). Molecular modeling in drug discovery. *Informatics in Medicine Unlocked*, *29*, 100880.

Drew, H. R., Wing, R. M., Takano, T., Broka, C., Tanaka, S., Itakura, K., & Dickerson, R. E. (1981). Structure of a B-DNA dodecamer: conformation and dynamics. *Proceedings of the National Academy of Sciences*, *78*(4), 2179-2183.

Dong, L., Du, M., & Lv, Q. (2019). Picropodophyllin inhibits type I endometrial cancer cell proliferation via disruption of the PI3K/Akt pathway. *Acta Biochimica et Biophysica Sinica*, *51*(7), 753-760.

Hausman, D. M. (2019). What is cancer?. *Perspectives in biology and medicine*, *62*(4), 778-784.

Krieger, E., Koraimann, G., Vriend, G. (2002) Increasing the precision of comparative models

with YASARA NOVA-a self-parameterizing force field, Proteins: Structure, Function, and

Bioinformatics, 47(3), 393-402.

Krieger, E., Vriend, G. (2014) YASARA View-molecular graphics for all devices—from

smartphones to workstations, Bioinformatics, 30(20), 2981-2982.

Lu, X., Wang, L., Mei, J., Wang, X., Zhu, X., Zhang, Q., & Lv, J. (2013). Picropodophyllin inhibits epithelial ovarian cancer cells in vitro and in vivo. *Biochemical and biophysical research communications*, *435*(3), 385-390.

Park, J. H., Liu, Y., Lemmon, M. A., & Radhakrishnan, R. (2012). Erlotinib binds both inactive and active conformations of the EGFR tyrosine kinase domain. *Biochemical Journal*, *448*(Pt 3), 417.

Rauf, S., Gooding, J. J., Akhtar, K., Ghauri, M. A., Rahman, M., Anwar, M. A., & Khalid, A. M. (2005). Electrochemical approach of anticancer drugs–DNA interaction. *Journal of pharmaceutical and biomedical analysis*, *37*(2), 205-217.

Ruddon, R. W. (2007). *Cancer biology*. Oxford University Press.

Sasaki, T., Hiroki, K., & Yamashita, Y. (2013). The role of epidermal growth factor receptor in cancer metastasis and microenvironment. *BioMed research international*, *2013*(1), 546318.

Tay, K.C., Tan, L.T.H., Chan, C.K., Hong, S.L., Chan, K.G., Yap, W.H., ... & Goh, B. H. (2019). Formononetin: a review of its anticancer potentials and mechanisms. *Frontiers in pharmacology*, *10*, 820.

Tewari, M. (2022). Cancer and its treatment: an overview. Int. J. Adv. Res. 10(03), 950-956

Trott, O., Olson, A. J. (2010) AutoDock Vina: improving the speed and accuracy of docking with a new scoring function, efficient optimization, and multithreading, Journal of computational chemistry, 31(2), 455-461.

CHAPTER 5

MOLECULAR DOCKING STUDIES OF GRISEOFULVIN AND NEOMYCIN MOLECULES USED IN STAPHYLOCOCCUS AUREUS AND E.COLI TREATMENTS

Assoc. Prof. Dr. Alev ER
Istanbul University
Science Faculty, Physics Department
https://orcid.org/0000-0002-3190-5342

Prof. Dr. Sefa CELIK
Istanbul University
Science Faculty, Physics Department
https://orcid.org/0000-0001-6216-1297

Prof. Dr. Aysen E. OZEL
Istanbul University
Science Faculty, Physics Department
https://orcid.org/0000-0002-8680-8830

1. INTRODUCTION

Griseofulvin ($C_{17}H_{17}ClO_6$), a fungistatic compound utilized for treating dermatophyte infections, has garnered significant interest recently for its ability to interfere with mitosis and cell division in human cancer cells, as well as to impede hepatitis C virus replication (Aris ve ark., 2022). Griseofulvin (GF), derived from Penicillium griseofulvum, is a thermally stable, chlorine-containing antibiotic. Research indicates that GF possesses several pharmacological actions, including

anti-inflammatory, antifungal, antiviral, and antitumor properties (Yu ve ark., 2024). Certain antibacterial medicines have significant efficacy against specific germs, while being nearly worthless against others. The antibacterial activity potential was assessed for 42 griseofulvin derivatives, with predictions made for 33 of them; hence, the antibacterial efficacy of griseofulvin and its derivatives was aimed to be tested against Gram-positive and Gram-negative bacteria (Geronikaki ve ark., 2020). Aminoglycosides, notably the neomycin family, have a wide variety among antibiotics generated from natural sources. Understanding the chemical syntheses within the neomycin family and the structure-activity connections is essential for developing future medications to combat bacterial resistance (Obszynski ve ark., 2022). Neomycin is the preferred antibiotic for treating swine enteritis induced by enterotoxigenic Escherichia coli (Subramani ve ark., 2023). Several derivatives of Tobramycin, Gentamicin, Neomycin, and Amikacin synthesized from vanillin were evaluated for antibacterial and antifungal activity against S. Aureus, Bacillus Sb, E. Coli, and Salmonella Sp, revealing modest antifungal effects (Munan ve ark., 2020). Staphylococcus aureus (PDB ID: 2W9G), classified by the World Health Organization (WHO) as a drug-resistant bacterial pathogen, is a highly aggressive Gram-positive organism responsible for several severe illnesses, including pneumonia and endocarditis. Urinary tract infections (UTIs) attributed to Escherichia coli (E. coli) bacteria represent a considerable worldwide health issue due to their widespread occurrence and escalating drug resistance (Ismail ve ark., 2025). Neomycin is an aminoglycoside antibiotic that functions by blocking bacterial protein synthesis and has predominantly bactericidal efficacy against Gram-negative bacteria. When taken orally, neomycin has less absorption into systemic circulation, thereby improving its effectiveness in addressing localized infections within the gastrointestinal tract (Veirup ve ark., 2023).

In this study to evaluate the binding mechanisms and interactions of griseofulvin and neomycin with Staphylococcus aureus and E. coli DNA gyrase, molecular docking studies were performed and binding energies of griseofulvin-6f86, neomycin-6f86, griseofulvin-2w9g and neomycin-2w9g complexes were determined.

2. METHODS AND CALCULATIONS

Figures 1 and 2 display the energy-minimized geometry of the griseofulvin and neomycin molecules, respectively. Both target proteins (PDB ID: 2W9G and PDB ID: 6F86) and ligands (griseofulvin and neomycin) were optimized

using the YASARA v22.9.24 software (Krieger ve ark., 2014) with the NOVA force field (Krieger ve ark., 2002). Molecular docking studies for each of the PDB ID:2W9G (Heaslet ve ark., 2009) and PDB ID:6F86 (Narramore ve ark., 2019) receptors obtained from the Protein Data Bank (PDB) (http://www.rcsb.org/pdb) with griseofulvin and neomycin molecules were performed using YASARA software (v22.9.24) and the VINA approach (Krieger ve ark., 2014). All water molecules and co-crystallized ligands were removed from the target protein, and polar hydrogen atoms were added to the protein structure to prepare it for docking. The target protein's Kollman charges were calculated with other parameters kept at their default values.

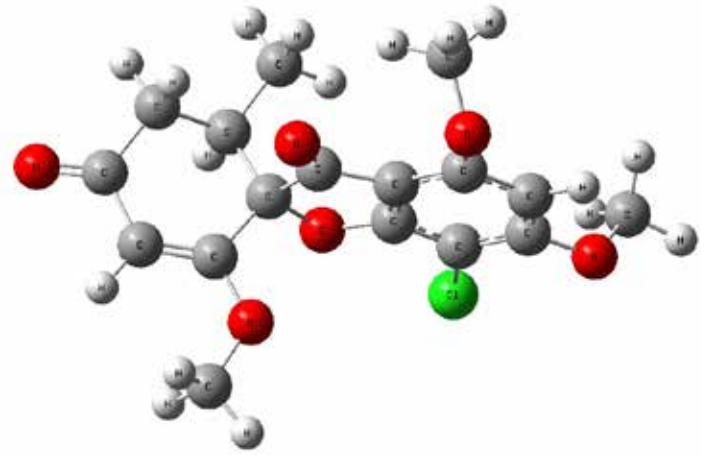

Figure 1. The optimized geometry of the griseofulvin

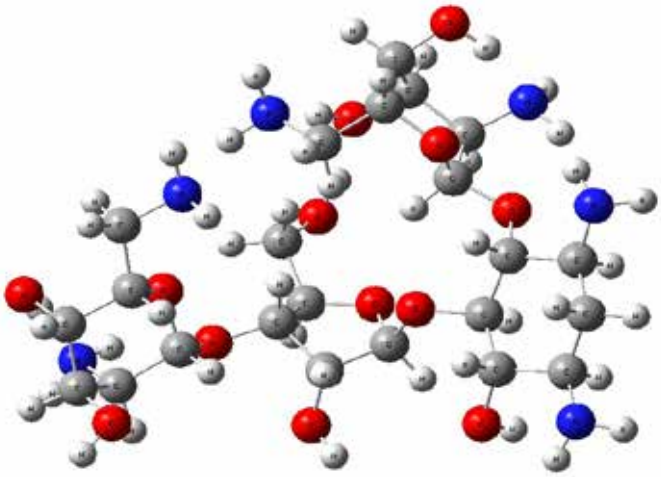

Figure 2. The optimized geometry of the neomycin

3. RESULTS

The docking results of the griseofulvin-2W9G and griseofulvin-6F86 complexes are shown in **Figures 3 and 4,** respectively. The griseofulvin molecule docked into the active site of the 2W9G receptor, exhibiting 3.71 Å length and 4.2 Å length alkyl interactions and 4.41 Å length pi-alkyl interaction with LEU20; 5.11 Å length alkyl interaction with LEU28; 2.92 Å length carbon hydrogen bond with SER49; 3.09 Å length carbon hydrogen bond with ILE50; 2.69 Å length carbon hydrogen bond and 5.58 Å length pi-pi stacked interaction PHE92 (**Figure 3**). The binding energy of the griseofulvin-2W9G complex was calculated to be -6.267 kcal/mol. The griseofulvin molecule docked into the active site of the 6F86 receptor exhibiting 2.4 Å length hydrogen bond with ASN46; 4.08 Å length pi-anion interaction with GLU50; 4.47 Å length alkyl interaction with ALA53; 2.38 Å length hydrogen bond and 3.96 Å length pi-cation interaction with ARG76; 2.77 Å length carbon-hydrogen bond with ILE78; 2.93 Å length carbon-hydrogen bond with PRO79 (**Figure 4**). The binding energy of the griseofulvin-6F86 complex was calculated to be -6.463 kcal/mol.

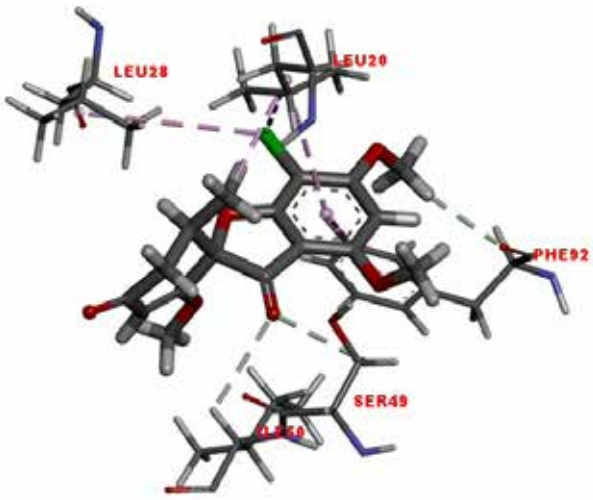

Figure 3. The docking outcomes of griseofulvin in the active site of 2W9G. The interacting residues were presented.

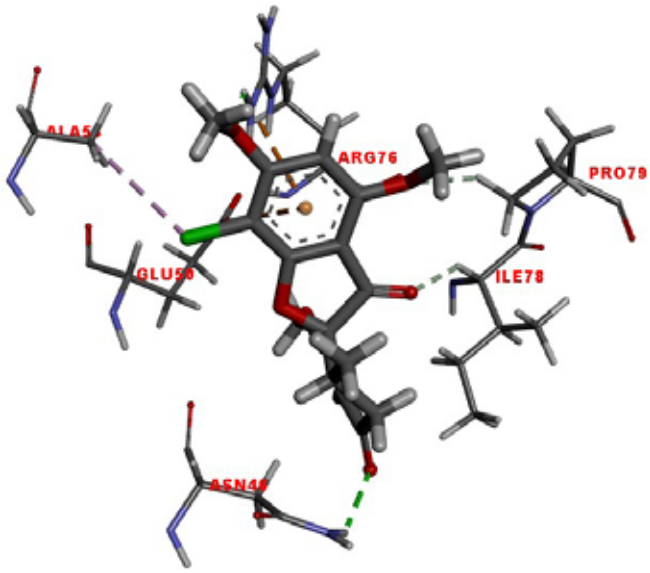

Figure 4. The docking outcomes of griseofulvin in the active site of 6F86. The interacting residues were presented.

The docking results of the neomycin-2W9G and neomycin-6F86 complexes are shown in **Figures 5 and 6,** respectively. The neomycin molecule docked into the active site of the 2W9G receptor, exhibiting 2.22 Å length hydrogen bond with LEU5; 1.91 Å length and 2.9 Å length hydrogen bonds with ILE14; 2.47 Å length hydrogen bond with ASN18; 2.56 Å length and 2.69 Å length carbon-hydrogen bonds with THR46; 2.64 Å length carbon-hydrogen bond and 2.14 Å length, 2.39 Å length, and 2.43 Å length hydrogen bonds SER49; 2.87 Å length and 2.88 Å length hydrogen bonds with ILE50; 2.66 Å length and 2.66 Å length hydrogen bonds with PHE92 (**Figure 5**). The binding energy of the neomycin-2W9G complex was calculated to be -7.754 kcal/mol. The neomycin molecule docked into the active site of the 6F86 receptor, exhibiting 2.03 Å length hydrogen bond with THR62; 2.69 Å length and 2.9 Å length hydrogen bonds with SER70; 2.33 Å length, 2.59 Å length and 2.99 Å length carbon-hydrogen bonds and 3.02 Å length hydrogen bond with GLN72; 2.5 Å length hydrogen bond with ASP73; 2.03 Å length and 2.09 Å length hydrogen bonds with GLN135; 2.9 Å length hydrogen bond with ARG206 (**Figure 6**). The binding energy of the neomycin-6F86 complex was calculated to be -6.403 kcal/mol

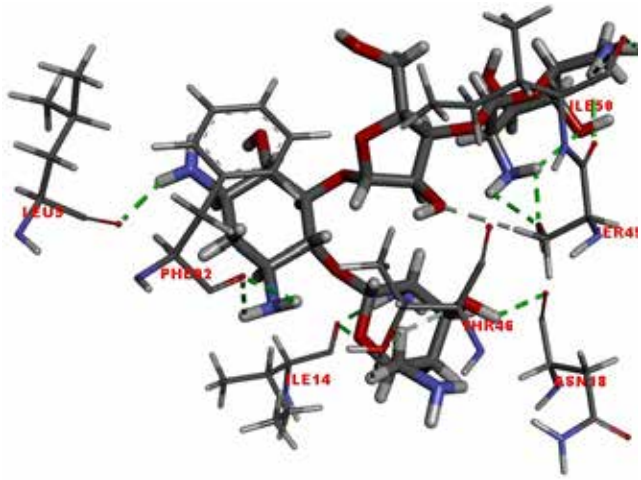

Figure 5. The docking outcomes of neomycin in the active site of 2W9G. The interacting residues were presented.

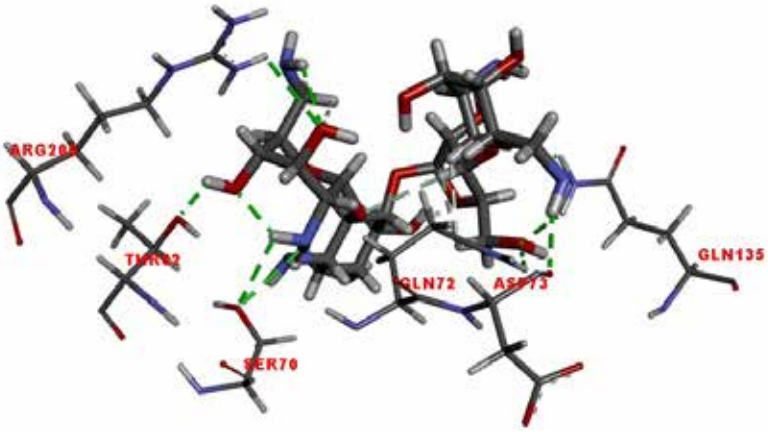

Figure 6. The docking outcomes of neomycin in the active site of 6F86. The interacting residues were presented.

4. CONCLUSIONS

This study indicates that the predicted binding energies of griseofulvin and neomycin, analyzed using molecular docking, imply these antibiotics may be effective against the tested microorganisms. By inhibiting both Gram-positive and Gram-negative bacteria, they may provide a way to address the demand for novel antibiotics to tackle resistant microorganisms.

REFERENCES

Aris, P., Wei, Y., Mohamadzadeh, M., & Xia, X. (2022). Griseofulvin: an updated overview of old and current knowledge. *Molecules*, *27*(20), 7034.

Geronikaki, A., Kartsev, V., Petrou, A., Akrivou, M. G., Vizirianakis, I. S., Chatzopoulou, F. M., ... & Poroikov, V. (2020). Antibacterial activity of griseofulvin analogues as an example of drug repurposing. *International Journal of Antimicrobial Agents*, *55*(3), 105884.

Heaslet, H., Harris, M., Fahnoe, K., Sarver, R., Putz, H., Chang, J., ... & Miller, J. R. (2009). Structural comparison of chromosomal and exogenous dihydrofolate reductase from Staphylococcus aureus in complex with the potent inhibitor trimethoprim. *Proteins: Structure, Function, and Bioinformatics*, *76*(3), 706-717.

Ismail, M. A., Faisal, A. N., Hadi, Q. N., & Mohsein, O. A. (2025). Exploring the genetic variability of Escherichia coli pathotypes in urinary tract infections: implications for diagnostics and treatment. *Central Asian Journal of Medical and Natural Science*, *6*(1), 179-191.

Krieger, E., Koraimann, G., & Vriend, G. (2002). Increasing the precision of comparative models with YASARA NOVA—a self-parameterizing force field. *Proteins: Structure, Function, and Bioinformatics*, *47*(3), 393-402.

Krieger, E., & Vriend, G. (2014). YASARA View—molecular graphics for all devices—from smartphones to workstations. *Bioinformatics*, *30*(20), 2981-2982.

Munan A., Khan A.J., Khan M., Abbas G., Ahmad E., Hussain A., Khan S., Khan AK., Yousaf A.H. (2020). Antibacterial and antifungal activities of tobramycin, gentamycin, neomycin and amikacin derivatives, derived from vanillin. *Drug Discovery*, Volume 16, Issue 37, January - June, 2022.

Narramore, S., Stevenson, C. E., Maxwell, A., Lawson, D. M., & Fishwick, C. W. (2019). New insights into the binding mode of pyridine-3-carboxamide inhibitors of E. coli DNA gyrase. *Bioorganic & medicinal chemistry*, *27*(16), 3546-3550.

Obszynski, J., Loidon, H., Blanc, A., Weibel, J. M., & Pale, P. (2022). Targeted modifications of neomycin and paromomycin: Towards resistance-free antibiotics?. *Bioorganic Chemistry*, *126*, 105824.

Subramani, P., Menichincheri, G., Pirolo, M., Arcari, G., Kudirkiene, E., Polani, R., ... & Guardabassi, L. (2023). Genetic background of neomycin resistance in clinical Escherichia coli isolated from Danish pig farms. *Applied and Environmental Microbiology*, *89*(10), e00559-23.

Veirup N, Kyriakopoulos C. Neomycin. 2023 Nov 12. In: StatPearls [Internet]. Treasure Island (FL): StatPearls Publishing; 2025 Jan–. PMID: 32809438.

Yu, N., Fu, Y., Fan, Q., Lin, L., Ning, Z., Leng, D., ... & She, T. (2024). Antitumor properties of griseofulvin and its toxicity. *Frontiers in Pharmacology*, *15*, 1459539.

CHAPTER 6

ANTIBACTERIAL POTENTIAL OF CEFACLOR AND EMBELIN: MOLECULAR DOCKING ANALYSIS

Assoc. Prof. Dr. Alev ER
Istanbul University
Science Faculty, Physics Department
https://orcid.org/0000-0002-3190-5342

Prof. Dr. Sefa CELIK
Istanbul University
Science Faculty, Physics Department
https://orcid.org/0000-0001-6216-1297

1. INTRODUCTION

Cefaclor is a monohydrate of the chemical formula 3-chloro-7-d-(2-phenylglycinamido)-3-cepham-4-carboxylic acid (Lorenz, 1981). Cefaclor, a derivative of cephalexin monohydrate, is a novel semi-synthetic cephalosporin antibiotic. The antimicrobial spectrum of cefaclor closely resembles that of cefalexin, encompassing a diverse range of gram-negative and gram-positive bacteria; notably, Escherichia coli, Klebsiella spp., Proteus mirabilis, Salmonella spp., and Haemophilus influenzae exhibit greater susceptibility to clinically attainable concentrations of cefaclor compared to cefalexin (Derry, 1981). A 1978 research evaluated cefaclor (CCL), a cephalosporin, in vitro against 602 clinical isolates (271 anaerobic and 331 aerobic). CCL at 16 μg/ml inhibited 68% of all studied aerobic bacteria and 80% of 211 enteropathogenic organisms (Escherichia coli, Salmonella, and Shigella) isolated from instances of infantile diarrhea (Bach ve ark., 1978). Staphylococcus aureus is recognized as a significant human pathogen that can induce severe skin and soft tissue infections.

Embelin (2,5-dihydroxy-3-undecyl-p-benzoquinone) is identified as the active pharmacological constituent of Embelia ribes, commonly utilized in traditional medicine for the treatment of several diseases. Embelin has several biological actions, including anti-inflammatory, antibacterial, and antidiabetic properties. It is recognized to markedly augment the antibacterial efficacy of ciprofloxacin, nalidixic acid, tetracycline, and vancomycin against S. aureus (Chitra ve ark., 1994; Chitra ve ark., 2003; McCaig ve ark., 2006; Raman ve ark., 2009; Singh ve ark., 2014; Mazlan ve ark., 2019). Embelin exhibited inhibitory activity against methicillin-resistant Staphylococcus aureus, Escherichia coli, and dermatophyte fungi, including Epidermophyton floccosum, Microsporum canis, Microsporum gypseum, Trichophyton mentagrophytes, and Trichophyton rubrum, with minimum inhibitory concentration (MIC) values ranging from 50 to 100 µg/ml (Feresin ve ark., 2003). A 2018 study created an ointment using embelin as the active ingredient and assessed its antibacterial and physicochemical qualities. The antibacterial efficacy of the prepared ointment at various doses was evaluated against two Gram-positive bacteria (Staphylococcus aureus and Streptococcus epidermidis) and two Gram-negative bacteria (Escherichia coli and Pseudomonas aeruginosa) with the disk diffusion technique. The prepared ointment demonstrated substantial antibacterial efficacy against all examined species, exhibiting an inhibition zone between 7.67 ± 0.58 and 12.00 ± 1.00 mm. The antibacterial efficacy identified in the ointment was ascribed to embelin, and it was shown that embelin's activity was effectively maintained upon formulation into an ointment (Sekar, 2018).

In this study, molecular docking studies were performed to evaluate the binding mechanisms and interactions of cefaclor and embelin with antibacterial targets.

2. METHODS AND CALCULATIONS

Figures 1 and 2 illustrate the optimized geometries of the cefaclor and embelin molecules, respectively. The target proteins (PDB ID: 2W9G and PDB ID: 6F86) and ligands (cefaclor and embelin) were optimized utilizing YASARA v22.9.24 software (Krieger ve ark., 2014) with the NOVA force field (Krieger ve ark., 2002). Molecular docking analyses for PDB ID:2W9G (Heaslet ve ark., 2009) and PDB ID:6F86 (Narramore ve ark., 2019) receptors, sourced from the Protein Data Bank (PDB) (http://www.rcsb.org/pdb), were conducted utilizing YASARA software (v22.9.24) and the VINA methodology (Krieger

ve ark., 2014) with cefaclor and embelin compounds. All water molecules and co-crystallized ligands were eliminated from the target protein, and polar hydrogen atoms were incorporated into the protein structure to facilitate docking. The Kollman charges of the target protein were computed while maintaining other parameters at their normal settings.

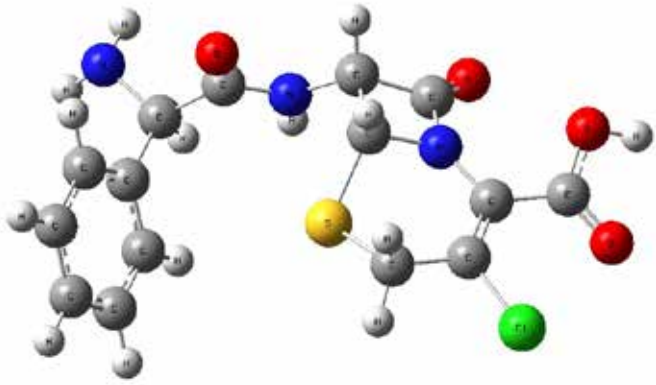

Figure 1. The optimized geometry of the cefaclor

Figure 2. The optimized geometry of the embelin

3. RESULTS

The docking results of the cefaclor-2W9G and cefaclor-6F86 complexes are shown in **Figures 3 and 4,** respectively. The cefaclor molecule docked into the active site of the 2W9G receptor, exhibiting 2.76 Å length carbon-hydrogen bond and 5.11 Å length alkyl interaction with ILE14; 2.46 Å length hydrogen bond with ASN18; 4.38 Å length alkyl interaction with LEU20; 3.96 Å length pi-alkyl interaction with LYS45; 2.81 Å length and 2.87 Å length carbon-hyd-

rogen bonds and 3.01 Å length hydrogen bond SER49; 5.74 Å length pi-sulfur interaction with PHE98 (**Figure 3**). The binding energy of the cefaclor-2W9G complex was calculated to be -8.428 kcal/mol. The cefaclor molecule docked into the active site of the 6F86 receptor, exhibiting 2.01 Å length and 2.13 Å length hydrogen bonds with ASN46; 5.06 Å length pi-alkyl interaction with ILE78; 2.37 Å length hydrogen bond and 2.83 Å length carbon hydrogen bond with GLY117; 2.18 Å length hydrogen bond with VAL118 (**Figure 4**). The binding energy of the cefaclor-6F86 complex was calculated to be -6.955 kcal/mol.

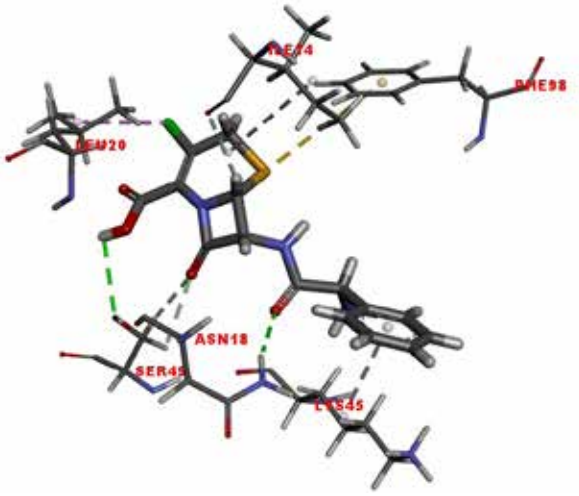

Figure 3. The docking outcomes of cefaclor in the active site of 2W9G. The interacting residues were presented.

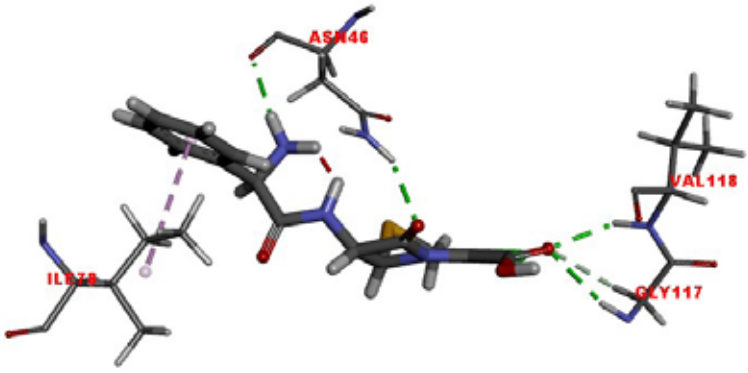

Figure 4. The docking outcomes of cefaclor in the active site of 6F86. The interacting residues were presented.

The docking results of the embelin-2W9G and embelin-6F86 complexes are shown in **Figures 5 and 6,** respectively. The embelin molecule docked into the active site of the 2W9G receptor, exhibiting 4.63 Å length alkyl interaction with VAL6; 4.42 Å length alkyl interaction with ILE14; 2.59 Å length carbon-hydrogen bond with GLY15; 2.35 Å length hydrogen bond with ASN18; 2.32 Å length carbon-hydrogen bond with THR46; 2.67 Å length carbon-hydrogen bond with SER49; 5.32 Å length pi-alkyl interaction with PHE98 (**Figure 5**). The binding energy of the embelin-2W9G complex was calculated to be -6.735 kcal/mol. The embelin molecule docked into the active site of the 6F86 receptor, exhibiting 2.91 Å length, 2.97 Å length hydrogen bonds and 4.83 Å length pi-cation interaction with ARG76; 5.06 Å length alkyl interaction with ILE78; 4.04 Å length pi-alkyl interaction with PRO79; 2.12 Å length hydrogen bond with ARG136 (**Figure 6**). The binding energy of the embelin-6F86 complex was calculated to be -5.228 kcal/mol.

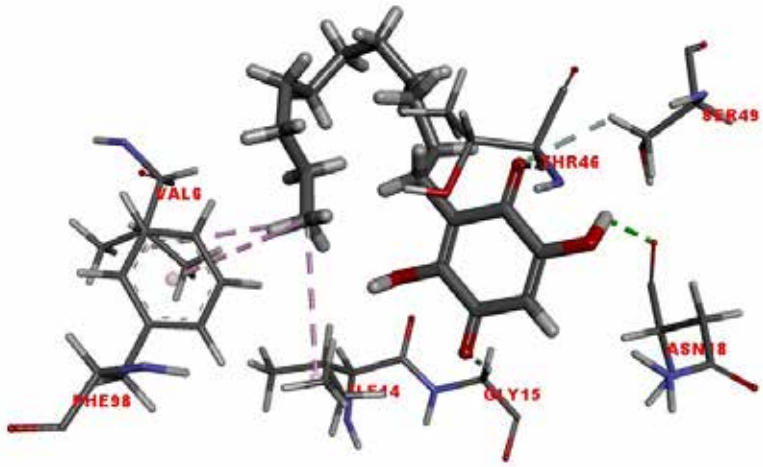

Figure 5. The docking outcomes of embelin in the active site of 2W9G. The interacting residues were presented.

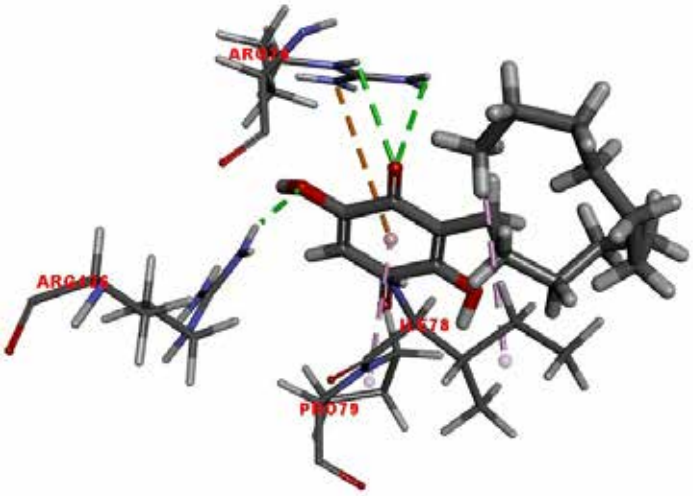

Figure 6. The docking outcomes of embelin in the active site of 6F86. The interacting residues were presented.

4. CONCLUSIONS

These compounds may have biological activity against Staphylococcus aureus and Escherichia coli, according to the molecular docking studies of embelin and cefaclor that were reported in this work. This suggests that these compounds might be useful antibacterial drugs.

REFERENCES

Bach, V. T., Khurana, M. M., & Thadepalli, H. (1978). In vitro activity of cefaclor against aerobic and anaerobic bacteria. *Antimicrobial Agents and Chemotherapy*, *13*(2), 210-213.

Chitra, M., Sukumar, E., Suja, V., & Devi, S. (1994). Antitumor, anti-inflammatory and analgesic property of embelin, a plant product. *Chemotherapy*, *40*(2), 109-113.

Chitra, M., Shyamala Devi, C. S., & Sukumar, E. (2003). Antibacterial activity of embelin. *Fitoterapia*, *74*(4), 401-403.

Derry, J. E. (1981). Evaluation of cefaclor. *American Journal of Hospital Pharmacy*, *38*(1), 54-58.

Feresin, G. E., Tapia, A., Sortino, M., Zacchino, S., de Arias, A. R., Inchausti, A., ... & Schmeda-Hirschmann, G. (2003). Bioactive alkyl phenols and embelin from Oxalis erythrorhiza. *Journal of Ethnopharmacology*, *88*(2-3), 241-247.

Heaslet, H., Harris, M., Fahnoe, K., Sarver, R., Putz, H., Chang, J., ... & Miller, J. R. (2009). Structural comparison of chromosomal and exogenous dihydrofolate reductase from Staphylococcus aureus in complex with the potent inhibitor trimethoprim. *Proteins: Structure, Function, and Bioinformatics*, *76*(3), 706-717.

Krieger, E., Koraimann, G., & Vriend, G. (2002). Increasing the precision of comparative models with YASARA NOVA—a self-parameterizing force field. *Proteins: Structure, Function, and Bioinformatics*, *47*(3), 393-402.

Krieger, E., & Vriend, G. (2014). YASARA View—molecular graphics for all devices—from smartphones to workstations. *Bioinformatics*, *30*(20), 2981-2982.

Lorenz, L. J. (1981). Cefaclor. In *Analytical profiles of drug substances* (Vol. 9, pp. 107-123). Academic Press.

Mazlan, N. A., Azman, S., Ghazali, N. F., Yusri, P. Z. S., Idi, H. M., Ismail, M., & Sekar, M. (2019). Combinatory effect of embelin with antibiotics against Staphylococcus aureus. *Drug Invention Today*, *12*(1), 18-20.

McCaig, L. F., McDonald, L. C., Mandal, S., & Jernigan, D. B. (2006). Staphylococcus aureus–associated skin and soft tissue infections in ambulatory care. *Emerging infectious diseases*, *12*(11), 1715.

Narramore, S., Stevenson, C. E., Maxwell, A., Lawson, D. M., & Fishwick, C. W. (2019). New insights into the binding mode of pyridine-3-carboxamide inhibitors of E. coli DNA gyrase. *Bioorganic & medicinal chemistry*, *27*(16), 3546-3550.

Raman, B. V., Ramkishore, A. S., Maheswari, M. U., & Radhakrishnan, T. M. (2009). Antibacterial activities of some folk medicinal plants of eastern Ghats.

Sekar, M. (2018). Formulation and evaluation of antibacterial ointment containing embelin isolated from Embelia ribes. *International Journal of Green Pharmacy (IJGP)*, *12*(03).

Singh, B., Guru, S. K., Sharma, R., Bharate, S. S., Khan, I. A., Bhushan, S., ... & Vishwakarma, R. A. (2014). Synthesis and anti-proliferative activities of new derivatives of embelin. *Bioorganic & medicinal chemistry letters*, *24*(20), 4865-4870.

CHAPTER 7

SYNERGISTIC EFFECTS OF BORAX, ALUMINUM HYDROXIDE, AND MAGNESIUM HYDROXIDE ON THE FLAME RETARDANCY, THERMAL STABILITY, AND VERTICAL BURNING BEHAVIOR OF EPOXY COMPOSITES

Hasan TÜRKMEN
Department of Metallurgical and Materials Engineering,
Pamukkale University, Denizli, 20160, Türkiye
https://orcid.org/0000-0003-0129-5974

Rüçhan YILDIZ
Department of Metallurgical and Materials Engineering,
Pamukkale University, Denizli, 20160, Türkiye
https://orcid.org/0000-0002-5973-5496

1. INTRODUCTION

In modern societies, rapid scientific and technological developments accompanying industrialization and population growth have significantly increased the likelihood of fires and the associated loss of life and property. To mitigate this risk, plastics, construction materials, paper and textile products, and wood-based materials that are widely used in daily life are commonly designed by incorporating flame-retardant additives into their matrices. Flame retardants improve the flammability performance of materials—thereby helping to minimize fire-related damage—through mechanisms such as delaying ignition, reducing the heat release rate, limiting the formation of smoke and toxic gases,

and promoting the development of a protective char or barrier layer. Accordingly, flame retardants are additives that, when materials are exposed to flame or elevated temperatures, prevent or delay ignition and, even if ignition occurs, impart self-extinguishing behavior to the material (Aytan, 2021).

Polymers are widely used in construction chemicals, coatings, tissue engineering, and applications requiring high physical durability due to their chemical stability and superior mechanical/functional performance. In general, they are classified into two main categories as organic and inorganic: inorganic polymers, whose main chain consists of elements such as silicon or phosphorus, inherently exhibit better fire resistance, whereas organic polymers with long carbon backbones are more prone to combustion. The onset of burning requires exposure to an external heat source; as the surface temperature increases, thermo-oxidation and thermal degradation (pyrolysis) processes are triggered, and volatile species—often toxic and flammable—are released as a result of chain scission and side-group elimination. These species react with oxygen in the flame zone to generate heat, which is fed back to the surface; consequently, pyrolysis accelerates and, as long as the fuel–heat–oxygen triad is maintained, the material may continue to burn autonomously until the polymer phase is depleted. Interrupting this feedback loop through flame retardants—by reducing the heat release rate and promoting radical scavenging and the formation of a protective char/barrier layer—constitutes the principal strategy for improving the flammability performance of polymers. A contemporary approach to enhancing the resistance of composite materials against flames is the integration of flame-retardant additives into the matrix composition. These particles exhibit beneficial effects under critical environmental conditions, thereby increasing the overall effectiveness and durability of the material (Çakır and Berberoğlu, 2018). However, in the development of flame-retardant materials, identifying benign additives to minimize the environmental impact of the solution is a fundamental requirement (Samper ve ark., 2014). Many conventional thermal barrier coatings contain toxic chemicals that can adversely affect the sustainability of the coating. Therefore, continuous research and development efforts are essential to ensure that materials remain both effective and environmentally friendly. In this context, environmentally friendly flame-retardant (FR) compounds that are free from harmful chemicals are emerging as promising additives for fire-retardant composite coatings (Jamali et al. 2018).

Halogenated flame retardants—particularly bromine-based inhibitors—have played a defining role in flame-retardancy mechanisms for many years. However, environmental and health-related concerns such as toxicity, bioac-

cumulation, and persistence are increasingly shifting research focus toward halogen-free flame-retardant systems. Indeed, many recent publications and patent applications have concentrated on the design, synthesis, and application performance of halogen-free flame-retardant compounds (Aytan, 2021; Zhu ve ark., 2022). Among polymer additives, flame retardants are widely used to meet flammability requirements, especially in furniture, textiles, electronic equipment, and thermal insulation applications. By inducing functions that delay ignition, limit flame spread and help reduce smoke formation in plastics and other consumer products, these additives enhance overall safety levels. Depending on the type of application, various chemical classes are preferred in thermoset systems, on textile surfaces, and in coating formulations that aim to prevent ignition and suppress flame propagation (Demirci and Avcı, 2017).

Historically, certain halogenated flame retardants have been subjected to regulatory scrutiny due to concerns regarding environmental persistence, bioaccumulation, and toxicity, which has accelerated the market shift toward halogen-free alternatives. Accordingly, phosphorus- and nitrogen-based systems (e.g., phosphorus–nitrogen synergistic schemes, phosphonate/phosphinate derivatives, melamine and its condensates), silicon-containing hybrid networks, and inorganic/nanoscale barrier-forming additives ($Al(OH)_3$, $Mg(OH)_2$, clay/silica derivatives) have attracted significant research interest in recent years. These approaches provide performance through multiple modes of action, including (i) promoting char formation in the condensed phase to generate a protective carbonized layer that limits heat and mass transfer, (ii) interrupting free-radical chain reactions in the gas phase via radical scavenging/dilution mechanisms, and (iii) absorbing heat through endothermic decomposition accompanied by the release of water or inert gases (Lu ve ark., 2017).

Magnesium hydroxide (MDH) and aluminium hydroxide (ATH) are two non-toxic and environmentally friendly flame retardants that stand out—when appropriately formulated and applied—due to their effectiveness in reducing smoke and toxic gas formation during fires. Their wide availability, low cost, and lack of halogens and heavy metals offer significant advantages in terms of human health and environmental safety. Their flame-retardant action is associated with the endothermic dehydration process, during which they absorb heat and release water vapor, thereby limiting the heat flux under direct flame exposure (Lu ve ark., 2017). In particular, the decomposition reactions of both hydroxides can be represented as follows (Li, 2026; Mohd Sabee ve ark., 2022):

Dehydration of magnesium hydroxide (MDH): $Mg(OH)_2 \rightarrow MgO + H_2O$

(Endothermic process: heat absorption and dilution of flammable gases by the released water vapor)

Dehydration of aluminum hydroxide (ATH): $2Al(OH)_3 \rightarrow Al_2O_3 + 3H_2O$

(Endothermic process: heat absorption, dilution by water vapor, and formation of an Al_2O_3 layer that acts as a protective thermal barrier on the surface)

These mechanisms contribute to the reduction of smoke and toxic gas formation and to the decrease in burning rate through several effects: a portion of the heat is consumed in the chemical decomposition (endothermic effect), the released water vapor dilutes flammable species and free radicals, thereby disrupting flame propagation, and the inorganic oxides formed (MgO, Al_2O_3) create a barrier layer on the surface that limits heat and mass transfer (Lu ve ark., 2017; Li, 2026; Mohd Sabee ve ark., 2022).

Both dehydration reactions are characterized by a high reaction enthalpy (endothermic effect); therefore, once triggered, they absorb a substantial amount of heat during direct flame impingement, producing a pronounced cooling effect on the polymer-based coating. The water vapor released in the course of dehydration dilutes combustible gases and suppresses flame growth, limits smoke formation by absorbing smoke particles, lowers the thermal load by cooling the surface, and generates a stable Al_2O_3 or MgO layer that acts as a protective barrier against heat and mass transfer. These fillers can be incorporated into formulations in powder form or as pre-dispersed slurries and are compatible with various types of coatings, including waterborne, solvent-borne, and powder coatings (Alonso ve ark., 2022).

Various studies have shown that the incorporation of $Mg(OH)_2$ and $Al(OH)_3$ fillers significantly improves the flame-retardant performance of materials; the heat release rate and smoke production are reduced, while the time to ignition is prolonged (Alonso ve ark., 2022; Pérez-Salinas ve ark., 2019; Peng ve ark., 2019). Accordingly, the effectiveness of $Mg(OH)_2$ and $Al(OH)_3$ as FR fillers in composite coatings has been quantitatively evaluated. Li et al. enhanced the fire performance of epoxy resins by loading zinc borate onto magnesium hydroxide and surface-functionalizing it with 3-aminopropyltriethoxysilane to develop a MH–ZBO–APES hybrid flame retardant. When this hybrid additive was incorporated into the epoxy matrix, it increased the glass transition temperature, decreased the maximum degradation rate, and markedly improved thermal stability. Cone calorimetry and LOI results confirmed a pronounced flame-retardant effect, with a substantial reduction in heat release rate and smoke generation. The study demonstrated that surface-modified MH/ZBO hybrids can serve

as efficient flame-retardant and smoke-suppressant additives in epoxy-based systems. Therefore, this hybrid system represents a strong candidate for the design of high-performance, halogen-free, and environmentally benign epoxy composites (Li, 2023).

Thermogravimetric analysis (TGA) quantitatively resolves thermal events in MDH/ATH-filled epoxy composites and makes it possible to track the evolution of flame-retardant efficiency as a function of filler loading, atmosphere, and heating rate. In addition, TGA is a key technique for elucidating the influence of flame-retardant additives on the thermal degradation behavior and char-forming mechanism of polymers. Afzal et al. developed multifunctional CFRP structures by incorporating inorganic flame retardants based on potassium alum (KA) and magnesium hydroxide (MH) into carbon-fabric-reinforced epoxy composites. TGA results showed that, particularly with increasing KA content, the residual char after combustion increased markedly, with the epoxy matrix residue rising from 16.5 wt% to 71.2 wt% in the EP80KA20 formulation. These findings indicate that KA/MH additives shift the thermal decomposition pathway toward char formation, thereby significantly enhancing the thermal stability and flame-retardant performance of the matrix (Afzal, 2020).

In MDH- and ATH-filled epoxy composites, UL-94 flammability performance is evaluated under flame exposure in terms of dripping behavior, extinguishing times, and the total flaming duration after the second ignition. ATH undergoes endothermic dehydration at approximately 180–220 °C, releasing water vapor and forming an Al_2O_3 barrier on the surface, thereby limiting heat release and flame propagation; MDH, on the other hand, decomposes at around 300–350 °C and similarly reduces the thermal load via H_2O release and the formation of an MgO barrier. These mechanisms reduce the ignitability of the molten drips and facilitate self-extinguishing behavior, making it possible to approach the V-0/V-1 classification (Sonnier ve ark., 2016; Chen ve ark., 2011).

In this study, the fire performance and thermal behavior of epoxy-based composite coatings containing different ratios of ATH and MDH are systematically investigated. The flame-retardant performance of the specimens is assessed using the UL-94 vertical burning test, while their thermal degradation and char-forming behavior are evaluated by thermogravimetric analysis (TGA). The effects of filler type and loading on critical degradation temperatures, residual mass, ignition and extinguishing times are elucidated. In this way, the study aims to identify optimum formulations for halogen-free ATH/MDH systems and to define design parameters for improving the fire safety of epoxy-based coatings.

2. MATERIALS AND METHOD

In this study, a two-component transparent casting epoxy system, L350D/LH300, was used as the matrix material. The system consists of component A, the resin (L350D), and component B, the hardener (LH300). The density of component A is 1.15 g·cm ^{3} and that of component B is 1.05 g·cm ^{3}, while the viscosity of the mixture lies in the range of 600–900 mPa·s. Curing preparation was carried out in accordance with the manufacturer's specifications at a resin-to-hardener ratio of 100:50 (±2 g) by mass. In this work, borax (B), aluminum hydroxide (ATH), and magnesium hydroxide (MDH) were incorporated as additives at different ratio in order to improve the flame-retardant and fire-performance properties of the epoxy resin matrix. The properties of these additives are given in Table 1 (Kaynak, 2012; Özcan, 2021; Aksoy, 2023; Ataman Kimya, 2025).

Table 1. Properties of the flame-retardant additives.

Property / Additive	**Borax (B)**	**Aluminum hydroxide (ATH)**	**Magnesium hydroxide (MDH)**
Chemical class	Inorganic borate (hydrated salt)	Inorganic metal hydroxide	Inorganic metal hydroxide
Density (g·cm ^{3})	1.7	2.4	2.3
Thermal threshold / decomposition	75–320 °C: loss of crystal water; formation of a borate glassy phase	180–220 °C: dehydroxylation to AlO(OH) / Al_2O_3	300–350 °C: dehydroxylation to MgO
Flame-retardant mechanism	Glassy borate barrier and promotion of char formation limiting gas diffusion	Endothermic decomposition + dilution by water vapor; formation of an Al_2O_3 barrier layer	Endothermic decomposition + dilution by water vapor; formation of an MgO barrier layer
Smoke / toxic gas effect	Contributes to reduced smoke and dripping	Low smoke	Low smoke

Table 2 presents the epoxy–hardener and flame-retardant additive ratios in terms of both weight percentage and mass. In the formulations prepared in this study, the total mass was fixed at 40 g, and the resin–hardener ratio was maintained at 100:50 by mass in accordance with the manufacturer's recommendation. In the flame-retardant system, the borax content was fixed at 2 wt% (0.8 g). The additive ratio of ATH and MDH were first set to 0, 2, 4, 8, and 16 wt%; the corresponding individual masses were adjusted to 0.0, 0.8, 1.6, 3.2, and 6.4 g, respectively, with equal incremental steps. As the total additive content increased, the matrix components were redistributed to keep the total mass constant; the corresponding epoxy/hardener amounts were determined as 26.67/13.33 g, 25.07/12.53 g, 24.00/12.00 g, 21.87/10.93 g, and 17.60/8.80 g.

Figure 1 summarizes the specimen fabrication steps followed in this study. For the preparation of the specimens to be used in the UL-94 vertical burning and thermal wear tests, silicone molds were first produced using 3D-printed master parts that were scaled up by 1.5% relative to the original specimen dimensions. In mold production, an RTV-2 type mold silicone with a Shore D hardness of 20 was employed.

Table 2: Epoxy–hardener and flame-retardant additive formulations.

Sample code	**Total additive content (wt%)**	**Borax (B), 2 wt% fixed) (g)**	**Aluminum hydroxide (ATH) (g)**	**Magnesium hydroxide (MDH) (g)**	**Epoxy (g)**	**Hardener (g)**
a	0	0.0	0.0	0.0	26.67	13.33
b	2	0.8	0.8	0.8	25.07	12.53
c	4	0.8	1.6	1.6	24.00	12.00
d	8	0.8	3.2	3.2	21.87	10.93
e	16	0.8	6.4	6.4	17.60	8.80

Figure 1. Schematic representation of the specimen fabrication steps followed in this study.

As flame-retardant components, borax, aluminum hydroxide (ATH), and magnesium hydroxide (MDH) were weighed and added to the epoxy resin prior to the incorporation of the hardener, in accordance with the composition ratios given in Table 2. To adjust the viscosity of the resulting mixture to a workable range and to achieve a preliminary dispersion of the additives, the system was held at 50 °C for 20 minutes. Subsequently, to ensure homogeneous distribution of the additives within the resin, the mixture was stirred for 10 minutes using a mechanical mixer operating at 130 rpm.

After this stage, the hardener was added and the system was mixed again to ensure compositional integrity. The prepared additive–epoxy mixtures were then poured into the silicone molds, and the molds were kept under a vacuum of approximately 100 mmHg (≈0.1 bar) for 60 minutes to remove entrapped air bubbles. The solidified specimens were demolded and left under ambient conditions for 5 days to complete the final curing process.

The dimensions of the UL-94 vertical burning test specimens are shown in Figure 2, and six specimens were produced for each formulation, including one spare.

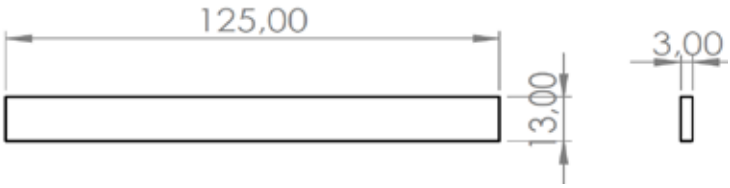

Figure 2. Dimensions of the UL-94 vertical burning test specimens.

To investigate the burning behavior and flame-retardant properties of the composites, the UL-94 vertical burning test, schematically illustrated in Figure 3, was employed. In this method, the specimens were exposed to a controlled flame source for a specified duration; during testing, particular attention was paid to whether the dripping melt ignited the underlying cotton layer, as well as to the structural changes and integrity of the specimens observed after burning.

In this study, in addition to the UL-94 vertical burning test, thermogravimetric analysis (TGA) was employed to investigate the contribution of the flame-retardant system containing borax, aluminum hydroxide (ATH), and magnesium hydroxide (MDH) to the fire performance, thermal stability, and degradation behavior of the composites. In this way, the influence of these additives on the overall performance of epoxy-based composites under high-temperature and fire conditions was comparatively evaluated.

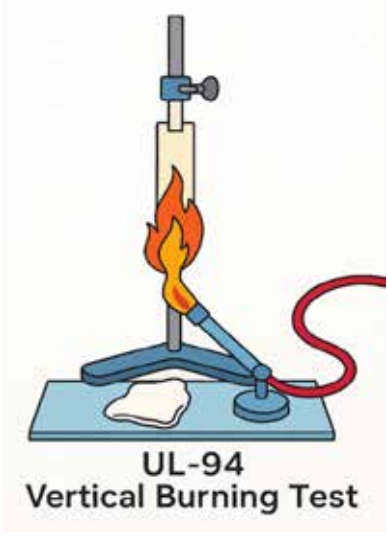

Figure 3. Schematic illustration of the UL-94 vertical burning test

TGA is a fundamental thermal analysis technique based on monitoring the mass change of a material under a controlled heating program. Using this method, the degradation steps, onset temperatures of decomposition, thermal stability limits, and residual mass of the composites modified with borax/ATH/MDH can be determined; consequently, the effects of the flame-retardant phases on char formation behavior and fire performance can be quantitatively revealed. The findings obtained are important for defining the safe service temperature ranges of the composites and their resistance in high-temperature environ-

ments. In this study, TGA measurements were carried out in the temperature range of 25–800 °C at a heating rate of 10 °C/min.

3. RESULTS AND DISCUSSION

During the UL-94 vertical burning tests, the overall burning behaviors of the specimens with different additive ratio are shown in detail in Figure 4, while their macroscopic appearances after testing are presented in Figure 5. In addition, the data obtained for the UL-94 vertical burning classifications of the specimens are summarized in Table 5, and these results qualitatively reveal the effect of additive content on the flame-retardant performance of the epoxy-based composites.

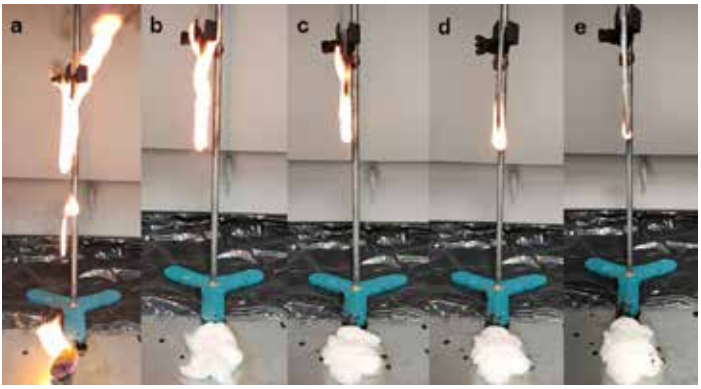

Figure 4: General burning behavior of specimens with different additive contents during the UL-94 vertical burning test. (a: neat reference sample; b: 2 wt% borax + 2 wt% ATH + 2 wt% MDH; c: 2 wt% borax + 4 wt% ATH + 4 wt% MDH; d: 2 wt% borax + 8 wt% ATH + 8 wt% MDH; e: 2 wt% borax + 16 wt% ATH + 16 wt% MDH).

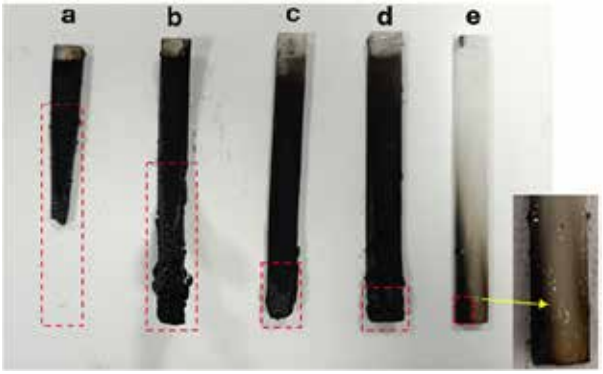

Figure 5: General appearance of specimens with different additive contents after the UL-94 vertical burning test. (a: neat reference sample; b: 2 wt% borax + 2 wt% ATH + 2 wt% MDH; c: 2 wt% borax + 4 wt% ATH + 4 wt% MDH; d: 2 wt% borax + 8 wt% ATH + 8 wt% MDH; e: 2 wt% borax + 16 wt% ATH + 16 wt% MDH)

Table 5: UL-94 vertical burning classification

Samples	**UL-94 Rating**	**Dripping**	**Cotton catching fire with dripping particles**	**Did it burn down to the sample holder?**
a	BC	Yes	Yes	Yes
b	V2	No	No	Yes
c	V2	No	No	Yes
d	V1	No	No	No
e	V0	No	No	No

In this formulation series, neat epoxy (sample a) was compared with systems containing a fixed borax ratio of 2 wt% (0.8 g) and gradually increasing ATH/MDH ratios of 2, 4, 8 and 16 wt% for samples b–e, respectively (ATH and MDH in equal amounts, Table 5). The UL-94 vertical burning responses of these specimens are summarized in Table 5 and visually illustrated in Figures 4 and 5. The additive-free reference (sample a) exhibits the most critical fire scenario: during testing, a tall, sustained flame develops along the entire bar, intense melt dripping occurs, and the dripping particles readily ignite the underlying cotton. Consequently, the specimen burns completely down to the holder and fails to satisfy any UL-94 classification, remaining at the BC level.

This behavior is also reflected in Figure 5a, where almost the whole length of the bar appears heavily charred and deformed, indicating an unprotected epoxy matrix with no effective barrier formation. Upon introducing the borax/ATH/MDH package, a stepwise improvement in burning behavior is observed. At low total additive ratios (samples b and c, 2 and 4 wt% ATH+MDH with 2 wt% borax), dripping and cotton ignition are already fully suppressed (Table 5), suggesting that the melt becomes more cohesive and the formation of flaming droplets is effectively prevented. Nevertheless, the flame front still propagates from the ignition point to the lower end of the specimen, and both formulations continue to burn down to the holder, which limits the classification to V2. This is consistent with the images in Figure 4b–c, where a long flame column extends along the bar, and with Figure 5b–c, where the charred region still covers almost the entire specimen length, although some reduction in char thickness and a slightly more compact residue can be distinguished compared to the neat matrix. A more pronounced transition occurs at an intermediate additive ratio of 8 wt% ATH+MDH (sample d): the flame height and afterflame time visibly decrease (Figure 4d), the char length is shortened, and a distinct unburned region is retained in the lower part of the bar (Figure 5d). In line with these visual observations, sample d no longer burns down to the holder and attains the V1 rating without dripping or cotton ignition. The most striking enhancement is achieved at the highest total additive ratio (sample e, 16 wt% ATH+MDH + 2 wt% borax), where the specimen reaches the UL-94 V0 classification. In this case, the flame remains confined to a limited zone near the ignition region and self-extinguishes within a very short time, without any dripping or secondary ignition of the cotton (Table 5). The post-burning morphology in Figure 5e confirms this behavior: only a relatively thin, localized char layer is formed around the upper portion of the bar, while the majority of the specimen—including the region magnified in the inset—retains its original geometry with minimal thermal damage. Beyond the critical total ATH/MDH ratio between 8 and 16 wt%, heat absorption, gas dilution, increased melt viscosity and the formation of a foamed barrier layer collectively interrupt the supply of fuel and oxygen to the flame front, transforming the system from a dripping, self-sustaining fire scenario (BC–V2) into a non-dripping, self-extinguishing UL-94 V0 epoxy composite. This behaviour is most evident for the 16 wt% formulation (sample e), where the close-up in Figure 5e reveals numerous whitish bubbles distributed within the upper char, indicative of decomposition gases trapped in a viscous, borate-rich phase; the resulting foamed, cellular residue enhances thermal insulation and mass-transfer resistance, confines the combustion zone to a narrow

region and thus enables rapid self-extinguishing, consistent with the UL-94 V0 rating [21-26]. (Iqbal ve ark., 2018; Liu ve ark., 2022; Yiğit, 2022; Dun ve ark., 2024; Saputra and Fathurrahman, 2018; Yıldırım ve ark., 2023).

TG/DTG results reveal that, with increasing borax/ATH/MDH loading in the epoxy composites, a distinctly more pronounced multi-step and progressively slower degradation behavior develops.

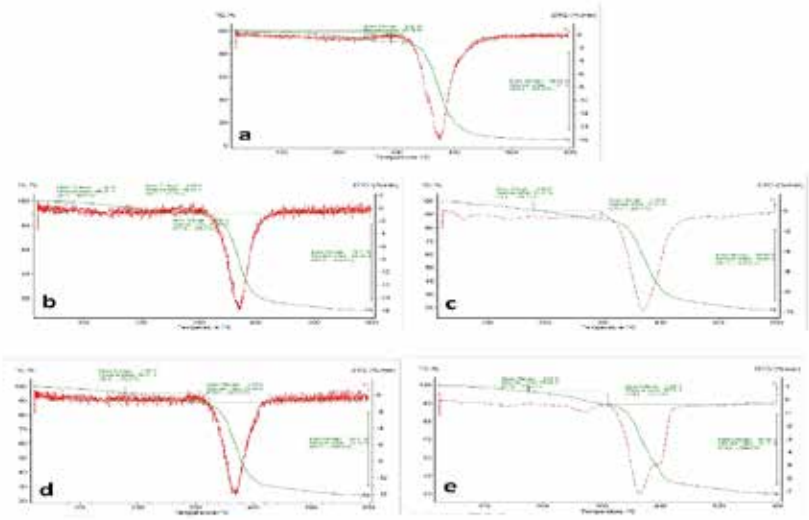

Figure 6. TG–DTG curves of epoxy composites containing different ATH/MDH ratio (a: neat reference sample; b: 2 wt% borax + 2 wt% ATH + 2 wt% MDH; c: 2 wt% borax + 4 wt% ATH + 4 wt% MDH; d: 2 wt% borax + 8 wt% ATH + 8 wt% MDH; e: 2 wt% borax + 16 wt% ATH + 16 wt% MDH).

In the reference specimen (Figure 6a), a single, sharp main degradation step is observed between 289 and 600 °C, with only 4.61 wt% residual mass at 600 °C. In contrast, as the ATH and MDH contents are increased (4–16 wt%), additional mass losses appear in the 80–310 °C range due to moisture and crystal water release, and the main degradation step above 300 °C shifts to higher temperatures and becomes markedly slower. In particular, for the specimen with the highest additive loading (2 wt% borax + 16 wt% ATH + 16 wt% MDH, Figure 6e), the main DTG peak intensity is reduced to approximately half of that of the reference, while the residual mass at 600 °C increases to 39.74 wt%. These findings indicate that non-combustible inorganic/carbonaceous phases

become dominant in the system. This behavior indicates that the B/ATH/MDH system activates multiple flame-retardant mechanisms simultaneously. First, the endothermic dehydroxylation of ATH and MDH in the 200–350 °C range provides substantial heat absorption, preventing a rapid temperature rise in the matrix, while the released water vapor dilutes the atmosphere and lowers the concentration of flammable gases (Murad ve ark., 2025). Second, the dehydroxylation products Al_2O_3 and MgO, together with the glassy borate phases formed in the presence of borax and the charred carbonaceous structure, generate a continuous, low-porosity protective barrier layer on the surface. This layer both restricts oxygen and heat flux—thereby delaying further degradation of the underlying polymer—and hinders the diffusion of volatile combustible products (Zhu ve ark., 2024).

It is presumed that borax enhances the carbonaceous residue yield by creating an environment that promotes additional crosslinking and char formation between epoxy chains, and that, together with the inorganic phases originating from ATH/MDH, it contributes to the development of a mechanically integrated, crack-resistant char/oxide composite layer (Yıldız ve ark., 2025). In this way, both the heat release rate and the evolution of flammable gases are significantly suppressed during thermal degradation, the tendency to drip is reduced, and the advance of the flame is physically impeded (Tian ve ark., 2024). The TGA/DTG data obtained confirm that the B/ATH/MDH additive package substantially reinforces the thermal stability and char-forming tendency of the epoxy coatings and, consequently, is in full agreement with the improved fire performance observed in the UL-94 vertical burning test (Liu ve ark., 2022).

REFERENCES

[1] Aytan, E. (2021). *Çok gözenekli (mezopor) yanma geciktirici malzeme içeren polimerik kompozitlerin geliştirilmesi ve özelliklerinin incelenmesi* (Yüksek lisans tezi). Marmara Üniversitesi, İstanbul, Türkiye.

[2] Çakır, M., & Berberoğlu, B. (2018). "*E-cam elyaf takviyeli epoksi matrisli kompozit malzemelerin elyaf oranındaki artış ile mekanik özelliklerindeki değişimlerin incelenmesi*", *ECJSE*, 5(3), 734–740. https://doi.org/10.31202/ecjse.415482

[3] Samper, M. D., Petrucci, R., Sànchez-Nácher, L., Balart, R., & Kenny, J. M. (2014). "*Effect of silane coupling agents on basalt fiber–epoxidized vegetable oil matrix composite materials analyzed by the single fiber fragmentation technique"*. *Polymer Composites, 36*(7), 1205–1212. https://doi.org/10.1002/

pc.23023

[4] Jamali, N., Rezvani, A. R., Khosravi, H., & Tohidlou, E. (2018). "*On the mechanical behavior of basalt fiber/epoxy composites filled with silanized graphene oxide nanoplatelets". Polymer Composites, 39*(S4). https://doi.org/10.1002/pc.24766

[5] Zhu, X., Chen, Y., & Zang, C. (2022). "*Flame retardant properties and mechanical properties of polypropylene with halogen and halogen-free flame retardant system". Journal of Physics: Conference Series*, 2160(1), 012031. https://doi.org/10.1088/1742-6596/2160/1/012031

[6] Demirci, İ., & Avcı, A. (2017). "*Deniz suyu korozyon ortamında bazalt/epoksi kompozitlerin mekanik davranışlarının incelenmesi". Selçuk-Teknik Dergisi, 16*(2), 44–54.

[7] Lu, Z., Xie, J., Zhang, H., & Li, J. (2017). "*Long-term durability of basalt fiber-reinforced polymer (BFRP) sheets and the epoxy resin matrix under a wet–dry cyclic condition in a chloride-containing environment". Polymers, 9*(12), 652. https://doi.org/10.3390/polym9120652

[8] Li, F.F. (2023). "*Comprehensive review of recent research advances on flame-retardant coatings for building materials: Chemical ingredients, micromorphology, and processing techniques". Molecules, 28*, 1842.

[9] Mohd Sabee, M. M., Itam, Z., Beddu, S., Zahari, N. M., Mohd Kamal, N. L., Mohamad, D., Zulkepli, N. A., Shafiq, M. D., & Abdul Hamid, Z. A. (2022). *Flame-retardant coatings: Additives, binders, and fillers*. *Polymers, 14*, 2911.

[10] Alonso, C., Manich, A., Campo, A. D., Felix-De Castro, P., Boisseree, N., Coderch, L., & Martí, M. (2022). "*Graphite flame-retardant applied on polyester textiles: Flammable, thermal and in vitro toxicological analysis". Journal of Industrial Textiles, 51*, 4424S–4440S.

[11] Pérez-Salinas, C., Castro, C., Patín, G., Peña, A. M. de l., & Paredes, D. R. (2019). "*Application of flame retardants aluminum hydroxide and magnesium hydroxide in a material composed of glass fiber with polymeric matrix and its influence on the flammability index". Key Engineering Materials, 818*, 128–133. https://doi.org/10.4028/www.scientific.net/kem.818.128

[12] Peng, H., Wang, X., Li, T., Lou, C., Wang, Y., & Lin, J. (2019). "*Mechanical properties, thermal stability, sound absorption, and flame retardancy of rigid PU foam composites containing a fire-retarding agent: Effect of magnesium hydroxide and aluminum hydroxide". Polymers for Advanced Technologies, 30*(8), 2045–2055. https://doi.org/10.1002/pat.4637

[13] Li, P., Li, L., Ji, L., Dang, L., Lan, S., & Zhu, D. (2023). "*Functionalized magnesium hydroxide with zinc borate and 3-aminopropyltriethoxysilane for enhanced flame-retardant and smoke suppressant properties of epoxy resins*". *Journal of Applied Polymer Science, 140*(23). https://doi.org/10.1002/app.53941

[14] Afzal, A., Tariq, A., Shakir, H. F., Satti, A. N., Taimoor, M., Ghani, U., & Khaliq, Z. (2020). "*Development and characterization of multifunctional carbon fabric-reinforced polymer composites incorporated with inorganic flame retardants*". *Polymer Composites, 41*(8), 3043–3051. https://doi.org/10.1002/pc.25596

[15] Sonnier, R., Viretto, A., Dumazert, L., Longerey, M., Buonomo, S., Gallard, B., & Freitag, A. (2016). "*Fire retardant benefits of combining aluminum hydroxide and silica in ethylene-vinyl acetate copolymer (EVA)*". *Polymer Degradation and Stability, 128*, 228–236. https://doi.org/10.1016/j.polymdegradstab.2016.03.030

[16] Chen, H., Chen, K., Yang, R., Yang, F., & Gao, W. (2011). "*Use of aluminum trihydrate filler to improve the strength properties of cellulosic paper exposed to high temperature treatment*". *BioResources, 6*(3), 2399–2410. https://doi.org/10.15376/biores.6.3.2399-2410

[17] Kaynak, E. (2012). *Polipropilen esaslı tekstil malzemelerine kaplama yöntemiyle uygulanabilen güç tutuşur malzemeler geliştirilmesi* (Yüksek lisans tezi). Anadolu Üniversitesi, Türkiye.

[18] Özcan, T. (2021). *Alev geciktirici katkı içeren polipropilen kompozitlerin karakterizasyonu ve yanma özelliklerinin incelenmesi* (Yüksek lisans tezi). Marmara Üniversitesi, Türkiye.

[19] Aksoy, K. (2023). "*Flame-retardant compounds used in epoxy resins*". *Yüzüncü Yıl Üniversitesi Fen Bilimleri Enstitüsü Dergisi, 28*(2), 775–802.

[20] Ataman Kimya A.Ş. (2025). *BORAKS*. Ataman Chemicals. Erişim tarihi: 18 Kasım 2025, https://www.atamanchemicals.com/borax_u25509/?lang=TR

[21] Iqbal, M. A., Iqbal, M. A., & Fedel, M. (2018). "*Fire retardancy of aluminum hydroxide reinforced flame retardant modified epoxy resin composite*". *Russian Journal of Applied Chemistry, 91*, 680–686. https://doi.org/10.1134/S1070427218040225

[22] Liu, Y., Tang, Z., & Zhu, J. (2022). "*Synergistic flame retardant effect of aluminum hydroxide and ammonium polyphosphate on epoxy resin*". *Journal of Applied Polymer Science, 139*(46), e53168.

[23] Yiğit, N. Ç. (2022). "*Current approaches to the synthesis of flame retardant polymers". Journal of Innovative Engineering and Natural Science, 2*(2), 95–113.

[24] Dun, L., Ouyang, Z., Sun, Q., Yue, X., Wu, G., Li, B., Kang, W., & Wang, Y. (2024). "*A simple and efficient magnesium hydroxide modification strategy for flame-retardancy epoxy resin". Polymers, 16*(11), 1471. https://doi.org/10.3390/polym16111471

[25] Saputra, A. H., & Fathurrahman, F. (2018). "*Synthesis and characterization of non-halogenic fire retardant composite with epoxy resin and additive combination* $Al(OH)_3/Mg(OH)_2$", *MATEC Web of Conferences, 156*, 05010.

[26] Yıldırım, S., Eren, O., Cetinkaya, M. K., Gürek, M., & Demirel, B. (2023). "*Elektrik kabloları için halojensiz alev geciktirici kılıf malzemesi üretiminde kullanılan kompozit malzemede çinko borat, alüminyum hidroksit ve magnezyum hidroksit kompozisyonunun optimizasyonu". Politeknik Dergisi, 26*(3), 1111–1119.

[27] Murad, M. S., Hamzat, A. K., Asmatulu, E., & Asmatulu, R. (2025). "*Flame-retardant fiber composites: Synergistic effects of additives on mechanical, thermal, chemical, and structural properties". Advanced Composites and Hybrid Materials, 8*, 31. https://doi.org/10.1007/s42114-024-01111-1

[28] Zhu, C., Li, J., Huang, C., et al. (2024). "*The investigation of flame-retardant fiber mats for high performance composites: Flame retardancy and structure performance". Textile Research Journal, 94*(19–20), 2147–2163. https://doi.org/10.1177/00405175241242148

[29] Yıldız, R., Can, H., & Türkmen, H. (2025). "*Enhanced mechanical and flame retardant properties of basalt fiber reinforced epoxy composites compared to glass fiber systems". In 17th International Istanbul Scientific Research Congress: Congress Proceedings Book*. https://doi.org/10.30546/19023.978-9952-8596-8-3.2025.0031

[30] Tian, L., Chen, R., Zhang, Y., et al. (2024). "*Improvement of flame retardancy and thermal stability of epoxy composites by modifying salen-based polyphosphazene microspheres with Co-based metal organic frameworks". High Performance Polymers, 37*(1), 50–63. https://doi.org/10.1177/09540083241303404

[31] Liu, B.-W., Zhao, H.-B., & Wang, Y.-Z. (2022). "*Advanced flame-retardant methods for polymeric materials". Advanced Materials, 34*(46), 2107905. https://doi.org/10.1002/adma.202107905

CHAPTER 8

THE AERODYNAMIC AND HYDRODYNAMIC DESIGN OF SAILING YACHTS

Öğr. Gör. Dr. Emin ÖZDEMİR
İstanbul Üniversitesi-Cerrahpaşa,
Mühendislik Fakültesi, İstanbul / Türkiye
emin.ozdemir@iuc.edu.tr
https://orcid.org/0000-0002-6517-9270

Ozan ERCAN
İstanbul Üniversitesi-Cerrahpaşa,
Mühendislik Fakültesi, İstanbul / Türkiye

1. INTRODUCTION

Sailing yachts represent one of the most refined integrations of physics, engineering, and environmental design. For thousands of years, they have played a central role in trade, exploration, and transportation. Although the modern era has been dominated by engine-powered vessels, the increasing global focus on sustainability, energy efficiency, and emissions reduction has renewed interest in wind-powered ships. That is not for nostalgia, but as a practical response to environmental and economic challenges (Fossati, 2009; Kimball, 2009). Today, sailing yachts are once again gaining attention, not only in sport and recreation but also as viable contributors to greener maritime transport (Figure 1) (Souppez, 2024).

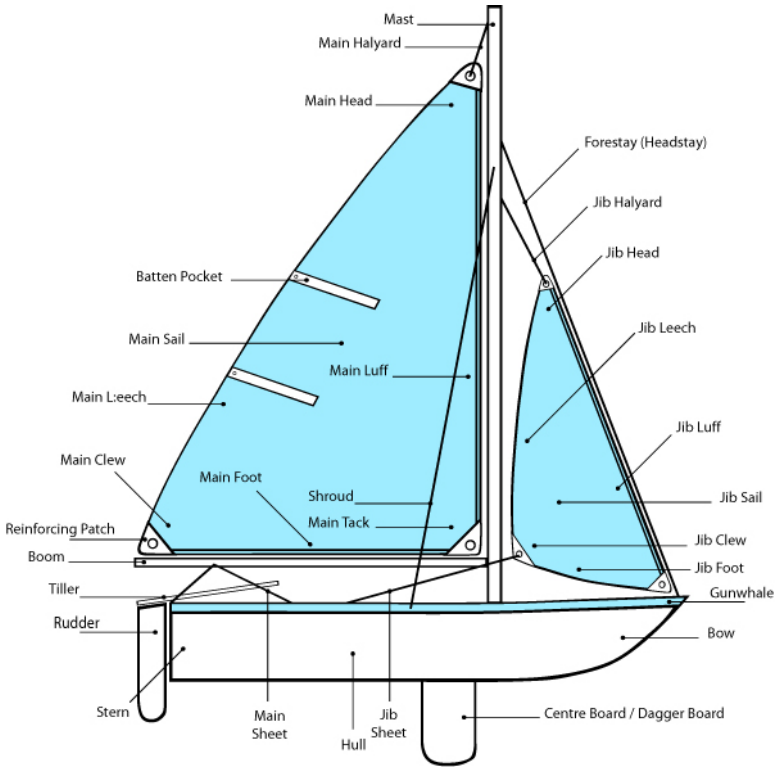

Figure 1. Main parts of a small sailboat: mast, boom, mainsail, jib, hull, keel, rudder, etc. (Jazzmanian, 2006).

The motion of a sailing yacht is driven by the power of the wind, yet this process is far from simple. It results from complex aerodynamic and hydrodynamic interactions between air, water, and the boat's structure. The aerodynamic lift generated by the sails and the hydrodynamic lift produced by the keel and hull must operate in harmony to create forward motion and maintain stability. These forces are influenced by numerous parameters, including wind speed and direction, sail geometry, hull design, heel angle, and leeway (Anderson, 2003; Marchaj, 1979; Milgram, 1996). The overall performance of a yacht is determined by how effectively these elements are optimized and balanced.

Sailing yachts utilize wind power in a dynamic and interactive manner. The sails function as airfoils, generating aerodynamic lift in the same way that an airplane wing does (Weltner, 1987; Anderson, 2010). Beneath the waterline, the keel and rudder generate hydrodynamic lift, resisting sideways drift and ensuring stability. The combined interaction of these aerodynamic and hydrod-

ynamic forces defines a yacht's propulsion, maneuverability, and efficiency. Understanding these mechanisms requires a systematic and scientific approach that connects theoretical foundations with practical engineering applications (Viola & Flay, 2011; Slooff, 2015).

Technological advancements have revolutionized yacht design by enabling detailed analysis and simulation of these forces. Modern design approaches integrate advanced computational and experimental methods, such as Computational Fluid Dynamics (CFD), Finite Element Analysis (FEA), and Velocity Prediction Programs (VPP), along with wind tunnel and towing tank experiments (Larsson, 1990; Larsson ve ark., 2003; Casalone ve ark., 2020). These tools allow engineers to visualize airflow over sails and water flow around the hull, optimize geometric configurations, and predict performance with high precision even before the yacht is built. This digital approach not only reduces development time and cost but also encourages innovation and environmental sustainability (Viola, 2009; Persson, 2025).

In addition to conventional sail systems, modern yachts increasingly employ rigid wing sails and solar-assisted sail technologies. These systems combine aerodynamic efficiency with renewable energy generation, offering dual benefits: enhanced propulsion and reduced reliance on fossil fuels (Silva ve ark., 2019; Kawecki ve ark., 2024). Solar-integrated sails, for example, can produce electricity during operation, powering onboard systems and minimizing the need for fuel-based generators. Similarly, hybrid wind–engine systems and rotor sails are being explored to enhance efficiency and reduce emissions in commercial vessels (He ve ark., 2015; Ding ve ark., 2025).

This study aims to provide a comprehensive understanding of the aerodynamic and hydrodynamic principles that govern sailing yacht performance. It examines key concepts such as lift and drag forces, sail–keel interaction, and the influence of environmental and design parameters on efficiency (Anderson, 2008; Wilson, 2010). Furthermore, it highlights the integration of modern optimization and modeling techniques ranging from multi-objective genetic algorithms and Fluid–Structure Interaction (FSI) modeling to Artificial Intelligence (AI)-based adaptive control as the next frontier in yacht design (Larsson, 2018; Gentry, 1988).

Ultimately, this work bridges theoretical aerodynamics and practical marine engineering to advance the development of smarter, greener, and more efficient sailing systems. The findings underscore the expanding role of computational modeling, intelligent control, and renewable energy technologies in shaping the future of sustainable maritime transportation (Viola, 2013; Claughton ve ark., 2006).

2. IMPORTANCE OF AERODYNAMICS IN YACHT DESIGN

The performance of a sailing yacht depends not only on hull geometry and sail plan but also on wind speed, apparent wind direction, heel angle, leeway, and the dynamic interaction between aerodynamic and hydrodynamic forces. These interactions require an integrated evaluation of both airflow around the sails and water flow beneath the hull (Figure 2). Modern yacht design approaches aim to **maximize aerodynamic efficiency** while minimizing **resistive drag**. To achieve this, designers employ computational and experimental methods that accurately model sail-hull-keel interactions under various sailing conditions (Viola, 2013).

Recent advances in computational modeling have significantly enhanced our understanding of yacht aerodynamics. Viola (2013) reviewed modern developments in sailing yacht aerodynamics, emphasizing CFD-based simulation techniques. Similarly, hydrodynamic analyses of hull resistance and wave interactions have been conducted to refine performance prediction models (Milgram, 1996). The integration of aerodynamic and hydrodynamic modeling enables precise evaluation of real-world sailing conditions, including turbulence, heel, and yaw effects (Marino ve ark., 2017).

In summary, sailboats should be examined from an aerodynamic perspective. A boat's performance is determined not only by the wind, but also by the interaction between the wind, sails, and hull. Therefore, a systematic understanding of aerodynamic principles and their integration into the design process is essential.

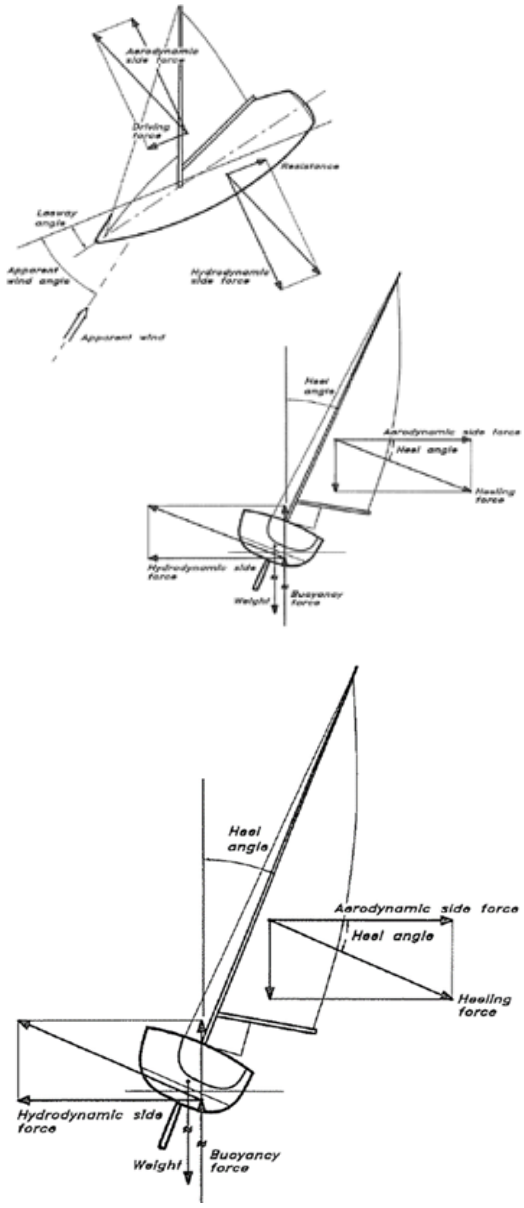

Figure 2. Schematic showing aerodynamic side force, driving force, apparent wind, hydrodynamic side force and resistance on a sailing yacht (Bayraktar ve ark., 2007).

Additionaly, key concepts employed throughout this study include:

Lift (L): The net force acting perpendicular to the direction of airflow.

Drag (D): The resistive force parallel to the direction of airflow.

Angle of Attack (α): The angle between the apparent wind and the referen-

ce chord line of the sail.

Apparent Wind (Va): The vector sum of the true wind and the boat velocity.

Heel / Leeway: The inclination and sideways drift of the yacht, respectively, both affecting hydrodynamic lift and drag.

Frictional Resistance: Drag due to shear forces along the wetted hull surface.

Wave Resistance: Resistance resulting from waves generated by the moving hull.

3. FUNDAMENTALS OF AERODYNAMICS

The fundamental mechanism behind the motion of a sailing yacht is the interaction between the wind flow and the sail surface, which generates **aerodynamic forces**. These forces are divided into two main components:

- **Lift (L)** – acting perpendicular to the direction of the apparent wind flow.
- **Drag (D)** – acting parallel to the wind direction and opposing the motion.

The sail behaves as an **airfoil**, similar to an aircraft wing. As air flows faster along the leeward (downwind) side and slower on the windward (upwind) side, a pressure differential arises according to **Bernoulli's principle**. This pressure difference generates the net aerodynamic lift that propels the yacht forward (Figure 3) (Anderson, 2010).

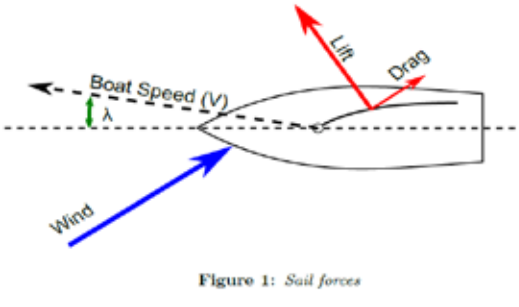

Figure 1: *Sail forces*

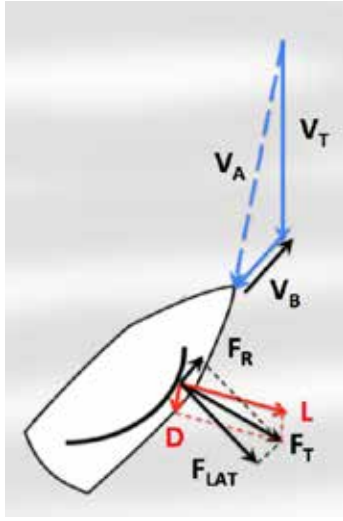

Figure 3. Decomposition of total aerodynamic force on a sail into lift and drag, and into driving (forward) and lateral components acting on the boat (Knudsen, 2013; HopsonRoad, 2015a).

In Figure3: $\mathbf{F_T}$ is the total force acting on the sail for the Apparent Wind ($\mathbf{V_A}$), shown. This resolves into forces felt by the sail, Lift (**L**) and Drag (**D**), with vectors shown in red. $\mathbf{F_T}$ also resolves into forces felt by the boat, Driving Force ($\mathbf{F_R}$) and Lateral Force ($\mathbf{F_{LAT}}$).

3.1. Bernoulli's Principle and Pressure Distribution

The aerodynamic behavior of sails is similar to that of airplane wings. When wind flows over the curved surface of the sail, it creates a pressure difference lower pressure on one side and higher on the other. This results in a lift force that propels the boat forward. Meanwhile, the keel under the water provides a counterforce to prevent the boat from sliding sideways and helps maintain stability. Bernoulli's Principle explains this interaction by showing how fluid (air or water) pressure decreases as its velocity increases. Understanding and applying this principle is key to improving sailing efficiency.

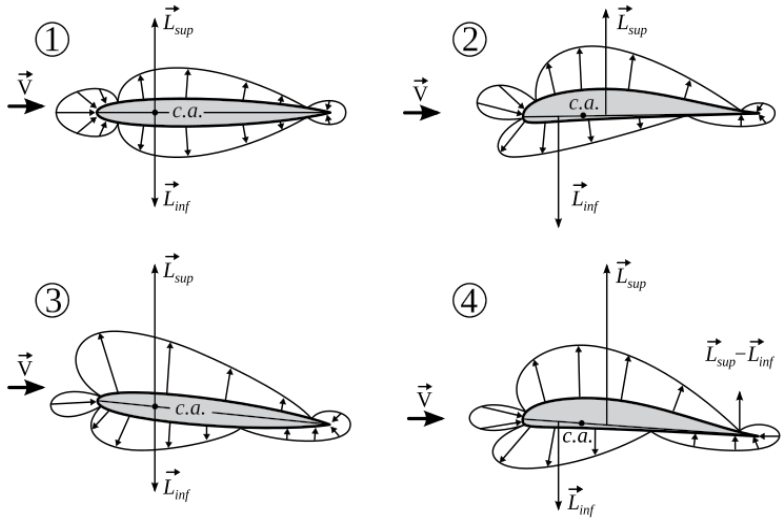

Figure 4**.** Pressure distribution diagram on an airfoil showing low pressure on the upper surface and higher pressure beneath, illustrating Bernoulli's principle in lift generation. 1: Symmetric profile zero lift angle of attack, 2: Asymmetric profile zero lift angle of attack, 3: Symmetric profile positive lift angle of attack, 4: Asymmetric profile positive lift angle of attack (Garcia, 2020).

The airflow around a sail can be described by Bernoulli's equation:

= constant

where:

P = static pressure,

ρ = air density,

υ = velocity of the airflow,

g = gravitational acceleration,

h = height.

For sail analysis, the height term is negligible, so the equation simplifies to:

= constant

As the flow velocity increases, static pressure decreases. On the leeward side of the sail, air moves faster and pressure drops; on the windward side, the flow slows and pressure increases. This pressure difference produces **aerodynamic lift**, the primary driving force for a sailing yacht (Figure 4). On the other hand, experimental and computational results confirm that the sail's lift arises not only from Bernoulli's principle but also from **flow turning**, which redirects the airflow to create momentum changes and pressure gradients (NASA Glenn Research Center, 2015).

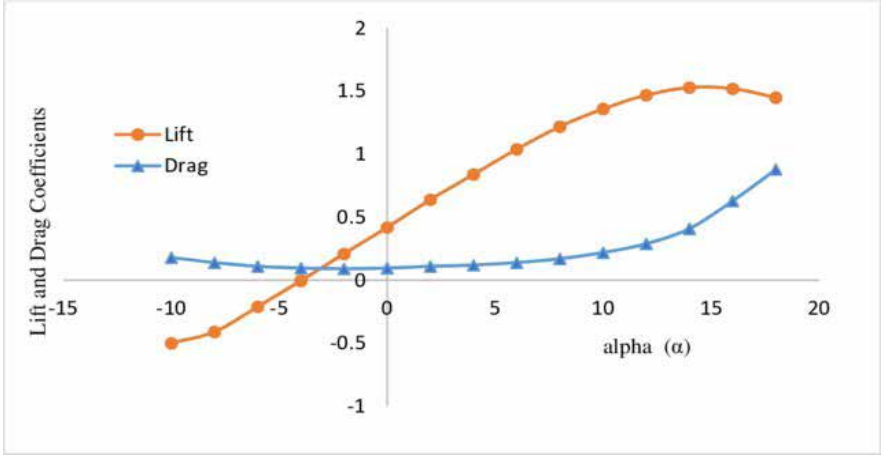

Figure 5. Variation of lift coefficient (C_L) and drag coefficient (C_D) with angle of attack (α) for a typical airfoil (Petinrin & Onoja, 2017).

3.2. Lift and Drag Coefficients

The aerodynamic forces acting on a sail are commonly expressed in nondimensional form as:

,

where:

L = lift force (N)

D = drag force (N)

ρ = air density (kg/m³)

V = apparent wind speed (m/s)

A = sail area (m²)

= lift coefficient

= drag coefficient

These coefficients depend on the **angle of attack (α)**, **camber (curvature)** of the sail, and the **Reynolds number (Re)** of the flow (Claughton ve ark., 2006). The graph in Figure 5 illustrates that lift increases linearly at small α until stall occurs, while drag rises gradually, then sharply after stall.

3.3. Angle of Attack and Flow Separation

The **angle of attack (α)** is the angle between the chord line of the sail and the direction of the apparent wind. It critically influences sail performance:

- At small angles (α), lift is low because the pressure differential is minimal.
- At moderate angles (α), lift increases rapidly, reaching a maximum value ().
- Beyond a critical angle (typically α=10–15° for most sails), flow separation occurs, the boundary layer detaches, and **stall** takes place — causing a rapid loss of lift and an increase in drag (Figure 5).

Wind-tunnel and CFD studies have shown that controlling the angle of attack near the optimal region significantly enhances sail efficiency (Figure 6) (Izaguirre Alza, 2012; Viola & Flay, 2011).

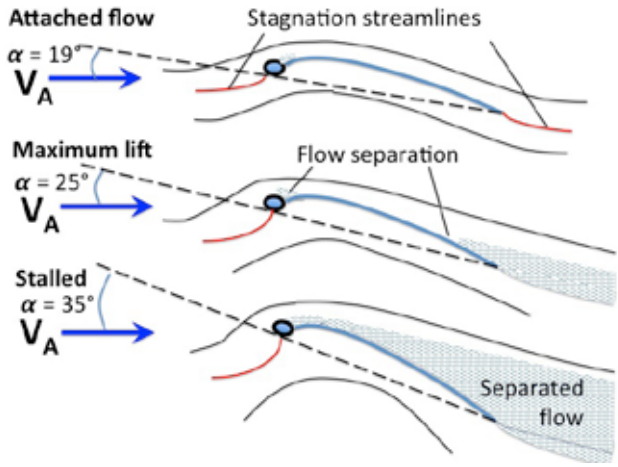

Figure 6. Sail angles of attack and resulting flow patterns, showing attached, maximum lift and stalled flow states. ($\mathbf{V_A}$); apparent wind vector and (α); angle of attack (HopsonRoad, 2015b).

3.4. Apparent Wind and Aerodynamic Interaction

When a yacht is in motion, the wind it perceives differs from the wind that would be felt if it were stationary. This resulting airflow is known as the ***apparent wind***. It is formed by the vector combination of the true wind and the yacht's own velocity, as illustrated in Figure 7a. During upwind sailing, **the apparent wind speed (AWS)** becomes greater than **the true wind speed (TWS)**. As a result, high-performance yachts can move at speeds exceeding that of the actual wind a phenomenon often described as the boat "creating its own wind" (Knudsen, 2013).

As the yacht moves through the water, its forward velocity modifies the effective wind perceived on the sails. The vector combination of the **true wind ($_t$)** and the **boat velocity-speed ($_s$)** defines the **apparent wind ($_a$)**:

$$\boldsymbol{a = t - s}$$

Sailboats cannot travel directly into the wind. Instead, they usually sail at a true wind angle ranging from 30° to 40°. Because the sails generate a lateral force, the vessel experiences a slight sideways drift through the water, as illustrated in Figure 7b. The angle between the intended heading and the actual path of motion is known as the *leeway angle* (λ). To evaluate a yacht's efficiency when sailing upwind, it is necessary to account for the true wind angle (TWA),

leeway angle, and boat speed. This overall performance measure is referred to as *Velocity Made Good* (VMG), which indicates how effectively the yacht advances in the direction of the wind (Knudsen, 2013). The VMG can be determined using the following relationship:

The direction of apparent wind shifts forward as boat speed increases. Therefore, trimming the sails correctly according to the apparent wind angle is critical for optimal propulsion. Maximum aerodynamic efficiency often occurs under **beam reach** conditions (when the apparent wind is roughly perpendicular to the boat's course), as both lift and drag are favorably balanced (Marchaj, 1979).

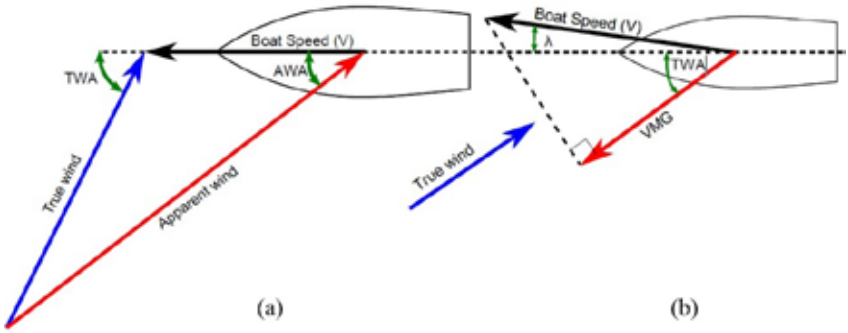

Figure 7. a) Apparent and true wind, the true wind angle (TWA), The apparent wind angle (AWA), b) Velocity made good (VMG) (Knudsen, 2013).

3.5. Lift-to-Drag Ratio (L/D) and Efficiency

The **lift-to-drag ratio (L/D)** is a key indicator of aerodynamic performance (Figure 5). A higher L/D ratio implies greater efficiency and less energy lost to resistance.

Typical L/D values for different sail systems:

- Traditional soft sails: ≈ 5–7
- Modern high-performance sails: ≈ 10–15
- Wing sails (rigid airfoils): > 20

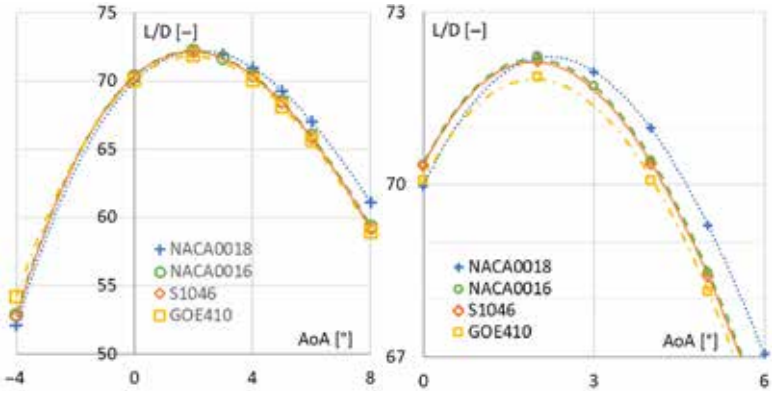

Figure 8. Comparison of aerodynamic efficiency (Lift-to-Drag Ratio) among traditional sails, modern laminate sails, and rigid wing sails, 2D simulation, (a) δ = 12◦; full range, (b) close-up (Kawecki ve ark., 2024).

Rigid wing sails, as used in *America's Cup* catamarans, operate under the same aerodynamic principles as aircraft wings, providing exceptional efficiency. Typical L/D values for different sail systems are shown in Figure 8, illustrating the superior aerodynamic efficiency of rigid wing sails (Kawecki, 2024; Caraher, 2021).

3.6. Flow Regime and Reynolds Number

The behavior of airflow around a sail depends strongly on the **Reynolds number (Re)**:

where L is a characteristic chord length and μ is the dynamic viscosity of air.

Typical values for sails range between 10^6 and 10^7, indicating **turbulent flow regimes** (Figure 9). Thus, laminar-flow assumptions are generally invalid, and appropriate turbulence models (such as k–ε or *SST* k–ω) are applied in CFD simulations (Izaguirre Alza, 2012; Viola & Flay, 2011).

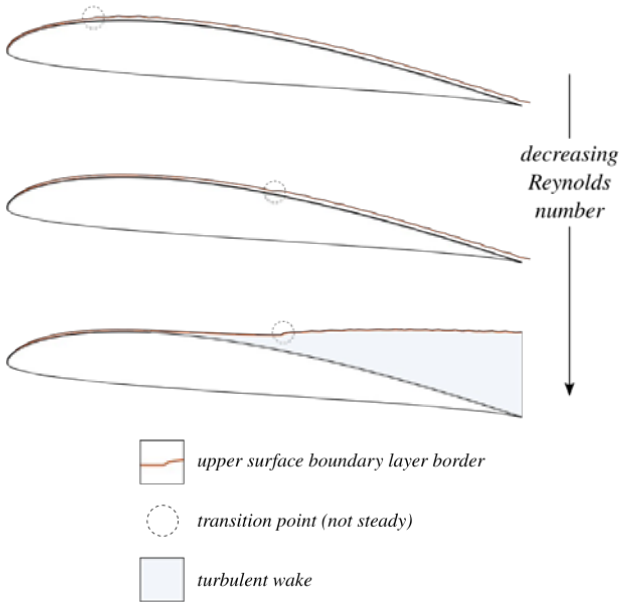

Figure 9. Effect of decreasing Reynolds number on flow over an airfoil: as Re decreases, the laminar region grows and flow separation occurs earlier (Barlow ve ark., 1999).

4. SAIL–HULL–KEEL INTERACTION AND HYDRODYNAMIC FORCES

The performance of a sailing yacht is governed not only by sail aerodynamics but also by the interaction between aerodynamic and hydrodynamic forces acting on the hull, keel, rudder, and other underwater appendages. This interaction defines the yacht's overall balance, stability, and propulsion efficiency (Milgram, 1996). Under this heading, the mechanisms of sail–hull–keel interaction are examined, focusing on the formation of hydrodynamic forces, resistance components, and the influence of hull geometry and appendage design on sailing performance. The keel's hydrodynamic lift counteracts the sails' side force; hull resistance components (frictional, wave-making, and induced) govern overall efficiency; and heel and leeway modify flow behavior. A plot of the aerodynamic and hydrodynamic forces acting on a sailing yacht, the interaction between sail lift force, hull resistance, keel side force, and the resulting balance of heel and yaw (leeway) angles in Figure 10. The aerodynamic side force generated by the sails is counteracted by the hydrodynamic lift from the keel and hull, maintaining equilibrium and directional stability (Viola & Flay,

2011). These concepts are critical to understanding the true performance of a sailboat and optimizing its design. Accurate modeling of these phenomena — using CFD, experimental data, and VPP analysis — is essential for optimizing performance and stability.

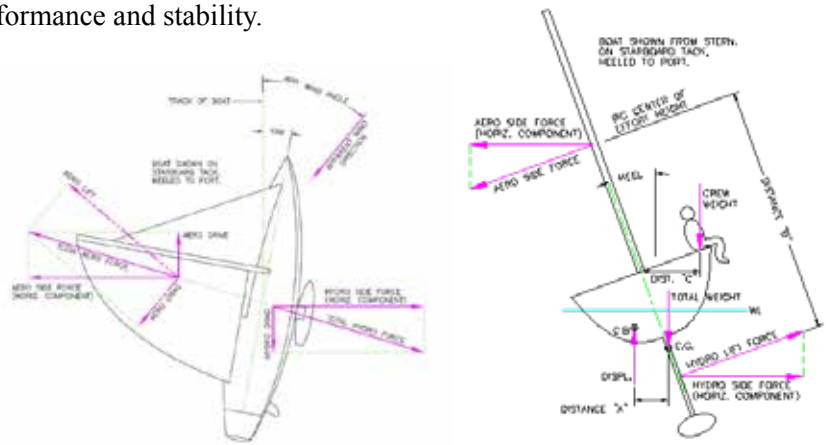

Figure 10**.** Sail–hull–keel interaction and hydrodynamic forces acting on a sailing yacht (Perrotti, 2019)

4.1. Lateral Forces and the Role of the Keel

The aerodynamic side force generated by the sails causes the yacht to drift sideways (leeway). To counteract this motion, the **keel** and **centerboard** generate a **hydrodynamic lift** that resists leeway and maintains directional stability. This lift originates from pressure differences between the two sides of the keel: the flow travels faster along the leeward side, reducing pressure and producing a net force perpendicular to the water flow. The hydrodynamic lift generated by the keel counteracts the lateral aerodynamic force from the sails, maintaining equilibrium and minimizing leeway **(**Figure 10**).** In equilibrium, the aerodynamic side force produced by the sails is balanced by the hydrodynamic lift from the keel and the restoring moment provided by the hull and ballast (Viola & Flay, 2011; Milgram, 1996).

4.2. Components of Hull Resistance

As the yacht moves through the water, it experiences several forms of hydrodynamic resistance:

- **Frictional resistance:** caused by viscous shear stresses along the wetted

surface of the hull.

- **Wave-making resistance:** caused by the generation of surface waves due to hull motion.
- **Induced drag:** created by the formation of vortices at the tips of the keel and rudder as they generate lift.

These resistance components depend on hull form, speed, heel angle, leeway, and appendage geometry. Frictional resistance is roughly proportional to the wetted surface area, while wave-making resistance increases sharply as the yacht approaches its "hull speed." The induced drag associated with the keel is a byproduct of lift generation and plays a major role in high-performance yacht design (Rawson & Tupper, 2001; Milgram, 1996). The main components of hull resistance that frictional, wave-making and induced drag are illustrated in Figure 11.

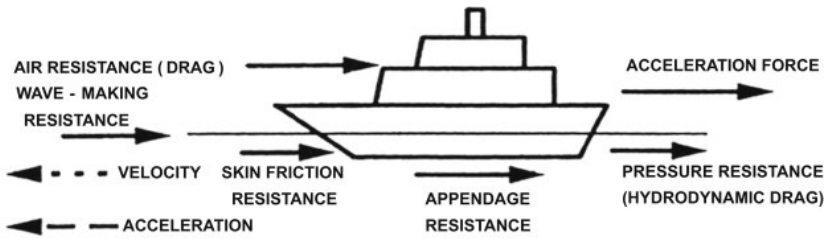

Figure 11. Breakdown of basic hull resistance components (Rawson & Tupper, 2001).

4.3. Sail–Hull Interaction

The pressure distribution around the sails directly affects the loads on the hull and underwater structures. The aerodynamic side force and heeling moment produced by the sails cause the hull to heel, altering the underwater flow pattern and the effective geometry of the submerged surfaces. Experimental and numerical analyses have demonstrated that the **combined modeling of sail and hull** provides significantly more accurate predictions than independent analyses, since flow interactions near the free surface, heel, and leeway strongly influence overall performance (Figure 12). Hull parameters such as beam, waterline length, and draft determine the range of heel angles and apparent wind angles for which the yacht operates most efficiently (Marino ve ark., 2017).

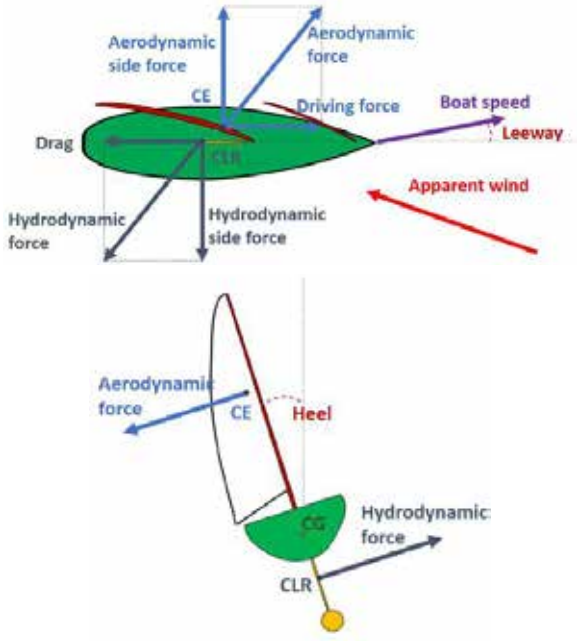

Figure 12. The forces equilibrium of a sailing boat. Top and rear view. CE: centre of e_ort, CG: centre of gravity, CLR: centre of lateral resistance (Kerdraon, 2017)

4.4. Keel Design and Hydrodynamic Lift

The keel performs multiple roles: it generates the side force necessary to resist leeway, contributes to stability by carrying ballast, and assists in directional control in combination with the rudder. High-performance yachts commonly employ **deep, narrow, high-aspect-ratio keels**, which produce greater lift with lower induced drag. Key design parameters include:

- Keel area and aspect ratio
- Cross-sectional foil profile (e.g., NACA series)
- Keel depth and span
- Winglets or tip fins, which reduce induced drag

Numerical simulations indicate that minimizing large-scale vortex formation around the keel reduces induced drag and improves the **lift-to-drag ratio (L/D)** (Mylonas & Sayer, 2012). Optimal design thus seeks to balance minimum wetted area with maximum hydrodynamic efficiency (Milgram, 1996).

4.5. Effects of Heel and Leeway

Heel and leeway have a profound effect on yacht hydrodynamics. As the yacht heels, the effective underwater geometry of the hull changes, altering the distribution of lift and drag forces. Increased heel typically enlarges the wetted surface, increasing viscous resistance. Similarly, excessive leeway alters the angle of attack of the keel and rudder, potentially causing flow separation and vortex shedding, which in turn increase induced drag. Therefore, yacht design aims to minimize these effects through optimized ballast placement, keel depth, and sail trimming strategies.

4.6. Performance Prediction and VPP Modeling

The **Velocity Prediction Program (VPP)** is a computational method used to estimate yacht performance by balancing aerodynamic and hydrodynamic forces. VPP models calculate the equilibrium between sail-generated thrust and hydrodynamic resistance to determine boat speed and optimal sailing angles for various wind conditions. These models integrate experimental and CFD-derived data on hull resistance, keel lift, and sail forces. Parameters such as induced drag, hull shape, and appendage performance significantly affect predicted velocities (Marino ve ark., 2017).

5. NUMERICAL AND EXPERIMENTAL ANALYSIS METHODS

Modern yacht design increasingly relies on the integration of **numerical simulation** and **experimental testing** to optimize both aerodynamic and hydrodynamic performance. The complex interactions among the sails, hull, and appendages cannot be fully understood through analytical models alone. Therefore, computational and experimental methods are used in combination to achieve accurate, validated results. Under this heading the primary numerical and experimental approaches applied in sailing yacht research are outlined and their advantages, limitations, and implementation are discussed in detail. CFD, VPP integration, wind tunnel, and towing tank experiments together form a comprehensive methodology for performance assessment. Combining these methods enables designers to optimize yacht geometry, predict behavior under realistic conditions, and enhance overall efficiency.

5.1. Numerical Simulation Techniques

5.1.1. Computational Fluid Dynamics (CFD) Applications

Computational Fluid Dynamics (CFD) is a powerful tool used to numerically solve fluid flow problems, enabling detailed analysis of aerodynamic and hydrodynamic behavior around yachts. Recent studies, such as those conducted at the University of Edinburgh, simulated downwind sailing at apparent wind angles of 45°, 105°, and 120°, achieving lift and drag predictions within 3% of experimental data (Viola, 2009). Another unsteady RANS (Reynolds-Averaged Navier–Stokes) study compared CFD results with full-scale measurements, showing a deviation of less than 2% (Casalone ve ark., 2020).

The general CFD workflow includes:

- **Geometry modeling:** defining sails, hull, keel, and rudder surfaces.
- **Mesh generation:** creating a grid for the computational domain, ensuring adequate resolution near the free surface (Levadou ve ark., 1998).
- **Boundary and initial conditions:** specifying wind speed, angle of attack, heel, leeway, and wave parameters.
- **Turbulence modeling:** selecting appropriate models such as k–ε or *SST* k–ω (Larsson, 2018).
- **Solver setup and convergence testing.**
- **Post-processing:** extracting lift, drag, pressure fields, vortex structures, and velocity contours.

CFD offers the benefit of simulating multiple design scenarios early in the design process. However, it demands significant computational resources and rigorous validation.

5.1.2. VPP Integration and Six-Degree-of-Freedom Simulations

The **Velocity Prediction Program (VPP)** traditionally relies on empirical relationships between aerodynamic and hydrodynamic forces. Modern approaches integrate **CFD outputs** and **6-DOF (six degrees of freedom)** dynamic simulations — accounting for surge, sway, heave, roll, pitch, and yaw motions — to capture the full dynamic behavior of yachts (Persson, 2025). Such models can simulate free-surface effects, sail deformation, and coupled air–water interactions, enabling more realistic performance predictions under varying sea states.

5.2. Experimental Testing Methods

5.2.1. Wind Tunnel Testing

Wind tunnel experiments are indispensable for validating aerodynamic models and CFD results. Scaled or full-size sail sections are tested at different angles of attack to measure lift and drag coefficients. Experiments reveal the influence of heel angle, sail curvature, and rig tension on aerodynamic forces (Gentry, 1988). The main advantages of wind tunnel testing are the controlled environment and repeatability. However, real-world effects — such as unsteady winds, waves, and hull interaction — cannot be fully replicated (He, 2015).

5.2.2. Towing Tank Testing

Towing tank experiments are conducted to analyze hydrodynamic resistance, wave formation, and hull efficiency. Scaled models of yacht hulls are towed through calm or wavy water to measure drag and lift under controlled conditions. Casalone et al. (2020) demonstrated excellent correlation between towing tank results and unsteady RANS simulations, with less than 2% difference. Although costly and time-consuming, towing tank experiments provide invaluable validation for CFD and VPP models.

5.3. Hybrid Verification and Validation

A hybrid approach combining CFD simulations with experimental data yields the most reliable performance predictions. Discrepancies between CFD and experimental results are analyzed to refine turbulence models, boundary conditions, and mesh resolutions. For example, Viola (2009) reported that increasing mesh density from 1 million to 6.5 million elements changed lift and drag coefficients by less than 3%, confirming CFD accuracy. Such iterative validation ensures that numerical tools can confidently replace or complement physical testing in yacht design.

5.4. Applied Case Studies

- **Autonomous Sailing Systems:** CFD-optimized **wing–tail sail** configurations have been shown to increase lift coefficients by up to **30%** while reducing drag, enhancing maneuverability and energy efficiency (Ding ve ark., 2025).
- **Sail Shape Optimization:** Using CFD-based shape optimization, im-

provements of up to **0.7% in VMG (Velocity Made Good)** have been achieved under wind speeds of 4–8 m/s, illustrating the precision of modern numerical methods (Knudsen, 2013).

These studies confirm that the integration of CFD and experimental methods significantly improves yacht design reliability and performance forecasting.

5.5. Limitations and Future Prospects

Despite their accuracy, both numerical and experimental techniques have inherent limitations:

- **CFD limitations:** computational cost, sensitivity to turbulence modeling, challenges in simulating sail deformation and air–water interface effects.
- **Experimental limitations:** scaling errors, restricted degrees of freedom, and difficulties replicating realistic sea and wind conditions.

Future research trends include:

- **Fluid–Structure Interaction (FSI)** modeling to account for sail flexibility and real-time deformation.
- **Artificial Intelligence (AI) and Machine Learning** for performance prediction and design optimization.
- **Sustainable design applications**, using aerodynamic principles for wind-assisted commercial ships (Souppez, 2024).

6. APPLICATIONS

The knowledge of aerodynamic and hydrodynamic principles presented in the previous topics provides the foundation for designing efficient, stable, and high-performance sailing yachts. This topic focuses on practical applications of these principles — from competitive yacht design to autonomous sailing systems — and concludes with key insights and recommendations for future developments in sailing aerodynamics.

6.1. Applications in Modern Yacht Design

6.1.1. High-Performance Racing Yachts

In professional racing classes such as the *America's Cup* and *IMOCA 60*,

designers integrate **CFD-validated aerodynamic and hydrodynamic simulations** to achieve superior speed and maneuverability (Rosen ve ark., 2000; Viola, 2009). The introduction of **rigid wing sails** and **hydrofoils** has dramatically increased lift-to-drag ratios, enabling yachts to reach speeds exceeding 40 knots while maintaining stability (Silva ve ark., 2019).

By coupling aerodynamic and hydrodynamic modeling, engineers can optimize:

- Sail camber and twist distribution,
- Foil geometry and incidence angle,
- Keel and rudder configuration for dynamic balance.

Such high-precision design processes are supported by *Velocity Prediction Programs (VPP)* that incorporate CFD-generated data and full-scale experimental validation (Soupez, 2024).

6.1.2. Wind-Assisted Commercial Vessels

Beyond competitive sailing, aerodynamic optimization is increasingly applied to **wind-assisted propulsion systems** for commercial ships. Rigid sails, rotor sails (Flettner rotors), and kite systems are used to reduce fuel consumption and greenhouse gas emissions in accordance with the **IMO's decarbonization targets** (Souppez, 2024). CFD-based optimization has shown that hybrid wind–engine configurations can achieve **10–20% reductions in fuel usage**, contributing significantly to sustainable maritime transportation.

6.1.3. Autonomous and Robotic Sailboats

Recent advances in automation and renewable energy have led to the development of **autonomous sailboats** equipped with CFD-optimized **wing–tail systems** and AI-based control algorithms. These vessels are capable of performing long-duration missions such as oceanic environmental monitoring, route optimization, and data collection (Ding ve ark., 2025). The combination of aerodynamic efficiency, low energy consumption, and autonomous operation represents a transformative application of sailing aerodynamics.

6.2. Integration of CFD and Experimental Approaches

Effective design and performance evaluation require the **integration of**

CFD, experimental, and analytical methods. Wind tunnel and towing tank experiments provide essential validation for CFD simulations, while full-scale testing bridges the gap between theoretical predictions and real-world behavior. For instance, combined studies conducted at MARIN and the University of Edinburgh demonstrated deviations of less than **3%** between CFD and experimental results when analyzing downwind sail configurations (Viola, 2009; Casalone ve ark., 2020). This integrated framework forms the backbone of modern yacht research and ensures reliability in both simulation and practice.

6.3. Design Optimization and Performance Enhancement

Optimization in sailing aerodynamics involves balancing multiple, often conflicting objectives, minimizing drag, maximizing lift, maintaining stability, and adhering to design constraints such as weight and material limits.

Modern optimization approaches include:

- **Multi-objective genetic algorithms (MOGA)** for sail shape optimization.
- **Fluid–Structure Interaction (FSI)** analyses for deformable sail modeling.
- **AI and Machine Learning** methods for adaptive control and real-time trim adjustment (Souppez, 2024).

These techniques enable continuous refinement of design parameters, allowing engineers to achieve high-performance results while reducing prototype and testing costs.

7. CONCLUSIONS

This study has systematically examined the aerodynamic and hydrodynamic mechanisms governing sailing yacht performance. The main conclusions can be summarized as follows:

- **Aerodynamic forces** generated by the sails and **hydrodynamic forces** acting on the hull and keel are dynamically interdependent and must be analyzed as a coupled system.
- **CFD and experimental methods** provide a reliable framework for performance prediction and design validation.

- **Optimization of sail and appendage geometry** through integrated numerical–experimental approaches leads to measurable gains in efficiency and speed.
- The **integration of AI and sustainable propulsion systems** marks the next evolutionary step in yacht design and maritime transport.

Ultimately, the aerodynamic science of sailing combines physics, computational modeling, and innovative engineering to transform wind energy into motion — an elegant intersection of nature and technology that continues to inspire advances in fluid mechanics, design, and sustainability.

On the other hand, the future of sailing aerodynamics will be shaped by advances in computational power, sensor technology, and sustainability-driven innovation. Emerging research areas include:

- **Real-time CFD simulation** for on-board performance optimization.
- **Smart materials and morphing sails** capable of actively adjusting their shape in response to wind conditions.
- **AI-based digital twins**, integrating live data and simulation for predictive maintenance and dynamic trimming.
- **Wind-assisted cargo ships** as a key technology in decarbonized maritime transport.

These developments indicate a shift toward **data-driven and adaptive sailing systems**, where aerodynamic understanding becomes the foundation of intelligent, energy-efficient maritime mobility.

REFERENCES

Anderson, B. D. (2003). The physics of sailing explained. Sheridan House.

Anderson, B. D. (2008). The physics of sailing. Physics Today, 61(2), 38–43.

Anderson, J. D. (2010). Fundamentals of aerodynamics (5th ed.). McGraw-Hill Education.

Barlow, J. B., Rae, W. H., & Pope, A. (1999). Low-speed wind tunnel testing. John wiley & sons.

Bayraktar, S., Özdemir, Y. H., & Yılmaz, T. (2007). Computational analysis of wind velocity and direction effects on a sail.

Caraher, S. P., Hobson, G. V., & Platzer, M. F. (2021). Aerodynamic analysis and design of high-performance sails. Modern Ship Engineering, Design and Operati-

ons, 3.

Casalone, P., Dell'Edera, O., Fenu, B., Giorgi, G., Sirigu, S. A., & Mattiazzo, G. (2020). Unsteady RANS CFD simulations of sailboat's hull and comparison with full-scale test. Journal of Marine Science and Engineering, 8(6), 394.

Claughton, A. R., Wellicome, J. F., & Shenoi, R. A. (2006). Sailing yacht design: practice. University of Southampton.

Ding, T., Tian, C., Wang, H., Xu, C., Ye, J., Gong, A., & Xia, T. (2025). Performance enhancement of autonomous sailboats via CFD-optimized wing–tail sail configurations. Journal of Marine Science and Engineering, 13(9), 1640.

Fossati, F. (2009). Aero-hydrodynamics and the performance of sailing yachts: The science behind sailing yachts and their design. A&C Black.

Garcia, J. P. (2019). Polytechnic University of Cartagena, Fluid mechanics course lecture notes.

Gentry, A. E. (1988, November). The application of computational fluid dynamics to sails. In Symposium on Hydrodynamic Performance Enhancement for Marine Applications.

He, J., Hu, Y., Tang, J., & Xue, S. (2015). Research on sail aerodynamics performance and sail-assisted ship stability. Journal of Wind Engineering and Industrial Aerodynamics, 146, 81–89.

HopsonRoad. (2015a). Resolution of total force on sails into lift and drag and forward and lateral force [Diagram]. Wikimedia Commons. https://commons.wikimedia.org/wiki/File:Resolution_of_Total_Force_on_sails_into_Lift_and_Drag_and_Forward_and_Lateral_Force.jpg

HopsonRoad. (2015b). Sail angles of attack and resulting flow patterns [Diagram]. Wikimedia Commons. https://commons.wikimedia.org/wiki/File:Sail_angles_of_attack_and_resulting_flow_patterns.jpg

Izaguirre Alza, P. (2012). Numerical and Experimental Studies of Sail Aerodynamics (Doctoral dissertation, Navales).

Jazzmanian. (2006). Parts of sailboat [Diagram]. Wikimedia Commons. https://commons.wikimedia.org/wiki/File:Parts_of_sailboat.jpg

Kawecki, B., Kulak, M., & Lipian, M. (2024). Wing sails: Numerical analysis of high-performance propulsion systems for a racing yacht. Energies, 17(3), 549.

Kerdraon, P. (2017). Design and models optimisation of asailing yacht dynamic simulator.

Kimball, J. (2009). Physics of sailing. CRC Press.
Larsson, L. (1990). Scientific methods in yacht design. Annual Review of

Fluid Mechanics, 22(1), 349–385.

Knudsen, S. S. (2013). Sail Shape Optimization with CFD.

Larsson, L., Stern, F., & Bertram, V. (2003). Benchmarking of computational fluid dynamics for ship flows: The Gothenburg 2000 workshop. Journal of Ship Research, 47(1), 63–81.

Larsson, L. (2018). Computational fluid dynamics in sailing research. In Proceedings of the SNH2018 Conference. Chalmers University of Technology.

Levadou, M., Prins, H. J., & Raven, H. C. (1998). Application of advanced computational fluid dynamics in yacht design.

Marchaj, C. A. (1979). Aero-hydrodynamics of sailing. Adlard Coles. Milgram, J. H. (1996, June). Hydrodynamics in advanced sailing design. In 21st Symposium on Naval Hydrodynamics (pp. 74–97). Trondheim, Norway.

Marino, A., Tagliaferri, F., & Shi, W. (2017, October). Aerodynamic and hydrodynamic interactions between two yachts sailing upwind. In The 5th International Conference on Advanced Model Measurement Technology for the Maritime Industry.

Milgram, J. H. (1996, June). Hydrodynamics in advanced sailing design. In 21st Symposium on Naval Hydrodynamics. Pre-prints Wednesday and Thursday sessions. Trondheim, Norway (pp. 74-97).

Mylonas, D., & Sayer, P. (2012). The hydrodynamic flow around a yacht keel based on LES and DES. Ocean engineering, 46, 18-32.

NASA Glenn Research Center. (2015). What is Lift? Retrieved from https://www1.grc.nasa.gov/beginners-guide-to-aeronautics/what-is-lift/

Perrotti, T. J. (2019). Balance. The Model Yacht, 20, 2.

Persson, A. (2025). Predicting yacht performance in waves using a CFD velocity prediction program.

Petinrin, M. O., & Onoja, V. A. (2017). Computational study of aerodynamic flow over NACA 4412 airfoil. British Journal of Applied Science & Technology, 21(3), 1-11.

Rawson, K. J., & Tupper, E. C. (2001). Basic ship theory: Hydrostatics and strength (Vol. 1). Butterworth-Heinemann.

Rosen, B., Laiosa, J., & Davis, Jr, W. (2000). CFD design studies for America's Cup 2000. In 18th Applied Aerodynamics Conference (p. 4339).

Silva, M. F., Friebe, A., Malheiro, B., Guedes, P., Ferreira, P., & Waller, M. (2019).

Rigid wing sailboats: A state-of-the-art survey. Ocean Engineering, 187, 106150.

Slooff, J. W. (2015). The aero- and hydromechanics of keel yachts. Springer. Souppez, J. B. R. (2024). Recent advances in wind-assisted ship and yacht sail aerodynamics. Journal of Marine Science and Engineering, 12(4), 722.

Viola, I. M. (2009). Downwind sail aerodynamics: A CFD investigation with high grid resolution. Ocean Engineering, 36(12–13), 974–984.

Viola, I. M. (2013). Recent advances in sailing yacht aerodynamics. Applied Mechanics Reviews, 65(4), 040801.

Viola, I. M., & Flay, R. G. (2011). Sail aerodynamics: Understanding pressure distributions on upwind sails. Experimental Thermal and Fluid Science, 35(8), 1497–1504.

Weltner, K. (1987). A comparison of explanations of the aerodynamic lifting force. American Journal of Physics, 55(1), 50–54.

Wilson, R. M. (2010). The physics of sailing. JILA and Department of Physics, University of Colorado.

CHAPTER 9

ELECTRIC VEHICLE CHARGING STATIONS

Serhat ERYAMAN
Istanbul University-Cerrahpasa, Institute of Graduate Studies, Department of Electrical - Electronics Engineering
https://orcid.org/0000-0002-5090-4388

Prof. Dr. Cengiz Polat UZUNOGLU
Istanbul University-Cerrahpasa, Engineering Faculty, Department of Electrical - Electronics Engineering
https://orcid.org/0000-0002-4891-3963

1. INTRODUCTION

The global proliferation of electric vehicles (EVs) is of strategic importance in terms of reducing transport-related emissions, improving urban air quality and efficiency improvement of power systems. The pace of this transformation is determined by the technical adequacy of the electric vehicle charging station (EVCS) infrastructure, the availability of charging rate options (AC Level 1–2, DC fast, XFC), and the integration of systems with sustainable energy sources [1]. Recent literature highlights both power electronics solutions that meet fast charging requirements and the integration of photovoltaic (PV) based generation with battery energy storage systems (BESS). PV-first feeding aims to reduce grid dependency while balancing the pressure that fast charging can place on the grid [2].

EVCS architectures offer a wide design space with on-grid, off-grid and hybrid (PV/FC/BESS) options. In addition to PV, the use of fuel cells (FC) ensures continuity by maintaining DC bus voltage balance during low radiation or

night-time hours; field applications have demonstrated DC fast charging at 48 V–200 A using boost converters, MPPT, and variable chargers [3]. On the other hand, vehicle-to-grid (V2G) capability increases grid flexibility by providing ancillary services (e.g. active power support during peak hours) with bidirectional power flow; it has been reported that V2G contributes to load balancing in daily operation in experimentally installed PV-based stations containing bidirectional DC-DC and bidirectional DC-AC inverters [4].

The expansion of charging infrastructure also brings power quality (PQ) issues. Fast charging devices with non-linear load characteristics generate harmonics; therefore, PQ and synchronous reference frame (SRF) approaches based on active power filters (APF) have been shown to be effective in improving PQ [5]. In parallel, reactive power compensation (Q-comp) with voltage source converter (VSC) control has been implemented in three-phase grid-connected PV-EVCS configurations to ensure current quality within IEEE-519 limits, even under unbalanced/distorted grid conditions. The same structure also enables simultaneous active-reactive power management in G2V/V2G modes [6].

On the operational side, load management supported by energy management systems (EMS) and local energy market (LEM) designs are prominent. Station load can be limited with constant/variable current-based slot control; waiting times and grid demand can be balanced by implementing inter-station quota sharing with blockchain and smart contract-supported local capacity markets [7]. Sizing & siting and techno-economic assessments, meanwhile, demonstrate the benefits of PV-BESS hybrids, such as peak power reduction, peak shaving and load levelling, in a cost-effective manner; the combined design of single-axis tracking PV, multi-hour BESS and bidirectional converter layers plays a key role in this regard [8].

On the source side, maximum power point tracking (MPPT) is critical for managing variability in field conditions. Advanced algorithms such as Fuzzy MPPT have been reported to increase energy harvested from PV, improve stability under irradiance-temperature variability, and enable more balanced power transfer to the grid [9]. Furthermore, simulation-based studies using MATLAB/Simulink and facility planning tools (e.g. SIMARIS) demonstrate that EVCS performance and grid integration can be systematically optimised and quantitatively reveal the contribution of harmonic mitigation and control strategies to station efficiency [10].

2. CHARGING TECHNOLOGIES AND LEVELS

In electric vehicle (EV) charging infrastructure, charging rate and charging technology choices are decisive in terms of user experience (charging time), grid impacts (instantaneous power demand), power electronics design (converter topologies), and safety/standard compliance. The literature commonly categorises charging into AC Level 1–2 (on-board charging), DC fast and extreme fast charging (XFC) (off-board, high-power charging). As power and current levels increase, thermal management, cable/connector and EMC/PQ requirements become more stringent [1]. Particularly, DC fast charging solutions in the 20–350 kW range and XFC solutions above 350 kW accelerate widespread EV adoption by reducing charging time to minutes, while also tightening the boundary conditions for grid and station-internal DC bus design [1,2].

AC Level 1–2 solutions utilise single-phase/split-phase AC power supply via an on-board charger; typical power ratings range from 1.4–19.2 kW. These levels offer a cost-effective solution for residential/private applications, while applying a softer load profile to the grid with long state of charge (SoC) recovery times and low demand power [1]. On the DC fast/XFC side, off-board power electronics (e.g. bidirectional DC-DC + VSI) are used to operate at voltage levels of 300–800 Vdc (and ≥1000 Vdc in XFC), enabling high currents; this approach lightens the vehicle, transfers heat to the station side, and pushes issues such as thermal derating and current sharing to the station design [1,2]. In advanced stations, the impact of fast/XFC demand on the grid can be mitigated with PV-priority energy flow, battery energy storage system (BESS) buffering, and dynamic power source management algorithms [2].

Vehicle-to-grid (V2G) capability is naturally compatible with DC fast charging architectures: The bidirectional DC-DC and bidirectional DC-AC inverter layers located at the station enable bidirectional power flow, providing active/reactive support to the grid during peak hours; experimental stations have demonstrated the contribution of this architecture to load balancing in daily operation [4]. In this context, the choice of connector/standard (e.g. IEC 61851, IEC 62196, SAE J1772) determines AC or DC suitability depending on the charging level, permitted current/voltage ranges, and communication/protection requirements [1].

Table 1. Typical power/supply/usage summary by charge level [1].

Charge Level	Typical Power	Type of Supply	Charging Device	Typical Use
AC Level 1	1.44–1.9 kW	120/230 Vac, single-phase	On-board (slow)	Residental
AC Level 2	3.1–19.2 kW	208/240 Vac, single/split-phase	On-board (semi-fast)	Private / corporate
DC fast	20–350 kW	300–800 Vdc, rectification from three-phase AC	Off-board (fast)	Commercial / long haul
XFC	>350 kW	≥1000 Vdc, polyphase infrastructure	Off-board (ultra-fast)	Motorway corridors

At AC Level 1–2, on-board kW-level powers determine the vehicle's thermal management and power factor conditions, while in DC fast/XFC, control performance indicators such as converter efficiency, low overshoot, and low steady-state error become critical at off-board powers of hundreds of kW. For example, in a DC fast charging structure using a chaotic dragonfly optimised PI with a modified bidirectional Zeta-KY converter, ~97% efficiency and a 0.10 s settling time can be achieved in boost/buck modes [2]. At high DC power levels, cable ampacity, connector temperature rise, fault clearing times, and insulation coordination requirements also increase; bidirectionality in V2G operation further tightens these requirements [1,2,4].

Hybrid (PV/FC/BESS) powered stations have demonstrated uninterrupted fast charging capability by utilising boost converter + MPPT and variable DC charger (e.g. 48 V, 200 A) structures to sustain DC bus voltage under low irradiation/night conditions [3]. In PV-dominant fast charging facilities, the demand charge effect is reduced through PV-priority control and BESS buffering, while dynamic power source management algorithms regulate power flow from the grid to the station/from the station to the grid according to operational constraints [2].

3. CHARGING STATION ARCHITECTURES

Electric vehicle charging station (EVCS) architectures are categorised into three main classes based on the power supply, DC bus topology, bidirectional power flow requirements, energy management system (EMS), and interaction with the grid: on-grid, off-grid, and hybrid. Architecture selection is determined by the target charging rate (AC Level 1–2, DC fast, XFC), site constraints (grid access, climate, space), power quality (PQ) and ancillary services requirements, as well as total cost of ownership [1,2]. On-grid systems synchronise with the grid via a voltage source converter (VSC) at the point of common coupling (PCC), while off-grid systems operate in islanded mode with photovoltaic (PV) + battery energy storage system (BESS) (or fuel cell (FC)). Hybrid architectures combine the advantages of both worlds with PV-priority energy flow, dynamic power source management and/or V2G/V2H support [2–4].

In three-phase PV-based stations, VSC control provides both G2V/V2G active power flow and reactive power compensation (Q-comp); operation within IEEE-519 current limits has been demonstrated even under degraded/unstable grid conditions [6]. On-grid fast charging stations transfer PV production to the DC link via DC-DC (e.g. boost) with MPPT; bidirectional DC-DC manages bidirectional power flow between the EV battery and the grid via a bidirectional DC-AC inverter [2]. This structure is suitable for supporting the grid during peak hours and reducing demand charges [1,2,6].

Off-grid stations operate independently using PV + BESS (or supercapacitor). Maximum power is drawn from the PV using MPPT; the BDDC (bidirectional DC-DC) manages charging/discharging between the EV battery and the DC bus, as well as DC bus voltage regulation. This architecture has demonstrated reliable charging with PV-BESS alone in field applications; MATLAB/Simulink-based design-simulation studies validate stable operation under different irradiation/temperature and load scenarios [11,12].

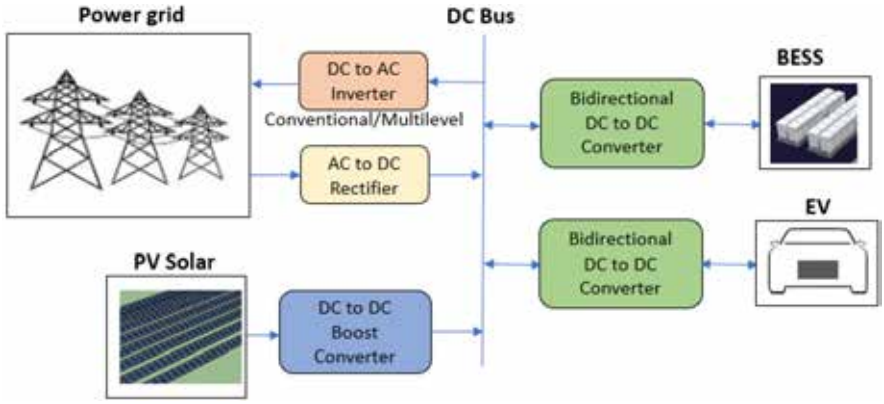

Figure 1. General block diagram of the PV-BESS-Grid-supported EVCS [8].

The hybrid station buffers variable PV production with BESS while maintaining DC bus balance by engaging the FC during low irradiation/night hours. In experimental setups, fast charging at 48 V–200 A was achieved using a boost converter + MPPT for PV, an FC converter for the fuel cell, and a variable DC charger [3]. In large-scale installations, peak shaving/load levelling effects have been reported with single-axis tracking PV and multi-hour BESS; grid feedback (surplus export) has been achieved with bidirectional converter layers [8]. Advanced control strategies such as chaotic-dragonfly optimised PI provide low overshoot, short settling time, and high converter efficiency in hybrid systems [2].

In hybrid/on-grid structures, bidirectional power flow with V2G can be utilised for ancillary services (active/reactive power, voltage support). In experimental V2G stations, load balancing and PV profile integration into the grid have been demonstrated in daily operation [4,6]. In multi-station systems, EMS regulates inter-station capacity exchange through constant/variable current slot control, local energy market (LEM), and smart contract-based quota sharing, thereby reducing queues and grid demand [7].

Layers common to architectures:

- PV-side DC-DC (with MPPT)
- BESS with BDDC
- DC fast/XFC interface for EV connection (mostly off-board)
- On-grid is an AC interface with VSC + LC filter.

Connector/standard selection and voltage-current ranges (e.g. 300–800 Vdc; ≥1000 Vdc in XFC) determine the architecture's cabling, thermal management and protection coordination [1,2].

4. POWER ELECTRONICS TOPOLOGIES

Electric vehicle charging station (EVCS) power layer:

- MPPT-equipped DC-DC converter for the PV/FC side,
- Bidirectional DC-DC converter (isolated/non-isolated) between the EV battery and the DC bus,
- Voltage source converter (VSC) and rectifier/inverter stages for the grid interface,
- It consists of filtering and protection units.

Topology selection is determined based on the target charging rate (AC L1–L2, DC fast, XFC), V2G requirement (bidirectional power), power quality (PQ), efficiency/thermal limits, and standard compliance [1,2,6].

To manage the variability of PV production, boost converters + MPPT are commonly used; in field studies, the continuity of fast charging has been ensured by regulating the DC bus voltage with the boost stage [3,11]. Advanced fuzzy MPPT approaches particularly increase power harvesting and improve DC link stability in radiation/temperature variability [9]. In hybrid stations, the fuel cell (FC) converter supplements PV during low irradiation/night-time to maintain DC bus balance [3].

Bidirectional DC-DC is mandatory for fast charging with V2G/G2V support.

- Non-isolated solutions: Buck-boost, Cuk/SEPIC/Zeta-KY derivatives provide low cost and high-power density; with control optimisations, low overshoot, short settling time and ~97% efficiency have been reported [2].
- Isolated solutions: Soft-switching structures such as Dual-Active-Bridge (DAB), phase-shifted full-bridge, and LLC are preferred for high voltage levels and safe isolation (especially in the XFC class) [2].

In this layer, interleaving/current sharing, thermal management and fault-tolerant design become critical due to cable/connector heating and ampacity requirements at currents of hundreds of amps [1,2].

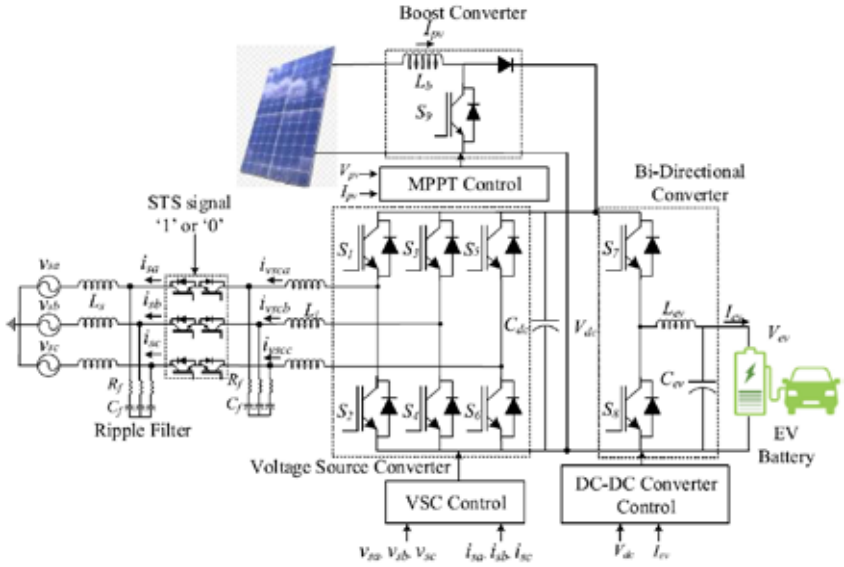

Figure 2. EVCS power layers: PV/FC MPPT-Boost, BDDC (EV/BESS), VSC-grid interface [6].

In on-grid stations, synchronisation is achieved via PCC using a three-phase VSC, providing both active power flow and reactive power compensation (Q-comp). In experimental studies, current harmonics were maintained within IEEE-519 limits even under unbalanced/distorted grid conditions [6]. In DC fast/XFC architectures, front-end PWM rectifiers or VSC-based two/three-level topologies (2-Level, NPC/T-type) with L/LCL filtering are used; bidirectional DC-AC enables V2G [2,6]. From a PQ perspective, harmonics from non-linear load charging devices are suppressed using APF approaches (P-Q, SRF) [5,6].

The battery energy storage system (BESS) connects to the DC bus via BDDC and supports peak shaving/load levelling and surplus export functions; economic/operational gains have been reported in large-scale installations with single-axis tracking PV and multi-hour BESS [8]. EMS manages coordination between converters while observing constraints such as PV priority, source switching, and current limits [1,2].

5. MPPT AND ENERGY MANAGEMENT

Maximum power point tracking (MPPT) and energy management system (EMS) are core functions that determine both DC bus stability and grid effects in photovoltaic (PV)-based or hybrid (PV/FC/BESS) electric vehicle charging station (EVCS) architectures. The MPPT layer extracts maximum power from the PV under variable irradiation/temperature conditions; the EMS coordinates PV-priority, BESS buffering, fuel cell (FC) engagement, G2V/V2G transitions, slot-based constant/variable current control, and local energy market (LEM) interaction [1,2,7,8].

In practice, P&O and incremental conductance (INC) are widely used and see extensive application due to their low computational load; fuzzy MPPT and ANN-based methods, however, provide higher tracking accuracy and less fluctuation under irradiance/temperature variability, thereby improving DC link ripple and converter response [4,9,11]. Experimental/simulation-based studies show that fuzzy MPPT provides additional harvest and stability gains compared to classical methods, while P&O/INC offers advantages in terms of simplicity/applicability [4,9,11]. In hybrid stations, the MPPT-boost chain transfers PV power to the DC bus, while the FC converter is activated under low irradiation or night conditions to maintain bus voltage [3,8].

Table 2. Comparison of MPPT methods: tracking accuracy, dynamic response and ease of implementation [4,9,11].

MPPT method	**Tracking accuracy**	**Dynamic response (irradiance change)**	**Application complexity**	**Typical usage**
P&O	Medium	Medium (prone to fluctuation)	Low	Education/ experiment, small-medium PV
INC	Medium-High	Medium-High	Medium	Grid-connected PV, medium-to-large power
Fuzzy MPPT	High	High (more stable)	Medium-High (rule base required)	Rapidly changing environment, EVCS-PV

EMS:

- PV → DC bus power flow (MPPT output),
- BESS ↔ DC bus bidirectional DC-DC (BDDC) control (SoC, peak shaving, load levelling),
- EV ↔ DC bus BDDC control (charge/discharge current and SoC targets),
- Active/reactive power exchange with the grid via VSC,
- LEM/blockchain-based capacity sharing and quota sharing implement high-level decisions in real time [1,2,6–8].

Simulation-based studies have numerically demonstrated the effect of MPPT-EMS coordination on harmonic mitigation, efficiency, and reliability using MATLAB/Simulink and planning tools (e.g. SIMARIS) [10]. In on-grid PV-EVCS configurations, reactive power compensation (Q-comp) with VSC control and current quality within IEEE-519 limits in unbalanced/distorted grids are achieved, while EMS integrates this control with resource planning [6].

Load management and market interaction. In multi-point station topologies, slot-based current reduction/shutdown strategies using constant current/variable current methods aim to meet charging deadline constraints without exceeding grid limits; inter-station capacity exchange (surplus/deficit) is executed at the upper level using blockchain and smart contract-based LEM with iterative market clearing procedures [7]. This structure reduces demand charge effects while lowering waiting times and dampens grid peak demands in conjunction with PV/BESS usage [1,2,7,8].

6. GRID INTEGRATION AND V2G/V2H

Grid integration; vehicle-to-grid (V2G)/vehicle-to-home (V2H) functions rely on the coordinated operation of bidirectional DC-DC and bidirectional DC-AC inverter (VSC-based) layers. The station synchronised to the grid via the point of common coupling (PCC) charges the EV battery in G2V mode; in V2G/V2H modes, it can provide active power export and reactive power compensation (Q-comp) ancillary services [6]. Experimental and field-validated studies have demonstrated that the three-phase PV-EVCS architecture remains within IEEE-519 current limits even under unbalanced/distorted grid conditions and achieves simultaneous active-reactive power management [6]. In V2G designs, the station-side PV-MPPT + bidirectional DC-DC + bidirec-

tional inverter chain enables PV-priority operation during daylight hours when PV is dominant; during cloudy/night conditions, it enables grid interaction with the BESS buffer [1,4,8].

In V2G, VSC current references are derived based on active power (P) and reactive power (Q) targets; SRF-based current/voltage separation and PCC synchronisation via PLL are achieved. This enables:

- Active power export for peak shaving/load levelling,
- Voltage regulation for Q-comp,
- Current shaping is possible for harmonic mitigation [6].

Due to the non-linear load characteristics of fast charging, harmonics are suppressed using the APF approach (P-Q, SRF) to reduce grid impacts [5,6]. The EMS layer manages G2V/V2G/V2H transitions, along with grid contract limits, while considering SoC and charging deadline constraints; in multi-station structures, inter-station capacity exchange can be implemented using the local energy market (LEM) and quota sharing [1,7].

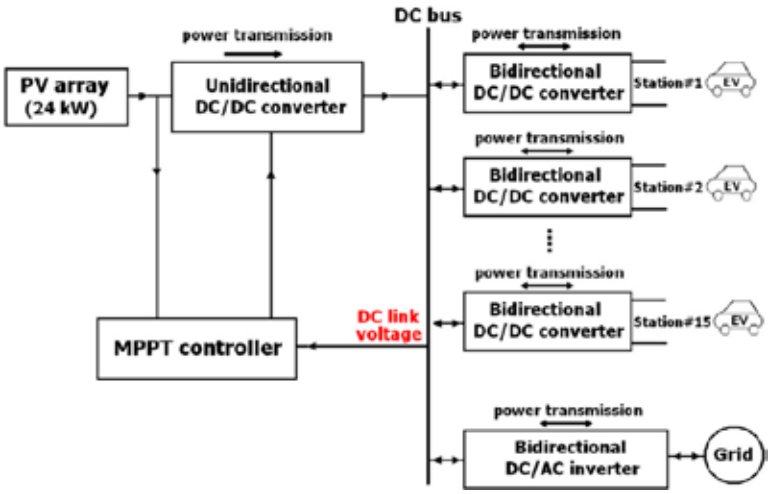

Figure 3. General diagram of bidirectional power flow for V2G/V2H [4].

V2H is a variant of V2G at the home microgrid/home energy management scale: via a bidirectional charger, the EV battery can supply home loads in island mode or provide power to reduce the home's grid draw according to time-of-use tariffs. In this case, the same VSC and BDDC structure is connected to the in-home AC bus instead of the PCC; control targets are updated according to load priorities [4,6].

In MW-scale PV-BESS-V2G installations, scenarios involving surplus export, demand charge reduction, and local grid support using single-axis tracking PV and multi-hour BESS have been reported [8]. Simulation-based studies (MATLAB/Simulink and facility planning tools) reveal the quantitative effects of V2G/V2H strategies on charging station efficiency, reliability, and grid integration [10]. Furthermore, hybrid (PV/FC/BESS) architectures enhance V2G/V2H continuity by maintaining DC bus balance with fuel cell (FC) support during low irradiation/night conditions [1,3,8].

7. POWER QUALITY AND HARMONIC REDUCTION

Electric vehicle charging station (EVCS) power stages exhibit non-linear load characteristics, particularly in DC fast/XFC modes, leading to power quality (PQ) issues such as current/voltage harmonics, power factor distortion and unbalance. The literature indicates that these effects can be effectively suppressed using shunt active power filters (SAPF) with P–Q (instantaneous reactive power) and synchronous reference frame (SRF) based control, ensuring compliance with IEEE-519 limits [5,6]. In grid-connected PV-EVCS architectures, the voltage source converter (VSC) also performs reactive power compensation (Q-comp), approximating the PCC current to a sinusoidal waveform; even with unbalanced/distorted voltages, synchronous and low total demand distortion (TDD) currents can be produced using positive-sequence extraction and SRF-PLL [6]. Simulation-based studies quantitatively report the harmonic mitigation effect of these strategies and their contribution to station efficiency [10].

Table 3. Qualitative comparison of active filtering approaches (P–Q and SRF) in EVCS [5,6].

Criteria	P–Q based SAPF	SRF based SAPF
Transformation	Clarke (αβ)	Park (dq) + positive series
Calculation load	Low–Medium	Medium (PLL, sequence separation)
Unbalance/ Distortion resistance	Medium (additional measures may be required)	High (with positive series/PLL)

Q-comp integration	Possible (with p–q separation)	Directly (with reference to i_q)
THD reduction effect	High (proven in multiple charges) [5]	High (IEEE-519 compliant) [6]
Application field	Multi-directional loaded stations	Three-phase PV-EVCS, V2G supported

The Clarke (αβ0) transformation is used to generate a compensating current reference from the instantaneous p–q components; this is injected into the abc space via inverse Clarke transformation using hysteresis/PR current controllers. Current harmonics are significantly reduced even with multiple chargers; a marked decrease in THD has been reported in comparisons with/without APF [5]. The method is applicable in real time with a light computational load (measurement + matrix operations).

The fundamental components are separated into DC and AC (2ω, 6ω, …) components using the Park (dq0) transformation; selective filtering is performed using LPF/HPF and compensating current is generated. Under unbalance/distortion, positive-sequence voltage estimation is added to precisely determine the i_d–i_q current references; PCC current quality is brought within IEEE-519 limits and simultaneous Q-comp is possible [6]. In high-power stations, high bandwidth is achieved with LCL filters and carrier-based PWM.

EMS adjusts the G2V/V2G flow while observing SoC/deadline constraints and current limit/ramp rate and demand charge limits; on the VSC side, network current shaping is performed through peak shaving/load levelling by coordinating P/Q targets and APF references [6,10]. This softens the instantaneous demand of fast charging with the BESS buffer; in PV-priority situations, DC bus fluctuations are reduced with MPPT-controlled power transfer [1,10].

RCD/MCB coordination, thermal monitoring, and fast fault clearing times for overcurrent should be reviewed to mitigate risks associated with harmonic-induced RMS heating, neutral/PE currents, and transformer derating. Interleaved BDDC, appropriate LC/DC-link sizing, and current sharing are recommended to limit the effect of high-frequency ripple on BESS ageing [1,6]. PCC measurements (current/voltage THD, TDD, PF) and event logging are essential for continuous PQ performance; simulation-based planning should be completed with field validation tests [10].

8. REACTIVE POWER SUPPORT AND VOLTAGE STABILITY

In grid-connected EVCS architectures, the voltage source converter (VSC) undertakes both reactive power compensation (Q-comp) and selective harmonic mitigation tasks to improve the point of common coupling (PCC) voltage profile. Particularly in DC fast/XFC operation, sudden active power fluctuations increase bus voltage regulation and feeder voltage rise risks; therefore, the combined use of Q-control (constant Q, Volt–Var droop, P–Q simultaneous optimisation) and SRF-PLL-based synchronisation is recommended [6]. In three-phase PV-based stations, IEEE-519 current limits are maintained even under unbalanced/distorted grid conditions thanks to the separation of i_d–i_q current references via positive-sequence extraction, while simultaneous P/Q management has been successfully demonstrated in V2G/G2V modes [6]. EMS dynamically updates Q-setpoint allocation and Volt–Var curve parameters, considering PV-priority, BESS buffering, and SoC constraints; in MW-scale installations, this coordination integrates with peak shaving/load levelling and surplus export strategies [1,8,10].

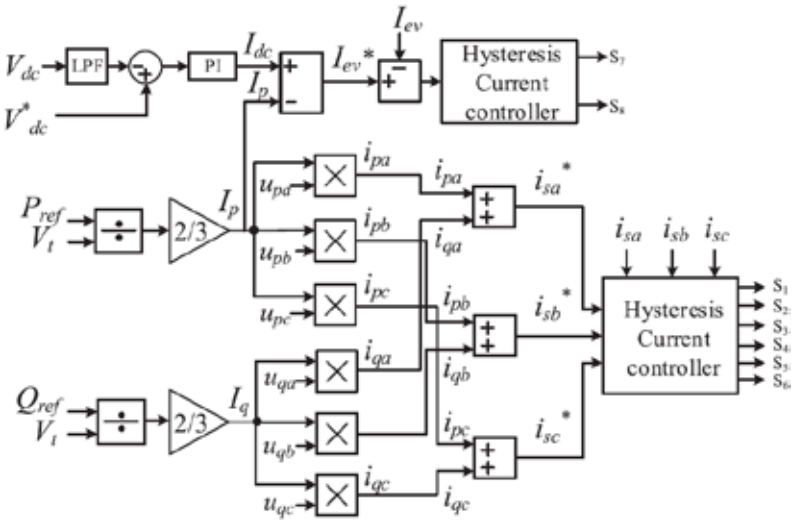

Figure 4. Block diagram of reactive power (Q) control based on VSC [6].

Control approaches:

- Fixed-Q/Power factor control: A method that respects current limits during high demand charge periods and has a low calculated load; the PF target directly determines the i_q reference [6].
- Volt–Var (Q(V)) droop: Local voltage support is provided by defining

the slope between the PCC voltage and Q; it is effective in limiting feeder voltage and works in harmony with neighbouring stations [1,6].

- P–Q simultaneous control: During V2G, active power export and Q-comp are performed simultaneously; i_d/i_q sharing is updated by the EMS under current limit/thermal derating constraints [6,10].

In PV/FC/BESS hybrid systems, while the DC bus stability is maintained with the FC converter under low irradiation/night conditions, the BESS is used for ramp rate smoothing and short-term Q support [3,8]. Planning studies have reported that the combination of single-axis tracking PV + multi-hour BESS contributes to both demand charge reduction and voltage deviation limitation [8,10]. At the field/validation level, voltage/synchronisation stability has been maintained under unbalanced conditions with the Q-comp capability of the VSC [6].

During Q-comp, current limits and junction temperature limits must not be exceeded; overvoltage and EMI risk should be reduced through LCL filter design and dv/dt control. Islanding detection and fast fault clearing times are important for safe separation in V2G mode. Continuous measurement of PCC voltage and currents (V, THD/TDD, PF) and adaptation of Volt–Var parameters are necessary for long-term voltage stability [1,6,10].

9. PROTECTION, SAFETY AND STANDARDS

Safety, protection, EMC and standard compliance in electric vehicle charging station (EVCS) installations are essential for both user safety and grid-compatible, sustainable operation. The standard framework includes IEC 61851 (charging modes/operation), IEC 62196/SAE J1772 (plug/connector and interface), IEEE-519 (current-voltage harmonic limits), and, in grid-connected architectures, reactive power compensation (Q-comp) and power quality conditions on the VSC side [1,6,13].

IEC 61851 defines charging modes and operational coordination (AC Level 1–2, DC fast/XFC); IEC 62196/SAE J1772 specifies connector types, permitted voltage/current ranges, and communication/protection requirements. The Sustainable Charging Stations study compiles Level 1–2–3/XFC power levels and socket/connector types; interface requirements that reduce charging time to minutes for DC connectors at ≥350–400 kW power levels [1]. The selection of these interfaces directly affects ampacity, temperature rise, insulation, and fault clearing times [1,13].

In on-grid PV-EVCS systems, when connecting to the grid via the point of common coupling (PCC) using a voltage source converter (VSC), the over-current (MCB/Breaker), residual current (particularly DC leakage detection), surge protection device (SPD), earthing, and islanding detection layers must work in coordination. In three-phase experimental verification, it has been demonstrated that compliance with IEEE-519 current limits is achieved even in unbalanced/distorted grids with VSC control, and that the voltage profile is improved with simultaneous Q-comp [6]. The technological overview study details safety-focused design criteria such as insulation coordination, clearance/creepage, touch voltage limits, thermal management, and connector derating in high-power DC fast/XFC applications [13].

Table 4. Basic standard–scope–implementation mapping for EVCS [1,6,13].

Standard	Scope	Application
IEC 61851	Charging modes, operation and protection coordination	AC L1–L2, DC fast/XFC; communication and security requirements [1]
IEC 62196 / SAE J1772	Socket/connector types, voltage-current limits	Type 1/2, CCS/CHAdeMO, etc.; ampacity, temperature rise and pin configuration [1]
IEEE-519	Harmonic limits (current/voltage)	PCC current quality; operation compatible with APF/VSC [6]
EMC/Isolation (design criteria)	dv/dt, common-mode, clearance/creepage, touch voltage	Filtered/shielded cable/grounding, insulation coordination, thermal safety [13]

The non-linear load characteristics of fast charging converters generate harmonics; PCC currents are approximated to sinusoidal waves using P–Q/SRF-based current shaping and active power filter (APF) approaches, with TDD/THD levels maintained within IEEE-519 [1,6]. From an EMC perspective, high dv/dt and common-mode currents must be controlled through appropriate L/LCL filtering, shielded cabling, and grounding architecture [13].

Lock-out/Tag-out (LOTO) procedures, remote software updates, and fa-

il-safe modes are mandatory in bidirectional DC-DC/DC-AC layers operating with BESS and EV. Thermal monitoring, current limit and derating curves in high current circuits; connector/cable thermal safety is implemented by the operating software [1,13]. Rapid disconnection in islanding situations, interlock conditions during transitions between G2V/V2G modes, and SoC/voltage mapping are considered critical for safety [6,13].

10. MEASUREMENT, BILLING AND SMART CONTRACTS

Accurate metering and reliable billing in electric vehicle charging station (EVCS) operations are critical for both user transparency and the station's revenue/verification processes. Advanced metering infrastructure (AMI) in practice:

- Energy measurement (grid, PV, BESS, EV output),
- Identity/authentication (RFID/APP),
- Automated billing,
- Combines remote monitoring and reporting chains [14].

The literature reports that automatic billing architecture can be successfully implemented in PV-based stations; measurement and data collection layers are integrated with IoT-based cloud services to automatically execute charge session initiation/termination and fee calculation processes [12,14]. In multi-point networks, load management with local energy market (LEM) frameworks and smart contract applications provide a framework for capacity sharing and tariff automation [1,7].

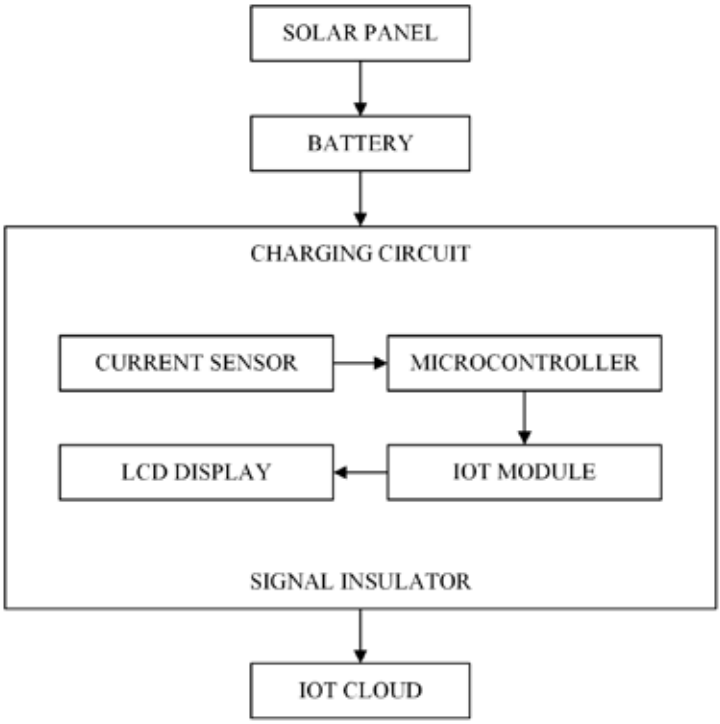

Figure 5. Automatic billing data flow diagram [14].

AMI separates the measurement of grid input (imported/exported energy), PV production, BESS charge/discharge meters, and EV output; thereby ensuring the station's income-expense balance and the energy unit price to be reflected to the user are consistent in net metering-like scenarios [8,14]. Simulation-based studies show that this separation facilitates the numerical tracking of costs and grid impacts when considered alongside station performance indicators (e.g. demand charge effect, peak shaving) [10]. In Smart EVCS applications, IoT components such as NodeMCU/ESP8266 have been used to remotely monitor and report battery SoC, instantaneous power/energy, and session status to the user [12].

In the automatic billing workflow, the user authenticates their identity via RFID/APP; the tariff engine (time-based, power-constrained, dynamic, or LEM-based) determines the unit price; the bill is generated using measurement data (kWh, duration, maximum power) and billing rules [7,14]. In BESS-buffered and PV-priority stations, tariff optimisation directly reflects billing because the demand charge effect can be reduced with peak shaving/load levelling [8,10]. In multi-station networks, LEM + smart contract designs, combined

with quota sharing and constraint management (e.g. grid contract power, current limits), enable autonomous closure of session-based costs [7].

Data integrity (measurement timestamp, time synchronisation), privacy (user data), business continuity (offline/edge recording), and falsification/loss (completeness checks) processes are considered critical in the measurement-billing chain [14]. Since harmonic currents and transients caused by non-linear loads in high-power fast charging can affect measurement accuracy, measurement points and filtering architecture should be planned in accordance with PQ requirements [1,10].

11. PROJECT PLANNING: DIMENSIONING, SITE SELECTION AND ECONOMIC ANALYSIS

The design of an electric vehicle charging station (EVCS) is a comprehensive engineering problem that addresses load demand and charger mix (AC L2, DC fast, XFC), PV–BESS sizing, DC bus/power electronics selection, grid connection, site constraints, and economic feasibility.

The starting point of the design is to derive daily/weekly kWh and instantaneous kW demand profiles, considering the effects of simultaneity and diversity. The number of DC fast/XFC points and AC L2 points is determined based on the expected fleet/visitor profile. This stage is integrated with demand charge management (peak limiting) for on-grid stations, PV priority and BESS buffer targets [8,10,15].

In on-grid scenarios, PV power is matched with the intraday distribution of charging demand and peak sun hours (PSH); BESS capacity (kWh) and duration (hours) are selected based on peak shaving/load levelling and tariff/demand charge targets. In a large-scale example, a 5 MWp PV and 4-hour BESS integration with single-axis tracking has been designed with surplus export capability and grid support [8]. In off-grid light EV stations, PV-BESS is determined based on target autonomy and night/low irradiation requirements; in stand-alone feasibility studies, climate/irradiation profile, LCOE, and logistical constraints directly influence sizing [16,17].

Table 5. Example design parameters and planning headings [8,15-17].

Title	**On-grid PV-EVCS (e.g.) [8,15]**	**Off-grid / Light EV (e.g.) [16]**	**Stand-alone Feasibility (e.g.) [17]**
Load/ Demand	AC L2 + DC fast hybrid; peak limiting	Low-medium power light EV load	Limited power according to local demand
PV	5 MWp (single-axis), GCR ≈ 36%, low mutual shading [8]	Elected with the goal of PSH and autonomy	High PSH climate advantage
BESS	4-hour configuration (peak/load balancing) [8]	Capacity to cover night/closed weather periods	Autonomy/ LCOE optimisation
Power Electronics	MPPT-boost, BDDC (EV/BESS), VSC/ PWM rectifier [8,15]	MPPT-boost + BDDC, island mode	Island operation-focused topology
DC Bus	300–800 Vdc (with XFC ≥1000 Vdc target)	Determined according to design capacity	Isolation/ protection priority
Connection / Network	PCC study, IEEE-519 compliance, demand-charge	None (island), backup strategy	None (island), no fuel/logistics
Economy	Tariff + demand charge optimisation	BESS cycle life is critical	Climate-focused LCOE/NPV

On the PV side, MPPT-boost is selected; on the BESS/EV side, bidirectional DC-DC (BDDC) is selected; on the grid interface, VSC/PWM rectifier is selected; DC bus voltage selection (e.g. 300–800 Vdc, ≥1000 Vdc for XFC) determines cabling ampacity, thermal management, insulation coordination, and protection coordination [8,11,15]. With EMS, PV → DC bus, BESS ↔ DC bus, EV ↔ DC bus, and Grid ↔ VSC flows are managed according to SoC, deadline, and grid contract power constraints [8,10].

Shading for PV, GCR, tilt/orientation; traffic access for the station, electrical proximity (PCC/transformer), permits/licences and EMC/noise limits are evaluated together. Single-axis tracking and low mutual shading (1%) targets in large fields increase annual production while affecting cabling/infrastructure costs [8]. In on-grid connections, voltage drop, short-circuit power, protection selectivity, and IEEE-519 compliance checks must be verified prior to the connection agreement [8,11,15].

In on-grid projects, CAPEX (PV, BESS, power electronics, construction), OPEX (maintenance, losses) and tariff/demand charge dynamics are considered together; demand charge reduction and revenue (kWh sales/service) maximisation are achieved through PV-priority + BESS strategies [8,10]. In stand-alone projects, LCOE is evaluated within a framework that is fuel/logistics-free but includes BESS renewal cycles; the technical and economic feasibility of a dual-green (renewable feed + low emissions) approach has been demonstrated in regions with high climate/irradiation profiles [17].

12. CONCLUSION

The findings indicate that coordination across all layers—from architectural selection (on-grid/off-grid/hybrid) to power electronics topologies, MPPT–EMS coordination, grid integration (V2G/V2H), and power quality (PQ) management—is critical for a sustainable and reliable EVCS. When the effects of AC Level 1–2, DC fast and XFC levels on field operation are evaluated alongside connector/standard requirements and charging time targets, the need for system design to be supported by PV-priority energy flow and BESS buffering becomes apparent.

In three-phase PV-based on-grid systems, simultaneous P/Q control with VSC enables compliance with IEEE-519 current limits even in unbalanced/distorted grids and allows reactive power compensation (Q-comp) and voltage regulation tasks to be performed simultaneously. Combining this control layer with P–Q and SRF-based active filtering approaches has been found to be effective in terms of harmonic mitigation; harmonics arising from the non-linear load characteristics of fast charging can be suppressed and TDD/THD values can be kept within operational limits.

MPPT (P&O/INC) methods provide a practical foundation due to their low computational load and widespread field applicability, while advanced approaches such as fuzzy MPPT offer additional gains in tracking accuracy under

variable irradiation/temperature conditions and DC link stability. The EMS fed by this layer manages PV → DC bus, BESS ↔ DC bus, EV ↔ DC bus, and Grid ↔ VSC flows according to SoC, deadline, and contract power constraints, enabling simultaneous optimisation of both technical (stability, efficiency) and economic (tariff, demand charge) objectives.

On the protection and safety side, the requirements of IEC 61851 (charging modes/operation) and IEC 62196/SAE J1772 (plug/connector) must be considered along with EMC, insulation coordination, clearance/creepage, touch voltage, residual current detection, and fast fault clearing times. Furthermore, integrating measurement and billing processes with AMI/IoT infrastructures (RFID/APP authentication, session-based measurement, tariff engine, and automatic billing) increases operational transparency and revenue accuracy.

From a design perspective, in on-grid examples, peak shaving/load levelling targets are achieved with single-axis tracking PV and hourly-scale BESS, while in stand-alone/off-grid scenarios, the climate/irradiance profile and LCOE-focused design determine the overall system. This comparison has revealed that details such as charger mix (AC L2 + DC fast/XFC), DC bus levels (300–800 Vdc; XFC ≥1000 Vdc), cabling ampacity, and thermal management must be evaluated alongside site selection and economic indicators.

Finally, it has been reported in the literature that artificial intelligence-based controllers (e.g. NN-based controllers) can further improve PQ and dynamic performance, providing additional stability/settling time gains over classical SRF/P-Q-based methods. This area represents a promising development axis for future work in high-power DC fast/XFC stations [18].

EVCS success:

- Standard-compliant and secure hardware,
- Efficient and correctly selected power electronics topologies,
- Real-time, constraint-sensitive coordination of the MPPT-EMS-VSC trio
- depends on the integrated design of measurement, billing and market integration.

This approach both reduces network effects and simultaneously improves user experience and facility economics.

REFERENCES

[1] C. Armenta-Déu and L. Sancho, "Sustainable charging stations for electric vehicles," *Eng*, vol. 5, no. 4, pp. 3115–3136, 2024, doi: 10.3390/eng5040163.

[2] C. Venkatesh and S. Yesuraj, "Efficient and reliable fast charging station for electric vehicles: Integrating PV system and optimized control," *Electric Power Components and Systems*, vol. 1, pp. 1–21, 2024, doi: 10.1080/15325008.2024.2320275.

[3] T. Fangsuwannarak, K. Fangsuwannarak and D. Prasertdee, "Electric Vehicle Charging Station Resourcing Hybrid Energy from Fuel Cell and Solar Systems," *2024 8th International Conference on Power Energy Systems and Applications (ICoPESA)*, Hong Kong, Hong Kong, 2024, pp. 640-645, doi: 10.1109/ICOPESA61191.2024.10743259.

[4] H. Fathabadi, "Novel solar powered electric vehicle charging station with the capability of vehicle-to-grid," *Solar Energy*, vol. 142, pp. 136–143, 2017, doi: 10.1016/j.solener.2016.11.037.

[5] M. S. Arjun, N. Mohan, K. R. Sathish, A. Patil, and G. Thanmayi, "Impact of electric vehicle charging station on power quality," *International Journal of Applied Power Engineering*, vol. 13, pp. 186–193, 2024, doi: 10.11591/ijape.v13.i1.pp186-193.

[6] V. Jain, S. Kewat and B. Singh, "Three Phase Grid Connected PV Based EV Charging Station With Capability of Compensation of Reactive Power," in *IEEE Transactions on Industry Applications*, vol. 59, no. 1, pp. 367-376, Jan.-Feb. 2023, doi: 10.1109/TIA.2022.3213530.

[7] S. Das, R. Vijay, Z. A. Lone, A. Firdous, P. Mathuria and R. Bhakar, "Electrical Vehicle Charging Station Load Management Using Novel Operational Approaches," *2024 IEEE 4th International Conference on Sustainable Energy and Future Electric Transportation (SEFET)*, Hyderabad, India, 2024, pp. 1-6, doi: 10.1109/SEFET61574.2024.10718135.

[8] A. Balal, T. Reid and R. Stewart, "Solar-Powered EV Charging Station with Battery Energy Storage System Integration," *2024 IEEE International Conference on Green Energy and Smart Systems (GESS)*, Long Beach, CA, USA, 2024, pp. 1-5, doi: 10.1109/GESS63533.2024.10784919.

[9] J. A. Medrano-Hermosillo, A. E. Rodríguez-Mata, L. Djilali, O. J. Suarez-Sierra and V. A. González Huitron, "Solar-Powered Electric Vehicle Charging Station with Fuzzy MPPT Algorithm," *2024 IEEE Colombian Conference on Applications of Computational Intelligence (ColCACI)*, Pamplona, Colombia, 2024, pp. 1-6, doi: 10.1109/ColCACI63187.2024.10666570.

[10] W. F. S. Díaz, J. T. Vargas, and F. Martínez, "Optimizing EV charging stations: A simulation-based approach to performance and grid integration," *Bulletin of*

Electrical Engineering and Informatics, vol. 13, no. 4, pp. 2922–2939, 2024, doi: 10.11591/eei.v13i4.8027.

[11] S. R. Singh, M. Kumar Behera, L. C. Saikia, R. Borthakur, T. Mallik and J. Gogoi, "Implementation of Solar PV-Battery Based Electric Vehicle Charging Station," *2023 IEEE Silchar Subsection Conference (SILCON)*, Silchar, India, 2023, pp. 1-6, doi: 10.1109/SILCON59133.2023.10404601.

[12] M. Ulagammai, "Smart Electric Vehicle Charging Station using Solar Power," *2024 IEEE 4th International Conference on Sustainable Energy and Future Electric Transportation (SEFET)*, Hyderabad, India, 2024, pp. 1-4, doi: 10.1109/SEFET61574.2024.10718108.

[13] R. P. Narasipuram and S. Mopidevi, "A technological overview and design considerations for developing electric vehicle charging stations," *Journal of Energy Storage*, vol. 43, p. 103225, 2021, doi: 10.1016/j.est.2021.103225.

[14] R. Santhoshkumar, G. Swetha, S. Ragava and K. S. Ragavendhar, "Desisn and Implementation of Solar-Powered Electric Vehicle Charging Station with Automatic Billing System," *2024 IEEE 4th International Conference on Sustainable Energy and Future Electric Transportation (SEFET)*, Hyderabad, India, 2024, pp. 1-6, doi: 10.1109/SEFET61574.2024.10718174.

[15] T. T. Makuwatsine and M. Singh, "Design and Simulation of on Grid Solar Powered Electric Vehicles Charging Station," *2024 International Conference on Computer, Electronics, Electrical Engineering & their Applications (IC2E3)*, Srinagar Garhwal, Uttarakhand, India, 2024, pp. 1-6, doi: 10.1109/IC2E362166.2024.10826613.

[16] A. Vasile, M. Pasetti, D. Astolfi, G. Zizzo, E. R. Sanseverino and A. Flammini, "Concept and Preliminary Design of a Stand-Alone Charging Station for Light Electric Vehicles," *2024 IEEE International Conference on Environment and Electrical Engineering and 2024 IEEE Industrial and Commercial Power Systems Europe (EEEIC / I&CPS Europe)*, Rome, Italy, 2024, pp. 1-5, doi: 10.1109/EEEIC/ICPSEurope61470.2024.10751193.

[17] J. O. Oladigbolu, A. Mujeeb, Y. A. Al-Turki and A. M. Rushdi, "A Novel Doubly-Green Stand-Alone Electric Vehicle Charging Station in Saudi Arabia: An Overview and a Comprehensive Feasibility Study," in *IEEE Access*, vol. 11, pp. 37283-37312, 2023, doi: 10.1109/ACCESS.2023.3266436.

[18] A. G. Krushna, V. Deekshith, P. Nani, K. G. Yashwanth and R. Uday, "Design and Analysis of NN Controller based EV Charging Station with Enhanced Power Quality," *2024 IEEE International Conference on Information Technology, Electronics and Intelligent Communication Systems (ICITEICS)*, Bangalore, India, 2024, pp. 1-5, doi: 10.1109/ICITEICS61368.2024.10625138.

CHAPTER 10

BIBLIOMETRIC MAPPING OF FEDERATED LEARNING AND ENERGY EFFICIENCY: AN ANALYSIS OF APPLICATIONS AND OPTIMIZATION TRENDS DURING 2020–2024

Dr. Ömer ALGORABİ
Istanbul University-Cerrahpaşa
Faculty of Engineering, Department of Industrial Engineering
https://orcid.org/0000-0002-2016-8674

1. INTRODUCTION

Today, energy systems play an important role in many areas of human life, particularly in the residential, industrial, and transportation sectors (Forootan ve ark., 2022). Responding to energy supply and demand, ensuring optimal performance, and minimizing environmental impacts are among the key objectives of these systems. Distributed energy resources provide an effective solution to existing energy management issues by enabling the localization of energy production and consumption (Cheng ve ark., 2022). These systems stand out with advantages such as high efficiency, low energy loss, low environmental pollution, and flexible operation. However, the intensive use of advanced communication networks such as smart grids, the Internet of Things (IoT), smart meters, and 5G in electricity supply ensures the formation of an integrated energy management infrastructure through advanced data management systems.

The rapid increase in the amount of data in energy systems is largely due to the widespread adoption of smart edge devices such as advanced measurement infrastructure (Zheng ve ark., 2024). This digitalization process has fundamentally changed approaches to energy management. The large volumes

of operational and non-operational data collected by smart systems enable the development of numerous innovative applications aimed at increasing the efficiency and optimization of energy systems. In this context, in order to enable early warning, problem prevention, and effective control in energy systems, it is necessary to securely, accurately, and efficiently store, process, and transmit the large amount of real-time data collected from edge and end devices (Otoum ve ark., 2022).

With the proliferation of big data technologies today, data privacy and security are prioritized over the sheer volume of data (Zhang C. ve ark., 2021). Data breaches have become a significant risk factor, heightening public awareness of data protection. Awareness and efforts to strengthen data security are rapidly increasing not only among individuals but also within organizations and society at large.

Federated Learning (FL) offers an innovative solution to data privacy issues by enabling model training without the need for data sharing (Mendes ve ark., 2024). In the FL approach, the model training process is carried out using edge devices and their local data. This method enables collaborative learning between multiple edge devices. Once training is complete, each device transmits the weights (parameters) obtained in its own model to the central server, and the global model is updated by combining these weights. FL has a flexible structure that can be applied to different machine learning models and can therefore be used in many applications that use a client-server architecture (Almanifi ve ark., 2023). FL is currently considered a natural evolution of machine learning in the IoT field.

Despite its advantages, using FL over wireless networks creates challenges in terms of energy efficiency (Dang ve ark., 2024). The importance of Federated Learning in terms of energy efficiency is particularly evident in IoT and wireless network environments where edge devices have limited resources. Energy costs must be carefully balanced in both local training and communication processes of the devices.

In this study, academic research on federated learning in the context of energy efficiency and energy applications was examined through a comprehensive bibliometric analysis. The study identified the most influential publications, authors, institutions, and countries; it also analyzed the most frequently used terms at the keyword, title, and abstract levels. Through these analyses, research trends over the years were revealed, and thematic maps were used to assess the future directions of work in the field of federated learning.

2. BACKGROUND: FEDERATED LEARNING AND ENERGY EFFICIENCY

Federated Learning (FL) is an innovative artificial intelligence approach developed to overcome the challenges of data privacy, data fragmentation, and centralized data collection. FL enables model training without the need to share data, thereby preserving privacy while also allowing learning from distributed data sources. In the field of energy systems, FL is used in numerous applications such as demand forecasting, large-scale grid management, renewable energy production optimization, smart meter data analysis, and energy consumption forecasting. These applications make energy production and consumption processes more efficient while contributing to sustainable energy management goals by protecting data privacy and security.

Numerous studies have been conducted in the literature on energy demand forecasting using the federated learning approach. Mendes et al. (2024) developed a federated learning-based model to predict the temporal net energy demand of buildings in transactive energy communities. The study aims to optimize energy management processes in these communities by combining demand and production forecasts. In another study, a federated learning approach was used to predict the energy demand of electric vehicles in the state of Colorado. In the study, blockchain technology and regression-based algorithms were used together to increase the security and accuracy of the prediction process (Kauser ve ark., 2024). In addition to demand forecasting, energy consumption forecasting has also been addressed in the studies as it is considered important for planning purposes. Wang et al. (2024) used personalized federated learning methods for building energy consumption estimation and proposed a deep learning model based on an expert mixture to support heterogeneous data distribution. In another study conducted in 2024, a model combining adaptive and federated learning approaches was developed for short-term residential energy forecasting (Abdulla ve ark., 2024). In this method, the central server created a general model that aggregates forecasts from different regions, identifies data discrepancies, and improves forecast accuracy.

The federated learning approach is also increasingly being used in the field of renewable energy. In a study conducted in Iran, a cyber-resilient hybrid model based on Federated Learning and CNN was proposed to predict short-term wind energy production (Moayyed ve ark., 2022). The architecture, consisting of nine clients, created a generalizable global prediction model by processing data obtained from different regions based on the principle of privacy. Hosseini et al. (2023) focused on the problem that distributed photovoltaic (PV) systems

located behind the meter (BTM) cannot be directly monitored by public utilities. In this context, a federated learning-based BTM PV prediction model that preserves grid flexibility and ensures data privacy has been developed; a multi-layer perceptron (MLP) architecture was used as the basis for the model. In a study, a dynamic planning framework was developed for a biomass-solar hybrid energy system (Dolatabadi ve ark., 2024). A controlled federated neural network search technique was applied to reduce unnecessary computational load.

Another important problem focused on in federated learning research is smart energy grids. Work in this area aims to make processes such as energy management, demand forecasting, fault detection, and energy optimization more efficient and reliable while protecting data privacy. Wen et al. (2021) developed a privacy-preserving federated learning framework for detecting energy theft in smart grids. The proposed model integrates local differential privacy and homomorphic encryption methods to preserve data privacy and improve detection accuracy. Jithis et al. (2023) developed a federated learning-based smart grid anomaly detection system based on training machine learning models locally on smart meters. The integrity and reliability of the system were enhanced by using the SSL/TLS protocol for the secure transmission of model parameters. In a study, a federated learning-based hybrid deep learning model was proposed for load forecasting in smart grids (Sarker ve ark., 2024). The model's hyperparameters were optimized using particle swarm optimization, and the aggregation mechanism was developed using pruning-based methods to reduce computational cost. Contributions were made towards efficient and scalable load forecasting in smart grids.

Energy efficiency is also a prominent issue in federated learning applications. When federated learning is used, communication costs, computational load, and device energy consumption directly impact system performance. Therefore, developing energy-efficient federated learning approaches is critical for both sustainability and application efficiency. Kim et al. (2023) proposed a green quantized FL framework to reduce energy consumption in federated learning. In the approach, both local training and data transmission were performed at a limited accuracy level using quantized neural networks, thereby reducing computational and communication costs. Additionally, a multi-objective optimization model that balances energy efficiency and model accuracy has been developed. In a study, a new federated learning model was developed to optimize energy consumption in IoT systems for autonomous vehicles. Experiments conducted using TensorFlow Federated reported that the model significantly reduced communication and training time, resulting in substantial energy savings and high accuracy (Kaleem ve ark., 2024).

3. METHODOLOGY: BIBLIOMETRIC ANALYSIS FRAMEWORK

Bibliometric analysis is a method based on the systematic examination of scientific publications to reveal development trends, impact levels, and structural relationships within a research field (Passas, 2024). The process involves collecting information from databases, organizing and standardizing this data, and evaluating it using various analysis techniques. Frequently preferred for examining large-scale scientific data today, this method has become an important tool for understanding the general orientation of the field and academic interaction networks. Today, the Web of Science (WoS) and Scopus databases are among the most reliable and comprehensive sources for bibliometric analysis (Duplančić Leder ve ark., 2023). Both platforms have a broad interdisciplinary coverage and include studies published in high-quality, peer-reviewed journals.

Web of Science (WoS) is a comprehensive database that has enabled the tracking of scientific publications, citation relationships, and research trends worldwide since 1990 (Li, ve ark., 2020). The WoS Core Collection, the core component of WoS, includes high-impact journals and academic sources from various disciplines. WoS is recognized as a global standard reference tool for examining the structure of the literature, its impact level, and scientific collaborations.

In this study, a bibliometric analysis was conducted using the Web of Science (WoS) Core Collection database. These data were accessed on October 5, 2025. The general research design of the study is presented in Figure 1. The search process combined the keywords “Federated Learning” and “Energy”, “Smart Grid”, “Renewable”, “Power”, or “Electricity.” In the first stage, a total of 946 publications were identified. When the time range was limited to 2020–2024, 709 publications were obtained. A significant portion of the studies published during the period under review consisted of research articles and conference papers. Only article-type studies were selected from these publications, and 472 articles were included in the analysis.

Bibliometric and visualization analyses were conducted using the Bibliometric Analysis Platform, Biblioshiny, VOSviewer, and Excel software. The analysis examined authors, countries, institutions, journals, keywords, and thematic maps, aiming to reveal the research structure, collaboration networks, and trends in the fields of federated learning and energy systems.

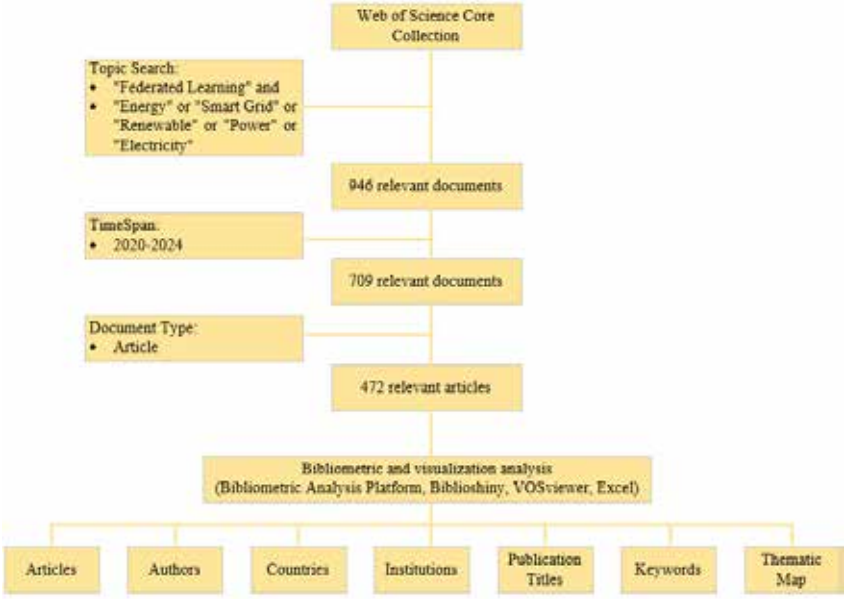

Figure 1. Research design

4. RESULTS AND DISCUSSION

This study examined 472 articles related to federate learning research conducted in energy systems. Figure 2 shows the distribution of these publications according to WoS categories. According to the findings, the majority of the studies are in the Engineering Electrical Electronic field, which accounts for approximately 60% of the total publications. This is followed by the Telecommunications field, which also represents approximately 54% of the total. This indicates that the research is primarily conducted within a framework focused on engineering and communication technologies. Additionally, the Computer Science Information Systems (168 publications) and Energy Fuels (48 publications) categories also have a significant share.

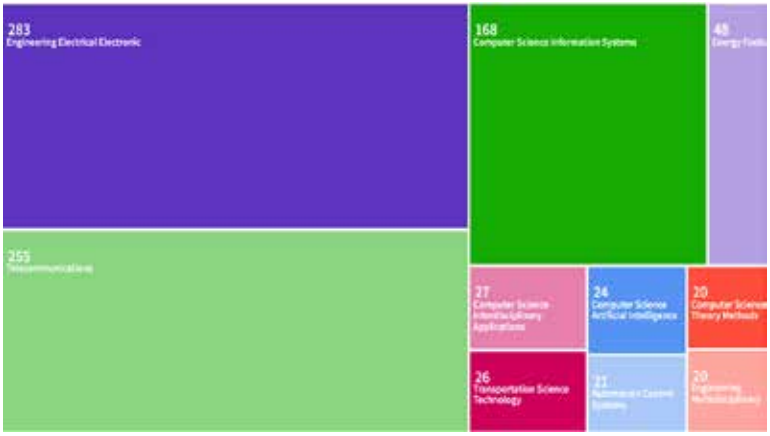

Figure 2. Publications according to WoS categories

The distribution of publications on federated learning in energy systems by year is shown in Figure 3. Starting with only 6 publications in 2020, this research area began to gain momentum in 2021, reaching 35 publications. The number of publications rose to 78 in 2022 and 140 in 2023. The most notable increase occurred in 2024, when the number of publications reached 213. This trend indicates that federated learning is increasingly being adopted in the field of energy systems and that rapid research expansion is taking place in this area.

Figure 4 shows the annual total citation (TC) count and the average citations per publication (TC/TP) values. When examining the studies conducted between 2020 and 2024, it was determined that there was an average of 21.9 citations per publication. While 2022 was the year with the most citations, with a total of 3723 citations, 2021 had the highest average number of citations per article, with a TC/TP ratio of 80.2. These findings indicate that the studies published in 2021 and 2022 are the most influential, highly visible, and fundamental studies for subsequent research in the field.

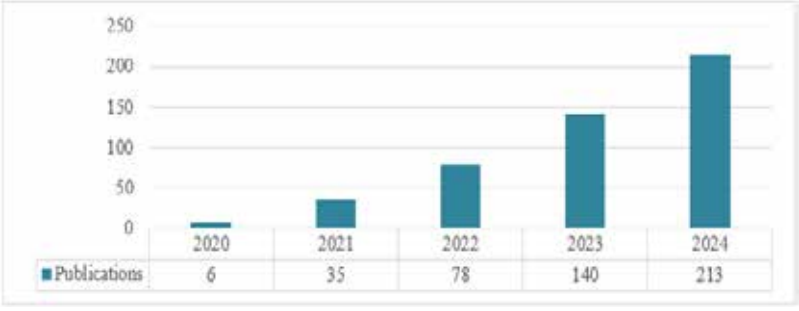

Figure 3. Number of publications by year.

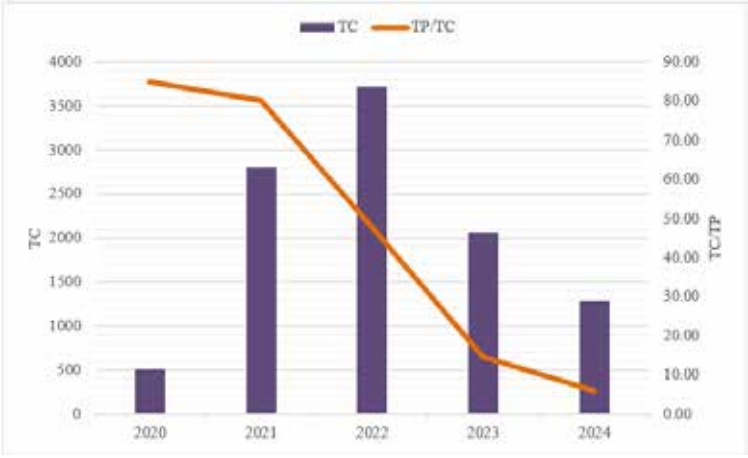

Figure 4. Number of citations by year.

Table 1 shows the top 10 most influential publications ranked by the highest number of citations. The most cited work is the article titled "Energy Efficient Federated Learning Over Wireless Communication Networks" published by Yang et al. (2020), which tops the list with 695 citations. This is followed by the work of Vaezi et al. (2022) titled "Cellular, Wide-Area, and Non-Terrestrial IoT: A Survey on 5G Advances and the Road Toward 6G" with 379 citations. Each of the top three articles has received over 300 citations, placing them among the leading studies in the field. Overall, the top 10 articles have received an average of over 150 citations.

Table 1. Most cited publications.

Rank	**Author**	**Year**	**Article Title**	**Total Citation**
1	Yang, ZH; Chen, MZ; Saad, W; Hong, CS; Shikh-Bahaei, M	2020	Energy Efficient Federated Learning Over Wireless Communication Networks	695
2	Vaezi, M; Azari, A; Khosravirad, SR; Shirvanimoghaddam, M; Azari, MM; Chasaki, D; Popovski, P	2022	Cellular, Wide-Area, and Non-Terrestrial IoT: A Survey on 5G Advances and the Road Toward 6G	379

3	Samarakoon, S; Bennis, M; Saad, W; Debbah, M	2019	Distributed Federated Learning for Ultra-Reliable Low-Latency Vehicular Communications	312
4	Zhang, WT; Yang, D; Wu, W; Peng, HX; Zhang, N; Zhang, HK; Shen, XM	2021	Optimizing Federated Learning in Distributed Industrial IoT: A Multi-Agent Approach	223
5	Li, Y; Wei, XH; Li, YZ; Dong, ZY; Shahidehpour, M	2022	Detection of False Data Injection Attacks in Smart Grid: A Secure Federated Deep Learning Approach	207
6	Lu, YL; Huang, XH; Zhang, K; Maharjan, S; Zhang, Y	2020	Communication-Efficient Federated Learning for Digital Twin Edge Networks in Industrial IoT	189
7	Liu, DZ; Simeone, O	2020	Privacy for Free: Wireless Federated Learning via Uncoded Transmission With Adaptive Power Control	177
8	Li, Y; Wang, RN; Li, YZ; Zhang, M; Long, C	2023	Wind power forecasting considering data privacy protection: A federated deep reinforcement learning approach	168
9	Su, Z; Wang, YT; Luan, TH; Zhang, N; Li, F; Chen, T; Cao, H	2021	Secure and Efficient Federated Learning for Smart Grid With Edge-Cloud Collaboration	163
10	Li, Y; Li, JZ; Wang, Y	2021	Privacy-Preserving Spatiotemporal Scenario Generation of Renewable Energies: A Federated Deep Generative Learning Approach	157

Table 2 lists the most influential authors in the field of federated learning and energy systems. Dusit Niyato is the most productive researcher in this field, with a total of 9 publications. However, Li Yang is the most cited author; this researcher's work has received a total of 585 citations and has thus made a significant impact in the area. Li Yang also stands out in terms of the citation/publication ratio (CP/PC), with an average of 117.00 citations per article, de-

monstrating a remarkable level of impact.

When evaluated in terms of another important metric, the h-index, Yuan Wu (h=7) is the author who stands out in this field. These indicators reveal the contributions of different authors in the areas of federated learning and energy systems in terms of the number of publications, citation impact, and scientific visibility.

Table 2. The most influential authors.

Rank	Author	TP	TC	TC/TP	H-Index
1	Dusit Niyato	9	91	10.11	5
2	Yuan Wu	8	219	27.38	7
3	Viet Quoc Pham	5	263	52.60	5
4	Li, Yang	5	585	117.00	4
5	Zhu Han	5	129	25.80	4

Figure 5 shows the most influential institutions in the field of federated learning and energy systems. The institutions contributing most to this area are the State Grid Corporation of China, Nanyang Technological University, and Beijing University of Posts and Telecommunications, each standing out with 16 publications. These institutions are followed by Zhejiang University (15 publications), Southeast University China (13 publications), and the Chinese Academy of Sciences (13 publications).

Overall, research productivity appears to be largely concentrated in China-based institutions. However, institutions such as the University of Sydney (Australia) and the University of London (UK) are also making significant contributions in this field, and federated learning research is becoming increasingly international in nature.

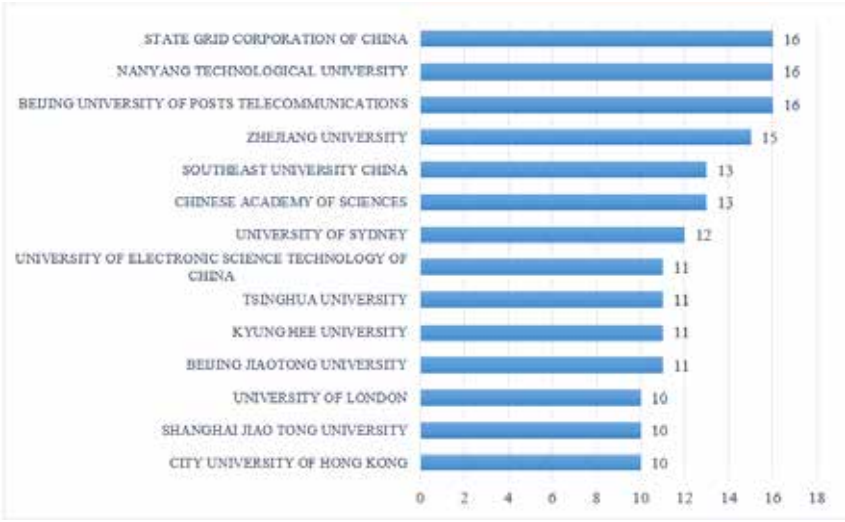

Figure 5. The most productive institutions.

Country-based analysis results show that research in federated learning and energy systems is largely concentrated in specific regions. China is by far the most productive country, with a total of 258 publications between 2020 and 2024. China is followed by the United States (88 publications), Canada (51 publications), and Australia (41 publications). South Korea (40 publications), the United Kingdom (27 publications), and India (26 publications) have contributed less in this field.

As shown in Figure 2, a clear upward trend in countries' publications in this field has been observed since 2020. In particular, China's rapid rise after 2022 demonstrates a remarkable increase in research productivity in this area. The United States and Canada, on the other hand, have shown a more stable but steadily increasing growth curve.

Furthermore, the significant increase in production in recent years in countries such as Saudi Arabia (25 publications), Singapore (24 publications), and the United Arab Emirates (19 publications) indicates that federated learning applications in the energy sector are rapidly spreading in Asia and the Middle East.

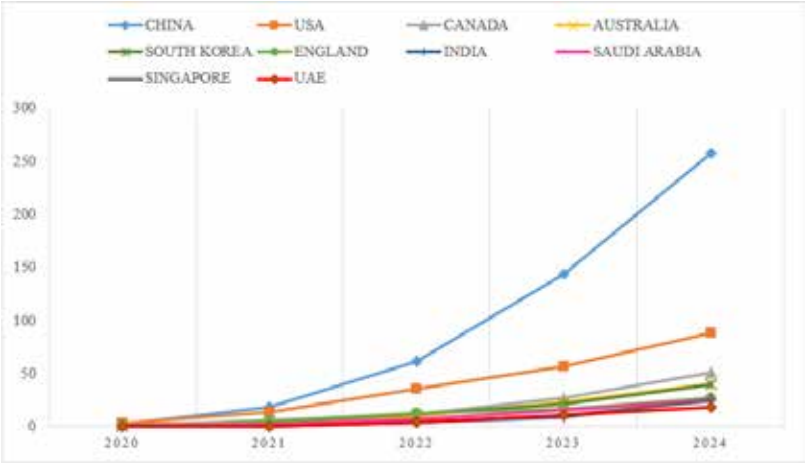

Figure 6. Publication growth by country over the years.

Figure 7 shows the distribution of publications in the fields of federated learning and energy systems by journal. According to the results obtained, the majority of studies are concentrated in IEEE publications. The IEEE Internet of Things Journal is the journal with the highest contribution, with a total of 47 publications. This journal is followed by IEEE Access (37 publications) and IEEE Transactions on Wireless Communications (30 publications). Additionally, IEEE Transactions on Vehicular Technology (19), IEEE Transactions on Industrial Informatics (16), and IEEE Transactions on Green Communications and Networking (14) are other prominent sources in the field.

Among journals outside of IEEE, Applied Energy (11 publications), Electronics (9 publications), Sensors (8 publications), and Energies (8 publications) stand out. This indicates that federated learning research is not limited to the fields of computer and communication engineering, but also extends to different disciplines such as energy systems and industrial applications.

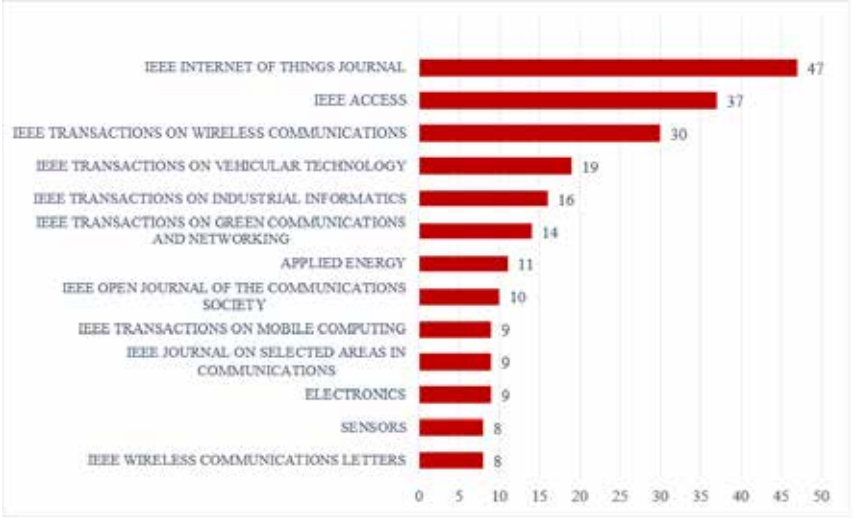

Figure 7. The most influential journals.

As part of the bibliometric analysis, author keywords were examined to identify key concepts in the research field, and the resulting word cloud is presented in Figure 8. The term "federated learning" is by far the most frequently used keyword, appearing 305 times. This is followed by terms such as 'training' (123 times), "computational modeling" (94 times), "energy consumption" (93 times), and "servers" (87 times). Furthermore, concepts such as "data models," "energy efficiency," "optimization," "privacy," "smart grid," and "resource management" are also seen to be among the prominent keywords in the field. These findings reveal that federated learning research does not focus solely on data privacy and model optimization, but is also intensively applied in the areas of energy management and energy efficiency.

Additionally, Keywords Plus data provided by WoS was also evaluated in the bibliometric analysis. Keywords Plus refers to words or word groups that do not appear in article titles but are derived from the titles of cited sources, and in this respect, it plays an important role in determining conceptual relationships in the literature. According to the word cloud shown in Figure 9, the most frequently occurring terms were "networks" (54 times), "resource allocation" (45 times), "communication" (39 times), and 'optimization' (39 times). These were followed by the concepts "design", "internet", "framework", and "convergence." These results show that federated learning research is strongly related to areas such as network structures, resource allocation, and communication optimization in energy systems.

Figure 8. Author Keywords Cloud.

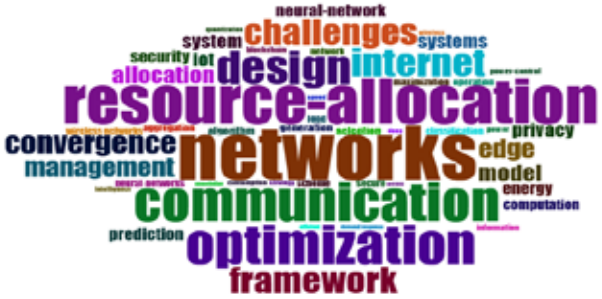

Figure 9. Keywords Plus Cloud.

Figure 10 shows the annual distribution of title bigrams between 2022 and 2024. According to the findings, the term “federated learning” is by far the strongest theme in all three years, showing a particularly marked increase in 2024. An increasing trend is also observed in the topics of “reinforcement learning,” “resource allocation,” “deep reinforcement,” and “edge computing” starting from 2023. The themes of “energy consumption,” “load forecasting,” and “energy management” have also been studied recently.

Overall, 2022 was a period when the foundations of federated learning were laid, while 2023 saw an increase in learning-based and resource management-focused studies. By 2024, research has shifted towards advanced topics such as energy optimization, reinforcement learning, and edge computing. In contrast, themes such as “smart grid”, and “energy-efficient federate,” were found to be relatively less frequent in 2024 compared to previous years.

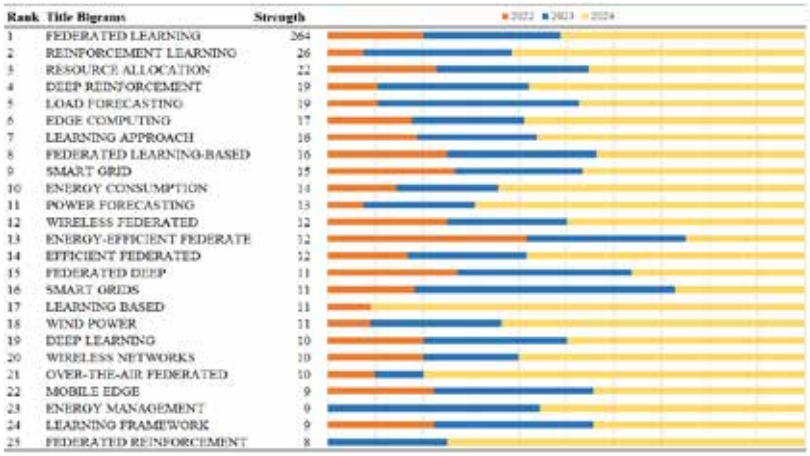

Figure 10. Most frequently used title bigrams.

Figure 11. Most frequently used abstract bigrams.

Figure 11 shows the distribution of abstract bigrams by year. According to the findings, the term “energy consumption” was used 96 times in 2023 and 157 times in 2024, showing an increase of approximately 60%. Similarly, the term “learning federated” was used 74 times in 2023 and 135 times in 2024, while the term “machine learning” was used 52 times in 2023 and 104 times in 2024, showing a significant increase. The theme “data privacy” was seen 37 times in 2023 and 62 times in 2024. Notably, the term “wind power” has increased approximately three times compared to 2023. In contrast, the terms “edge devices” and “load forecasting” have decreased compared to 2023.

Figure 12 shows collaborative research networks between countries. Evaluating collaborative work is important in terms of revealing the level of interaction and knowledge sharing networks in the field on a global scale. When examining the connections between countries, it is seen that China is the country with the most international collaboration in the fields of federated learning and energy systems.

China has established strong partnerships, particularly with the United States, Canada, Australia, and Singapore, and the high intensity of collaboration with these countries is noteworthy. This finding demonstrates that China has become a significant contributor to knowledge production in the field, not only in terms of the number of publications but also by positioning itself at the center of international research networks. Furthermore, it is observed that European countries such as Germany, France, Italy, and Spain have also established strong collaborations within their own regions.

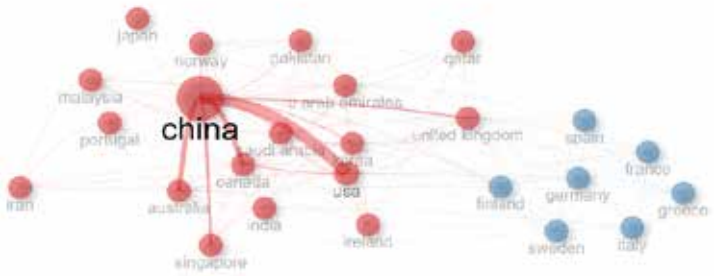

Figure 12**.** Cooperation between countries.

Figure 13 shows the collaboration networks between institutions. According to the visualization, Nanyang Technological University and Beijing University of Posts and Telecommunications stand out as the institutions with the most collaboration in this field. Nanyang Technological University has established a close partnership with Zhejiang University in particular, while Beijing University of Posts and Telecommunications has strong research links with the University of Electronic Science and Technology of China. The thickness of the links indicates that the relationship between Zhejiang University and the University of Macau represents the strongest joint research collaboration.

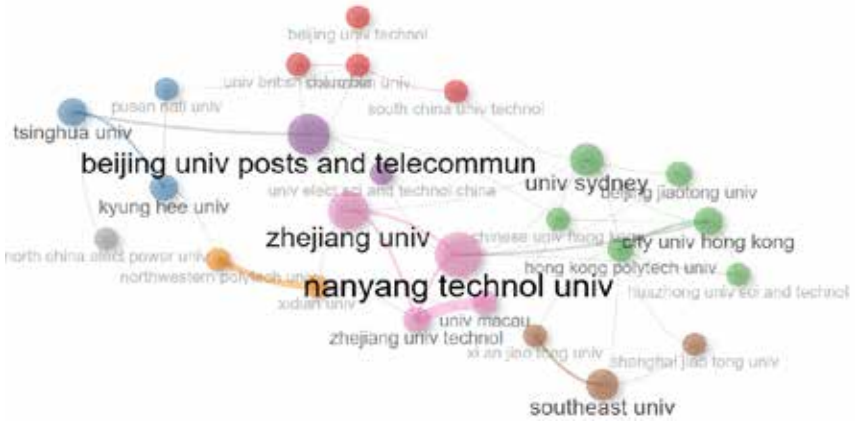

Figure 13. Cooperation between institutions.

Thematic maps are analytical tools that visually represent the current structure and future development potential of a research field. In these maps, themes are derived from keywords in publications and evaluated based on density and centrality values. Density indicates the integrity and level of development within the theme itself, while centrality shows the degree of connection with other themes. These two criteria determine the importance and sustainability of a topic in the field. Themes in thematic maps are evaluated in four groups according to their position: themes with high density and high centrality represent "Motor Themes"; those with low density but high centrality represent " Basic Themes"; those with low density and low centrality represent "Emerging or Declining Themes"; and those with high density but low centrality represent "Niche Themes".

Figure 14, created as part of a bibliometric analysis conducted in the energy industry, shows a thematic map based on keywords in the federated learning literature. The themes on the map reveal the current structure and development directions of the field. According to the visual, topics such as "artificial intelligence", "optimization", "smart grid", "privacy" and "load forecasting" are among the basic themes with high centrality and relatively low density values; this shows that the topics forming the theoretical basis of the field are associated with a broad research network.

On the other hand, topics such as "distributed energy resources", "frequency control", "false data injection", and "energy efficiency" are classified as motor themes; these themes are powerful focus areas that shape the future direction of the field and determine the research agenda. Headings such as "ai-enabled",

"electric vehicle" "quantum computing", and "power system stability" are considered niche themes with high intensity but low centrality values; these themes represent specialized studies concentrated in specific application areas.

Furthermore, topics such as "generative adversarial network", "integrated energy system" "data heterogeneity" and "photovoltaic power prediction" fall into the category of themes that emerge or disappear with low centrality and density levels. These themes point to new application potentials for federated learning in energy systems and can be considered as potential emerging areas that will determine the direction of future research.

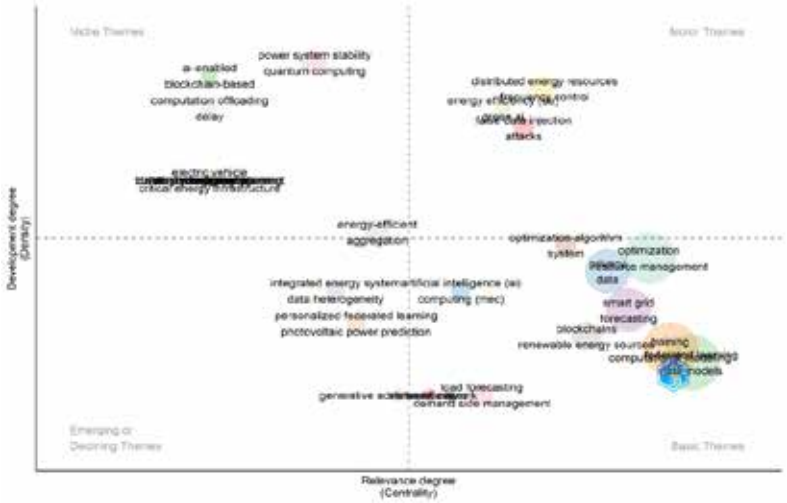

Figure 14. Thematic map based on author keywords.

Figure 15 shows the thematic map created using bigrams obtained from the titles. According to the map, the terms "federated learning", "energy management", "edge learning", and "machine learning-based" are among the basic themes and define the general research framework of the field. Topics such as "reinforcement learning", "energy system", "microgrid energy", and "load forecasting" stand out as driving themes with high density and centrality values. Meanwhile, topics such as "connected vehicles", and "intelligent decision" are niche themes, while concepts such as "energy resources" have low centrality and density values, indicating that these themes are emerging or declining areas.

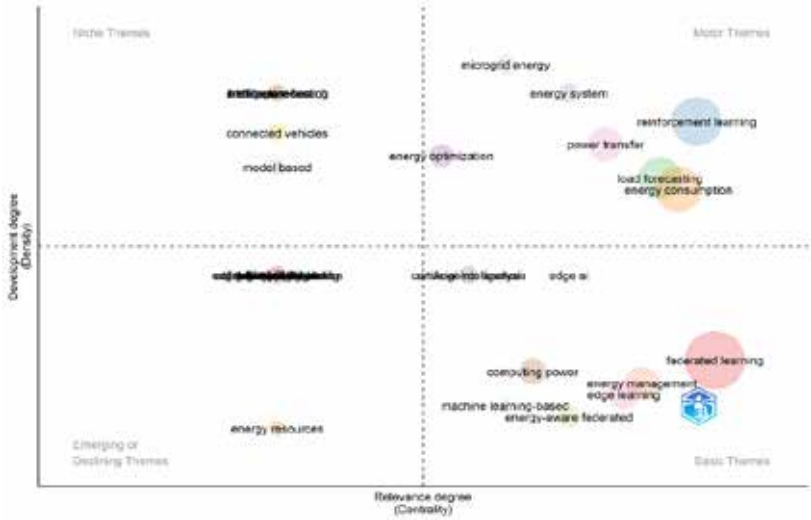

Figure 15. Thematic map based on title bigrams.

5. CONCLUSION

Federated learning is a rapidly evolving technology that offers significant advantages, particularly in terms of data privacy, big data management, and the effective use of distributed data sources. Today, energy systems stand out as one of the fundamental elements of sustainable living. In this context, the use of federated learning in energy forecasting, planning, and optimization processes has great potential in terms of both increasing efficiency and privacy-focused smart energy management.

This study conducted a comprehensive bibliometric analysis of federated learning applications in energy systems. The findings reveal that the number of publications in this field in 2024 increased by approximately 50% compared to 2023. Overall, a rapid upward trend has been observed in the literature. When examined by country, China and the US were found to be among the most productive countries, with Chinese institutions contributing significantly to publications. According to the thematic analysis results, the topics “electric vehicle,” “power system stability,” and “blockchain based” stand out as niche themes, while the themes “generative adversarial network,” “data heterogeneity,” and “photovoltaic power prediction” are among the emerging or declining topics.

In future studies, it is recommended that a systematic literature review based on cluster analysis be conducted to enable a more in-depth examination of the

trends of federated learning in the field of energy systems. Furthermore, evaluating energy efficiency in federated learning applications through more specific and quantitative indicators will contribute significantly to the field from both an algorithmic optimization and a sustainable artificial intelligence perspective.

REFERENCES

Abdulla, N., Demirci, M., & Ozdemir, S. (2024). Smart meter-based energy consumption forecasting for smart cities using adaptive federated learning. *Sustainable Energy, Grids and Networks*, 38, 101342.

Almanifi, O. R. A., Chow, C. O., Tham, M. L., Chuah, J. H., & Kanesan, J. (2023). Communication and computation efficiency in federated learning: A survey. *Internet of Things*, 22, 100742.

Cheng, X., Li, C., & Liu, X. (2022). A review of federated learning in energy systems. *2022 IEEE/IAS industrial and commercial power system Asia (I&CPS Asia)*, 2089-2095.

Dang, X. T., Vu, B. M., Nguyen, Q. S., Tran, T. T. M., Eom, J. S., & Shin, O. S. (2024). A survey on energy-efficient design for federated learning over wireless networks. *Energies*, 17(24), 6485.

Dolatabadi, A., Abdeltawab, H., & Mohamed, Y. A. R. I. (2024). SFNAS-DDPG: A Biomass-Based Energy Hub Dynamic Scheduling Approach via Connecting Supervised Federated Neural Architecture Search and Deep Deterministic Policy Gradient. *IEEE Access*, 12, 7674-7688.

Duplančić Leder, T., Baučić, M., Leder, N., & Gilić, F. (2023). Optical satellite-derived bathymetry: An overview and WoS and Scopus bibliometric analysis. *Remote sensing*, 15(5), 1294.

Forootan, M. M., Larki, I., Zahedi, R., & Ahmadi, A. (2022). Machine learning and deep learning in energy systems: A review. *Sustainability*, 14(8), 4832.

Hosseini, P., Taheri, S., Akhavan, J., & Razban, A. (2023). Privacy-preserving federated learning: Application to behind-the-meter solar photovoltaic generation forecasting. *Energy Conversion and Management*, 283, 116900.

Kaleem, S., Sohail, A., Babar, M., Ahmad, A., & Tariq, M. U. (2024). A hybrid model for energy-efficient Green Internet of Things enabled intelligent transportation systems using federated learning. *Internet of Things*, 25, 101038.

Kausar, F., Al-Hamouz, R., & Hussain, S. (2024). Energy demand forecasting for electric vehicles using blockchain-based federated learning. *IEEE Access*, 12,

41287-41298.

Kim, M., Saad, W., Mozaffari, M., & Debbah, M. (2023). Green, quantized federated learning over wireless networks: An energy-efficient design. *IEEE transactions on wireless communications*, 23(2), 1386-1402.

Li, Y., Li, J., & Wang, Y. (2021). Privacy-preserving spatiotemporal scenario generation of renewable energies: A federated deep generative learning approach. *IEEE Transactions on Industrial Informatics*, 18(4), 2310-2320.

Li, Y., Wang, R., Li, Y., Zhang, M., & Long, C. (2023). Wind power forecasting considering data privacy protection: A federated deep reinforcement learning approach. *Applied Energy*, 329, 120291.

Li, Y., Wei, X., Li, Y., Dong, Z., & Shahidehpour, M. (2022). Detection of false data injection attacks in smart grid: A secure federated deep learning approach. *IEEE Transactions on Smart Grid*, 13(6), 4862-4872.

Li, Y., Xu, Z., Wang, X., & Wang, X. (2020). A bibliometric analysis on deep learning during 2007–2019. *International Journal of Machine Learning and Cybernetics*, 11(12), 2807-2826.

Liu, D., & Simeone, O. (2020). Privacy for free: Wireless federated learning via uncoded transmission with adaptive power control. *IEEE Journal on Selected Areas in Communications*, 39(1), 170-185.

Lu, Y., Huang, X., Zhang, K., Maharjan, S., & Zhang, Y. (2020). Communication-efficient federated learning for digital twin edge networks in industrial IoT. *IEEE Transactions on Industrial Informatics*, 17(8), 5709-5718.

Mendes, N., Mendes, J., Mohammadi, J., & Moura, P. (2024). Federated learning framework for prediction of net energy demand in transactive energy communities. *Sustainable Energy*, Grids and Networks, 40, 101522.

Moayyed, H., Moradzadeh, A., Mohammadi-Ivatloo, B., Aguiar, A. P., & Ghorbani, R. (2022). A cyber-secure generalized supermodel for wind power forecasting based on deep federated learning and image processing. *Energy Conversion and Management*, 267, 115852.

Otoum, S., Al Ridhawi, I., & Mouftah, H. (2022). A federated learning and blockchain-enabled sustainable energy trade at the edge: A framework for industry 4.0. *IEEE Internet of Things Journal*, 10(4), 3018-3026.

Passas, I. (2024). Bibliometric analysis: the main steps. Encyclopedia, 4(2).

Samarakoon, S., Bennis, M., Saad, W., & Debbah, M. (2019). Distributed federated learning for ultra-reliable low-latency vehicular communications. *IEEE Transactions on Communications*, 68(2), 1146-1159.

Sarker, M. A. A., Shanmugam, B., Azam, S., & Thennadil, S. (2024). Enhancing smart grid load forecasting: An attention-based deep learning model integrated with federated learning and XAI for security and interpretability. *Intelligent Systems with Applications*, 23, 200422.

Su, Z., Wang, Y., Luan, T. H., Zhang, N., Li, F., Chen, T., & Cao, H. (2021). Secure and efficient federated learning for smart grid with edge-cloud collaboration. *IEEE Transactions on Industrial Informatics*, 18(2), 1333-1344.

Vaezi, M., Azari, A., Khosravirad, S. R., Shirvanimoghaddam, M., Azari, M. M., Chasaki, D., & Popovski, P. (2022). Cellular, wide-area, and non-terrestrial IoT: A survey on 5G advances and the road toward 6G. *IEEE Communications Surveys & Tutorials*, 24(2), 1117-1174.

Wang, R., Bai, L., Rayhana, R., & Liu, Z. (2024). Personalized federated learning for buildings energy consumption forecasting. *Energy and Buildings*, 323, 114762.

Wen, M., Xie, R., Lu, K., Wang, L., & Zhang, K. (2021). FedDetect: A novel privacy-preserving federated learning framework for energy theft detection in smart grid. *IEEE Internet of Things Journal*, 9(8), 6069-6080.

Yang, Z., Chen, M., Saad, W., Hong, C. S., & Shikh-Bahaei, M. (2020). Energy efficient federated learning over wireless communication networks. *IEEE Transactions on Wireless Communications*, 20(3), 1935-1949.

Zhang, C., Xie, Y., Bai, H., Yu, B., Li, W., & Gao, Y. (2021). A survey on federated learning. *Knowledge-Based Systems*, 216, 106775.

Zhang, W., Yang, D., Wu, W., Peng, H., Zhang, N., Zhang, H., & Shen, X. (2021). Optimizing federated learning in distributed industrial IoT: A multi-agent approach. *IEEE Journal on Selected Areas in Communications*, 39(12), 3688-3703.

Zheng, R., Sumper, A., Aragüés-Peñalba, M., & Galceran-Arellano, S. (2024). Advancing power system services with privacy-preserving federated learning techniques: A review. *IEEE access*, 12, 76753-76780.

11. BÖLÜM

FISHBONE TECHNIQUE FOR CAUSE-AND-EFFECT ANALYSIS OF BIOLOGICAL RISKS IN MUSEUM TEXTILES

Seda ŞANSAL POLAT
Marmara University Goztepe Campus, 34722 İstanbul, Turkey
sedasansall@gmail.com

Asst. Prof. Dr. Ferhat GÜNGÖR
Marmara University Goztepe Campus, 34722 İstanbul, Turkey
(ferhatgungor@gmail.com)

Assoc. Prof. Dr. Meral ÖZOMAY
Marmara University, Research and Devoelopment Center for
Textile and Manuscript Heritage
meralozomay@gmail.com
https://orcid.org/0000-0003-0138-0060

1. INTRODUCTION

Museum textiles are highly susceptible to biological activity because of their organic origin. Biological pests such as mould, bacteria, and insects can cause irreversible damage to the fiber structure of the textiles. This study aimed to identify the main causes of biological risk for textile artifacts in museum collections. In this context, the Fishbone (Ishikawa) diagram was used to analyze the different sources causing biological activity. Thanks to this method, root causes have been evaluated under the main causes. Accordingly, it has been shown that early detection and monitoring of biological activity risks plays a critical

role in increasing the effectiveness of preventive conservation procedures. The findings indicate that a risk-based approach should be adopted for the long-term preservation of museum textiles.

The basic raw material used in textiles is fiber. According to the Textile Institute's definition, fiber is characterized by elasticity and fineness, and has a high length/fineness (diameter) ratio (Hockenberger, 2004). All fibers, whether obtained directly from nature or through chemical processes (Hockenberger, 2004) (except for inorganic fibers), are carbon compounds with a polymer structure (Başer, 2002). The number of monomers in polymers is called the "degree of polymerization" (Başer, 2002). Polymers exhibit a crystalline and amorphous mixture in their structure, with parallel arrangements in some regions of the fiber and an irregular arrangement in others. (Başer, 2002; Hockenberger, 2004). The region with parallel and regular arrangement is called the "crystalline region," while the region with irregular and complex arrangement is called the "amorphous region." The ratio of amorphous and crystalline regions is characteristic of each fiber type and affects the structural properties (Table 1) (Başer, 2002).

Table 1. Differences Between Amorphous and Crystalline Regions.

Fibers with a High Amorphous Regions Ratio	Fibers with a High Crystalline Region Ratio
Highly absorbent structure	Less absorbent structure
Less durable	More durable
More susceptible to chemical reagents	More resistant to chemical reagents
Easier to paint	More difficult to paint
Softer touch	Harsh feel
Plastic and easily bendable.	Difficult bending

Fibers obtained directly from nature are classified into two categories based on their source, plant fibers and animal fibers (Başer, 2002).

1.1. Plant (Cellulosic) Fibers

Wood is 40% cellulose by weight, flax is 60-85%, and cotton is 85-90% cellulose. Fibers such as hemp, flax, and jute contain lignin and pectin along with

cellulose. According to elemental analysis, cellulose contains 44.4% Carbon (C), 6.2% Hydrogen (H), and 49.4% Oxygen (O). Its empirical formula is given as $(C_6H_{10}O_5)n$. The formula indicates that cellulose is a carbohydrate (Başer, 2002). Cellulose fibers have hygroscopic properties. The amount of hygroscopic moisture in the fiber can vary greatly depending on the humidity of the air (Tarakçıoğlu, 1979).

1.1.1.Cotton

Raw cotton contains cellulose along with oils and waxes, hemicellulose, pectin, and proteins. The proportions of these substances in cotton are given in Table 2.

Table 2. Composition of Cotton

Substance	Rate (%)
Cellulose	%88-96
Hemicellulose and Pectin	%4-6
Protein and Coloring Substances	%1,5-5
Inorganic Substances	%1-1,2
Wax and Oils	%0,5-0,6

Cotton's polymer structure degrades due to UV radiation from sunlight, airborne oxygen, humidity, and polluted air conditions. It easily absorbs moisture from the air. Sunlight combined with hot and humid air, in particular, reduces the durability of cotton material (Başer, 2002).

1.1.2. Flax

Materials made from linen dating back to prehistoric times have been found in settlements along Swiss lake shores and in ancient Egyptian tombs. This reveals that the processes for turning linen into yarn and fabric have been developed for thousands of years. Linen fiber is obtained from the stem and stalk of the plant. Linen contains lignin, a substance not found in cotton. The composition of linen is given in Table 3 (Başer, 2002).

Tablo 3. Composition of Flax

Substance	Rate (%)
Cellulose	%70-85
Hemicellulose	%18,5
Lignin	%2-3
Pectin	%2-7
Wax and Oils	%1-3
Protein	%2-2,5
Inorganic Substances	%0,5-1,5

Linen is more durable than cotton. It has a higher proportion of crystalline regions than cotton. It has a looser, stiffer, and more crunchy handle. Due to its low elasticity, it wrinkles easily. (Başer, 2002)

1.2. Animal Fibers

Fibers obtained from animals for use in textile production belong to this class. Since the building block of these fibers is protein, they are also called protein fibers. They are divided into two subclasses: hair-derived and secretory-derived (Başer, 2002).

Protein: Proteins are polymers whose macromolecules are composed of amino acids. All macromolecules are formed by the polymerization of α-amino acids (Hockenberger, 2004; Başer, 2002). They have high molecular weights. In elemental analysis, they contain carbon, hydrogen, oxygen, nitrogen, and small amounts of sulfur and phosphorus. The characteristic group in protein molecules is the (-CO-NH-) amide bond. This bond is also called a peptide bond (Başer, 2002). Proteins that can form fibers, such as keratin, fibroin, and collagen, are called scleroproteins. (Hockenberger, 2004).

Chemical Properties of Proteins: Proteins are organic compounds. Their properties depend on the amino acids in their structure. Their molecules contain both acidic and basic groups. Compounds that react with both acids and bases are called amphoteric compounds. Amino acids and the proteins they form are amphoteric compounds. Proteins are divided into two different clas-

ses: water-soluble and water-insoluble. insoluble. Water-insoluble proteins are also insoluble in dilute salts, bases, and acids. They all have a fibrillar (linear chain) structure. Wool protein keratin and silk protein fibroin belong to this class (Başer, 2002).

Hair origin fibers: The chemical building block of all hair origin leather fibers is keratin (Başer,2002).

Keratin: Keratin is the main component of wool. It is a complex protein containing all types of side groups in appropriate proportions and in large numbers. (Hockenberger, 2004) . Its structure is composed of carbon, oxygen, hydrogen, nitrogen, and sulfur elements. The high amount of sulfur distinguishes it from other proteins. The main amino acids and their proportions in the chemical structure of keratin are given in Table 4 (Başer, 2002).

Table 4. Amino Acids in Keratin

Amino Acids	Rate (%)
Glutamic acid	%12,2-16
Arginine	%7,1-10,4
Cystine	%11-13,1
Serine	%9,5-11,5
Aspartic Acid	%6,7-7,3
Glycine	%5,8-6,5
Alanine	%4,4-5,5
Leucine	%7,6-8,1
Tyrosine	%4-6,1
Pyrroline	%7,5-8,1
Threonine	%6,6-7,0

In the keratin chain, these acids are linked to each other by chemical bonds.

Peptide Bonds: These are covalent bonds formed when amino acids polymerize to form proteins.

Salt Bonds: In amino acid units, some R side groups contain acidic (-COOH)

or basic (-NH2) groups. If there are carboxyl and amino groups that have not participated in peptide bonding on a long protein chain, these free groups form salt bonds with each other. These bonds are ionic in character.

Sistine Bonds: Wool, keratin, and cystine have covalent bonds that form side chains (cross-linked chains). They are formed by the binding of the amino acid cystine to two separate protein chains.

H Bond: The amide (CO-NH-) groups in the keratin chain readily form hydrogen bonds. The carbonyl group forms hydrogen bonds with amino groups at different points in the chain.

Keratin has a crystalline region of 25-30% and an amorphous region of 70-75%, exhibiting a highly irregular structure. These characteristic bonds in the keratin structure determine the physical and chemical properties of hair fibers. It plays an effective role in reactions with chemical reagents (Başer, 2002).

1.2.1.Wool

Wool has a circular cylindrical structure. A coarse fiber also exhibits three layers (Hockenberger, 2004). When a cross-section of a wool fiber is examined, it is seen to consist of an outermost layer of epidermis (cuticle, scale), a middle layer of cortex, and an innermost layer of medulla (Başer, 2002; Hockenberger, 2004).

Epidermis (Cuticle): The epidermis is the outermost surface of the fiber visible under a microscope (Başer, 2002). These lifeless, flattened epithelial cells, resembling fish scales, cover the fiber (Hockenberger, 2004). This appearance can be easily examined under a microscope and is characteristic of identifying wool fibers (Başer, 2002).

The high hydrophobicity of the fiber surface is the reason why this layer makes the surface more resistant to the effects of chemicals and enzymes. On the other hand, weather conditions or mechanical stresses can cause the epicuticle membrane on the surface of the fibers to tear in places (Hockenberger, 2004).

Cortex: The main part of the fiber, located beneath the epithelial cells and making up 90% of the fiber. (Hockenberger, 2004; Başer, 2002). It is not homogeneous. It does not exhibit the same characteristics throughout. It consists of two parts: the middle cortex and the paracortex (Hockenberger, 2004). The structure of cortical cells determines the wool's durability, elastic properties, natural color, and dyeability (Başer, 2002). The middle cortex swells more easily, absorbing chemicals more readily and in greater quantities. It is easily

affected by enzymes and is more easily soluble (Hockenberger, 2004).

Medulla: A narrow channel located in the central part of the cortex. The composition of raw wool obtained from animals (Table 5) and washed wool is quite different (Başer, 2002).

Table 5. Chemical Composition of Raw Wool

Substance	Rate (%)
Keratin (Wool protein)	%33
Dirt and grime	%26
Sweat salts	%28
Wool wax	%12
Inorganic substances	%1

1.2.2.Silk

One of the simplest protein fibers (Hockenberger, 2004) When the cross-section of silk is examined, two distinct structures are seen. (Başer, 2002). The central part consists of fibrous tissue made up of fibroin, secreted from two separate glands, while the outer part is coated with an adhesive substance called sericin, which both binds the two sections together and covers the entire fiber (Başer, 2002; Şahan, 2011; Tarakçıoğlu, 1983). This sticky substance gives the fiber a stiff, rigid, and dull appearance. Therefore, raw silk is dull and stiff. Its color is yellowish-white. This slightly yellowish color is largely due to carotene, xanthophyll, and plant pigments. The chemical composition of raw silk (Table 6) varies depending on the production conditions and the source of the insect (Başer, 2002).

Table 6. Chemical Composition of Silk

Substance	Rate (%)
Fibroin	%63-67
Sericin	%22-25
Water	%7-11
Wax	%0,5-11
Inorganic Substances	%1-1,7

Fibroin: Fibroin is the protein that is the main component of silk. It has a fibrous structure and is insoluble in water. Its chemical composition includes a total of sixteen amino acids. The main amino acids that make up fibroin are given in Table 7 (Başer, 2002).

Table 7. Structure of Fibroin

Amino acid	Rate (%)
Glycine	%30-36
Alanine	%18-20
Serine	%7,8-10
Tyrosine	%14,7

Due to the high ratio of glycine and alanine in the structure, the molecule exists in the β-form. The β-form fibroin chains are folded. This structure increases the likelihood of crystalline region formation (Başer, 2002). The majority of fibroin is crystalline (Tarakçıoğlu, 1983), accounting for 65-70% (Başer, 2002).

Sericin: Sericin is the second protein component of silk (Table 8). It coats the fibroin, the main component of the fiber. It is soluble in water, acidic and basic solutions. It can be removed from raw silk by processes such as degumming. As a result of this process, the silk acquires a soft and lustrous appearance (Başer, 2002).

Table 8. Structure of the Sericin

Amino acid	Rate (%)
Glycine	%3,5-5,8
Alanine	%3,7-9,2
Serine	%30,1
Tyrosine	%3,2-5,7
Aspartic Acid	% ~9
Glutamic Acid	% ~2,5
Arginine	% ~3,7
Tyrosine	% ~3,8

1.3. The Biological Degradation Process of Historical Textiles

Textile fibers are complex polymeric materials and are subject to a range of aging processes (Smith, 1999). The main degradation factors that cause textile materials to deteriorate are light, air pollution, microorganisms, insects, chemical attack, mechanical effects, and contamination (Smith, 1999).

The mechanical and chemical properties of textile fibers composed of natural polymers are altered from time to time not only by environmental factors such as heat, humidity, ozone, and light, but also by microbial colonies (Elmaaref, Marouf, Mohamed, & Wahab, 2023). All textile fibers are at risk of degradation by some biological pests (Tarakçıoğlu, 1983). Mould, bacteria, and moths are the most common biological pests found in museums (Table 9-10). (Özomay, Özomay, Türkmen, & Özhakun, 2021).

Table 9. The Effect of Biological Organisms on Cellulosic Fibers (URL-2, 2008)

Damaging	Cotton	Flax
Mould and Bacteria	*In conditions of high temperature, humidity, and pollution, mould, a type of fungus, and certain bacteria can cause odors, stains, and decay.	-------
Insects	* The larvae of clothing moths and carpet beetles do not attack cellulose. However, contamination in textiles provides a food source for many insects and can cause damage. * Silverfish eat starched cotton.	* Silverfish eat starched flax

Table 10. The Effect of Biological Organisms on Protein Fibers (URL-2, 2008).

Damaging	Silk	Wool
Mould and Bacteria	* It has high resistance to microorganisms	* Mould will form if stored in humid conditions
Insects	* It can be destroyed by carpet beetle larvae.	* It becomes particularly attractive to the larvae of clothing moths and carpet beetles when it is dirty

1.3.1. Mould and Fungal Growth

According to the Turkish Language Association (TDK), mould is a often green fungus that forms on organic materials under the influence of moisture and heat (URL-5) Mould spores are always present and suspended in the air (URL-1, 2008; URL-4, 2022) However, it grows in environments with high relative humidity (Smith, 1999; URL-1, 2008). The risk of mould growth is high at relative humidity above 75% (Smith, 1999). When relative humidity reaches 90%, mould forms in just a few days (URL-1, 2008). Relative humidity levels should not be allowed to reach 90% for more than one or two days (Smith, 1999). Some soils serve as a nutrient source for mould, insects, and other harmful biological activities (URL-3, 2013). Storing textile collections in undisturbed, dark, warm environments with poor air circulation can provide an ideal habitat for insects (URL-3, 2013; URL-1, 2008). When the humidity level is reduced below 60% and air circulation is ensured, the likelihood of mould formation decreases (URL-1, 2008). Ideal temperature settings are also important to prevent mould formation (URL-1, 2008). Bacteria are usually carried by contaminated floodwaters or can form in stagnant water in buildings. They can also be transmitted through the air and other particles (URL-4, 2022).

Textile fibers, due to their hygroscopic nature, react rapidly to relative humidity in the atmosphere. They lose or gain water depending on increases or decreases in relative humidity (Smith, 1999). Due to their hygroscopic nature, cellulosic fabrics are very susceptible to fungal growth. The presence of light

and oxygen promotes fungal growth. UV radiation causes oxidation of bonds in the amorphous region of the fibers. The broken bonds allow fungi to penetrate the lumen where they can multiply (Mazzon, 2020). Mould poses a risk to both cellulosic and protein-based textile materials (URL-1, 2008).

The destructive stage of mould is the fungal fibers (URL-4, 2022). Mould growth on textile surfaces causes acidity. Mould leaves black or gray stains composed of thousands of tiny fibers that are inseparable from the textile fibers. The textile material weakens and becomes contaminated with the excrement of organisms (Landi, 1992) or leads to consequences such as complete destruction (URL-1, 2008). Moulds use the surface on which they grow as a food source by digesting it. (URL-4, 2022). Although cellulosic fibers are particularly susceptible, protein fibers can also be affected. Dirt, stains, and starchy finishes provide a food source for microorganisms. Their presence increases the attraction of microorganisms and causes stains that are impossible to remove. They also weaken textile fibers, potentially even causing them to break down. (URL-1, 2008).

Mould may exhibit a velvety, white or colored growth (Figure 1). This appearance is accompanied by an odor. In the early stages of mould, sporadic disfiguring spots may be visible (URL-1, 2008). To reduce mould growth, adverse environmental conditions such as leaking pipes in storage areas and cracks in windows and exterior walls must be eliminated (URL-1, 2008).

Figure 1. Mould Growth on Textile Surfaces (URL-4, 2022)

1.3.2. Bacterium

They cause biochemical degradation of protein or cellulose-based textile products (Bhatia, Bose, & Patel, 2024). Enzymes from bacteria and other microorganisms break down cellulose. The glycosidic ether bonds of the polymer are broken through degradation. A living organism wants to break down cellulose into smaller products (possibly glucose) that are suitable nutrients. (

Balázsy & Eastop, 1998). In protein-based fibers, they break peptide bonds, leading to a decrease in fiber strength and elasticity (Adel, Ozomay , Ozomay, Massadikova, & Nasir, 2025). Because they are detected later than mould, the problem is usually not limited to the surface (Tarnowski, McNamara, Bearce, & Mitchell, 2004). The presence of contaminants such as sweat and oil stains on the artwork, combined with prolonged high humidity levels, increases the risk of these bacteria adhering to the artwork (Figure 2) (Møllebjerg, Palmén, Gori, & Meyer, 2021). Prolonged exposure to bacteria on textile surfaces can lead to discoloration and staining, which are chemical changes caused particularly by organic acids (Konsa, Kormpaki, & Turu, 2022).

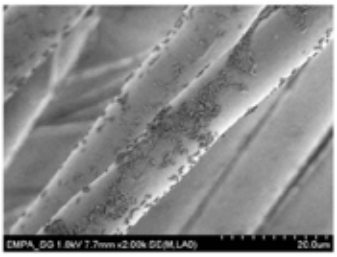

Figure 2. Bacterial Formation on Textile Surfaces. (Hemmatian, Lee, & Kim, 2021)

1.3.3. Moth

Although there are many biological pests affecting wool fibers, the most important of these are: Tineola Bisselliela Hum (webbing clothes moth) (Figure 3), Tinea Pellionella L. (fur moth) (Figure 4), Tricophaga Tapetiella L. (tapeworm moth), Anthrenus Scophularide (common carpet beetle), and Attagenus Pellis L. (fur beetle). Bunlar esas olarak keratin proteinine saldırırlar (Tarakçıoğlu, 1983; Smith, 1999). The webing clothes moth is not very harmful to protein fibers other than wool. The carpet beetle, on the other hand, damages leather, silk, fur, and bird feathers in addition to wool. (Tarakçıoğlu, 1983).

Moth larvae are quite harmful because they consume wool and cause holes in fabrics (Smith, 1999; URL-3, 2013). However, they also eat the fibers on the surface of the fabric, leaving marks (Smith, 1999). If synthetic or cotton fabrics block the path to the food source, the moth will attack them in order to reach the food source (URL-3, 2013).

Figurel 3. Tineola bisselliella
(URL-4, 2022)

Figure 4. Tinea pellionella
(URL-4, 2022)

Adult winged clothes moths do not feed on wool. Their function is reproduction. They lay their eggs, which hatch into maggots or larvae. It is these larvae that damage the wool and cause significant harm (Figure 5) (Basuk & Behera, 201

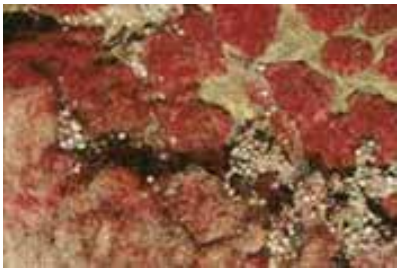

Figure 5. Moth Damage (URL-4, 2022)

Silk, being a protein-based material, is susceptible to damage from heat, light, moisture, chemicals, pollutants, and microorganisms (Yükseloğlu & Canoğlu). Some insects, like booworm, attack silk directly, but most insects chew through silk to reach more attractive materials like wool or leather (Balázsy & Eastop, 1998). Silverfish (Lepisma saccharina) (Figure 6) can damage fabrics as they try to access food sources such as starch present in some cotton textiles. Rodents and other animals gnaw, tear, and soil textiles (URL-3, 2013).

Figure 6. Lepisma saccharina (URL-4, 2022)

Uncontrolled nesting activities by birds, pollution, insect pests, and dead carcasses will all contribute to the creation of an unhealthy environment. Rodent activity is related to food availability. The fur and droppings of rodents are attractive to insects that feed on keratin and protein. (URL-4, 2022). Strategies for dealing with pests in museums include preventive procedures such as building maintenance and good landscaping. Lower temperatures not only reduce chemical degradation of textiles, but also significantly decrease the incidence of harmful insects. Similarly, low relative humidity offers significant benefits in terms of reducing pest and light damage. (URL-3, 2013; Massadikova, Ozomay, Ozomay, & Hasanova, 2022).

2. THE FISHBONE DIAGRAM

The fishbone diagram is also called an Ishikawa diagram or cause-and-effect diagram. A fishbone diagram resembles the skeleton of a fish. It is a management science technique commonly used in cause-and-effect analysis to identify the causes of a particular problem or phenomenon (Coccia, 2020)

This technique begins by identifying the event. The main categories that caused the event are then identified. (Gören, 2023). The root causes of each category (Gören, 2023) are grouped under the categories in order to systematically analyze the cause-and-effect relationship (Coccia, 2020).

It groups various possibilities. It doesn't just focus on solving problems. It helps improve business processes and reduce costs. The approach helps ensure quality management in the process (Fersi, 2025)

It can show every possible cause of complex events in a single diagram. This is an advantage for in-depth scientific analysis. The diagram shows the cause of problems in a particular process and the factors influencing those problems from a better perspective (Coccia, 2020) .

The Fishbone diagram visually illustrates the relationship between all possible causes of a focused problem. It creates a common understanding of potential causes and solutions. It ensures the efficient use of time and resources. It generates potential causes for intervention. It makes the scope of the assessment more manageable and applicable. These are all among the advantages of applying this technique (Kumah, Nwogu, Issah, Obot, & Kanamitie, 2024).

Potential hazards in museums will turn into risks if preventive measures are not taken. Risk analysis studies should be given importance to prevent the de-

terioration or loss of historical object. Data obtained from risk analysis studies should be evaluated using quantitative methods such as 5x5 Matrix, Fine-Kinney, Failure Mode and Effects Analysis (FMEA), and statistical analyses, as well as qualitative methods such as SWOT, brainstorming, and fishbone diagrams. Or studies should be conducted using both methods (Kuzucuoğlu, 2014).

In a fishbone diagram, the head represents the problem being focused on. Long bones indicate possible primary causes and their relationship to the problem. Short bones indicate specific contributing causes and their relationship to the primary causes (Kumah, Nwogu, Issah, Obot, & Kanamitie, 2024).

This study focuses on the causes of biological activity observed in museum textiles. Factors causing biological damage have been examined. The root causes underlying the main causes were investigated using the fishbone diagram technique. This method, which is a quality management tool, has been integrated into museum activities.

3. CONCLUSION

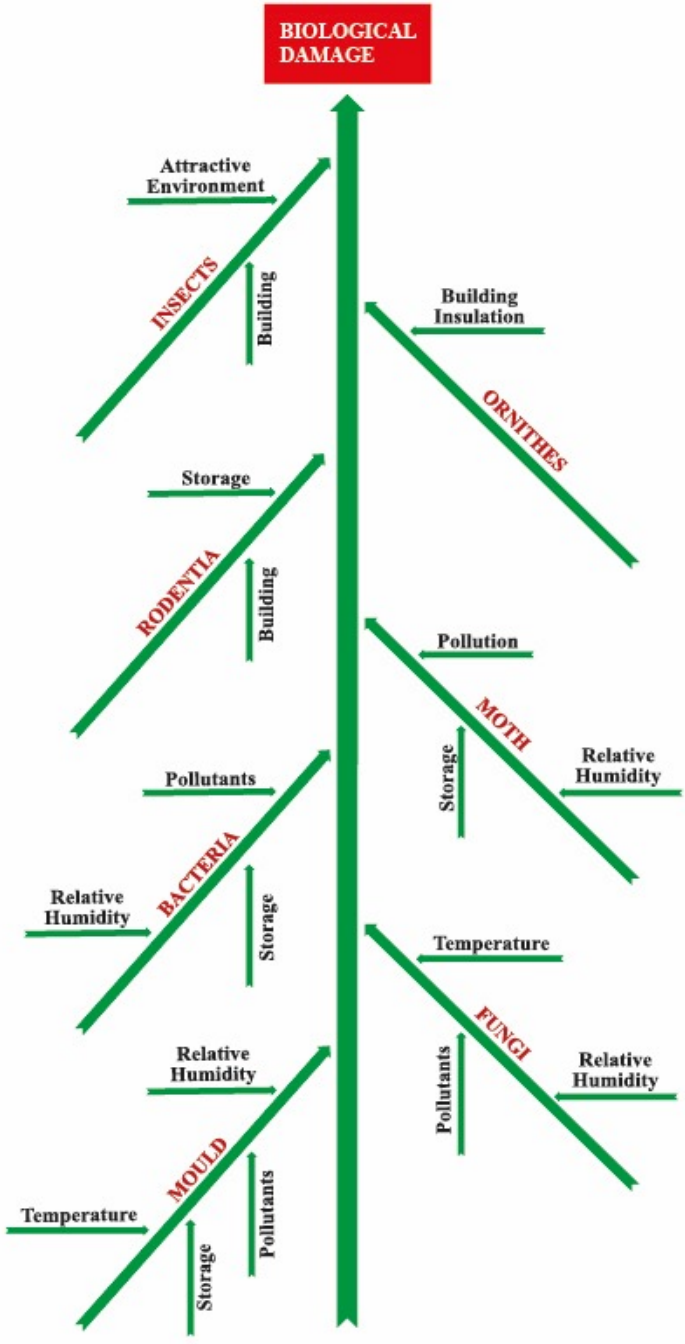

Figure 7. Fıshbone Technıque For Cause-And-Effect Analysıs Of Bıologıcal Rısks In Museum Textıles

The fishbone diagram shows the main causes of biological damage. It also gives specific causes that could lead to these main causes. This approach has provided a framework for identifying risks and prevention methods. Contact points and precautions to be taken have been determined. Adopting a risk-based approach has been shown to allow for the early detection of problems. It has also been shown to enable the effective use of preventive conservation methods. In conclusion, establishing and maintaining pest control procedures for the museum will ensure the efficient use of resources. The most important outcome is that prevention procedures will ensure a longer lifespan for museum textiles.

Acknowledgements

This study was conducted within the scope of project number FDK-2024-11246, supported by the Marmara University Scientific Research Projects Coordination Unit (BAPKO). We would like to thank Marmara University BAPKO for their support.

This study was conducted at the "Textile and Manuscript Conservation and Restoration Application and Research Center," established with project number TR10/18/YMP/0137, supported by İSTKA (Istanbul Development Agency).

REFERENCES

Adel, S., Ozomay , M., Ozomay, Z., Massadikova, G., & Nasir, S. (2025). Microbial Pigments in Fashion, Art, and Packaging. *Microbial ColorantsChemistry,Biosynthesis and aplication*, s. 385-395.

Balázsy, Á. T., & Eastop, D. (1998). *Chemical Principles of Textile Conservation.* London: Routledge.

Basuk , M., & Behera, J. (2018, March 03). *A Review on Woolen Cloth's Moth and its Remedies.* 11 04, 2021 tarihinde Textile Today: https://www.textiletoday.com.bd/review-woolen-cloths-moth-remedies/ adresinden alındı

Başer, İ. (2002). *Elyaf Bilgisi* (2 b.). İstanbul: Marmara Üniversitesi.

Bhatia, T., Bose, D., & Patel, D. (2024). A Review on Cellulose Degrading Microbes and its applications. *Industrial Biotechnology, 20*(1), s. 26-39.

Coccia, M. (2020). Fishbone Diagram for Technological Analysis and Foresight. *Int. J. Foresight and Innovation Policy, 14*(2-3-4), s. 225-247.

Elmaaref, M. A., Marouf, M., Mohamed, W. S., & Wahab, W. A. (2023). A comparative Study for The Effect of Laboratory Aging and Fungal Infection on Properties of Raw and Dyed Linen Textiles. *Advanced Research in Conservation Science, 4*(1), s. 71-83. doi:10.21608/arcs.2023.199033.1037

Fersi, Y. (2025). Cost Optimization Efficiency in Textile Industry. *Vilnius Universty Business School International Project Management Programme*.

Gören, N. (2023). Causes of Qulity Errors in Production Processes and Quality Improvement Techniques. *ETU Synthesis Journal of Economic and Administrative Sciences*(11), s. 21-44. doi:10.47358/sentez.2023.38

Hemmatian, T., Lee, H., & Kim, J. (2021). Bacteria Adhesion of Textiles Influenced by Wettability and Pore Characteristics of Fibrous Substrates. *Polymers, 13*(2), s. 223.

Hockenberger, A. (2004). *Tekstil Fiziği.* İstanbul: Alfa/Aktüel Kitabevi.

Konsa, K., Kormpaki, T., & Turu, J. (2022). Biologial Damage to Textile and Prevention Methods. *Handbook of Museum Textile, 2*, s. 23-43.

Kumah, A., Nwogu, C. N., Issah, A.-R., Obot, E., & Kanamitie, D. T. (2024). Cause-and-Effect (Fishbone) Diagram: A Tool for Generating and Organizing Quality Improvement Ideas. *Glob J Qual Saf Healthc, 7*, s. 85-87. doi:10.36401/JQSH-23-42

Kuzucuoğlu, A. H. (2014). Arşiv ve Kütüphanelerdeki Risklere Yönelik Pasif Korumanın Önemi. *Türk Kütüphaneciliği, 28*(3), s. 338-351.

Landi, S. (1992). *The Textile Conservator's Manual* (Second Edition b.). London: Routledge.

Massadikova, G., Ozomay, M., Ozomay, Z., & Hasanova, R. (2022). Analytıcal Charactaerization of Bible and Textile Artıfacts Fom Sinope Balatlar Church Excavitions for Conservation Purposes. *Mediterranean Archaeology and Archaeometry, 22*(3).

Mazzon, G. (2020). Protective Treatments in Fabrics Conservation. *Universitá Degli Studi di Trieste Universitá Ca' Foscari di Venezia*.

Møllebjerg, A., Palmén, L., Gori, K., & Meyer, R. L. (2021). the Bacterial Life Cycle in Textiles is Governed by Fiber Hydrophobicity. *Microbiology Spectrum, 9*(2).

Özomay, M., Özomay, Z., Türkmen, F. N., & Özhakun, Ö. (2021). Kültürel Değerlerimiz Tekstil ve Yazma Eserlerde Tahribatsız ve Mikroanaliz Yöntemleri. *Kültür Tarihi ve Disiplinlerarası Sanat/Tasarım* (Cilt 1, s. 201-214). içinde Artikel Akademi.

Smith, A. W. (1999). An Introduction to Textile Materials: Their Structure, Properties and Deterioration. *Journal of the Society of Archivists, 20*(1), s. 25-39. doi:10.1080/003798199103703

Şahan, Ü. (2011). *İpekböcekçiliği* (1. b.). Bursa: Dora .

Tarakçıoğlu, I. (1979). *Tekstil Terbiyesi ve Makinaları* (Cilt 1). İzmir: Ege Üniversitesi Matbaası.

Tarakçıoğlu, I. (1983). *Tekstil Terbiyesi ve Makineleri* (Cilt 2). Bursa: Uludağ Üniversitesi Basımevi.

Tarnowski, A., McNamara, C., Bearce, K., & Mitchell, R. (2004). Sticky Microbes and Dust on Objects in Historic Houses. *In american Institue for the Conservation of historic and Artistic Works (AIC) 32nd Annual Meeting*, (s. 9-14). Portland.

URL-1. (2008). *Mould Growth on Textiles – Canadian Conservation Institute (CCI) Notes 13/15*. Aralık 26, 2025 tarihinde Canada Conservation Institue: https://www.canada.ca/en/conservation-institute/services/conservation-preservation-publications/canadian-conservation-institute-notes/mould-growth-textiles.html adresinden alındı

URL-2. (2008). *Natural Fibres – Canadian Conservation Institute (CCI) Notes 13/11*. Aralık 27, 2025 tarihinde Canada conservation Institue: https://www.canada.ca/en/conservation-institute/services/conservation-preservation-publications/canadian-conservation-institute-notes/natural-fibres.html adresinden alındı

URL-3. (2013). *Textiles and the Environment – Canadian Conservation Institute (CCI) Notes 13/1*. Aralık 27, 2025 tarihinde Canada Conservation Insitue: https://www.canada.ca/en/conservation-institute/services/conservation-preservation-publications/canadian-conservation-institute-notes/textiles-environment.html adresinden alındı

URL-4. (2022). *Agent of Deterioration: Pests*. Aralık 27, 2025 tarihinde Canada Conservation Institue: https://www.canada.ca/en/conservation-institute/services/agents-deterioration/pests.html adresinden alındı

URL-5. (tarih yok). Aralık 27, 2025 tarihinde TDK Sözlük: https://sozluk.gov.tr/ adresinden alındı

Yükseloğlu, S. M., & Canoğlu, S. (tarih yok). Silk Fibre Degradation and Analysis by Proteomics . *Annals of The Universty of Oradea Fascicle of Textiles, Leatherwork*.